

**New Formulation for Noble Metal (Au, Pd)  
Supported Metal Oxides and Their  
Catalytic Applications**

**Thesis Submitted to AcSIR  
For the Award of Degree of  
DOCTOR OF PHILOSOPHY  
In  
Chemical Sciences**



**By  
Yogita**

**Registration Number: 10CC13A26025**

**Under the Guidance of**

**Dr. Vinod C. Prabhakaran**

**CSIR-National Chemical Laboratory**

**Pune-411008, India**



# सीएसआईआर - राष्ट्रीय रासायनिक प्रयोगशाला

(वैज्ञानिक तथा औद्योगिक अनुसंधान परिषद)

डॉ. होमी भाभा मार्ग, पुणे - 411 008. भारत



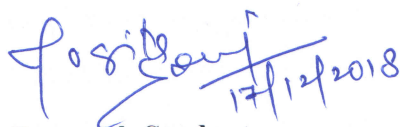
## CSIR - NATIONAL CHEMICAL LABORATORY

(Council of Scientific & Industrial Research)

Dr. Homi Bhabha Road, Pune - 411 008, India

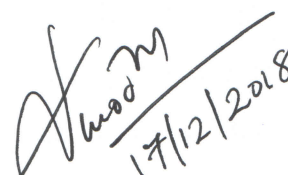
### CERTIFICATE

This is to certify that the work incorporated in this PhD thesis entitled “*New Formulation for Noble Metal (Au, Pd) Supported Metal Oxides and Their Catalytic Applications*” submitted by Ms. Yogita to Academy of Scientific and Innovative Research (AcSIR) in fulfilment of the requirements for the award of the Degree of *Doctor of Philosophy* in *Chemical Sciences*, embodies the original research work under my supervision. I further certify that this work has not been submitted to any other University or Institute in part or full for the award of any degree and diploma. Research materials obtained from other sources have been duly acknowledged in the thesis. Any text, illustration, table etc. used in this thesis from other sources have been duly cited and acknowledged.

  
17/12/2018

Research Student

Yogita

  
17/12/2018

Research Guide

(Name and Signature)

Dr. Vinod C. Prabhakaran

डॉ. विनोद सी. प्रभाकरन / Dr. Vinod C. Prabhakaran  
प्रधान वैज्ञानिक, उत्प्रेरक एवं अकार्बनिक रसायन प्रभाग  
Principal Scientist, Catalysis & Inorganic Chemistry Divn.  
सीएसआईआर-राष्ट्रीय रासायनिक प्रयोगशाला  
CSIR - NATIONAL CHEMICAL LABORATORY  
पुणे-411008 भारत / Pune - 411008 India



Communication  
Channels

NCL Level DID : 2590  
NCL Board No. : +91-20-2590 2000  
EPABX : +91-20-2589 3300  
: +91-20-2589 3400

FAX

Director's Office : +91-20-2590 2601  
COA's Office : +91-20-2590 2660  
COS&P's Office : +91-20-2590 2664

WEBSITE

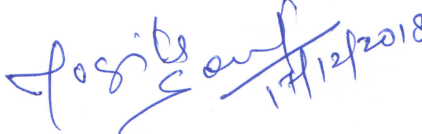
www.ncl-india.org

## DECLARATION

I hereby declare that the work described in the thesis entitled "*New Formulation for Noble Metal (Au, Pd) Supported Metal Oxides and Their Catalytic Applications*" submitted for the degree of *Doctor of Philosophy* in *Chemical Sciences* to the Academy of Scientific and Innovative Research (AcSIR), New Delhi, has been carried out by me at the Catalysis and Inorganic Chemistry Division, CSIR-National Chemical Laboratory, Pune-411008, Maharashtra, India under the supervision of **Dr. Vinod C. Prabhakaran**. I further declare that the material obtained from sources has been duly acknowledged in the thesis. The work presented in this thesis is original and has not been submitted in part or full by me for any other degree or diploma to this or any university/institute.

**Date: 17-12-2018**

**CSIR-National Chemical Laboratory**

  
17/12/2018

**Yogita**

**Research Student**

---

---

## **Acknowledgements**

Accomplishing this thesis work would never have been realized without the encouragement, love and support of some of the incredible people who made this PhD journey a lifetime experience. All the precious moments which I have spent here in CSIR-NCL especially in my CAT & MOSS family will always be cherished. I would like to acknowledge all my teachers, family members, friends and well wishers who always motivated me to complete this long journey with confidence.

First and foremost I would like to express my deepest gratitude and respect to my research supervisor Dr. C. P. Vinod who gave me an opportunity to be a part of this wonderful CAT & MOSS group. I am deeply indebted to him for his constant encouragement, guidance, patience and support throughout my research tenure in NCL. The extensive lab facilities and creative freedom from his side were instrumental to the success of this journey. He always acted like a friend, a philosopher and a true mentor whose thoughtful advices always motivated me to keep going during my most difficult times in research as well as personal life. Thank you sir for believing in me and guiding me at each and every step of my PhD work.

I would like to thank Prof. Ashwini Kumar Nangia, Director NCL, Dr. V. K. Pillai (former director), Dr. C. S. Gopinath, Head of Catalysis Division, Dr. D. Srinivas (former HOD) for providing me opportunity to complete my PhD work in this prestigious laboratory. I thank CSIR for research fellowship. I extend my sincere thanks to Dr. T. Raja, Dr. Nandini Devi, Dr. Dinesh Jagadeeshan, Dr. Ajithkumar and Dr. E. Balaraman for their support. My sincere gratitude goes to my DAC members Dr. B. L. V. Prasad, Dr. Kavita Joshi and Dr. J. Nithyanandan for their timely evaluation and suggestions throughout my PhD program.

I would like to acknowledge Prof. Emiel Hensen for giving me an opportunity to work in the reputed institute, Eindhoven University of Technology (TU/e), The Netherlands. It was a great experience working there which helped me to polish my personality. I would also like to thank Dr. Fernanda TU/e and Prof. Biswajit Chowdhary, IIT-ISM Dhanbad for their suggestions during our collaborations. I also thank Emma for taking care of all the official tasks during my visit to Eindhoven. I thank Lingqian Meng for helping to carry out my research work in Eindhoven. I always miss our hot chocolate session where conversation would range from PhD work discussion to gossiping. I thank all lab mates in TU/e and technical staff for assisting me to finish my work there. And last but not the least I express my heartfelt thanks to Dr. Shamayita Kanungo and Dr. Shauvik De for taking care of me during my stay in Eindhoven. It was a pleasure knowing you both and working with you Shamayita. I will always remember the time we spent together in Eindhoven, and India.

---

---

---

I acknowledge Dr. Dibyendu Bhattacharya and Chandrani Nayak from BARC, Mumbai and RRCAT, Indore for helping me to perform XAS experiments on Synchrotron Beamline. It was a wonderful experience visiting RRCAT and learning the functionality of Synchrotron radiations. I also feel grateful to Dr. Leonard Francis Deepak for carrying out STEM analysis at Iberian Nanotechnology Laboratory, Portugal.

I take this occasion to thank all my seniors in NCL Dr. Sreedhala, Dr. Vysakh, Dr. Sunil Sekhar, Dr. Anish, Dr. Tanmay, for their support and helping me during the initial years of my PhD work. I thank my colleagues Dr. Rikta, Sharad, Preeti, Govind, Sumanata, Mahesh, Besty and Anuradha for creating a family atmosphere and making my PhD tenure easy and joyous. I always appreciate their care and concern towards me. Thank you guys for your love and support. I personally thank all my juniors Shivaganga, Nidheesh, Milda and Bonsy who helped me to put up my thesis in current format. I wish you all the best for your bright future. I also thank all the M.Tech and M. Sc. trainees Shilpa, Vidya, Joes, Cygnet, Neethu, Irine, Aswathy, Yadukiran, Arun, Shebin, Anila for their support. I would like to thank my friends in NCL Garima (my four year roommate, thank you for bearing me for such a long time), Shakuntala, Ragini, Aditya, Dr. Ashok. Dr. Anju, Sudheesh, Manikandan, Aswathy, Periyasami, Prabu M., Prabu K., Manoj, Mahindra, Shrikant, Kavya for their help to complete my work. I thank all the technical staff in NCL Ms. Violet Samuel, Mr. R. K. Jha, Mr. Gholap for helping me to do various characterization. Thanks to all my non-NCL friends Renu, Preeti, Pooja, Garima and Adarsh for always being there during my difficult times.

Finally the most integral part of my life, my parents and my family whose immense love and faith made it possible to complete my thesis successfully. I do not have words to express my gratitude to Mummy and Papa who always gave me freedom, strength and confidence to achieve my goals. Mummy, you are not with me but I know your love and blessings are there which always keep me motivated and determined to pursue my dreams. Sincere thanks to my elder sisters, brother, brother-in-laws and sister-in-law for taking care of me and making me feel protected. I thank Bhawana, my younger sister and my best friend who always stood by me. Lots of thanks and love to my nephews and nieces Ishika, Kanishka, Tanishq, Divyanshi and Rishi for making this journey cheerful.

Above all, praises and thanks to Almighty God for his showers of blessing and granting me the capability to proceed successfully.

**Yogita**

---

---

---

**.....Dedicated to My Parents.....**

---

---

---

## Table of Contents

|  |           |
|--|-----------|
| <b>Chapter 1: General Introduction.....</b>                            | <b>1</b>  |
| <b>1.1 Catalysis.....</b>  | <b>2</b>  |
| <b>1.2 Homogeneous Catalysis.....</b>                                  | <b>3</b>  |
| <b>1.3 Heterogeneous Catalysis.....</b>                                | <b>4</b>  |
| <b>1.4 Metal Nanoparticles in catalysis.....</b>                       | <b>5</b>  |
| <b>1.5 Synthesis of Supported Metal Nanoparticles.....</b>             | <b>6</b>  |
| 1.5.1 Physical Routes.....   | 6         |
| 1.5.2 Chemical Routes.....   | 7         |
| 1.5.2.1 Wet Impregnation.....  | 7         |
| 1.5.2.3 Precipitation.....   | 7         |
| 1.5.2.4 Sol Immobilization.....  | 8         |
| 1.5.2.5 Melt Infiltration.....   | 8         |
| <b>1.6 Common Supports.....</b>  | <b>8</b>  |
| <b>1.7 Catalytic Reactions over Nanostructured Catalysts.....</b>      | <b>9</b>  |
| 1.7.1 CO Oxidation.....  | 9         |
| 1.7.2 H <sub>2</sub> O <sub>2</sub> Mediated Olefin Epoxidation.....   | 11        |
| 1.7.3 CO <sub>2</sub> Hydrogenation.....                               | 12        |
| 1.7.4 Reductive N-alkylation of nitro compounds to N-alkyl amines..... | 13        |
| <b>1.8 Characterization of Nanocatalysts.....</b>                      | <b>14</b> |
| 1.8.1 UV-visible Spectroscopy.....                                     | 14        |
| 1.8.2 X-ray Diffraction.....   | 15        |
| 1.8.3 Fourier Transform Infrared Spectroscopy.....                     | 16        |
| 1.8.4 Raman Spectroscopy.....  | 16        |
| 1.8.5 Nuclear Magnetic Resonance.....                                  | 17        |
| 1.8.6 N <sub>2</sub> Porosimetry.....                                  | 17        |
| 1.8.7 Inductively Coupled Plasma Spectroscopy.....                     | 18        |
| 1.8.8 X-ray Photoelectron Spectroscopy.....                            | 18        |
| 1.8.9 X-ray Absorption Spectroscopy.....                               | 19        |
| 1.8.10 Transmission Electron Microscopy.....                           | 20        |
| 1.8.11 Scanning Electron Microscopy.....                               | 21        |
| <b>1.9 Scope and Objective of the Thesis.....</b>                      | <b>21</b> |

---

|      |                  |    |
|------|------------------|----|
| 1.10 | References ..... | 23 |
|------|------------------|----|

## **Chapter 2: Synthesis of Au@Ti-SiO<sub>2</sub> Nanocatalysts for CO Oxidation and Propene Epoxidation Reactions.**

|          |   |    |
|----------|---|----|
| 2.1      | Introduction.....                                 | 29 |
| 2.2      | Experimental.....                                 | 31 |
| 2.2.1    | Synthesis of Core-Shell Au@SiO <sub>2</sub> ..... | 31 |
| 2.2.2    | Synthesis of Au@Ti-SiO <sub>2</sub> .....         | 31 |
| 2.2.3    | Catalysts Characterization.....                   | 31 |
| 2.2.4    | Catalytic Activity Test.....                      | 34 |
| 2.2.4.1  | CO Oxidation.....                                 | 34 |
| 2.2.4.2  | Propene Epoxidation.....                          | 35 |
| 2.3      | Results and Discussion.....                       | 35 |
| 2.3.1    | X-ray Diffraction Analysis.....                   | 35 |
| 2.3.2    | ICP-AES Analysis.....                             | 36 |
| 2.3.3    | DRUV-visible Spectroscopy Analysis.....           | 36 |
| 2.3.4    | N <sub>2</sub> Porosimetry Analysis.....          | 37 |
| 2.3.5    | Electron Microscopy Studies.....                  | 38 |
| 2.3.6    | IR Spectroscopy Analysis.....                     | 42 |
| 2.3.7    | Raman Spectroscopy Analysis.....                  | 43 |
| 2.3.8    | X-ray Absorption Spectroscopy Study.....          | 45 |
| 2.3.9    | X-ray Photoelectron Study.....                    | 47 |
| 2.3.10   | Catalytic Activity.....                           | 47 |
| 2.3.10.A | CO Oxidation.....                                 | 47 |
| 2.3.10.B | Direct Synthesis of Propene oxide.....            | 52 |
| 2.4      | Conclusion.....                                   | 56 |
| 2.5      | References.....                                   | 59 |

## **Chapter 3: Ligand Exchange Method for Overcoming Deposition Precipitation (DP) Challenges for Making M (Au, Pd)-SiO<sub>2</sub> Catalyst.**

|       |                                       |    |
|-------|---------------------------------------|----|
| 3.1   | Introduction.....                     | 63 |
| 3.2   | Experimental Section.....             | 65 |
| 3.2.1 | Synthesis of SBA-15.....              | 65 |
| 3.2.2 | Synthesis of Au/SBA-15 Catalysts..... | 65 |



---

|  |            |
|--|------------|
| 3.2.3 Synthesis of Pd/SBA-15.....  | 66         |
| 3.2.4 Catalysis Characterization.....  | 66         |
| 3.2.5 Catalytic Activity for CO Oxidation.....   | 67         |
| <b>Part 3A. Au/SBA-15 Catalysts for Room Temperature CO Oxidation</b>  |            |
| 3A.1 UV-Visible Spectroscopy Analysis.....   | 68         |
| 3A.2 X-ray Diffraction Analysis.....   | 70         |
| 3A.3 Textural Analysis by N <sub>2</sub> Porosimetry.....  | 71         |
| 3A.4 Transmission Electron Microscopy Study.....   | 72         |
| 3A.5 Raman Analysis.....   | 72         |
| 3A.6 Solid State NMR Study.....  | 73         |
| 3A.7 X-ray Photoelectron Spectroscopy study.....   | 75         |
| 3A.8 CO Oxidation Activity.....  | 77         |
| <b>Part 3B. Pd/SBA-15 Catalyzed Low Temperature CO Oxidation</b>   |            |
| 3B.1 UV-visible Analysis.....  | 83         |
| 3B.2 ICP-AES Analysis.....   | 84         |
| 3B.3 X-ray Diffraction Study.....  | 84         |
| 3B.4 Transmission Electron Microscopy Study.....   | 85         |
| 3B.5 CO Oxidation Activity.....  | 86         |
| <b>3.3 Conclusion.....</b>   | <b>94</b>  |
| <b>3.4 References.....</b>   | <b>96</b>  |
| <br><b>Chapter 4: A Templated Approach for the Synthesis of Mesoporous Titanosilicates as support for gold nanoparticles for H<sub>2</sub>O<sub>2</sub> Mediated Olefin Epoxidation.</b> |            |
| <b>4.1 Introduction.....</b>   | <b>101</b> |
| <b>4.2 Experimental Section.....</b>   | <b>102</b> |
| 4.2.1 Synthesis of Mesoporous Titanosilicate Nanospheres.....  | 102        |
| 4.2.2 Synthesis of Au NPs Supported Titanosilicate Nanospheres.....  | 103        |
| 4.2.3 Catalyst Characterization.....   | 103        |
| 4.2.4 Catalyst Screening for Liquid and Gas Phase Olefin Epoxidation.....  | 104        |
| <b>4.3 Results and Discussions.....</b>  | <b>105</b> |
| 4.3.1 DRUV Analysis.....   | 105        |
| 4.3.2 X-Ray Diffraction Study.....   | 106        |

---

---

|  |            |
|--|------------|
| 4.3.3 N <sub>2</sub> Porosimetry Analysis.....       | 107        |
| 4.3.4 Scanning Electron Microscopy Analysis.....     | 108        |
| 4.3.5 Transmission Electron Microscopy Study.....    | 109        |
| 4.3.6 IR Analysis.....                               | 110        |
| 4.3.7 X-ray Photoelectron Spectroscopy Study.....    | 111        |
| 4.3.8 Catalytic activity for Olefin Epoxidation..... | 112        |
| <b>4.4 Conclusion.....</b>                           | <b>118</b> |
| <b>4.5 References.....</b>                           | <b>120</b> |

## **Chapter 5: Pd/SBA-15 Catalyzed Hydrogenation Reactions**

### **Part 5A. Atmospheric pressure CO<sub>2</sub> hydrogenation over Ti modified Pd/SBA-15 catalyst**

|  |            |
|--|------------|
| <b>5A.1 Introduction.....</b>  | <b>123</b> |
| <b>5A.2 Experimental Section.....</b>                                    | <b>125</b> |
| 5A.2.1 Synthesis of Pd/SBA-15 catalyst.....                              | 125        |
| 5A.2.2 Modification of Pd/SBA-15 with titanium.....                      | 125        |
| 5A.2.3 Catalyst Characterization.....                                    | 125        |
| 5A.2.4 Gas Phase Atmospheric Pressure CO <sub>2</sub> Hydrogenation..... | 126        |
| <b>5A.3 Results and Discussions.....</b>                                 | <b>127</b> |
| 5A.3.1 DRUV Analysis.....  | 127        |
| 5A.3.2 X-ray Diffraction Study.....                                      | 128        |
| 5A.3.3 Transmission Electron Microscopy including EDX.....               | 129        |
| 5A.3.4 N <sub>2</sub> Porosimetry Analysis.....                          | 130        |
| 5A.3.5 X-ray Photoelectron Spectroscopy Study.....                       | 132        |
| 5A.3.6 CO <sub>2</sub> Hydrogenation Activity Results.....               | 135        |

### **Part 5B. Nitrobenzene reduction to N-ethyl aniline over Pd/meso-SiO<sub>2</sub> catalyst.**

|  |            |
|--|------------|
| <b>5B.1 Introduction.....</b>                              | <b>142</b> |
| <b>5B.2 Experimental Methods.....</b>                      | <b>144</b> |
| 5B.2.1 Synthesis of Pd/meso SiO <sub>2</sub> catalyst..... | 144        |
| 5B.2.2 Nitrobenzene Alkylation.....                        | 144        |
| <b>5B.3 Results and Discussions.....</b>                   | <b>144</b> |
| 5B.3.1 DRUV Analysis.....                                  | 144        |

---

|   |            |
|---|------------|
| 5B.3.2 XRD Analysis.....  | 145        |
| 5B.3.3 SEM-EDAX Analysis.....   | 146        |
| 5B.3.4 TEM Analysis.....  | 146        |
| 5B.3.5 Surface Area Analysis by N <sub>2</sub> Porosimetry.....         | 147        |
| 5B.3.6 X-ray Photoelectron Spectroscopy Study.....                      | 148        |
| 5B.3.7 Catalyst Screening for Reductive Alkylation of Nitrobenzene..... | 149        |
| <b>5.1 Conclusion.....</b>  | <b>157</b> |
| <b>5.2 References.....</b>  | <b>159</b> |
| <b>Chapter 6: Summary and Conclusion.....</b>                           | <b>162</b> |
| <b>Appendix.....</b>  | <b>167</b> |
| <b>List of Publications.....</b>  | <b>171</b> |
| <b>About the Author.....</b>  | <b>172</b> |

---

## List of Abbreviations

|         |   |
|---------|---|
| UV-Vis  | Ultraviolet-Visible                                     |
| DRUV    | Diffuse Reflectance Ultraviolet                         |
| XRD     | X-ray Diffraction                                       |
| SEM     | Scanning Electron Microscopy                            |
| TEM     | Transmission Electron Microscopy                        |
| STEM    | Scanning Transmission Electron Microscopy               |
| HAADF   | High Angle Annular Dark Field                           |
| EDAX    | Energy Dispersive X-ray Analysis                        |
| BET     | Brunauer-Emmett-Teller                                  |
| BJH     | Barrett-Joyner-Halenda                                  |
| ICP-AES | Inductively Coupled Plasma Atomic Emission Spectroscopy |
| SSNMR   | Solid State Nuclear Magnetic Resonance                  |
| XPS     | X-ray Photoelectron Spectroscopy                        |
| XAS     | X-ray Absorption Spectroscopy                           |
| XANES   | X-ray Absorption Near Edge Spectroscopy                 |
| EXAFS   | Extended X-ray Absorption Fine Spectroscopy             |
| IR      | Infra Red   |
| GC      | Gas Chromatography                                      |
| TCD     | Thermal Conductivity Detector                           |
| FID     | Flame Ionization Detector                               |
| DP      | Deposition Precipitation                                |
| WI      | Wetness Impregnation                                    |
| SI      | Sol Immobilization                                      |
| PZC     | Point of Zero Charge                                    |
| SBA     | Santa Barbara Amorphous                                 |

---

|       |                                   |
|-------|-----------------------------------|
| MCM   | Mobil Crystalline Materials       |
| KIT   | Korea Institute of Technology     |
| PVP   | Poly Vinyl Pyrrolidone            |
| APTMS | Amino Propyl Trimethoxy Silane    |
| TEOS  | Tetraethyl Ortho Silicate         |
| TIP   | Titanium Tetraisopropoxide        |
| LH    | Langmuir-Hinshelwood              |
| PO    | Propene Oxide                     |
| NPs   | Nanoparticles                     |
| CTAC  | Cetyl Trimethyl Ammonium Chloride |
| SPR   | Surface Plasmon Resonance         |
| FWHM  | Full Width at Half Maxima         |
| FCC   | Face Centred Cubic                |
| RT    | Room Temperature                  |
| RWGS  | Reverse Water Gas Shift           |

---

## List of Figures

| <b>Figure No.</b> | <b>Figure Caption</b>  | <b>Page No.</b> |
|-------------------|--|-----------------|
| 1.1               | Representation of energy profile of a catalysed and uncatalyzed reaction with reaction coordinates.  | 3               |
| 1.2               | Schematic illustration of dependence of band gap on particle size.   | 5               |
| 1.3               | CO <sub>2</sub> hydrogenation to various chemicals and fuels.  | 13              |
| 1.4               | Schematic representation of SPR phenomenon in metal NPs.   | 15              |
| 1.5               | Schematic illustration of X-ray absorption edge.   | 20              |
| 2.1               | XRD plots of as synthesized and calcined AS and ATS catalysts.   | 36              |
| 2.2               | DRUV-visible spectra of (a) as synthesised (b) reduced and calcined catalysts.   | 37              |
| 2.3               | N <sub>2</sub> adsorption and pore size distribution of AS and ATS catalysts.  | 38              |
| 2.4               | TEM images of (a, b) AS (c, d) ATS 50 and (e, f) ATS 10 catalysts.   | 39              |
| 2.5               | HRTEM image of (a) ATS 50 (no phase segregated TiO <sub>2</sub> particles) (b) ATS 10 showing the presence of phase separated TiO <sub>2</sub> .             | 40              |
| 2.6               | (a) HAADF-STEM image of ATS 50. (b-f) STEM-EDS mapping of individual elements.   | 41              |
| 2.7               | (a) HAADF-STEM image of ATS 10. (b-f) STEM-EDS mapping of individual elements.   | 41              |
| 2.8               | TEM images of ATS 5 catalyst.  | 42              |
| 2.9               | IR spectra of AS and ATS catalysts.  | 43              |
| 2.10              | Raman and UV Raman spectra of ATS 10 and 50 catalysts in different regions. 632 nm and 234 nm Lasers were used for Raman and UV-Raman analysis respectively. | 44              |
| 2.11              | XANES and EXAFS spectra of ATS samples.  | 46              |
| 2.12              | Ti 2p XPS plot for ATS 50 calcined and reduced catalyst.   | 47              |

|              |   |    |
|--------------|---|----|
| <b>2.13</b>  | CO oxidation activity of AS and ATS calcined and reduced catalyst   | 48 |
| <b>2.14</b>  | CO Oxidation activity of ATS catalyst after reduction.  | 50 |
| <b>2.15</b>  | Time on Stream CO oxidation plot of ATS 10 and 50 at 100 °C.  | 51 |
| <b>2.16</b>  | TEM images of spent (a) ATS 50 and (b) ATS 10 catalysts.  | 51 |
| <b>2.17</b>  | Possible reaction mechanism of propene epoxidation on Au-Ti system.   | 53 |
| <b>2.18</b>  | (a) Comparison of conversion of propylene and selectivity for PO and<br>(b) Selectivity of all the products over ATS catalysts at 200 °C. | 54 |
| <b>3A.1</b>  | UV-visible spectra of Au precursor compared with precursor modified with NH <sub>4</sub> Cl of different millimoles in liquid state.      | 69 |
| <b>3A.2</b>  | DRUV spectra of AS-x (a) as synthesized (b) calcined catalysts.   | 69 |
| <b>3A.3</b>  | (a) Small angle XRD (b) Wide angle XRD of as synthesized and (c) calcined AS catalysts.   | 70 |
| <b>3A.4</b>  | N <sub>2</sub> adsorption-desorption isotherms of AS catalysts.   | 71 |
| <b>3A.5</b>  | TEM images of (a) AS 1 (b) AS 2 (c) AS 3 (d) AS 4 nanocatalysts along with particle size distribution.                                    | 72 |
| <b>3A.6</b>  | Raman spectra of gold complex in different conditions.  | 73 |
| <b>3A.7</b>  | <sup>15</sup> N and <sup>1</sup> H solid state NMR spectra of AS 4 compared with <sup>15</sup> NH <sub>4</sub> Cl and SBA-15.             | 74 |
| <b>3A.8</b>  | <sup>1</sup> H solid state NMR of pristine NH <sub>4</sub> Cl.  | 75 |
| <b>3A.9</b>  | XPS analysis of Au 4f and N 1s core levels under different conditions.  | 76 |
| <b>3A.10</b> | Comparison of CO oxidation activity of AS x samples.  | 78 |
| <b>3A.11</b> | (a) Arrhenius plot for activation energy calculation of AS 4 (b) Time on stream plot of AS 4 catalyst at room temperature and 200 °C.     | 78 |
| <b>3A.12</b> | TOS plot of AS 4 catalyst at room temperature at double GHSV.   | 81 |
| <b>3A.13</b> | TEM images with particle size histogram of spent AS 4 catalyst after 48 h TOS. Scale Bar- 50 nm.  | 81 |
| <b>3A.14</b> | (a) TEM image of AS 4 catalyst calcined at 600 °C (b) Catalytic activity comparison of AS 4 catalyst calcined at 400 and 600 °C.          | 82 |

|              |  |     |
|--------------|--|-----|
| <b>3A.15</b> | Comparison of CO oxidation activity of AS 4 catalyst with AS NH <sub>4</sub> OH catalyst.  | 82  |
| <b>3B.1</b>  | UV visible spectra of (a) Pd precursor in liquid state (b) supported Pd-SBA-15 in solid state.   | 83  |
| <b>3B.2</b>  | XRD analysis of Pd/SBA-15 catalyst synthesized via different methods.  | 84  |
| <b>3B.3</b>  | TEM images of (a, b)Pd-S-N (c) Pd-S-NaOH (d) Pd-S-WI catalysts. Yellow arrows show the Pd NPs.   | 85  |
| <b>3B.4</b>  | Particle size calculation from TEM images of different Pd/SBA-15 catalyst.   | 86  |
| <b>3B.5</b>  | CO oxidation activity of calcined Pd/SBA-15 catalysts synthesized by different methods (a) temperature dependent CO conversion (b) activation energy of different catalysts. | 87  |
| <b>3B.6</b>  | (a) Comparative XPS plots of (a) calcined (b) spent Pd/SBA-15 catalysts and (c) comparison of % Pd species in fresh and spent calcined catalysts as calculated from XPS.     | 88  |
| <b>3B.7</b>  | Comparison of Pd-S-N calcined and reduced catalysts (a) CO oxidation activity (b) time on stream plots at 115 °C and 90 °C respectively.                                     | 89  |
| <b>3B.8</b>  | Comparison of CO Oxidation activity of different reduced catalysts.  | 89  |
| <b>3B.9</b>  | XPS spectra of (a) reduced and (b) spent catalysts (c) comparison of different Pd species in reduced and spent catalyst.   | 90  |
| <b>3B.10</b> | TEM analysis of reduced Pd-S-N catalyst after 24 h time on stream reaction.  | 91  |
| <b>4.1</b>   | UV-visible spectra of (a) TS x and (b) AuTS x catalysts.   | 105 |
| <b>4.2</b>   | XRD analysis of TS and AuTS x catalysts.   | 106 |
| <b>4.3</b>   | N <sub>2</sub> adsorption desorption isotherms of TS-x catalysts compared with silica alone.   | 107 |
| <b>4.4</b>   | SEM images of (a) SiO <sub>2</sub> Nanospheres (b) TS-150 (c) TS-100 (d) TS 50 and (e) TS-100 N.   | 108 |
| <b>4.5</b>   | TEM images of (a) TS 150 (b) AuTS 150 (c) TS 100 (d) AuTS 100 (e) TS 50 (f) AuTS 50 (g, h) TS 100 N. Yellow arrows show Au NPs.  | 109 |
| <b>4.6</b>   | IR spectra of TS x catalysts compared with SiO <sub>2</sub> and TS 100 N.  | 110 |



|              |   |     |
|--------------|---|-----|
| <b>4.7</b>   | (a) Ti 2p XPS spectra of TS x catalysts (b) relative fraction of different titanium species present in different catalysts.   | 111 |
| <b>4.8</b>   | (a) Selectivity of different products and (b) yield of PO on AuTS x catalysts at 423 K.   | 115 |
| <b>4.9</b>   | Stability test of AuTS 100 catalyst under reaction conditions at different temperatures.  | 118 |
| <b>5A.1</b>  | DRUV spectra of PdTS-x catalysts with different titanium content.   | 127 |
| <b>5A.2</b>  | XRD analysis of Pd/SBA-15 and PdTS-x catalysts.   | 128 |
| <b>5A.3</b>  | TEM images of (a, b) Pd/SBA-15 (c) PdTS-50 (d) PdTS-25 (e) PdTS-10 (f) PdTS-5 and (g) PdTS-1 and (h) Pd/TiO <sub>2</sub> catalysts.   | 130 |
| <b>5A.4</b>  | N <sub>2</sub> Adsorption isotherm of PdTS-x catalysts compared with Pd/SBA-15.   | 131 |
| <b>5A.5</b>  | (a) Ti 2p XPS spectra of reduced PdTS-x catalysts compared with Pd/TiO <sub>2</sub> (b) % fraction of different Ti species present in the catalysts. All the catalysts were reduced at 400 °C in H <sub>2</sub> flow. | 132 |
| <b>5A.6</b>  | (a) Pd 3d XPS spectra of reduced PdTS-x, Pd/TiO <sub>2</sub> and Pd/SBA-15 (b) % fraction of different Pd species present in different catalysts.   | 133 |
| <b>5A.7</b>  | XPS spectrum of TS-5 support after reduction.   | 134 |
| <b>5A.8</b>  | (a) CO <sub>2</sub> hydrogenation activity of different catalyst w.r.t temperature (b) comparison of activity and selectivity for CH <sub>4</sub> at 673 K.   | 135 |
| <b>5A.9</b>  | CO <sub>2</sub> hydrogenation activity of PdTS-5 and Pd/TS-5 catalysts.   | 136 |
| <b>5A.10</b> | Comparison of CO and CH <sub>4</sub> selectivity of different catalysts w.r.t. temperature.   | 137 |
| <b>5A.11</b> | Time on stream reaction of PdTS-5 catalyst at 673 K.  | 139 |
| <b>5A.12</b> | TEM images of spent PdTS-5 catalyst after 24 h TOS at 673 K.  | 139 |
| <b>5A.13</b> | (a) Ti 2p (b) Pd 3d XP spectra of spent PdTS-5 catalyst compared with Pd/SBA-15 and Pd/TiO <sub>2</sub> .   | 140 |
| <b>5B.1</b>  | DRUV spectra of different Pd/meso-SiO <sub>2</sub> catalysts after calcination and reduction  | 144 |
| <b>5B.2</b>  | XRD Analysis of Pd/meso-SiO <sub>2</sub> catalysts  | 145 |
| <b>5B.3</b>  | SEM images of (a) Pd-SBA-N-3 (b) Pd-MCM-N-3 (c) Pd-KIT-N-3. The table in the figure shows EDAX results of these catalysts   | 146 |

|              |   |     |
|--------------|---|-----|
| <b>5B.4</b>  | TEM images (a) SBA-15 (b) Pd-SBA-N-3 (c) KIT-6 (d) Pd-KIT-N-3 (e) MCM-41 (f) Pd-MCM-41  | 147 |
| <b>5B.5</b>  | N <sub>2</sub> adsorption-desorption isotherm of silica and Pd supported silica.  | 147 |
| <b>5B.6</b>  | (a) Comparison of XPS spectra of Pd/meso-SiO <sub>2</sub> catalysts after reduction<br>(b) percentage of different Pd species present in different catalysts. | 149 |
| <b>5B.7</b>  | (a) Conversion and (b) selectivity of nitrobenzene to N-ethyl aniline over Pd-SBA-N-3 red catalyst.   | 150 |
| <b>5B.8</b>  | Selectivity for N-ethyl aniline over different Pd/meso-SiO <sub>2</sub> catalysts   | 151 |
| <b>5B.9</b>  | Effect of Pd particle size on the selectivity of N-ethyl aniline.   | 153 |
| <b>5B.10</b> | Effect of Pd loading on the selectivity for Pd-SBA-N catalysts.   | 155 |
| <b>5B.11</b> | XRD analysis of Pd-SBA-N catalyst with different Pd weight loading  | 156 |
| <b>5B.12</b> | Hot filtration test over Pd-SBA-N-3 catalyst to test the heterogeneity of the catalyst.   | 157 |
| <b>A.1</b>   | UV-visible spectra of ATS catalysts   | 168 |
| <b>A.2</b>   | XRD analysis of ATS catalysts   | 168 |

---

## List of Schemes

| <b>Scheme No.</b> | <b>Scheme Caption</b>   | <b>Page No.</b> |
|-------------------|---|-----------------|
| <b>2.1</b>        | Synthesis of Au@SiO <sub>2</sub> /Au@Ti-SiO <sub>2</sub> catalyst via sol gel method  | 32              |
| <b>3.1</b>        | Synthesis of M/SBA-15 catalyst using modified DP method   | 66              |
| <b>4.1</b>        | Synthesis of mesoporous (gold supported) titanosilicate nanospheres   | 103             |
| <b>5A.1</b>       | Possible reaction pathway of CO <sub>2</sub> hydrogenation to CO and CH <sub>4</sub> via RWGS.                                | 137             |
| <b>5B.1</b>       | Nitrobenzene reduction over Pd/meso-SiO <sub>2</sub> catalyst   | 149             |
| <b>5B.2</b>       | Formation of acetaldehyde from ethanol in the presence of H <sub>2</sub> over 10% Pd/C catalysts and corresponding alkylation | 152             |
| <b>5B.3</b>       | Nitrobenzene reduction to N-ethyl aniline using acetaldehyde as alkylation source.  | 153             |

---

## List of Tables

| <b>Table No.</b> | <b>Table Caption</b>   | <b>Page No.</b> |
|------------------|--|-----------------|
| <b>2.1</b>       | Fitting results of EXAFS where $r$ is Ti-O bond distance, C. No. is coordination no. around Ti atom and $\sigma^2$ is the Debye Waller factor. | 46              |
| <b>2.2</b>       | PO formation rates with respect to temperature over ATS 50   | 56              |
| <b>2.3</b>       | Effect of reaction temperature on selectivity to PO over ATS 50 catalyst.  | 56              |
| <b>3A.1</b>      | Textural properties of different AS x catalysts.   | 71              |
| <b>3A.2</b>      | XPS binding energy values of Au precursor in different conditions.   | 77              |
| <b>4.1</b>       | Textural properties of titanosilicate nanospheres  | 108             |
| <b>4.2</b>       | Olefin epoxidation results over TS x catalyst.   | 113             |
| <b>4.3</b>       | Gas phase propene epoxidation with H <sub>2</sub> and O <sub>2</sub> over Au based catalysts.  | 116             |
| <b>4.4</b>       | Activity results of AuTS 100 catalyst at different temperatures.   | 117             |
| <b>4.5</b>       | Selectivity of AuTS 100 for different products at different temperatures   | 117             |
| <b>5A.1</b>      | Textural Properties of PdTS-x catalysts  | 131             |
| <b>5B.1</b>      | Textural properties of Pd/meso-SiO <sub>2</sub> catalysts compared with silica   | 148             |
| <b>5B.2</b>      | Optimization of parameters for reduction of nitrobenzene.  | 150             |
| <b>5B.3</b>      | Catalytic activity for different Pd/SBA-15 catalysts with different Pd size  | 154             |
| <b>5B.4</b>      | Effect of different H-source on the selectivity of N-ethyl aniline   | 156             |
| <b>A.1</b>       | CO Oxidation activity comparison of AS-4 catalysts with reported Au/Silica catalysts   | 169             |
| <b>A.2</b>       | Comparison of CO oxidation activity of Pd-S-N reduced catalyst (synthesised by modified DP) with reported Pd based catalysts.                  | 170             |

# **CHAPTER-1**

## **General Introduction**

## 1.1 Catalysis

Catalysis and catalytic reactions are an integral part of mankind touching almost everything that comes across the day to day life.<sup>1</sup> The term catalysis was coined by Berzelius in 1836 and described it as a new force which is operative for carrying out chemical reactions. The word catalysis has Greek origin which basically means ‘to loosen’. Catalysis – a tool to carry out reactions had already been utilized much earlier in the processes such as fermentation. One of the interesting examples of early catalytic reactions is production of sulphuric acid in small quantities by burning sulphur with nitric acid in the presence of air. Large production of sulphuric acid was realized in 1746 by using lead as the construction material for reaction chambers. Clement and Desormes in 1793 proposed that amount of nitre could be minimized by using additional amount of air which acted as the oxidising agent. Hence they concluded that minimum of nitre could be used to produce large amount of sulphuric acid by using air as the oxidizing agent and nitre is what we would refer as catalyst. At the end of the eighteenth and beginning of nineteenth century various reactions catalysed by catalyst were studied and proved to be milestones. In 1813 Thenard found dissociation of ammonia on various hot metal surfaces. Humphry Davy’s investigation on the oxidation of coal gas in developing miner’s safety lamp was another pioneer work where metals such as platinum and palladium found to be active for combustion of coal gas to CO and CH<sub>4</sub>. Later in 1834 Faraday proposed that reactants have to successfully adsorb on the surface for a chemical reaction but could not fully explain the catalytic action. A refined definition of catalysis was further given by Ostwald in 1909 that the thermodynamic equilibrium of reactants and products is not influenced by catalyst but it actually affects the rates of chemical reactions. The industrial revolution in catalysis happened after Nobel Prize winning work of Fritz Haber and Carl Bosch for ammonia synthesis in 1918 over iron catalyst. Another Noble prize was given in the field of ammonia synthesis in 2007 to Gerhard Ertl for unravelling the details of ammonia synthesis at molecular level using surface science techniques. Various industrial catalytic processes have applications in oil industry, petrochemical industry, exhaust gas technology, polymer production, fine chemical synthesis, etc. Hence it would not be wrong to say that catalytic processes have emerged as a key to many fundamental problems in common man’s life and will continue to do so in coming future also.

A catalyst can be defined as a chemical moiety which can be added to the chemical reaction to speed up the rate of reaction without actually being affected itself in the reaction.

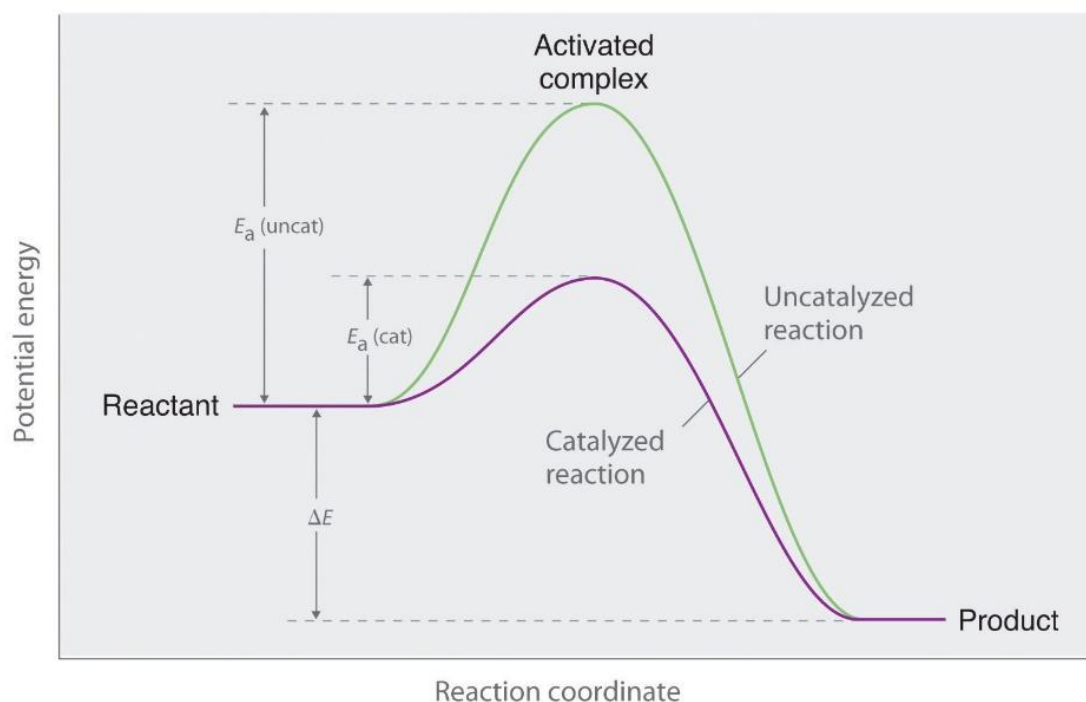


Figure 1.1 Representation of energy profile of a catalyzed and uncatalyzed reaction with reaction coordinates.

The energy profile of the chemical reaction as shown in Figure 1.1 clearly explains the role of catalyst. The activation energy of the transition state can be minimized in the catalysed reaction by diverting the route to a less energy pathway as compared to uncatalyzed reaction but the overall all energy of reaction remains constant irrespective of the reaction pathway followed. Thus by selecting a suitable catalyst the desired chemical reaction can occur in much energy efficient way with an optimum conversion and selectivity.

Based upon the phase of the reaction catalysis can be majorly defined as (i) homogeneous catalysis and (ii) heterogeneous catalysis.

## 1.2 Homogenous Catalysis

In homogeneous catalysis all the reactants and catalysts are present in one phase, usually liquid phase. A large variety of homogeneous catalysts are known but the modern homogeneous catalysis branch has been dominated by organometallic and coordination complexes since these have led to largest number of industrial reactions. Some of the homogenous catalytic reactions are hydroformylation,<sup>2</sup> polymerization of alkenes,<sup>3,4</sup> etc.

### **1.3 Heterogeneous Catalysis**

In heterogeneous catalysis, the catalyst is present in different phase with respect to reactants. Most heterogeneous catalysts are solid and interact with reactants commonly present either in liquid or gaseous phase. Heterogeneous catalysis is preferred over homogeneous catalysis in the ease of catalyst separation and recyclability. Heterogeneous catalysts are typically ‘supported’ where the catalyst is supported on second material (main constituent in quantity) to provide mechanical stability, surface area desired for an optimum catalyst. The active sites in supported heterogeneous catalysis are the atoms or ensemble of atoms or the crystal faces exposed of the metal where actual reaction (bond breaking and bond formation) occurs. The support can provide the effective surface area for optimum dispersion of these active sites and can also interact with these sites. These supports can sometimes play pivotal role in catalysing reaction where the interaction between catalyst and support can alter the rate of reaction in either of the way.

Although the conversion and selectivity are the backbones of any catalytic reaction, the catalyst separation, recyclability and the thermal stability are indispensable to design an efficient, sustainable, economical and thermally stable catalyst. Transition metal nanoparticles (NPs) based catalysis has circumvented the problems associated with homo and heterogeneous catalysis and a new class of catalysis has originated termed as “nanocatalysis”. Metal nanoparticles are the most commonly used nanocatalysts which themselves can be used as catalysts in colloidal form or can be heterogenized by fixing on heterogeneous solid supports. Thus nanocatalysis involves critical properties of both homogeneous and heterogeneous catalysis and can be referred as ‘semi-heterogeneous catalysis’.<sup>5</sup> This unique property of metal NPs based catalysis originates due to the reduction of the size of the metals to the nanometre range. Such size reduction results in the appearance of the quantization effects due to formation of discrete electronic states along with surface atoms with large under coordination. The formation of discrete energy levels (which is a continuum in the bulk form) depending upon the size of nanoparticles (Figure 1.2) ultimately results in altered physical and chemical properties as compared to their bulk counterparts. These nanoparticles can show surprising catalytic activity as compared to bulk due to modified electronic and geometric effects



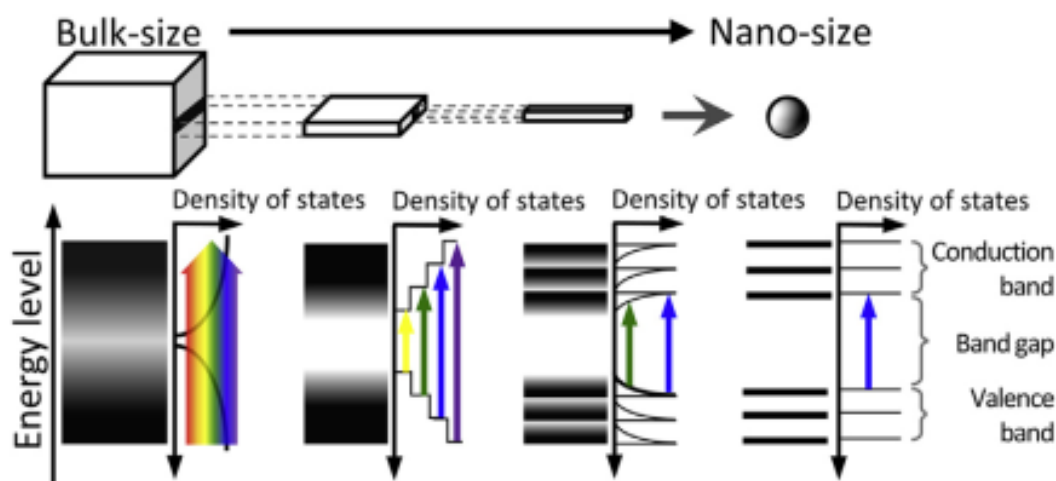


Figure 1.2 Schematic illustration of dependence of band gap on particle size.<sup>6</sup>

#### **1.4 Metal Nanoparticles in Catalysis**

Metal nanoparticles and their supported counterparts can catalyse variety of chemical reactions. Transition metal based noble metal (Au, Pt, Pd, Ru etc.) as well as non-noble metal (Co, Fe, Cu, Ni etc.) NPs are the main nanocatalysts which are used in catalysing many industrial important reactions.<sup>7-9</sup> The unique property of transition metals to show variable oxidation states is one of the reasons which make them most attractive in the field of nanocatalysis. The tunable properties of these metal nanoparticles such as size, shape, composition, support, oxidation state are appealing and can influence the catalytic activity and selectivity.<sup>10-14</sup> Usually the support is present in bulk form but decreasing its size to nano form can impart tremendous changes in the catalytic activity thereby exhibit the functionality of a nanocatalyst in its full sense. Thus fine tuning the size of metal NPs along with support material can tune the properties of nanocatalyst in a positive way by increasing the conversions and controlling the product selectivity.<sup>15,16</sup> Along with size of NPs the crystal facets exposed can alter the reaction rate by inducing different mode of adsorption of reactants and then desorption of product from the surface of the metal active sites.<sup>17,18</sup>

The most important property possessed by the NPs is presence of under coordinated sites. These are basically the atoms whose coordination is not fulfilled due to their nano size. These under coordinated atoms are the catalytic hot spots. Smaller is the size of metal NPs larger will be the under coordinated atoms.<sup>19,20</sup> Also the atoms at edges and corners are generally more reactive than the atoms present on the planes and their number is inversely proportional

to the size of the metal NPs. Thus controlling the size of metal NPs is imperative to obtain appreciable catalytic activity.

Variety of methods is available to synthesize metal NPs out of which two fundamental approaches are: bottom up and top down. In bottom up method colloidal metal NPs are synthesized from their organic or inorganic precursor preferably in chemical way. Top down approach usually deals with the physical ways of synthesizing metal NPs where the bulk material is shredded into nanoparticles. Among these two methods bottom up approach is widely used for synthesis of colloidal metal NPs where the capping agent/stabilizer can tune the size as well as shape of the metal NPs. Although the nanoparticles show remarkable properties such as providing ample amount active sites but their small size and high surface energy makes them thermally unstable which leads to particle growth, a phenomena termed as sintering, and can depreciate their catalytic activity. Arresting sintering of the metal NPs can be achieved by supporting them on solid support preferably confining them to porous support such as carbonaceous materials, metal oxides, mixed metal oxides, etc. While doing so the synergistic effect of NPs with support (commonly termed as SMSI- Strong Metal Support Interaction) can also fine tune the catalytic activity in terms of conversion, selectivity and stability of the catalyst. Some of the common methods of synthesis of supported metal NPs have been exemplified in the following section.

### **1.5 Synthesis of Supported Metal Nanoparticles**

Different routes of synthesis of supported metal NPs have been employed which can be divided into physical and chemical routes.

#### **1.5.1 Physical routes**

- A. Microwave Irradiation
- B. Sonochemistry
- C. Pulsed Laser Ablation (PLA)
- D. Plasma Reduction

Among all these, microwave irradiation and sonochemistry are the most commonly used methods due to the easy experimental protocol and control over the generation of small metal NPs. In microwave irradiation metal NPs of size 1-5 nm can be obtained with narrow size distribution. Also microwave irradiation provides instant heating unlike the conventional heating and reduces the time of catalyst preparation.<sup>21</sup>

## 1.5.2 Chemical routes

**1.5.2.1 Wetness Impregnation:** This is a common method of supporting metal NPs on the solid support. This approach necessitates the wetting of solid support with metal precursor (usually chlorides and nitrates) solution. Two different procedures can be employed for supporting metal on solid supports. The first approach follows via the addition of impregnating solution to the support which is either completely dried or evacuated. The volume of the impregnating solution is usually equal to the volume of support taken. This procedure is known as incipient wetness impregnation or dry impregnation.<sup>22</sup> Uptake of metal precursor into the pores of support occurs via the capillary pressure difference across the pores and represented by Young-Laplace equation<sup>23</sup>

$$\Delta p = \left[ \frac{2\gamma_{lv}}{r_p} \right] \times \cos \theta$$

where  $\Delta p$  is the capillary pressure difference across the pores,  $\gamma_{lv}$  of the surface tension between liquid and vapour interface and  $\theta$  is the angle between the solid and liquid. Analogous to incipient wetness impregnation, wet impregnation is another type of impregnation where the excess amount of precursor solution is used to completely immerse the solid support.

**1.5.2.2 Precipitation:** This method has long been used to synthesize supported metal catalyst where precipitation can be induced by change in pH, temperature and evaporation. Two common precipitation methods are:

**1.5.2.2.1 Co precipitation:** In this method salts of support and metal precursors are dissolved and precipitate together in the presence of basic reagent such as alkali hydroxides or carbonates in the form of metal hydroxides or carbonates. The low solubility of these components results in precipitation. This method has been utilized to synthesize most commonly used Ni-Alumina catalyst for steam reforming<sup>24</sup>, Fischer Tropsch catalyst<sup>25</sup> and also industrial Cu-ZnO<sub>2</sub>/Al<sub>2</sub>O<sub>3</sub> catalyst for CO<sub>2</sub> to methanol transformation.

**1.5.2.2.2 Deposition Precipitation:** Another way for the synthesis of supported metal catalyst is via precipitation. The principle of coprecipitation and deposition precipitation is similar i.e. conversion of highly soluble metal precursor to less soluble chemical entity which specifically precipitates on the provided support. The major difference between coprecipitation and deposition precipitation is that already synthesized support is added to the metal precursor which is then precipitated onto support in the presence of alkali while in

coprecipitation both support and metal precursors are precipitated together. The foremost requirement to obtain successful deposition precipitation catalyst is interaction between soluble metal precursor and surface of the support. If this interaction is absent the metal precursor will precipitates in the solution without getting loaded on to support. The most common precipitating agents used are urea, NaOH, Na<sub>2</sub>CO<sub>3</sub> etc. Various noble as well non noble metal NPs can be supported on metal oxides by this method.<sup>26-29</sup>

In general, this method allows the controlled deposition of metal precursor with strong metal support interaction and can result in highly dispersed catalytically active phase after thermal treatment.

**1.5.2.3. Sol-immobilization:** In this preparation method colloidal metal NPs are synthesised via chemical methods using polymers or other capping agent for stabilization against agglomeration. The synthesized colloidal particles are then supported on the solid support to obtain heterogeneous catalyst.

**1.5.2.4. Melt Infiltration:** In this method the metal salt is physically mixed with support (especially porous supports) and subsequently heated just above the melting temperature of the metal salt. The melt occupies the pores via capillary force as in impregnation method. The important condition for this synthesis to be successful is that the melting temperature and the decomposition temperature of metal salt should be sufficiently different. This method is also known as solid state impregnation, solid-solid method or solvent free method. Usually the transition metal nitrates with water of crystallization are most common precursors used for synthesizing the supported catalyst.<sup>30,31</sup>

The above discussed preparation techniques are the most commonly used methods for obtaining metal NPs supported on solid supports.

## **1.6 Common Supports**

The heterogeneous catalyst comprises of two components: metal and support. Though the metal forms the active phase of the catalyst, the role of support cannot be neglected. The support forms the major portion of heterogeneous catalyst and usually comprises of metal oxides, hydroxides, carbon based materials etc. Most commonly used support materials are SiO<sub>2</sub>, Al<sub>2</sub>O<sub>3</sub>, transition metal oxides such as Mn, Fe, Co, Ni- oxides, ZnO<sub>2</sub>, CeO<sub>2</sub>, TiO<sub>2</sub>, alkali and alkaline metal hydroxides and carbonates, oxides of lanthanides etc. Hence most of the elements in the periodic table can be used as support materials. Depending upon their role in

catalysis the support can be divided into active and inactive support. Transition metal oxides are the active supports due to their unique property to show variable oxidation state which helps in the stabilization of metal NPs and participating in reaction as well. But the supports like SiO<sub>2</sub>, Al<sub>2</sub>O<sub>3</sub> and carbon are considered to be inactive supports due to weak interaction with metal NPs. Even though metal-support interactions are weak, SiO<sub>2</sub> and Al<sub>2</sub>O<sub>3</sub> are most commonly used in heterogeneous catalysis. This is due to their low cost, abundant availability and thermal stability. Another important property of these supports especially SiO<sub>2</sub> and carbon is high surface area and tunable porosity. Depending upon the size of pores these porous materials can be divided into three categories:

- I. Microporous materials: pore size less than 2 nm
- II. Mesoporous materials : pores size falls in the range of 2-50 nm
- III. Macroporous materials: pore size above 50 nm

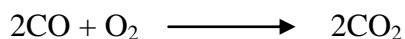
Among these materials mesoporous materials have attracted lot of attention due to their wide distribution of pores. The inherent large surface area and pore volume of these mesoporous materials makes them ideal candidate for supporting active phase in heterogeneous catalysis. Among the porous supports SiO<sub>2</sub> based materials are most commonly used due to their stability under thermal as well as harsh reaction conditions.<sup>32</sup> Mesoporous silica such as MCM-41, MCM-48, SBA-15 and KIT-6 , differentiated on the basis of size, shape and structure of their pores, are widely used for supporting metal NPs and.

### **1.7 Catalytic Reactions over Nanostructured Catalysts**

Metal NPs supported on solid supports are used for catalyzing various important catalytic reactions which have significance in resolving many environmental issues as well as organic transformations. Some of the catalytic reactions which have been performed in the present thesis are generalized and discussed in the following section:

1.7.1 CO Oxidation: Carbon monoxide is a colourless and odourless gas with a boiling point of -192 °C and melting point of -205 °C. Due to its high affinity for haemoglobin it is highly toxic to humans and animals. It can easily react with haemoglobin and form carboxyhaemoglobin leaving no sites for O<sub>2</sub> binding which results in failure of oxygen supply to body organs resulting in pronounced detrimental effects. The main source of evolution of CO in atmosphere is automobile exhaust, power plants and industrial and domestic activities.<sup>33</sup> CO is also the precursor to production of ground level ozone which can induce

many respiratory ailments.<sup>33</sup> These hazardous effects of CO on living beings prompted its abatement in air by converting it to non toxic chemicals. One of the major routes for converting CO to other chemicals is its oxidation to CO<sub>2</sub>.



CO oxidation is the most fundamental reaction which has attracted lot of attention of scientific community.<sup>34</sup> CO is also one of the most important probe molecule used to obtain the spectroscopic understanding of the catalyst.<sup>35</sup> The oxidation of CO involves activation of both CO and O<sub>2</sub> under the provided reaction conditions. Hence development of catalysts which can effectively catalyze CO to CO<sub>2</sub> under ambient reaction conditions is required. Gold based catalysts have been known to catalyze CO oxidation at remarkably low temperatures (less than 0 °C).<sup>36-38</sup> Other noble as well as non noble metals such as Pt, Pd, Rh, Ru, Co, Cu etc. are also known to effectively catalyze CO to CO<sub>2</sub> transformation.<sup>39-43</sup> The size of metal NPs and choice of support are two critical factors which decide the activity of employed catalyst for efficient CO oxidation reaction. For gold based catalyst it has been proved by Haruta et al that NPs of size 3-5 nm supported on redox supports are active for CO oxidation at low temperatures.<sup>44,45</sup> The mechanistic aspects of these reactions are unambiguous and three major mechanisms have been well documented in the literature which are (i) Langmuir-Hinshelwood (ii) Eley-Rideal and (iii) Mars van Krevlen mechanisms.<sup>46-48</sup> The Langmuir-Hinshelwood mechanism involves adsorption and activation of both CO and O<sub>2</sub> on the catalyst surface. This is the favoured operational mechanism for CO oxidation on most of the supported systems where the sites for the two reactant molecules can be same (metal NPs) or both support and metal. In general CO is adsorbed and activated on metal NPs while the O<sub>2</sub> gets adsorbed and activated either on the metal support interface or support itself. This mechanism usually operates on low to moderate coverage of reactants.<sup>48</sup> In Eley-Rideal mechanism O<sub>2</sub> is usually adsorbed and activated on the metal surface of the catalyst and reacts with the CO in gaseous form. Pt and Ru based catalyst are found to follow this mechanism but via a modified tri-molecular Eley-Rideal mechanism.<sup>49,50</sup> Mars van Krevlen mechanism operates under the conditions where support can provide lattice oxygen for reaction with adsorbed CO and molecular oxygen gets activated on the vacant lattice site and replenishes the lattice site.<sup>51-53</sup> Thus all the three mechanism can be followed on supported metal catalyst depending upon reaction conditions. In the present thesis Au and Pd NPs

supported on SiO<sub>2</sub> have been utilized for oxidation of CO to CO<sub>2</sub> and their size and activity correlation has been established.

1.7.2 H<sub>2</sub>O<sub>2</sub> mediated Olefins Epoxidation: Epoxidation is the chemical reaction which converts C-C double bond in to oxiranes (epoxides). Oxidation of olefins to their respective epoxide in the presence of green oxidant has always been attractive as the product is important in the manufacturing of many industrially important chemicals. Various organic and inorganic oxidants can be used which can oxidise C=C bond to epoxide via homogeneous as well as heterogeneous routes. Organic oxidants can efficiently form epoxides but produces copious amount of waste making them less economical and ecofriendly. H<sub>2</sub>O<sub>2</sub> is the most suitable alternate of organic oxidants for this purpose as the only by product formed is water and provides atom efficiency as the active oxygen content is more. Many transition metal based catalyst have been used for carrying out olefins epoxidation with H<sub>2</sub>O<sub>2</sub>.<sup>54-56</sup> The major drawback of using H<sub>2</sub>O<sub>2</sub> as an oxidant is its easy decomposition to water under reaction conditions which leads to the formation of undesired oxidation products. Thus the active sites which can stabilize H<sub>2</sub>O<sub>2</sub> and prevent its decomposition to water must be present on the catalyst surface. Most common catalyst used for this purpose is transition metal such as Ti, W, Nb, Fe, Mn which can perform efficiently in homo as well heterogeneous way.<sup>57-60</sup> Metals like Ti, W, Nb works efficiently when present in silica matrix as their respective silicates.<sup>61-63</sup> Their existence in silica lattice in the form of single sites or amorphous metal oxides can affect the activity as well as selectivity for epoxidation. Mostly single, isolated sites of these metals in silica lattice are active for getting optimum yield of epoxides.<sup>64,65</sup> There by suitable synthesis protocols have to be used so as to modify silica with isolated transition metal centres. Development of titanosilicates such as TS-1 and TS-2 has overcome this problem of maintaining the Ti centres in isolation in silica matrix.<sup>66</sup> Titanosilicates have been the most suitable catalyst used for epoxidation of variety of olefins in the presence of H<sub>2</sub>O<sub>2</sub> where the minimum decomposition of H<sub>2</sub>O<sub>2</sub> and maximum epoxide yield can be obtained.<sup>67,68</sup> Another attractive alternate to limit the use of commercial H<sub>2</sub>O<sub>2</sub> and prevent its decomposition is to insitu generate H<sub>2</sub>O<sub>2</sub> during reaction conditions in the presence of molecular H<sub>2</sub> and O<sub>2</sub>. Thus synthesized H<sub>2</sub>O<sub>2</sub> can be stabilized on isolated Ti centres and take part in epoxidation of olefin. Noble metal such as Pd, Au are known to produce H<sub>2</sub>O<sub>2</sub> from molecular O<sub>2</sub> and H<sub>2</sub>.<sup>69-71</sup> These metals when supported on titanosilicate produce H<sub>2</sub>O<sub>2</sub> which is transferred to nearby Ti centres for carrying out further reaction hence behaving as bi-functional catalyst.<sup>72,73</sup> In this thesis work titanosilicates and Au supported on

titanosilicates have been synthesized and their activity has been explored for olefin epoxidation.

**1.7.3 CO<sub>2</sub> hydrogenation:** Carbon dioxide is one of the major constituent of green house gases emitted into atmosphere. Anthropogenic CO<sub>2</sub> emission to atmosphere has raised severe environmental issues and global warming is one the major effect which is increasing earth's temperature continuously. Due to its negative impact on the global climate changes the major CO<sub>2</sub> emitting countries have pledged to decrease CO<sub>2</sub> emissions significantly to limit the temperature increase.<sup>74</sup> Thus the emission of CO<sub>2</sub> has been forecasted to be low in near future. However tens of thousands tons of CO<sub>2</sub> will still be emitted into earth's atmosphere by anthropogenic activities such as burning of fossil fuels for energy generation. A recent declaration by UNEP (United Nations Environment Programme) accounted that if no strict action is taken to reduce the CO<sub>2</sub> emissions then the earth's temperature might increase by > 2°C by year 2050 and by > 4°C by 2100.<sup>75</sup> In order to avoid this situation it is necessary to reduce CO<sub>2</sub> emission either by its storage or by its conversion to value added chemicals. Using CO<sub>2</sub> storage (CO<sub>2</sub> Sequestration) as an alternate may reduce the CO<sub>2</sub> emissions quickly<sup>76,77</sup> but has an issue of potential leakage. Thus conversion of CO<sub>2</sub> to chemicals is best option as the products can be utilized in various applications.<sup>78</sup> However the high stability of CO<sub>2</sub> (Bond Enthalpy= +809 kJ mol<sup>-1</sup>) creates the major obstacle for establishing industrial processes where CO<sub>2</sub> can be used as raw material. Conversion of CO<sub>2</sub> to chemicals can be achieved by photocatalysis,<sup>79,80</sup> electrocatalysis<sup>81</sup> and thermal catalysis. Photo and electrocatalysis often results in low efficiency limiting the commercialization aspect. Thermal catalysis is attractive but it requires large energy input. Conversion of CO<sub>2</sub> with high energy material is prominent solution and hydrogen produced from renewable sources is best candidate for this transformation. Thus hydrogenation of CO<sub>2</sub> in the presence of H<sub>2</sub> is the most appealing research direction which not only reduces the CO<sub>2</sub> emission but also decreases the dependence on fossil fuels.<sup>82</sup> CO<sub>2</sub> can be hydrogenated to various chemicals such as hydrocarbons, alcohols, syn gas and other valuable oxygenates. Various noble and non noble metals can be utilized for thermal conversion of CO<sub>2</sub> and may follow different paths as shown in Figure 1.3.



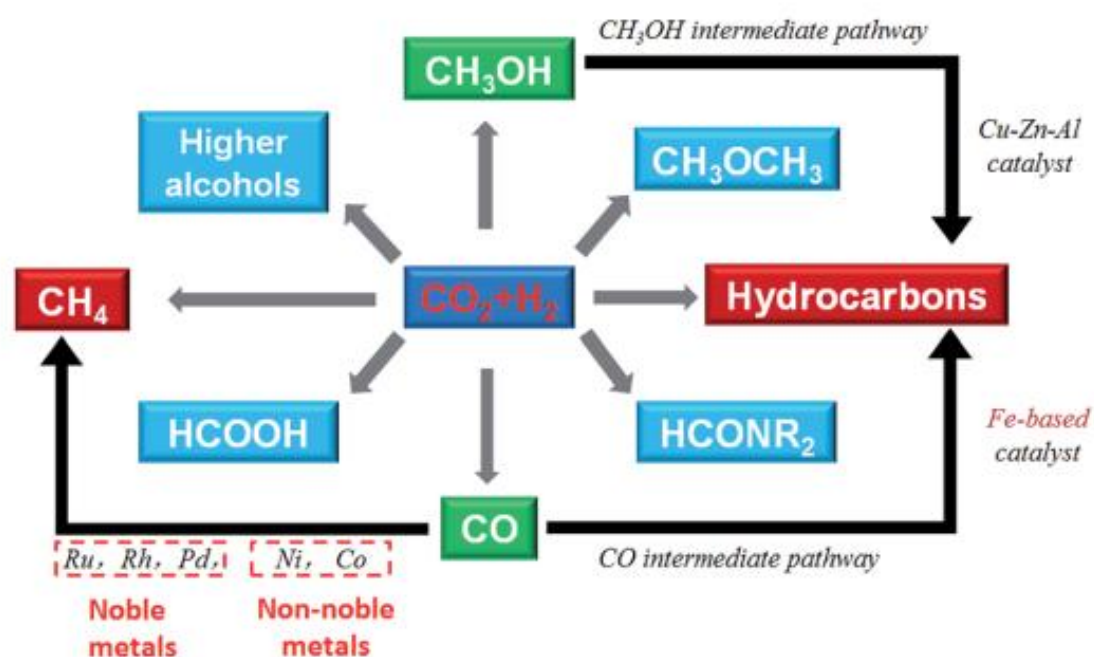


Figure 1.3 CO<sub>2</sub> hydrogenation to various chemicals and fuels.<sup>74</sup>

Metals like Ni, Ru, Rh are known to convert CO<sub>2</sub> to methane<sup>83-86</sup> while Fe is best known for syn gas and hydrocarbons production.<sup>87,88</sup> Metals like Cu, Pd, Ni, Ga, Ag in monometallic or bimetallic combinations are known to produce oxygenates such as methanol, ethanol, formate etc.<sup>89-96</sup> but require high pressures of CO<sub>2</sub> and H<sub>2</sub>. Cu-Zn/Al<sub>2</sub>O<sub>3</sub> is the industrial catalyst for methanol synthesis with a selectivity of 50% and works at >50 bar pressure. Pd based catalysts have emerged as captivating alternate because of low working pressure as compared to Cu based catalyst and the selectivity for oxygenates is also high.<sup>97,98</sup> While this is the case, support effects and its role in the selectivity of various products discussed above has not been discussed in literature so far. In the present work the influence of various supports on Pd based catalysts have tested for CO<sub>2</sub> hydrogenation at atmospheric pressure.

**1.7.4 Reductive N-alkylation of nitro compounds to N-alkyl amines:** Amines are considered one of the important organic compounds with their numerous applications in pharmaceutical and agrochemical industry. Some of the top selling drugs such as Abilify, Lidoderm, Crestor and Gleevac are amine compounds which emphasizes the importance of this class of compounds.<sup>99</sup> Due to increased demands of biological nitrogenous compounds it is important to develop easy and sustainable strategies for the synthesis of amine and its derivatives. Due to their potential use as pharmacophores, secondary amines are particularly more important. The common methods for their synthesis are direct alkylation of amines with alkyl halides<sup>99</sup>

amine-carbonyl reductive amination,<sup>100</sup> Buchwald-Hartwig<sup>101</sup> and Ulmann C-N cross coupling reactions.<sup>102,103</sup> Direct alkylation of amines using alkyl halides is the most common method but has serious drawbacks due to high cost of alkyl halides and generation of undesired by products. Coupling of amines with aldehydes/ketones is appealing due to their lower cost and generation of only water as the by product. But amines are produced from reduction of nitro compounds so an additional step is included and also nitro compounds are cheaper than amines. Thereby single step alkylation of nitro compounds to alkylated amines is fascinating due to prevention of hydrogenation step. In this regard using alcohols as the alkylating agents is more attractive due to their abundant availability and easy handling.<sup>104</sup> Many synthesis routes have been developed which involves transfer hydrogenation, reductive alkylation in the presence of hydrogen etc. Metals like Ru, Rh, Ir, Au, Pd, Ni, Mn, Fe etc have been used for the synthesis of N-alkylated amines.<sup>105-110</sup> In this thesis, Pd based heterogeneous catalyst for direct one pot conversion of nitroarenes to N-alkylated amines using aliphatic alcohols as the alkyl source is demonstrated.

## **1.8 Characterization of Nanocatalysts**

Characterization of nanocatalysts is important to establish structure-property-activity correlation. Many microscopic and spectroscopic techniques help to get a deeper understanding of catalytic system. The following section will provide a brief introduction of characterization tools which have been used for the nanocatalyst analysis in this thesis.

### **1.8.1 UV-visible Spectroscopy**

UV-visible spectroscopy is the absorption/reflectance of electromagnetic radiation in ultraviolet-visible spectral region. The metal nanoparticles possess free electron on their surface also called plasmons which when absorbs light can oscillate and there comes a situation when the energy of these oscillating electrons (plasmons) matches with frequency of incident light and gives origin to a phenomenon popularly known as surface plasmon resonance (SPR). The metal NPs such as Au, Ag, Cu show this phenomenon in UV-Vis range. Thus SPR is the collective oscillation of free electrons in solid or colloidal solution stimulated by the incident light.

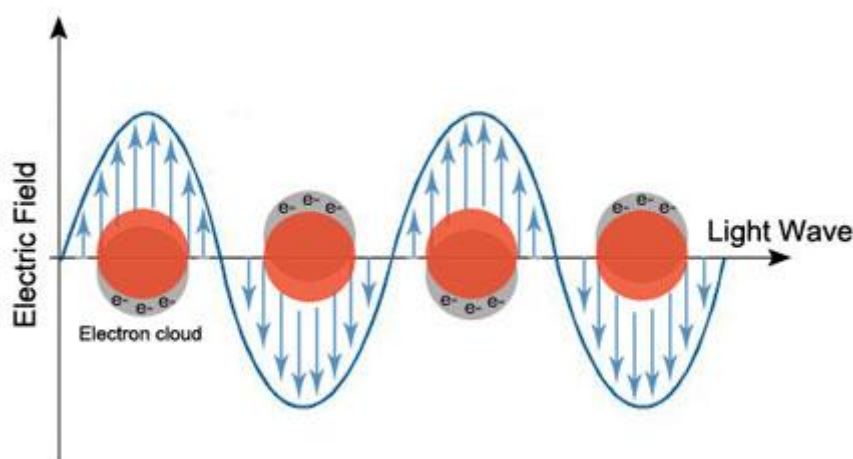


Figure 1.4 Schematic representation of SPR phenomenon in metal NPs.<sup>111</sup>

This property of metal NPs can vary with the size and shape thus making them useful for optical applications.<sup>112</sup> In this thesis UV-visible analysis and spectra were acquired using Shimadzu 2700 spectrophotometer equipped with a dual beam source of He and tungsten for UV and visible light respectively. Liquid sample analysis was done using water as the reference. DRUV analysis was performed for powder samples using BaSO<sub>4</sub> as the standard.

### 1.8.2 X-ray Diffraction Analysis

X-ray powder diffraction is widely used for the analysis of solids mainly crystalline or polycrystalline material giving useful information about unit cell parameter. The interaction of material with X-rays results in the diffraction of X-rays in specified direction and angle. The working principle of X-rays is based on Bragg's equation:

$$n\lambda = 2d\sin\theta$$

where  $n$  is the order of reflection which is normally an integer,  $\lambda$  is the wavelength of X-rays used,  $d$  is the interplaner distance and  $\theta$  is the angle between x-rays and reflecting lattice plane. The X-ray peaks have significance in calculating the crystallite size through Scherer equation which relates the crystallite size to full width at half maximum (FWHM) of the peak as:

$$\tau = \frac{k\lambda}{\beta \cos \theta}$$

where  $\tau$  is mean crystallite size,  $\lambda$  is the wavelength of X-rays,  $k$  is the constant often taken as 0.9,  $\beta$  is the FWHM,  $\theta$  is the angle between beam and normal to reflecting plane. In the

present thesis small and wide angle X-ray analysis on the powder catalysts were measured on Rigaku D MAX with a Cu K $\alpha$  source of wavelength 1.54 Å with an operational voltage of 40 kV and 15 mA current.

### 1.8.3 Fourier Transform Infrared Spectroscopy

FTIR is a useful technique to obtain the nature of chemical bond involved in molecule/material. The absorption of infrared induces vibrations in the chemical bonds which can change the dipole moment associated with the absorption. For a molecule to be IR active change in dipole is the required condition. The sample is subjected to interact with IR radiation and absorption spectrum is obtained when the absorption frequency of vibration resonates with the incident frequency. Thus obtained data points are Fourier transformed using mathematical models to get meaningful data in terms of absorption or transmittance with respect to wavelength absorbed.

The IR analysis in this thesis was performed on Bruker Tensor 27 FTIR spectrophotometer and Thermo Nicolet is50 using KBr as the reference. The samples were made into pellet using KBr in certain proportions. In situ IR analysis was performed on Thermo Nicolet 50 spectrophotometer equipped with KBr window.

### 1.8.4 Raman Spectroscopy

Raman spectroscopy gives vibrational, rotational and other low frequency modes in the material. It relies on the Raman scattering or inelastic scattering of monochromatic light from laser with suitable wavelength. The interaction of laser light produces vibrations in the system which results in energy shift of laser photons to up or down generating anti stroke or stroke Raman lines. The elastically scattered lines are termed as Rayleigh lines. The inelastic scattered light can give direct information about molecule under consideration. For present thesis work Raman analysis was performed both in visible and UV region. Raman analysis in visible region was acquired on LabRam spectrometer make HJY with a laser wavelength of 633 nm. Raman analysis in UV region was performed using 264 nm excitation wavelength generated by tunable Ti:sapphire Laser (Indigo, Coherent Inc.). The average power used was 0.6 mW. Calibration was done by recording the spectra of dimethylformamide, cyclohexane, acetonitrile, trichloroethylene with the known band position.

### 1.8.5 Nuclear Magnetic Resonance (NMR) Spectroscopy

NMR is a spectroscopic tool which acquires the information about the local magnetic field around atomic nuclei. Thus the physical and chemical nature of the material can be identified by utilizing the magnetic properties of atomic nuclei under consideration. The sample is placed in the external magnetic field and the spectrum is produced by interaction of atomic nuclei with the magnetic field under nuclear magnetic resonating conditions. In the solid state NMR spectroscopy the anisotropic properties on the solid are dominant which can result in peak broadening in convectional solution based NMR. Two important concepts are used to get a well defined solid state NMR data and those are proper sample orientation to limit most of the sample orientations and reduction of anisotropic nuclear magnetic interaction by sample spinning. The latter approach is obtained by fast spinning the sample around magic angle (MAS) for nuclei having  $\frac{1}{2}$  spin. The chemical shift values obtained after analysis can be used to identify the coordination environment around the nuclei which can be correlated with structure of the molecule in the material.

Solid state NMR studies in the chapter 3 were performed on Bruker HD 700 MHz spectrometer in a 4 mm double resonance probe with Larmor frequency of 70.94 MHz for  $^{15}\text{N}$  and the single pulse  $^1\text{H}$  MAS experiments were done at Bruker AV NEO 500MHz equipped with a 2.5mm trigamma probe at a sample rotation frequency of 32 kHz.

### 1.8.6 $\text{N}_2$ Porosimetry Analysis

$\text{N}_2$  Porosimetry is an important tool to obtain information about the textural properties of the supported materials using liquid  $\text{N}_2$  as a probe molecule. The working principle of this technique is based on the BET theory proposed jointly by Brunner, Emmet and Teller for multilayer adsorption of gas molecules on the solid surface. The BET equation can be represented as:

$$\frac{1}{V_a \left[ \frac{P^\circ}{P} - 1 \right]} = \frac{C - 1}{V_m C} \times \frac{P}{P^\circ} + \frac{1}{V_m C}$$

where P is the equilibrium absorption pressure,  $P^\circ$  is the saturation pressure of the adsorbate at analysis temperature,  $V_a$  is the volume of  $\text{N}_2$  adsorbed at pressure P and  $V_m$  is the volume of adsorbate for monolayer adsorption and C is the BET constant related to heat of adsorption and liquefaction. This method is widely used for measuring the surface area of solid material by physical adsorption of the gas molecule by the following equation:

$$S = \frac{V_m N_a}{m \times 22400}$$

where  $N$  is Avogadro constant,  $\alpha$  is the cross sectional area covered by one adsorbate molecule which is  $0.162 \text{ nm}^2$  for  $\text{N}_2$  and  $m$  is the weight of the sample.

In this thesis, surface area analysis on samples was performed on Autosorb 1C Quantachrome, USA. The sample was first activated at high temperature followed by adsorbing/ desorbing liquid  $\text{N}_2$  at different pressures at room temperature. The surface area was calculated at relative pressure 0.02-0.4 via BET model. The pore volume was measured from uptake of  $\text{N}_2$  at relative pressure of  $P/P_0=0.99$  and pore size was calculated using BJH model applied to the desorption branch of the isotherm.

#### 1.8.7 Inductively Coupled Plasma (ICP) Spectroscopy

This spectroscopy technique is used to quantify elements (metals or non metals) present in the material under consideration. The working principle of this technique is based on the generation of ions of the elements by inductively coupled plasma. The electromagnetic radiation generated by the interaction of plasma with elemental ions are detected and used for quantification of particular element.

The ICP analysis in chapter 2 was done on optical emission spectrometer Therm IRIS intrepid II XSP (CSIR-NCL) while in the chapter 3 analysis was done in CAMS Venture Centre, Pune. All the samples were completely digested in aqua regia and HF for analysis.

#### 1.8.8 X-ray Photoelectron Spectroscopy (XPS)

XPS is a surface sensitive spectroscopic technique that measures the elemental composition of active components in heterogeneous catalysis. XPS spectra are obtained by irradiating the sample with X-ray beam which results in excitation and ejection of electrons based on photoelectric effect and then measuring the kinetic energy of the ejected electrons. The mean free path of ejected electrons is 10 nm hence making the technique highly surface sensitive. The technique is usually called as ESCA (Electron Spectroscopy for Chemical Analysis) and provides useful information about the chemical nature, oxidation state and electronic environment around the element under consideration. The binding energy calculated from the following equation provides the oxidation state information:

$$\text{K.E.} = h\nu - \text{B.E.} - \Phi$$

where K.E. is the kinetic energy of the ejected electron, B.E. is the binding energy of the electron,  $h\nu$  is the incident photon energy and  $\Phi$  is the work function dependent both on spectrometer as well as material.

XPS measurements reported in the thesis were done on Thermo Kalpha+ spectrometer using micro focused and monochromated Al K $\alpha$  radiation with energy 1486.6 eV operating at a vacuum better than  $10^{-9}$  millibar. The pass energy for spectral acquisition was kept at 50 eV for individual core-levels and 100 eV for wide area scan. The peak fitting was done using XPSpeak41 software with Shirley type background

### 1.8.9 X-Ray Absorption Spectroscopy (XAS)

XAS is an important spectroscopic tool for determining electronic and geometric structure of the material. Also the information on local structure and unoccupied electronic states can be obtained through XAS analysis. The experiment is performed at synchrotron radiation facility which provides tunable and intense X-rays. These X-rays have sufficient energy to excite a core level electron of an atom into an empty bound state called as excitonic state below the ionization threshold or to the continuum which is above the ionization potential. Three main regions are found in a typical XAS data:

1. Absorption threshold which is determined by transition of excited electron to lowest unoccupied states.
2. XANES (X-ray Absorption Near Edge Spectroscopy) comprises the ejection of photoelectrons from core level to quasi bound state having kinetic energy in the range of 10-100 eV above the chemical potential. These transitions give rise to multiple scattering resonances of the photoelectron. The pre edge and near edge regions in the spectrum contribute to XANES spectrum.
3. EXAFS- The ejected photoelectrons have both particle and wave nature and can be scattered back from the neighbouring atoms in the lattice. This interaction can give rise to interference pattern at higher energy regions (beyond 100 eV) and gives rise to Extended X-ray Absorption Fine Structure (EXAFS).
4. X-ray Absorption Spectroscopy (XAS) analysis in Chapter 2 was carried out at Ti K edge in fluorescence mode at the Scanning EXAFS Beam line (BL-9) at the INDUS-2 Synchrotron Source (2.5 GeV, 100 mA) at the Raja Ramanna Centre for Advanced Technology (RRCAT), Indore, India.

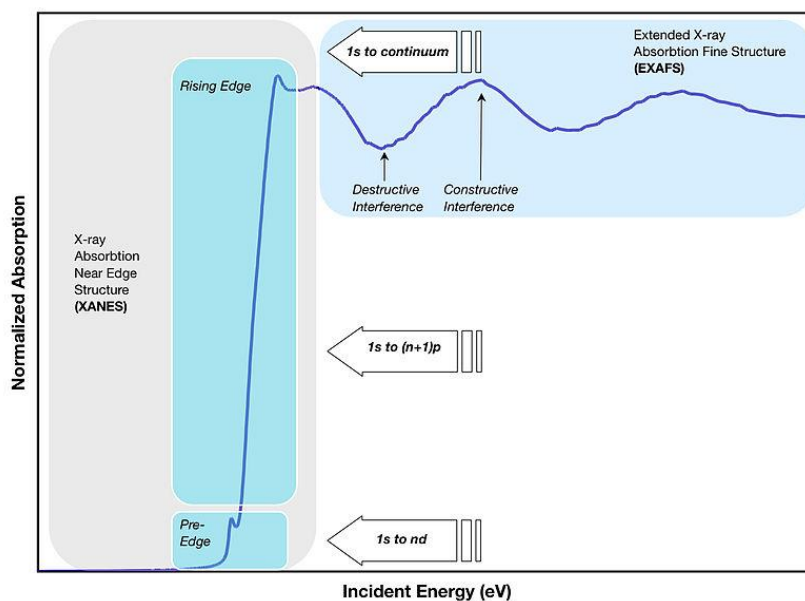


Figure 1.5 Schematic illustration of X-ray absorption edge. (Image Source Wikipedia)

#### 1.8.10 Transmission Electron Microscopy (TEM)

TEM is an electron microscopy technique in which a beam of high energy electrons is transmitted through the sample to produce a 2-D image of the sample. The sample is an ultrathin section <100 nm thick or suspension drop casted on a grid. The image is formed by interaction of incident electrons with the sample as the electron beam is transmitted through specimen. This image is magnified and then focused onto an imaging device such as a photographic film, charged coupled device (CCD) or a fluorescent screen. The advantage of using electrons over optical light source is lower de-Broglie wavelength which allows resolution in nanometre scale. Hence it is possible to get image of sample at atomic resolution by TEM instrument. TEM is widely used to understand the morphology of materials under consideration. Advanced features of TEM include STEM (Scanning Transmission Electron Microscopy) and HAADF (High Angle Annular Dark Field) imaging modes which are equipped with EDS (Energy Dispersive Spectroscopy) to get information of elemental composition and atomic distribution in nanomaterials. The conventional TEM analysis in this thesis in chapter 2 was done on FEI Technai instruments (TF-20) in CSIR-NCL by dropcasting the samples on carbon coated copper grids. The HAADF-STEM analysis was done in Portugal on Tecnai (Model F30) operating at 300 kV acceleration voltage. Further details of analysis have been provided in details in chapter 2.



### 1.8.11 Scanning Electron Microscopy (SEM)

SEM is used to get information about the morphology of the sample in a 3-D manner. The images are obtained by rastering focused high energy electron beam across the sample and backscattered or secondary electrons are detected. These electrons can provide information about the surface topography and sample composition. The SEM analysis in the present thesis was acquired on FEI model quanta 200 3D with EDX form elemental analysis.

## **1.9 Scope and objective of the thesis**

Designing a stable and sustainable heterogeneous catalyst via inexpensive route is always challenging and one of the major focus areas in the field of catalysis. The supported noble metal NPs has been testing ground for a large number of important reactions some of which are industrially produced through homogeneous routes. Hence it is obligatory to develop architecture of these systems by certain methods which can provide them sustainability while maintaining integral properties of heterogeneous catalyst. Conventional routes of synthesising noble metal NPs on solid supports such as impregnation, coprecipitation, deposition precipitation have many drawbacks such as larger sized NPs, poor dispersion, poor loading etc. especially on inactive supports like silica. But the unique properties of silica such as thermal stability, high surface area, tunable porosity, easy modification with other transition metals etc. make it most common and convenient support. But synthesising metal NPs of sizes 2-3 nm on silica support has always been challenging due to poor metal support interactions. This results in uncontrolled particle size growth under high temperature as well as reaction conditions which has a deleterious effect on the catalytic activity. Anchoring or encapsulating the small sized metal NPs in a porous silica support can impart high thermal stability by restricting the motion of NPs as well provide accessibility to active metal sites thereby confronting the problems associated with sintering of NPs. In the present thesis work strategies have been developed for the synthesis of Au, Pd NPs of small size supported on porous silica support which are easy, inexpensive, economical and scalable. The very first attempt in this regard has been made by developing a one pot method for the synthesis of gold core-silica shell (Au NPs size ~5 nm) which is further modified with titanium to make this system more versatile and catalytically active for various oxidation reactions such as CO oxidation and propene epoxidation. While, making metal encapsulated core-shell system have the advantage of preventing sintering during the course of the reaction or under thermal treatment, it is hugely challenging to bring the particle size close to 2-3 nm with good

dispersion and loading. Also, scaling up of the catalyst in such core-shell synthesis routes is limited. Conventional methods like deposition precipitation (DP) which provides very small NPs with high dispersion cannot be used for a support like silica due to its low PZC (~2). This bottle neck problem has been circumvented in the present thesis by modifying the conventional DP method. This modified DP method is inexpensive, easy and scalable with prime focus on maintaining the metal particle size, dispersion, desired loading and thermal stability. The method is general and can be employed to noble as well non noble methods.

Au and Pd NPs of size 2-3 nm supported on SBA-15 have been synthesized using the modified DP method and their catalytic activity has been explored for various oxidation as well hydrogenation reactions. The chapter two and three mainly deal with the low temperature CO oxidation over Au based catalyst. Also gas phase propene epoxidation in the presence of molecular O<sub>2</sub> and H<sub>2</sub> has been tested over Au NPs supported on titanosilicate in chapter two and four. Pd/SBA-15 catalyst has also been screened for different reactions such as CO oxidation in the second part of chapter three. The hydrogenation activity of this catalyst for CO<sub>2</sub> hydrogenation and reductive alkylation of nitrobenzene have been demonstrated and explained in chapter five. Mesoporous titanosilicate synthesised by sol gel route has also been tested for liquid phase epoxidation of alkenes using H<sub>2</sub>O<sub>2</sub> as oxidant. The developed catalysts have been well characterized with suitable microscopic and spectroscopic techniques to develop structure activity correlation for reactions employed. Thus, the prime objective of the present thesis work is development of synthesis routes of noble metals (Au, Pd) supported on metal oxide supports primarily silica for sustainable heterogeneous catalysis.

### 1.10 References

1. R. A. van Santen, J. W. N., *Chemical Kinetics and Catalysis*. 1995.
2. Ojima, I.; Tsai, C.; Tzamarioudaki, M.; Bonafoux, D., *Organic Reactions* **2004**, , John Wiley & Sons, Inc.
3. Sinn, H.; Kaminsky, W., In *Advances in Organometallic Chemistry*, **1980**, *18*, 99-149.
4. Coates, G. W.; Hustad, P. D.; Reinartz, S., *Angew. Chem. Int. Ed.* **2002**, *41* (13), 2236-2257.
5. Schätz, A.; Reiser, O.; Stark, W. J., *Chem. Eur. J.* **2010**, *16* (30), 8950-8967.
6. Bui, T. Q.; Ton, S. N.-C.; Duong, A. T.; Tran, H. T., *J. Sci. Adv. Mater. Dev.* **2018**, *3* (1), 107-112.
7. Dhakshinamoorthy, A.; Garcia, H., *Chem. Soc. Rev.* **2012**, *41* (15), 5262-5284.
8. Crooks, R. M.; Zhao, M.; Sun, L.; Chechik, V.; Yeung, L. K., *Acc. Chem. Res.* **2001**, *34* (3), 181-190.
9. Wang, Y.; De, S.; Yan, N., *Chem. Commun.* **2016**, *52* (37), 6210-6224.
10. Kotani, H.; Hanazaki, R.; Ohkubo, K.; Yamada, Y.; Fukuzumi, S., *Chem. Eur. J.* **2011**, *17* (9), 2777-2785.
11. Ahmadi, M.; Mistry, H.; Roldan Cuenya, B., *J. Phys. Chem. Lett.* **2016**, *7* (17), 3519-3533.
12. Mostafa, S.; Behafarid, F.; Croy, J. R.; Ono, L. K.; Li, L.; Yang, J. C.; Frenkel, A. I.; Cuenya, B. R., *J. Am. Chem. Soc.* **2010**, *132* (44), 15714-15719.
13. da Silva, A. G. M.; Rodrigues, T. S.; Slater, T. J. A.; Lewis, E. A.; Alves, R. S.; Fajardo, H. V.; Balzer, R.; da Silva, A. H. M.; de Freitas, I. C.; Oliveira, D. C.; Assaf, J. M.; Probst, L. F. D.; Haigh, S. J.; Camargo, P. H. C., *ACS Appl. Mater. Inter.* **2015**, *7* (46), 25624-25632.
14. Mistry, H.; Reske, R.; Zeng, Z.; Zhao, Z.-J.; Greeley, J.; Strasser, P.; Cuenya, B. R., *J. Am. Chem. Soc.* **2014**, *136* (47), 16473-16476.
15. Sirikajorn, T.; Mekasuwandumrong, O.; Praserttham, P.; Goodwin, J. G.; Panpranot, J., *Catal. Lett.* **2008**, *126* (3), 313.
16. Trovarelli, A.; Llorca, J., *ACS Catal.* **2017**, *7* (7), 4716-4735.
17. Zhang, Q.; Wang, H., *ACS Catal.* **2014**, *4* (11), 4027-4033.
18. Kuo, C.-H.; Mosa, I. M.; Thanneeru, S.; Sharma, V.; Zhang, L.; Biswas, S.; Aindow, M.; Pamir Alpay, S.; Rusling, J. F.; Suib, S. L.; He, J., *Chem. Commun.* **2015**, *51* (27), 5951-5954.
19. Hvolbæk, B.; Janssens, T. V. W.; Clausen, B. S.; Falsig, H.; Christensen, C. H.; Nørskov, J. K., *Nano Today* **2007**, *2* (4), 14-18.
20. Cao, S.; Tao, F.; Tang, Y.; Li, Y.; Yu, J., *Chem. Soc. Rev.* **2016**, *45* (17), 4747-4765.
21. White, R. J.; Luque, R.; Budarin, V. L.; Clark, J. H.; Macquarrie, D. J., *Chem. Soc. Rev.* **2009**, *38* (2), 481-494.
22. Munnik, P.; de Jongh, P. E.; de Jong, K. P., *Chem. Rev.* *115* (14), 6687-6718.
23. van Honschoten, J. W.; Brunets, N.; Tas, N. R., *Chem. Soc. Rev.* *39* (3), 1096-1114.

24. Villacampa, J. I.; Royo, C.; Romeo, E.; Montoya, J. A.; Del Angel, P.; Monzón, A., *Appl. Catal. A* **2003**, 252 (2), 363-383.
25. Khodakov, A. Y.; Chu, W.; Fongarland, P., *Chem. Rev.* **2007**, 107 (5), 1692-1744.
26. Guo, Y.; Gu, D.; Jin, Z.; Du, P.-P.; Si, R.; Tao, J.; Xu, W.-Q.; Huang, Y.-Y.; Senanayake, S.; Song, Q.-S.; Jia, C.-J.; Schüth, F., *Nanoscale* **2015**, 7 (11), 4920-4928.
27. Bamwenda, G. R.; Tsubota, S.; Nakamura, T.; Haruta, M., *Catal. Lett.* **1997**, 44 (1), 83-87.
28. van der Lee, M. K.; van Dillen, J.; Bitter, J. H.; de Jong, K. P., *J. Am. Chem. Soc.* **2005**, 127 (39), 13573-13582.
29. Putluru, S. S. R.; Schill, L.; Jensen, A. D.; Siret, B.; Tabaries, F.; Fehrmann, R., *Appl. Catal. B* **2015**, 165, 628-635.
30. Marceau, E.; Che, M.; Čejka, J.; Zukal, A., *ChemCatChem* **2010**, 2 (4), 413-422.
31. Yue; Zhou, Synthesis of Porous *Chem. Mater.* **2007**, 19 (9), 2359-2363.
32. Giraldo, L. F.; López, B. L.; Pérez, L.; Urrego, S.; Sierra, L.; Mesa, M., *Macro. Sym.* **2007**, 258 (1), 129-141.
33. Royer, S.; Duprez, D., *ChemCatChem* **2011**, 3 (1), 24-65.
34. Freund, H.-J.; Meijer, G.; Scheffler, M.; Schlögl, R.; Wolf, M., *Angew. Chem. Int. Ed.* **2011**, 50 (43), 10064-10094.
35. Lari, G. M.; Nowicka, E.; Morgan, D. J.; Kondrat, S. A.; Hutchings, G. J., *Phys. Chem. Chem. Phys.* **2015**, 17 (35), 23236-23244.
36. Lin, S. D.; Bollinger, M.; Vannice, M. A., *Catal. Lett.* **1993**, 17 (3), 245-262.
37. Haruta, M.; Tsubota, S.; Kobayashi, T.; Kageyama, H.; Genet, M. J.; Delmon, B., *J. Catal.* **1993**, 144 (1), 175-192.
38. Jia, C.-J.; Liu, Y.; Bongard, H.; Schüth, F., *J. Am. Chem. Soc.* **2010**, 132 (5), 1520-1522.
39. Fukuoka, A.; Kimura, J.-i.; Oshio, T.; Sakamoto, Y.; Ichikawa, M., *J. Am. Chem. Soc.* **2007**, 129 (33), 10120-10125.
40. Zhou, Y.; Wang, Z.; Liu, C., *Catal. Sci. Technol.* **2015**, 5 (1), 69-81.
41. Shang, L.; Bian, T.; Zhang, B.; Zhang, D.; Wu, L.-Z.; Tung, C.-H.; Yin, Y.; Zhang, T., *Angew. Chem.* **2014**, 126 (1), 254-258.
42. Xie, X.; Li, Y.; Liu, Z.-Q.; Haruta, M.; Shen, W., *Nature* **2009**, 458, 746.
43. Wang, W.-W.; Du, P.-P.; Zou, S.-H.; He, H.-Y.; Wang, R.-X.; Jin, Z.; Shi, S.; Huang, Y.-Y.; Si, R.; Song, Q.-S.; Jia, C.-J.; Yan, C.-H., *ACS Catal.* **2015**, 5 (4), 2088-2099.
44. Haruta, M., *Catal. Today* **1997**, 36 (1), 153-166.
45. Comotti, M.; Li, W.-C.; Spliethoff, B.; Schüth, F., *J. Am. Chem. Soc.* **2006**, 128 (3), 917-924.
46. Zhang, C.; Hu, P.; Alavi, A., *J. Am. Chem. Soc.* **1999**, 121 (34), 7931-7932.
47. Kim, H. Y.; Henkelman, G., *J. Phys. Chem. Lett.* **2013**, 4 (1), 216-221.
48. Baxter, R. J.; Hu, P., *J. Chem. Phys.* **2002**, 116 (11), 4379-4381.
49. Peden, C. H. F.; Goodman, D. W.; Weisel, M. D.; Hoffmann, F. M., *Surf. Sci.* **1991**, 253 (1), 44-58.

50. Zhang, X.; Lu, Z.; Xu, G.; Wang, T.; Ma, D.; Yang, Z.; Yang, L., *Phys. Chem. Chem. Phys.* **2015**, *17* (30), 20006-20013.
51. Lewandowski, M.; Groot, I. M. N.; Shaikhutdinov, S.; Freund, H. J., *Catal. Today* **2012**, *181* (1), 52-55.
52. Wang, C.; Gu, X.-K.; Yan, H.; Lin, Y.; Li, J.; Liu, D.; Li, W.-X.; Lu, J., *ACS Catal.* **2017**, *7* (1), 887-891.
53. Widmann, D.; Behm, R. J., *Angew. Chem. Int. Ed.* **2011**, *50* (43), 10241-10245.
54. Lane, B. S.; Burgess, K., *Chem. Rev.* **2003**, *103* (7), 2457-2474.
55. Mizuno, N.; Yamaguchi, K.; Kamata, K., *Coord. Chem. Rev.* **2005**, *249* (17), 1944-1956.
56. Wang, C.; Yamamoto, H., *Chem. Asian J.* **2015**, *10* (10), 2056-2068.
57. Hammond, C.; Straus, J.; Righettoni, M.; Pratsinis, S. E.; Hermans, I., *ACS Catal.* **2013**, *3* (3), 321-327.
58. Moretti, R. A.; Du Bois, J.; Stack, T. D. P., *Org. Lett.* **2016**, *18* (11), 2528-2531.
59. Hasan, K.; Brown, N.; Kozak, C. M., *Green Chem.* **2011**, *13* (5), 1230-1237.
60. Sawada, Y.; Matsumoto, K.; Katsuki, T., *Angew. Chem.* **2007**, *119* (24), 4643-4645.
61. Bregante, D. T.; Thornburg, N. E.; Notestein, J. M.; Flaherty, D. W., *ACS Catal.* **2018**, *8* (4), 2995-3010.
62. Ivanchikova, I. D.; Skobelev, I. Y.; Maksimchuk, N. V.; Paukshtis, E. A.; Shashkov, M. V.; Kholdeeva, O. A., *J. Catal.* **2017**, *356*, 85-99.
63. Koo, D. H.; Kim, M.; Chang, S., *Org. Lett.* **2005**, *7* (22), 5015-5018.
64. Jarupatrakorn, J.; Tilley, T. D., *J. Am. Chem. Soc.* **2002**, *124* (28), 8380-8388.
65. Kamegawa, T.; Suzuki, N.; Che, M.; Yamashita, H., *Langmuir* **2011**, *27* (6), 2873-2879.
66. M. Taramasso, G. P., B. Notari., U.S. Patent 4. **1983**, (410 501).
67. Lu, X.; Zhou, W.-J.; Wu, H.; Liebens, A.; Wu, P., *Appl. Catal. A* **2016**, *515*, 51-59.
68. Kamegawa, T.; Yamahana, D.; Seto, H.; Yamashita, H., *J. Mater. Chem. A* **2013**, *1* (3), 891-897.
69. Flaherty, D. W., *ACS Catal.* **2018**, *8* (2), 1520-1527.
70. Solsona, B. E.; Edwards, J. K.; Landon, P.; Carley, A. F.; Herzing, A.; Kiely, C. J.; Hutchings, G. J., *Chem. Mater.* **2006**, *18* (11), 2689-2695.
71. Landon, P.; Collier, P. J.; Papworth, A. J.; Kiely, C. J.; Hutchings, G. J., *Chem. Commun.* **2002**, (18), 2058-2059.
72. Feng, X.; Sheng, N.; Liu, Y.; Chen, X.; Chen, D.; Yang, C.; Zhou, X., *ACS Catal.* **2017**, *7* (4), 2668-2675.
73. Sinha, A. K.; Seelan, S.; Tsubota, S.; Haruta, M., *Angew. Chem. Int. Ed.* **2004**, *43* (12), 1546-1548.
74. Li, W.; Wang, H.; Jiang, X.; Zhu, J.; Liu, Z.; Guo, X.; Song, C., *RSC Adv.* **2018**, *8* (14), 7651-7669.
75. Yang, H.; Zhang, C.; Gao, P.; Wang, H.; Li, X.; Zhong, L.; Wei, W.; Sun, Y., *Catal. Sci. Technol.* **2017**, *7* (20), 4580-4598.
76. Ma, X.; Wang, X.; Song, C., *J. Am. Chem. Soc.* **2009**, *131* (16), 5777-5783.

77. Min, K.; Choi, W.; Kim, C.; Choi, M., *ACS Appl. Mater. Inter.* **2018**, *10* (28), 23825-23833.
78. Sakakura, T.; Choi, J.-C.; Yasuda, H., *Chem. Rev.* **2007**, *107* (6), 2365-2387.
79. Yuan, L.; Xu, Y.-J., *Appl. Surf. Sci.* **2015**, *342*, 154-167.
80. Li, K.; Peng, B.; Peng, T., *ACS Catal.* **2016**, *6* (11), 7485-7527.
81. Zhang, S.; Kang, P.; Ubnoske, S.; Brennaman, M. K.; Song, N.; House, R. L.; Glass, J. T.; Meyer, T. J., *J. Am. Chem. Soc.* **2014**, *136* (22), 7845-7848.
82. Wang, W.; Wang, S.; Ma, X.; Gong, J., *Chem. Soc. Rev.* **2011**, *40* (7), 3703-3727.
83. Rossetti, I.; Biffi, C.; Bianchi, C. L.; Nichele, V.; Signoretto, M.; Menegazzo, F.; Finocchio, E.; Ramis, G.; Di Michele, A., *Appl. Catal. B* **2012**, *117-118*, 384-396.
84. Sharma, S.; Hu, Z.; Zhang, P.; McFarland, E. W.; Metiu, H., *J. Catal.* **2011**, *278* (2), 297-309.
85. Tada, S.; Ochieng, O. J.; Kikuchi, R.; Haneda, T.; Kameyama, H., *Int. J. Hydrogen Energ.* **2014**, *39* (19), 10090-10100.
86. Swalus, C.; Jacquemin, M.; Poleunis, C.; Bertrand, P.; Ruiz, P., *Appl. Catal. B* **2012**, *125*, 41-50.
87. Yao, Y.; Liu, X.; Hildebrandt, D.; Glasser, D., *Ind. Eng. Chem. Res.* **2011**, *50* (19), 11002-11012.
88. Ding, F.; Zhang, A.; Liu, M.; Zuo, Y.; Li, K.; Guo, X.; Song, C., *Ind. Eng. Chem. Res.* **2014**, *53* (45), 17563-17569.
89. Behrens, M.; Studt, F.; Kasatkin, I.; Kühn, S.; Hävecker, M.; Abild-Pedersen, F.; Zander, S.; Girsdsies, F.; Kurr, P.; Kniep, B.-L.; Tovar, M.; Fischer, R. W.; Nørskov, J. K.; Schlögl, R., *Science* **2012**.
90. Spencer, M. S., *Top. Catal.* **1999**, *8* (3), 259.
91. Studt, F.; Sharafutdinov, I.; Abild-Pedersen, F.; Elkjær, C. F.; Hummelshøj, J. S.; Dahl, S.; Chorkendorff, I.; Nørskov, J. K., Discovery of a Ni-Ga catalyst for carbon dioxide reduction to methanol. *Nat. Chem.* **2014**, *6*, 320.
92. Ye, J.; Cammarota, R. C.; Xie, J.; Vollmer, M. V.; Truhlar, D. G.; Cramer, C. J.; Lu, C. C.; Gagliardi, L., *ACS Catal.* **2018**, *8* (6), 4955-4968.
93. Bai, S.; Shao, Q.; Wang, P.; Dai, Q.; Wang, X.; Huang, X., *J. Am. Chem. Soc.* **2017**, *139* (20), 6827-6830.
94. Caparrós, F. J.; Soler, L.; Rossell, M. D.; Angurell, I.; Piccolo, L.; Rossell, O.; Llorca, J., *ChemCatChem* **2018**, *10* (11), 2365-2369.
95. Mori, K.; Sano, T.; Kobayashi, H.; Yamashita, H., *J. Am. Chem. Soc.* **2018**, *140* (28), 8902-8909.
96. Li, X.; Zeng, Z.; Hu, B.; Qian, L.; Hong, X., *ChemCatChem* **2017**, *9* (6), 924-928.
97. Wang, X.; Shi, H.; Kwak, J. H.; Szanyi, J., *ACS Catal.* **2015**, *5* (11), 6337-6349.
98. Wang, J.; Lu, S.-m.; Li, J.; Li, C., *Chem. Commun.* **2015**, *51* (99), 17615-17618.
99. Cheung, C. W.; Hu, X., *Nat. Commun.* **2016**, *7*, 12494.
100. Lee, O.-Y.; Law, K.-L.; Yang, D., *Org. Lett.* **2009**, *11* (15), 3302-3305.
101. Lee, D.-H.; Taher, A.; Hossain, S.; Jin, M.-J., *Org. Lett.* **2011**, *13* (20), 5540-5543.

102. Ma, D.; Cai, Q.; Zhang, H., *Org. Lett.* **2003**, *5* (14), 2453-2455.
103. Bissember, A. C.; Lundgren, R. J.; Creutz, S. E.; Peters, J. C.; Fu, G. C., *Angew. Chem. Int. Ed.* **2013**, *52* (19), 5129-5133.
104. Shi, F.; Cui, X., *Catalytic Amination for N-Alkyl Amine Synthesis*, **2018**, Academic Press, 1-58.
105. Feng, C.; Liu, Y.; Peng, S.; Shuai, Q.; Deng, G.; Li, C.-J., *Org. Lett.* **2010**, *12* (21), 4888-4891.
106. Dennis, J. M.; White, N. A.; Liu, R. Y.; Buchwald, S. L., *J. Am. Chem. Soc.* **2018**, *140* (13), 4721-4725.
107. He, L.; Lou, X.-B.; Ni, J.; Liu, Y.-M.; Cao, Y.; He, H.-Y.; Fan, K.-N., *Chem. Eur. J.* **2010**, *16* (47), 13965-13969.
108. Kawahara, R.; Fujita, K.-i.; Yamaguchi, R., *J. Am. Chem. Soc.* **2010**, *132* (43), 15108-15111.
109. Zhao, Y.; Foo, S. W.; Saito, S., *Angew. Chem. Int. Ed.* **2011**, *50* (13), 3006-3009.
110. Elangovan, S.; Neumann, J.; Sortais, J.-B.; Junge, K.; Darcel, C.; Beller, M., *Nat. Commun.* **2016**, *7*, 12641.
111. Willets, K. A.; Duynes, R. P. V., *Ann. Rev. Phys. Chem.* **2007**, *58* (1), 267-297.
112. Kelly, K. L.; Coronado, E.; Zhao, L. L.; Schatz, G. C., *J. Phys. Chem. B* **2003**, *107* (3), 668-677.

## **CHAPTER-2**

### **Synthesis of Au@Ti-SiO<sub>2</sub> Nanocatalyst for CO Oxidation and Propene Epoxidation Reactions**

This Chapter is adapted from:

*A convenient route for Au@Ti-SiO<sub>2</sub> nanocatalyst synthesis and its application for low temperature CO oxidation.* Yogita Soni, E. A. Anumol, Chandrani Nayak, F. L. Deepak, C. P. Vinod, *J. Phys. Chem. C*, **2017**, 121 (9), 4946-4957.



## 2.1 Introduction

Gold in nanoform is known to catalyze several reactions including CO oxidation, epoxidation of alkenes, oxidation as well as hydrogenation of unsaturated hydrocarbons.<sup>1-7</sup> It is now well understood that the activity of spherical gold nanoparticles (hereafter NPs) is highly dependent on the size and type of support<sup>8</sup> with Au NPs of size below 5nm to be the most active for catalysis. Supported gold NPs of size less than 5nm are known to show low temperature activity for CO oxidation.<sup>9-11</sup> The catalytic activity of Au is defined by three major factors- particle size, support selection and contact between particle and support. Many supports such as TiO<sub>2</sub>, Fe<sub>2</sub>O<sub>3</sub>, NiO, CeO<sub>2</sub> are well known for their high activity for CO oxidation even at sub ambient temperatures.<sup>8-16</sup> But oxides like SiO<sub>2</sub> acts as an inactive support and show activity at much higher temperatures than those observed for active supports.<sup>17</sup> Since the CO oxidation activity is highly dependent on gold particle size,<sup>18</sup> it is highly desirable to control the gold particle size. In addition, selecting a proper support is also crucial as metal support interface can alter the CO oxidation activity. Since silica is a cheap and thermodynamically stable support, any modification in silica thereby improving the overall activity is definitely a great achievement. Silica can be modified with the first row transition metal such as titanium thus forming a new class of support known as titanosilicate. Titanosilicate is a well known catalyst for various oxidation reactions<sup>19,20</sup> especially epoxidation reactions<sup>21,23</sup> but its activity for CO oxidation is less known. There are only few reports of CO oxidation performed on Au/Ti-SiO<sub>2</sub>.<sup>24,25</sup> Titanium, both in TiO<sub>2</sub> or titanosilicate, can show variable oxidation states such as Ti<sup>3+</sup>/Ti<sup>4+</sup> working as a redox system. Due to this redox property there is a large scope for generating oxygen vacancies by tuning the synthesis conditions.<sup>26</sup> It is well known that the oxygen vacancies when present at metal support interface can activate oxygen molecule and contribute to enhanced CO oxidation activity in supported gold catalysts.<sup>27-28</sup> Thus controlling the size of gold NPs with enhanced metal support interfaces will show remarkably improved activity for CO oxidation. In our previous study we demonstrated Au@Ti-SiO<sub>2</sub> nanocatalyst with Au NPs size around 8-10 nm to show appreciable activity for CO oxidation (20% conversion at room temperature).<sup>29</sup> In the present work small gold NPs (3-5nm) are encapsulated inside Ti modified silica shell and demonstrated for CO oxidation activity at low temperature. Generally the oxide supported small Au nanoparticles are synthesised by deposition-

precipitation, co-precipitation or chemical vapour deposition method.<sup>8</sup> But the liquid phase methods are not efficient for support like silica due to weak interaction of gold NPs with silica which causes NPs agglomeration.<sup>8,30</sup> To maintain the size of gold NPs silica surface is generally modified with organic silanes forming functionalized silica.<sup>31-33</sup> Synthesis of Au@SiO<sub>2</sub> by conventional Stöbers method is difficult and works only for large size nanoparticles in a low yield.<sup>34</sup> This makes it difficult to achieve large-scale production with no significant interest to the catalysis community. Another method for synthesizing Au@SiO<sub>2</sub> with small sized gold NPs is by reverse micelle method<sup>35-36</sup> where the synthesis is done in organic medium. Synthesis of small sized gold NPs encapsulated in SiO<sub>2</sub> shell in aqueous medium with the exclusion of multiple steps is really a great challenge. The gold NPs have a strong tendency to agglomerate during encapsulation thereby losing their efficiency for catalytic reactions. In this chapter we report the synthesis of Au@SiO<sub>2</sub> catalyst for CO oxidation by sol gel method using APTMS as the organic modifier and linker to silica. The novelty of the work lies in the synthesis of Au@SiO<sub>2</sub> catalyst in aqueous medium in a short time using PVP as the stabilizer for the gold NPs of size ~ 5 nm. PVP is a well-known stabilizer for gold NPs and results in very small gold NPs.<sup>37,38</sup> The PVP stabilized gold ions have been encapsulated by co-condensation of 3-aminopropyltrimethoxysilane (APTMS) with tetraethylorthosilicate (TEOS) in aqueous medium. The encapsulated gold ions are further reduced by sodium borohydride (NaBH<sub>4</sub>) thus forming Au@SiO<sub>2</sub> catalyst. The silica shell once formed is again modified with titanium using titaniumtetraisopropoxide (TIP) as the Ti source forming highly active Au@Ti-SiO<sub>2</sub> catalyst. By this way the synthesis of core shell Au@Ti-SiO<sub>2</sub> with sub 5 nm size of gold NPs is reported for the first time. The amount of titanium is also varied by modifying the Si/Ti weight ratio. APTMS plays the role of linker between gold ions and silica thus enhancing the interaction of gold ions with silica<sup>39</sup>. The synthesised core shell material has been examined for gas phase CO oxidation and propene epoxidation

## **2.2 Experimental**

### **2.2.1 Synthesis of Core-shell Au@SiO<sub>2</sub>**

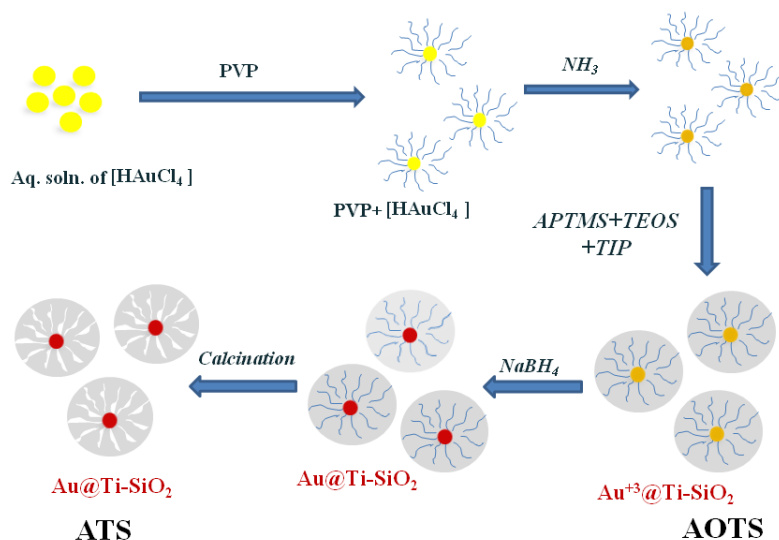
Au@SiO<sub>2</sub> catalyst was prepared by sol gel method with co- condensation of TEOS and APTMS. 15 mL of 8.3 mM gold precursor was taken and 500 mg of PVP was added to it. The solution was stirred for 20 min at room temperature. Then the solution was transferred to an oil bath already set at 40°C. To this solution 800 µL of NH<sub>3</sub> was added followed by the addition of APTMS and TEOS in a volume ratio of 10. The solution was stirred for 2-2.5 h at 40°C. The catalyst was collected by centrifugation and washed with millipore water thrice. The catalyst was kept for drying at 70°C. After drying, 350 mg of the catalyst was dispersed in 15 ml of water to which 1mL of freshly prepared 0.1 M ice cold NaBH<sub>4</sub> solution was added. The solution turned brown red indicating the reduction of gold ions to metallic gold. The catalyst was again centrifuged and washed with millipore water and dried at 70°C. Finally the catalyst was calcined at 550°C for 6 h to remove organic species and PVP, to form the Au@SiO<sub>2</sub> (AS) catalyst.

### **2.2.2. Synthesis of Au@Ti-SiO<sub>2</sub>**

The synthesis procedure for Au@Ti-SiO<sub>2</sub> catalyst was same as that of Au@SiO<sub>2</sub> except that TIP was added as titanium precursor. After the addition of TEOS silica precursor, the solution was stirred for 2-2.5 h. After this, required amount of titanium precursor TIP (dissolved in ethanol) was added. To maintain Si/Ti weight ratio 10, 100µL and for Si/Ti ratio 50, 30µL of TIP dissolved in 2mL of ethanol was added. The solution was again stirred for another 30 min. The rest of the procedure was same as that of Au@SiO<sub>2</sub> catalyst. The single batch synthesis yielded 350 mg of the catalyst. The synthesis procedure has been illustrated in scheme 2.1.

### **2.2.3 Catalysts Characterization**

To prepare the specimen for TEM/STEM, the samples were dispersed in ethanol by ultrasonication and a drop of this dispersion was placed on a holey carbon grid and dried. Transmission electron microscopy analysis was done with a Tecnai (Model F30) operating at 300 kV acceleration voltage. AC-TEM/STEM analysis at 80 kV was performed on Titan Cubed Themis 300 double corrected (probe and image) microscope equipped with a high brightness electron gun, monochromator, Super-X EDS detector and GatanEnfinium EELS spectrometer.

Scheme 2.1 Synthesis of Au@SiO<sub>2</sub>/Au@Ti-SiO<sub>2</sub> catalyst via sol gel method

STEM Images were acquired with the HAADF detector. TEM and HRTEM images were acquired with the CETA camera. EDS mapping, line scan analysis and spectra were collected with the BrukerEspirit software. HAADF-STEM tomography was performed on a FEI Titan ChemiSTEM equipped with a probe corrector. The tomography tilt series acquisition was carried out at an accelerating voltage of 80 kV. A convergence angle of 12 mrad and a probe current of 0.1 nA were employed. The specimen was loaded on to a FEI single tilt holder and automated tilt series acquisition was carried out using the tomography component in TIA software. HAADF images were acquired in the tilt range of -60° to +64° using a 3° increment up to 50° and 2° above that. The projection images were aligned using a cross-correlation algorithm and reconstructed using simultaneous iterative reconstruction technique (SIRT) using 20 iterations as implemented in the FEI Inspect 3D software. Amira software was used for 3D visualization.

UV-Visible analysis was done by Shimadzu 2700 Spectrophotometer with dual beam source equipped with diffuse reflectance attachment by taking BaSO<sub>4</sub> as the reference. Wide angle XRD analysis was recorded on Rigaku D MAX CuK $\alpha$  radiation with  $\lambda=1.54 \text{ \AA}$  from 10° to 90° at the scan rate of 4°/min. Nitrogen adsorption/desorption isotherms were collected by using Autosorb 1C Quantachrome, USA. The sample was first degassed at 250°C for 3h. After degassing the adsorption and desorption of N<sub>2</sub> was done at -196°C. The specific surface area was calculated by BET model. The pore

size distribution was calculated by using BJH method. The UV-resonance Raman spectroscopy analysis was done using 264nm excitation wavelength generated by tunable Ti:sapphire Laser (Indigo, Coherent Inc.). The average power used was 0.6 mW. Calibration was done by recording the spectra of dimethylformamide, cyclohexane, acetonitrile, and trichloroethylene with known band positions. Infrared spectroscopy measurements were done by Bruker FT-IR instrument using KBr as the reference. The sample was made in the form of KBr pellets.

X-ray Absorption Spectroscopy (XAS) had been carried out at Ti K edge in fluorescence mode at the Scanning EXAFS Beamline (BL-9) at the INDUS-2 Synchrotron Source (2.5 GeV, 100 mA) at the Raja Ramanna Centre for Advanced Technology (RRCAT), Indore, India. The beamline used a double crystal monochromator (DCM) which worked in the photon energy range of 4-25 KeV with a resolution ( $E/\Delta E$ ) of  $10^4$  at 10 KeV. A 1.5 m horizontal pre-mirror with meridional cylindrical curvature was used prior to the DCM for collimation of the beam and higher harmonic rejection. The second crystal of the DCM was a sagittal cylinder with radius of curvature in the range 1.28-12.91 meters which provided horizontal focusing to the beam while another Rh/Pt coated bendable post mirror facing down was used for vertical focusing of the beam at the sample position. For measurements in the fluorescence mode, the sample was placed at  $45^\circ$  to the incident X-ray beam and the fluorescence signal ( $I_f$ ) was detected using a Si drift detector placed at  $90^\circ$  to the incident X-ray beam. An ionization chamber detector was used prior to the sample to measure the incident X ray flux ( $I_0$ ) and the absorbance of the sample ( $\mu = \frac{I_f}{I_0}$ ) is

obtained as a function of energy by scanning the monochromator over the specified energy range.

The analysis of the EXAFS data had been carried out following the standard procedure using the IFEFFIT software package. This includes data reduction and Fourier transform to derive the  $\chi(R)$  versus  $R$  plots from the absorption spectra, generation of the theoretical EXAFS spectra starting from an assumed crystallographic structure and finally fitting of the experimental  $\chi(R)$  versus  $R$  data with the theoretical ones using the FEFF 6.0 code.

The structural parameters (i.e space group, lattice parameter, Wyckoff positions of the atoms), those had been used to generate the Fourier transformed theoretical  $\chi(R)$  versus  $R$

spectra were obtained from the Rietveld refined XRD data provided. The bond distances, coordination numbers (including scattering amplitudes) and disorder (Debye-Waller) factors ( $\sigma^2$ ), which give the mean-square fluctuations in the distances, had been used as fitting parameters. The  $k$  range for Fourier transform and the  $R$  range for data fitting had been chosen in such a way that in each case during fitting, the number of free variables were always kept below the upper limit set by Nyquist theorem ( $N_{\text{free}} = 2\Delta k\Delta r/\pi + 1$ ). The goodness of the fit in the above process is generally expressed by the  $R_{\text{factor}}$  which is defined as:

$$R_{\text{factor}} = \sum \frac{[\text{Im}(\chi_{\text{dat}}(r_i) - \chi_{\text{th}}(r_i))]^2 + [\text{Re}(\chi_{\text{dat}}(r_i) - \chi_{\text{th}}(r_i))]^2}{[\text{Im}(\chi_{\text{dat}}(r_i))]^2 + [\text{Re}(\chi_{\text{dat}}(r_i))]^2}$$

where,  $\chi_{\text{dat}}$  and  $\chi_{\text{th}}$  refer to the experimental and theoretical  $\chi(R)$  values respectively and Im and Re refer to the imaginary and real parts of the respective quantities.

XPS was done using VG ESCA 3000 model with Al  $K\alpha$ , dual anode as the X-Ray source (1486.6 eV) operating at a pass energy of 50 eV. Peak fitting was carried out using Casa XPS software with a Shirley background. All the binding energies were calibrated with respect to C1s as the reference (284.6 eV).

## 2.2.4 Catalytic Activity Test

### 2.2.4.1 CO Oxidation:

The applicability and stability of all the catalysts for CO oxidation were performed from room temperature to 300°C. The catalyst tests were performed under atmospheric pressure in a fixed bed reactor of diameter 14 mm. Mass flow controllers were used to control the flow of CO, O<sub>2</sub> and N<sub>2</sub> gases. The reactor was placed in a tubular furnace with a uniform heating zone of 4 cm furnished with a temperature controller radix 6400. A K-type thermocouple placed in the thermowell was used to measure the catalyst bed temperature. The flow rate of reaction gases was 50 mL/min (CO:O<sub>2</sub>:N<sub>2</sub>=1:5:19) with a GHSV (Gas Hourly Space velocity) of 30,000 cm<sup>3</sup>/g<sub>cat</sub>/h. The conversion reported was performed in the steady state with a ramping rate of 2°C/min and held at various temperatures for 10 min for equilibration. The reactor outflow was analyzed by using a gas chromatograph equipped with online gas sampling valve, 91.44 cm molecular sieve 13 × columns and a thermal conductivity detector (TCD). The percentage conversion of CO was calculated using the formula =  $\text{CO}_{\text{in}} - \text{CO}_{\text{out}}/\text{CO}_{\text{in}} \times 100$ .

**2.2.4.2 Propene Epoxidation:** Gas phase propene epoxidation reaction in the presence of molecular H<sub>2</sub> and O<sub>2</sub> were conducted in Technical University of Eindhoven, The Netherlands. Catalytic tests were performed at atmospheric pressure in a fix bed reactor. In a typical test, 150 mg of catalyst was loaded in a quartz reactor with inner diameter 6 mm and placed in a tubular oven. The flow of the reactant gases was adjusted to 25 ml/min (with a ratio of 1H<sub>2</sub>: 1O<sub>2</sub>: 1C<sub>3</sub>H<sub>6</sub>: 7Ar) with a GHSV of 10,000ml/g<sub>cat</sub>/h. A typical reaction cycle was 5 h followed by regeneration step in the presence of 10 vol% O<sub>2</sub> in He at 573 K for 1 h. The reaction cycles were carried out in the temperature range 423-493 K and rate of each cycle was calculated as the average rate for the reaction performed between 150 min to 300 min on time stream. The propylene conversion and selectivity to PO were expressed as:

$$\text{Conversion (\%)} = [\text{moles of (products)}/\text{moles of propene in feed}] \times 100$$

$$\text{Selectivity (\%)} = [\text{moles of PO}/\text{moles of (products)}] \times 100$$

H<sub>2</sub> efficiency was calculated as:

$$\text{H}_2(\%) = [r_{\text{PO}}/(r_{\text{PO}}+r_{\text{H}_2\text{O}})] \times 100$$

Where r<sub>PO</sub> and r<sub>H<sub>2</sub>O</sub> were rates of PO and H<sub>2</sub>O produced respectively.

## **2.3 Results and Discussion**

The synthesised Au@SiO<sub>2</sub> and Au@Ti-SiO<sub>2</sub> nanocatalysts were characterized by various spectroscopy and microscopy techniques such as XRD, ICP-OES, solid state UV-Visible Spectroscopy, Surface area measurement, IR spectroscopy, UV-Raman spectroscopy, Synchrotron X-ray Absorption Spectroscopy (XAS), XPS, TEM and STEM.

### **2.3.1 X-ray Diffraction**

The XRD pattern of the catalysts showed the reflections from different planes of FCC gold (Figure 2.1a). Here AOTS and AOS denoted gold encapsulated in titanosilicate and silica shell respectively prior to NaBH<sub>4</sub> reduction and calcination and ATS and AS denote the encapsulated gold in titanosilicate and silica respectively after NaBH<sub>4</sub> reduction and calcination. The numbers 10 and 50 in AOTS and ATS samples refer to the Si/Ti weight ratio. All the samples showed broad peaks at 2θ=23° of amorphous silica.

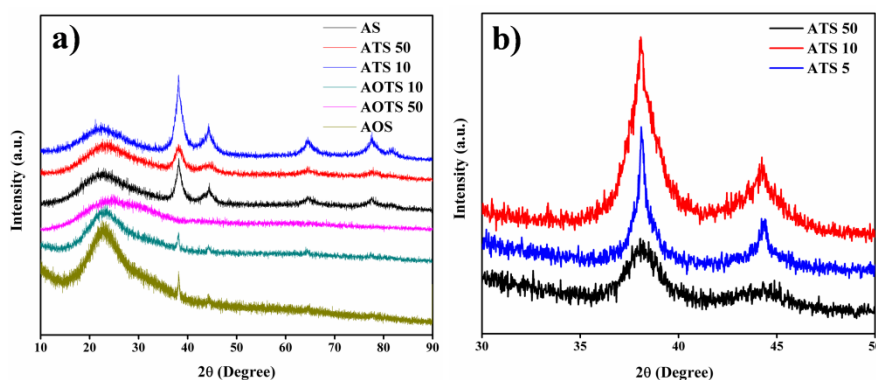


Figure 2.1 XRD plots of as synthesized and calcined AS and ATS catalysts.

The reflections for phase segregated  $\text{TiO}_2$  was absent in all the samples indicating the incorporation of titanium in the silica matrix. The possibility of small titania aggregates could not be ruled out, but was beyond the detection limit of XRD. All the samples showed the reflections of metallic gold at  $2\theta = 38.3^\circ$  indicating that gold was present in FCC phase but the intensity was substantially higher in AS and ATS samples due to the complete reduction of gold ions by  $\text{NaBH}_4$  and further after calcination. The appearance of gold reflections in AOTS was due to the reduction of some of the gold ions by PVP during synthesis, which grew further in size after  $\text{NaBH}_4$  reduction and calcination. In Figure 2.1b ATS 5 catalyst was also included to show that particle size increased after increasing the titanium loading from ATS 50 to ATS 5.

### 2.3.2 ICP-AES

ICP-AES analysis was done to estimate the loading of titanium in the ATS 10 and ATS 50. Ti loading for ATS10 and 50 were 2.5 and 0.98 wt % respectively. The gold loading for ATS 10 and ATS 50 as calculated by ICP analysis was 3.5wt% and for AS it was 4wt%. Though the gold precursor amount was same in all the samples, the difference in the ICP values in ATS and AS can be due to the repeated washing during centrifugation.

### 2.3.3 DRUV-visible Spectroscopy

DRUV-visible spectroscopy is a useful tool to know the coordination of Ti in silica matrix. The solid state UV visible spectra of as synthesised and calcined nanocatalysts were shown in Figure 2.2.



UV-Visible spectra for AOS and AOTS catalysts showed no peak in the region of 500-600 nm (Figure 2.2a) whereas all the reduced catalysts showed gold plasmon band at 515 nm (Figure 2.2b).

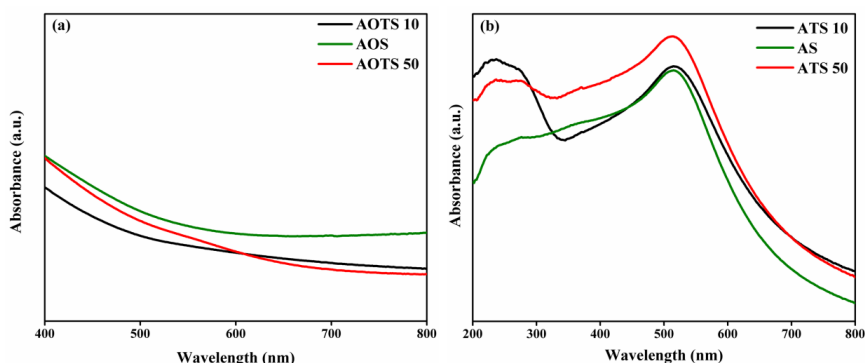


Figure 2.2 DRUV-visible spectra of (a) as synthesised (b) reduced and calcined catalysts. There was a slight shift in SPR band towards the higher wavelength for ATS 10, which indicates an increase in gold nanoparticles size. The band at 230 nm represents the titanium present in tetrahedral coordination in the silica matrix. The exact position of this band is 220 nm if titanium is isomorphously substituted in silica framework with tetrahedral coordination.<sup>29</sup> The red shift in this band is reported to be due to distorted tetrahedral coordination of titanium.<sup>40</sup> The band at 260-270 nm was also present which may be due to the presence of some penta or hexa coordinated Ti species due to ligation of titanium with water molecules or may be due to presence of some extra framework titanium species.<sup>41</sup> The absence of band after 330 nm confirms that bulk titania was not present in the sample.

### 2.3.4 N<sub>2</sub> Porosimetry

The textural property of the catalysts was evaluated by surface area analysis. Figure 2.3a shows the N<sub>2</sub> adsorption/desorption isotherm for the AS and ATS catalysts. All the samples showed type IV hysteresis loop which is indicative of mesoporous materials.<sup>42</sup> The surface area of gold-silica (AS) catalyst was 153 m<sup>2</sup>/gm. Incorporation of titanium in silica increased the surface area of both ATS catalysts. The surface area obtained for ATS10 and ATS50 were 244 and 203 m<sup>2</sup>/gm respectively. ATS10 and ATS50 showed H3 type hysteresis loop which could be attributed to the slit like pores present in the catalysts.<sup>42</sup>

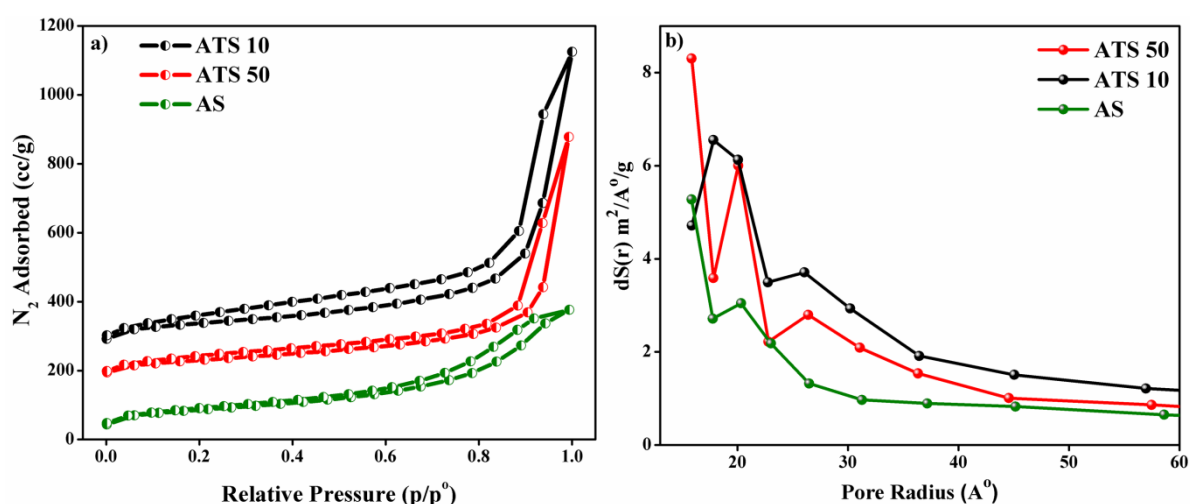


Figure 2.3 (a) N<sub>2</sub> adsorption and (b) pore size distribution of AS and ATS catalysts.

Figure 2.3b shows the pore size distribution of the three catalysts. The pore size was measured from BJH pore size distribution with average pore radius of 2.0 nm. The unmodified AS catalyst showed only one type of pore with radius around 2.0 nm. But ATS 10 and ATS50 catalysts showed bimodal pores with pore radius 2.0 nm and 2.5 nm. The appearance of larger pores in both the ATS catalysts can be due to incorporation of titanium in silica matrix. Since the ionic radius of Ti<sup>4+</sup> is greater than Si<sup>4+</sup> (Si<sup>4+</sup>=0.48 Å<sup>0</sup> and Ti<sup>4+</sup>=0.68 Å<sup>0</sup>) the exchange of some of the Si<sup>4+</sup> ions by Ti<sup>4+</sup> in silica matrix caused the pore enlargement.<sup>43</sup>

### 2.3.5 Electron Microscopy

The TEM analysis of our catalysts revealed the morphology and particle size of the catalysts. Figure 2.4 shows the TEM images of all the AS and ATS catalysts. The TEM images of AS (Figure 2.4a and b) nanocatalyst showed that gold NPs size is very small and are encapsulated in silica shell. Some particles were observed as agglomerated larger particles outside core shell organization, which could not get encapsulated during silica encapsulation. The TEM images also revealed that most of the gold NPs size was less than 5 nm. The overall particle size of core shell structure was around 20 nm. After the incorporation of titanium in silica matrix both the ATS catalysts retained the core shell morphology. Though the particle size increased after titanium loading (consistent with the UV-Vis observation) most of the particles fall in

the size regime of 5 nm. Figure 2.4 (c) and (d) show the TEM images of ATS 50 nanocatalyst.

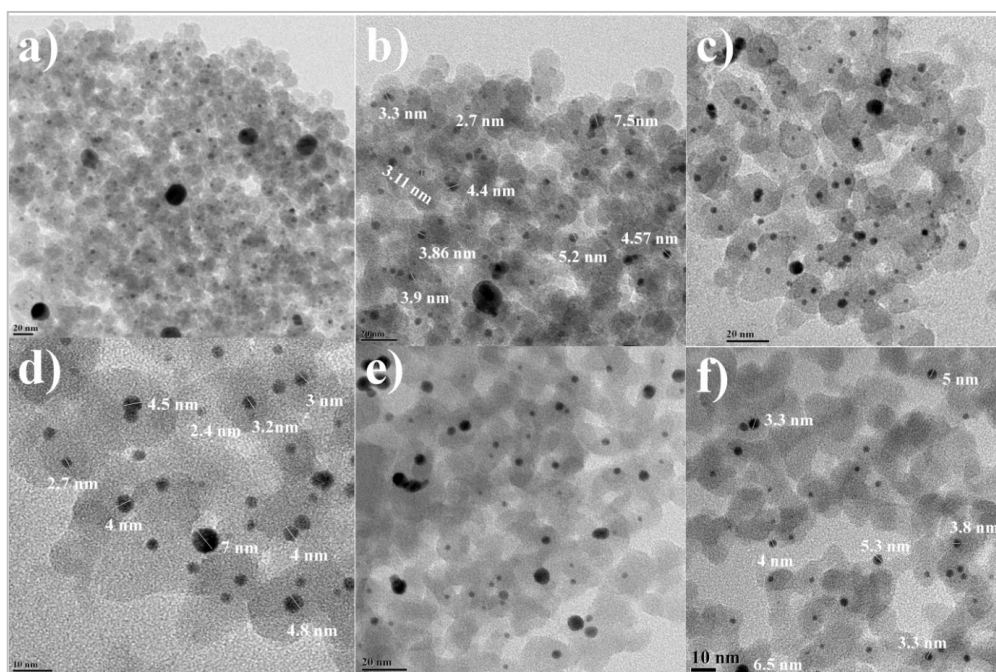


Figure 2.4 TEM images of (a, b) AS (c, d) ATS 50 and (e, f) ATS 10 catalysts. Scale bar: (a-c) 20 nm (d) 10 nm (e-f) 20 nm

The TEM images revealed that even after the incorporation of titanium in silica matrix most of the gold NPs were less than 5 nm in size and the catalyst did not lose its core shell morphology. The particle size calculated from Debye Scherer equation was 6.3 nm which is slightly higher than observed with TEM. This is due to the presence of some larger particles formed out of the silica shell and contributed to the overall increase in particles size from XRD. The TEM analysis of ATS 50 catalyst did not show the presence of phase separated titania which indicates the incorporation of titanium inside silica shell (Figure 2.5a). The particle size analysis from several TEM images showed that maximum particle size after titanium incorporation was 6-7 nm with most of the particle in the size regime of 2-4 nm. This shows the successful encapsulation of smaller gold nanoparticles via sol gel method. The TEM images of ATS 10 catalysts in Figure 2.4 (e and f) show some distortion in the morphology after increasing the titanium content which is obvious since introduction of foreign atom in silica lattice can destroy the core shell morphology. But the gold particle size was still lower even though some larger NPs were also present. Unlike ATS 50 catalyst the HR TEM image of ATS 10 (Figure 2.5b) catalyst shows the presence of phase segregated

nanodomains of titania in the silica matrix. The d spacing value 0.315 nm corresponds to (110) plane, 0.246 and 0.248 correspond to (101) planes of rutile  $\text{TiO}_2$  (JCPDS PDF# 782485). A careful observation of HRTEM shows that these titania particles are present in the close proximity of gold NPs as well as away from gold NPs.

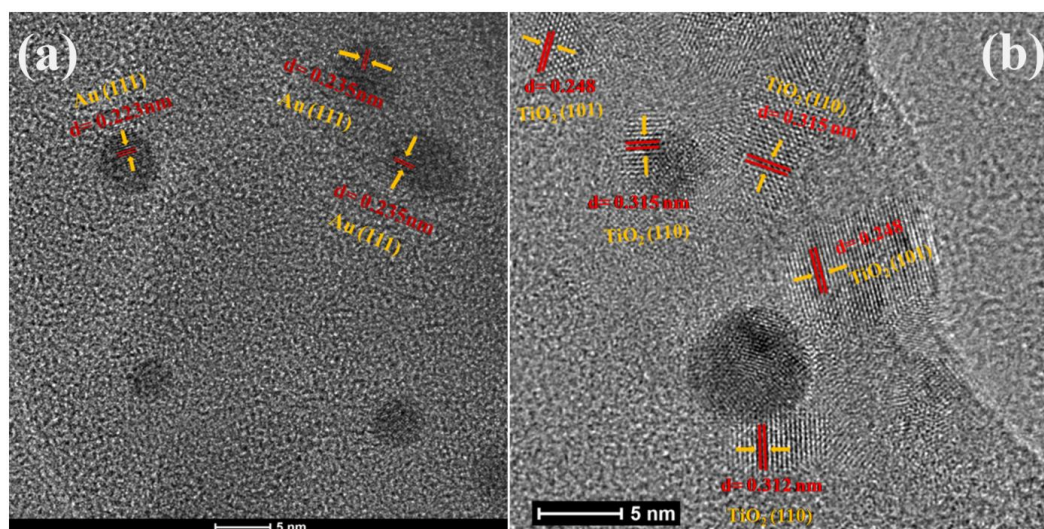


Figure 2.5(a) HRTEM image of ATS 50 (no phase segregated  $\text{TiO}_2$  particles). (b) HRTEM image of ATS 10 showing the presence of phase separated  $\text{TiO}_2$

The STEM EDS mapping of the ATS 50 in Figure 2.6 showed the presence of titanium which was evenly distributed inside silica lattice. Interestingly, the EDS mapping indicated that the larger gold nanoparticles which were not encapsulated lacked the proximity with titanium. Presence of titanium was clearly seen in silica shell along with smaller gold nanoparticles. Thus a combined HRTEM and STEM analysis of this catalyst did not show any features of phase separated  $\text{TiO}_2$  which indicates that ATS 50 had titanium which was incorporated in silica and in close proximity with small gold nanoparticles. STEM EDS images of ATS 10 catalyst can be seen in Figure 2.7. The presence of titanium in the form of small clusters was clearly visible in this catalyst.

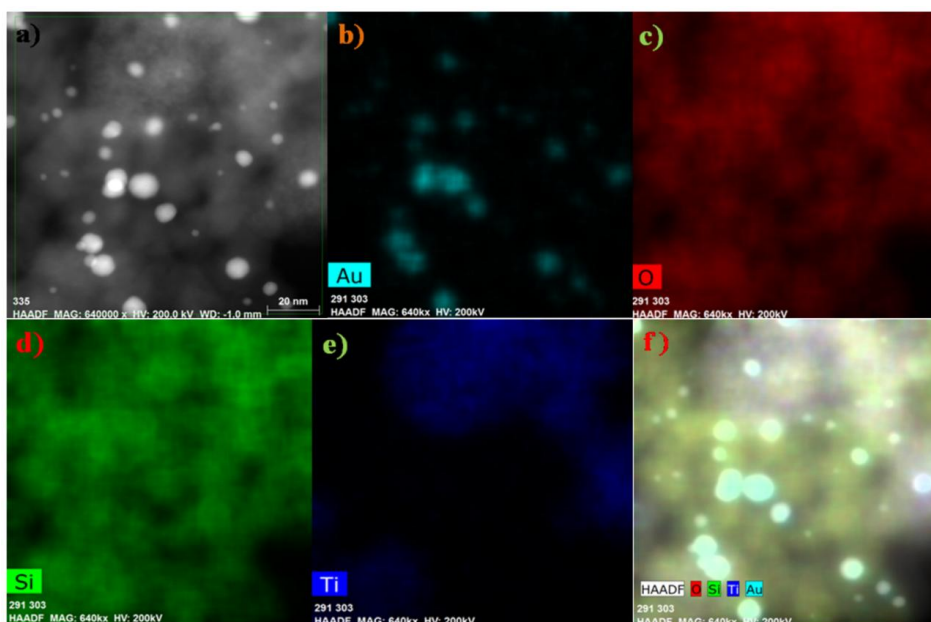


Figure 2.6 (a) HAADF-STEM image of ATS 50. (b-f) STEM-EDS mapping of individual elements. (Scale bar 20 nm)

These small clusters were visible in HRTEM (Figure 2.5b) as well as in STEM –HAADF images of ATS 10 catalyst (Figure 2.7b and f). These TiO<sub>2</sub> clusters were present in close proximity of gold nanoparticles and also outside the silica matrix.

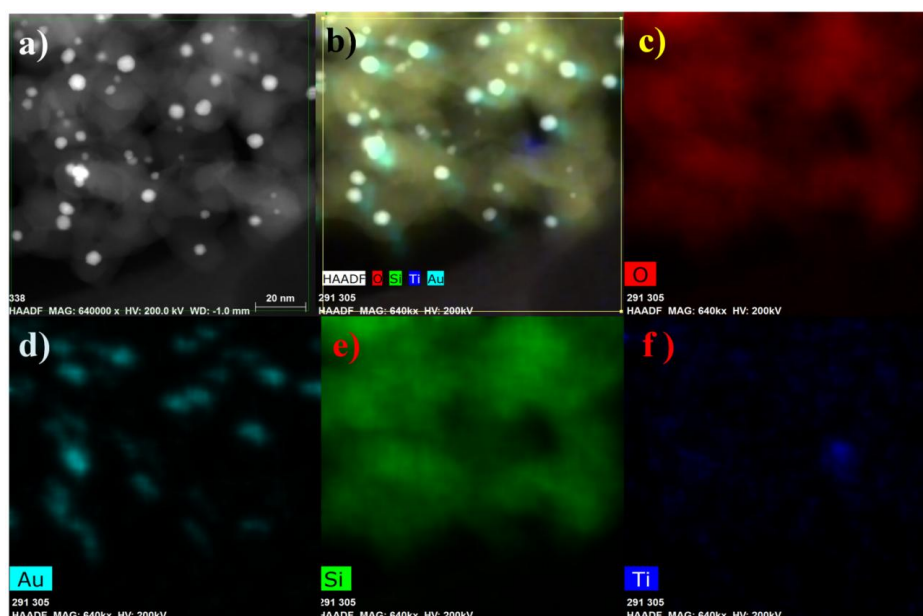


Figure 2.7(a) HAADF-STEM image of ATS 10. (b-f) STEM-EDS mapping of individual elements. (Scale bar 20 nm)

Thereby increase in the titanium loading showed a marginal increase in the particle size of along with phase segregation of  $\text{TiO}_2$ . Further increasing the Ti loading in the catalyst to Si/Ti ratio 5 and denoted by ATS 5 resulted in increased Au particle size (8-10 nm) as well complete loss in morphology (Figure 2.8). So we restricted our characterization and catalysis activity test to ATS 10 and ATS 50.

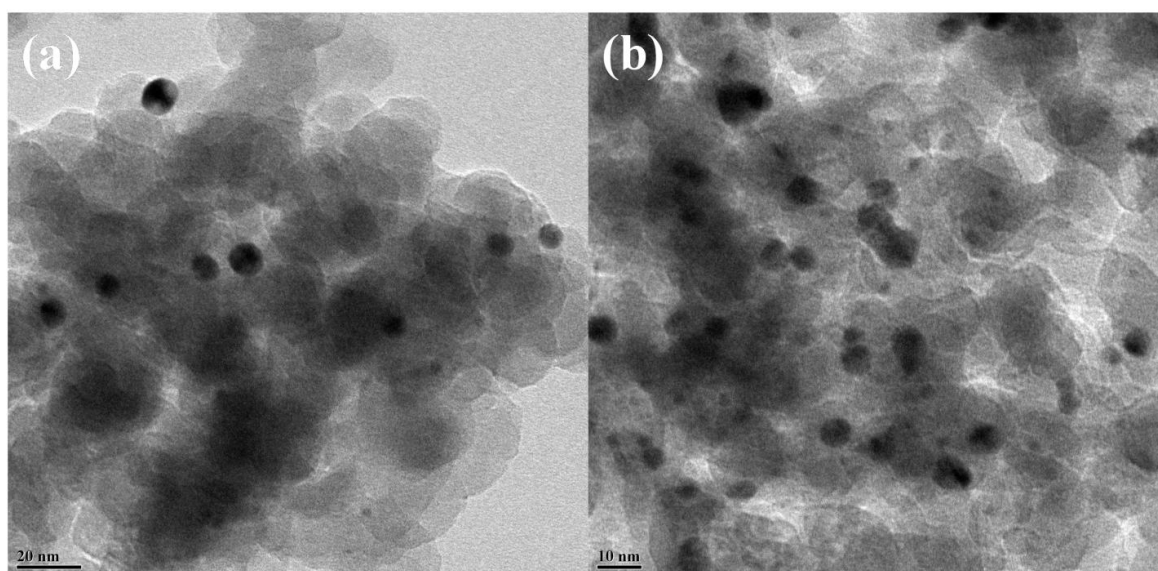


Figure 2.8 TEM images of ATS 5 catalyst. Scale bar: (a) 20 nm (b) 10 nm.

### 2.3.6 IR Spectroscopy

The incorporation of titanium in the silica matrix was examined by IR spectroscopy for both the ATS nanocatalysts and compared with AS. Figure 2.9 showed the IR spectra of pure AS and ATS catalysts. The vibrational band from  $1035\text{-}1228\text{ cm}^{-1}$  was originated from the asymmetric stretching vibration of Si-O-Si bond. There was slight broadening of this band after incorporation of titanium. The band at  $960\text{ cm}^{-1}$  observed for the catalysts has been interpreted by Boccuti *et al* to vibrations from Si-O-X bond (where X= H or Ti) .<sup>44</sup> This band became more pronounced as the titanium content increased indicating larger incorporation of titanium in silica matrix. The shift in this happened was due to increased degeneracy of elongation vibration of the tetrahedral structure of the  $\text{SiO}_4$  induced by incorporation of titanium.<sup>45</sup> The intensity of band at  $800\text{ cm}^{-1}$  decreased with increased loading of titanium which indirectly pointed to the replacement of some  $\text{Si}^{4+}$  with  $\text{Ti}^{4+}$  ions. The intensity of band at  $1630\text{ cm}^{-1}$  increased by incorporation of titanium in silica. This band corresponds to the bending frequency

of water and shows increase in hydrophilicity of the system after titanium incorporation.

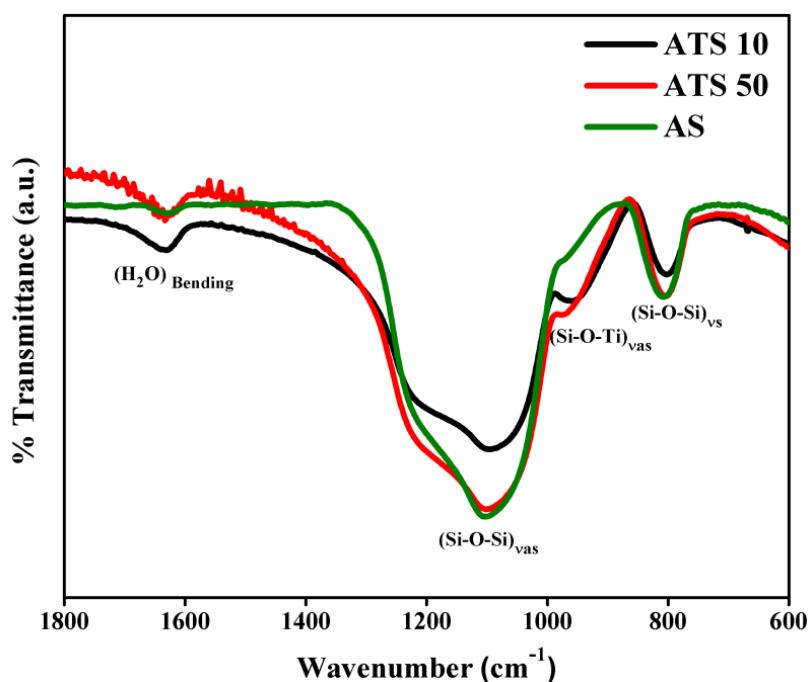


Figure 2.9 IR spectra of AS and ATS catalysts

### 2.3.7 Raman Spectroscopy

Figure 2.10 (a) shows the Raman and (b) UV-Raman spectra of ATS 10 and ATS 50 catalysts done at 632 nm and 264 nm laser wavelengths respectively. Raman analysis done at the visible laser source (632 nm) showed that ATS 10 catalyst had most of the reflections of titania. The band at 600-650  $\text{cm}^{-1}$  corresponds to anatase and rutile titania<sup>46</sup> and corroborates the HRTEM results of ATS 10 (Figure 2.5b). But this band is absent in ATS 50 catalyst which shows that the titanium is well distributed in silica matrix. However the band at 700  $\text{cm}^{-1}$  can be seen in Raman spectrum of Figure 2.10a of both the catalysts (more intense in ATS 10) which is due to the presence of amorphous non framework titanium species.<sup>47,48</sup> This band can be correlated with UV-visible band at 260-270 nm which corresponds to the penta or hexa coordinated titanium due to ligation of water or presence of amorphous non framework titanium.<sup>41</sup> But Raman analysis confirms that this multi coordination was due to presence of amorphous extra framework titanium species.

But ligation of water can be ruled out as the Raman band at  $700\text{ cm}^{-1}$  clearly shows the presence of amorphous extra framework titanium.<sup>47,48</sup> The 632 nm laser source gives very weak reflections for framework titanium which usually comes after  $1100\text{ cm}^{-1}$ . To overcome this difficulty we performed UV Raman analysis for both the samples at 264 nm laser source. UV Raman is a powerful tool to identify the incorporation of transition metals in the silica framework.<sup>49</sup> The transition metal ions substituted in the framework of silica show a charge transfer between metal ions and framework oxygen anions in the UV region. Therefore UV laser can be used to excite these transitions to obtain UV resonance Raman spectra. Taking advantage of this property framework transition metal ion can be selectively detected by UV Raman spectroscopy.<sup>50</sup> Thus, this technique is highly sensitive to the presence of framework and non framework Ti present in silica matrix.

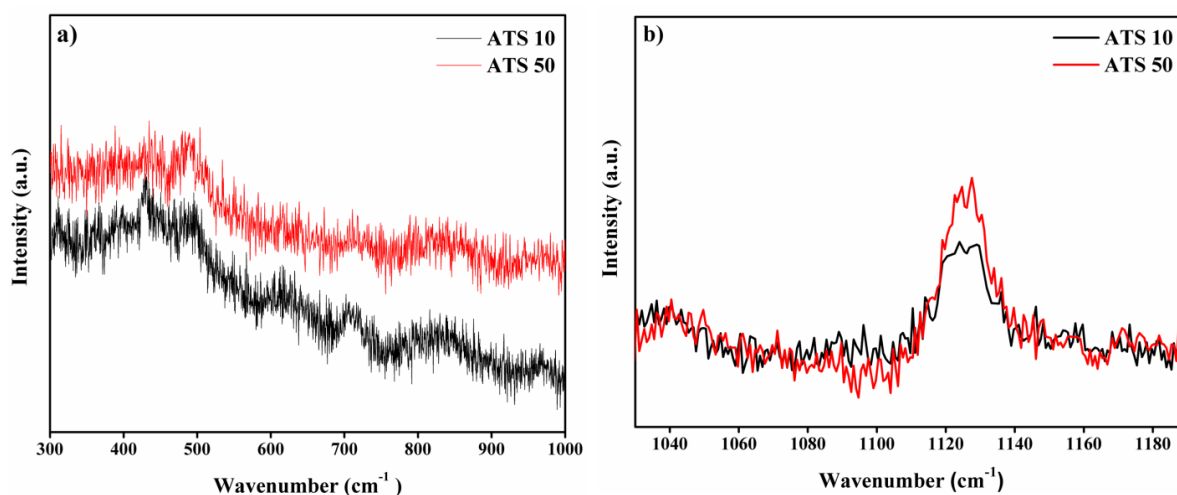


Figure 2.10 (a) Raman and (b) UV Raman spectra of ATS 10 and 50 catalysts in different regions. 632 nm and 234 nm Lasers were used for Raman and UV-Raman analysis respectively.

The band at  $1125\text{ cm}^{-1}$  in Figure 2.10b can be assigned to the framework titanium species<sup>49</sup>. But due to poor adjustment of laser in 400-800 nm window, we could not get useful information regarding framework and non framework titanium species so we restricted our spectrum in 1000-1200 window where we could get a well distinguished peak for framework titanium. Also the extra framework anatase or rutile titania bands were comparatively weaker than the framework titanium species when excited with UV Raman laser source which could be another reason of not getting



clear bands in 400-800 nm region. This phenomenon is due to the occurrence of non radiation and fluorescence processes in TiO<sub>2</sub> when excited with UV light.<sup>49</sup>

Hence Raman and UV Raman analysis confirmed the presence of both framework as well as non framework Ti species in ATS 10 and 50 samples and match well with UV-visible and HRTEM results.

### 2.3.8 X-ray Absorption Spectroscopy (XAS)

XANES represents the electronic transition from the inner levels to the outer unoccupied levels caused by the absorption of X-rays and gives the information about the local environment around the absorbing atom. To know about the coordination of titanium in the silica matrix XAS analysis was performed for ATS 10 and ATS 50 catalysts. To make this comparison clear we included ATS 5 sample with very high Si/Ti ratio 5. The characteristics feature in Ti K-edge is the pre edge caused by the excitation of 1s electrons into an empty bound state derived from d and p states of Ti and O<sup>41</sup>. XAS spectra of all the samples are shown in Figure 2.11. The XANES spectrum of ATS samples along with Ti metal and anatase TiO<sub>2</sub> standards was shown in Figure 2.11a. The pre edge intensity or shape of the Ti-K edge XANES spectrum determines the coordination of titanium in silica matrix. The XANES spectra of the samples showed pre edge feature at 4970 eV which is characteristic of four coordinated Ti cations.<sup>51</sup> The intensity of the pre edge peaks of all the ATS samples matched to the intensity of anatase TiO<sub>2</sub> standard but with a vastly different peak shape from anatase TiO<sub>2</sub>. It showed that along with the presence of distorted tetrahedral titanium some penta or hexa coordinated titanium was also present which made the pre edge peak less intense as well as broad.<sup>51</sup> This corroborates the HRTEM of ATS 10 which shows the presence of some TiO<sub>2</sub> clusters. Figure 2.11b showed the experimental (r) versus r plots of the ATS samples at Ti K edge along with the best fit theoretical plots. The results from fitting were tabulated in Table 2.1.

It was clear from the Table 2.1 that titanium was present in the tetrahedral coordination in all the samples. A slight increase in coordination no. with increase in titanium loading might be due to the presence of some octahedral titanium. Also the Ti-O bond distance was shorter than anatase TiO<sub>2</sub> (1.93 Å) showing the absence of bulk TiO<sub>2</sub>.

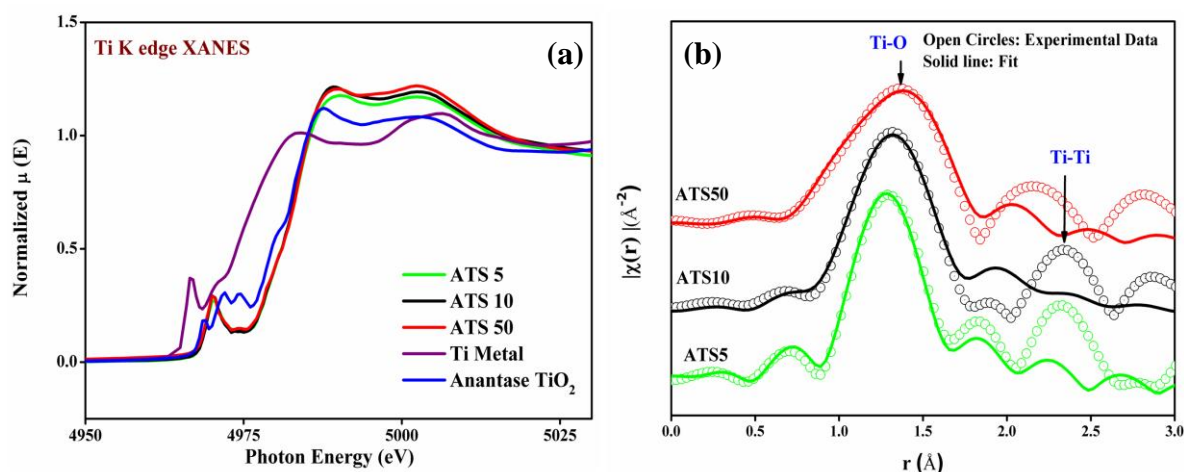


Figure 2.11 (a) XANES and (b) EXAFS spectra of ATS samples.

| Sample name | $r$ (Å) | C.No. | $\sigma^2$ |
|-------------|---------|-------|------------|
| ATS 5       | 1.83    | 4.2   | 0.004      |
| ATS 10      | 1.84    | 4.1   | 0.004      |
| ATS 50      | 1.85    | 3.8   | 0.007      |

Table 2.1 Fitting results of EXAFS where  $r$  is Ti-O bond distance, C. No. is coordination no. around Ti atom and  $\sigma^2$  is the Debye Waller factor.

The single scattering path of Ti by neighbouring Ti atoms in  $\text{TiO}_2$  is expected to give two peaks in the range of 2.7 Å and 3.6 Å corresponding to edge shared octahedra and corner shared octahedra respectively. These FT peaks were shifted down to lower values due to decreasing particle size as surface to volume ratio and number of distorted sites at the surface increases as particle size decreases.<sup>52</sup> Figure 2.11b showed the presence of a peak just below 2.5 Å in ATS 5 and ATS 10 samples which corresponds to the Ti-Ti coordination confirming the presence of small  $\text{TiO}_2$  clusters or hexacoordinated titanium in high loading ATS samples.<sup>52</sup> The coordination no. for all the three samples showed only slight variation which might be due to the presence of mixed states of Ti-O-Ti as well as Ti-O-Si.

### 2.3.9 X-ray Photoelectron Spectroscopy

Figure 2.12 showed the Ti 2p XPS plot of ATS 50 calcined and reduced samples. Reduction was done at 400°C for 1h in H<sub>2</sub> flow. Calcined sample showed a symmetric Ti 2p<sub>3/2</sub> peak at 459 eV typical for Ti<sup>4+</sup> ions which matches well with titanosilicates.<sup>53</sup> But after reduction treatment a well developed shoulder could be identified at 457.6 eV along with 459 eV peak. The former binding energy value matches well with Ti<sup>3+</sup> ions generated during the reduction of Ti<sup>4+</sup> underhydrogen.<sup>54</sup> These sites can contribute to the activity enhancement for catalytic reaction.

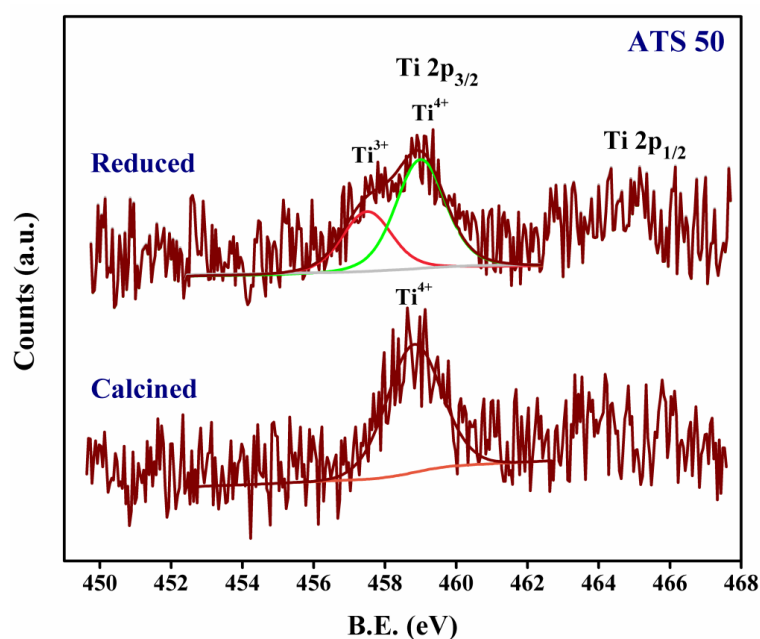


Figure 2.12 Ti 2p XPS plot for ATS 50 calcined and reduced catalyst.

### 2.3.10 Catalytic Activity

The synthesised nanocatalysts were tested for gas phase CO oxidation and propene epoxidation reactions. The details of the reaction procedures have been provided in the experimental section.

#### 2.3.10.A CO Oxidation

The catalytic activity of AS and ATS nanocatalysts was tested for CO oxidation. Figure 2.13a showed the activity of AS and ATS calcined nanocatalysts. The activity of the calcined AS catalyst started after 150°C and showed only 66% conversion up to 300°C. This is similar to Au-SiO<sub>2</sub> system reported previously.<sup>55-56</sup> But the catalytic

activity of ATS 10 and ATS 50 was much higher as compared to AS achieving full conversion after 180°C. This enhanced activity can be attributed to the incorporation of titanium in the silica matrix. Among all the calcined catalysts ATS 50 showed the highest activity with 15% conversion at 60°C. The reason for this enhanced activity in ATS 50 can be related to gold nanoparticles size. The frequency of smaller gold particles is higher in ATS 50 as compared to ATS 10 which is responsible for the low temperature activity of ATS 50. The optimum size of gold NPs to be catalytically active at room temperature is 3-5nm<sup>9</sup> which was more for ATS 50 catalyst.

Another reason for enhanced activity of ATS 50 calcined sample could be isomorphous distribution of titanium in silica matrix as can be seen from the STEM-EDS elemental mapping. The smaller gold NPs in close vicinity of titanium were able to catalyze the reaction at room temperature.

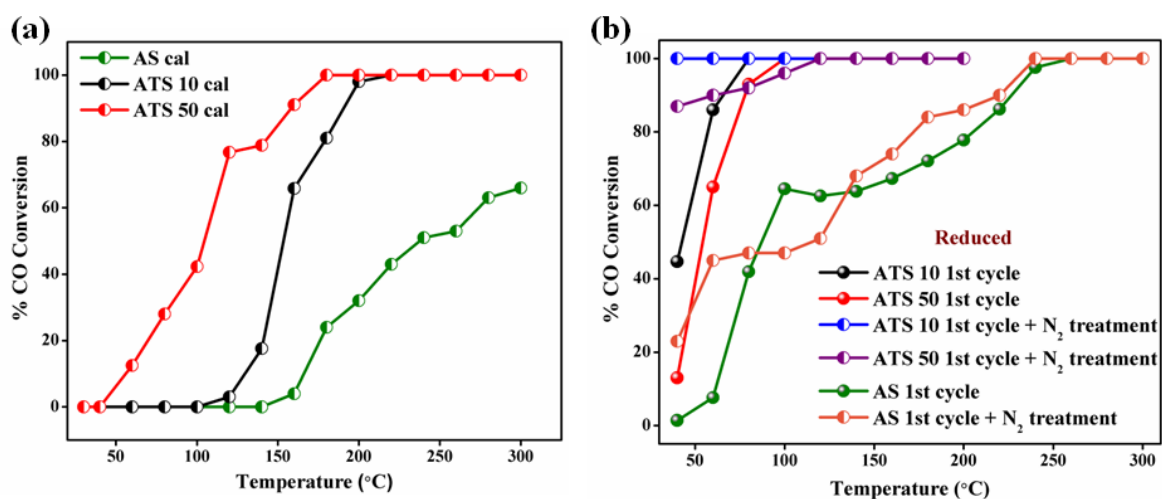


Figure 2.13 CO oxidation activity of AS and ATS (a) calcined and (b) reduced catalysts

Further the CO oxidation activity was tested for all the catalysts pre-treated in hydrogen flow at 400°C for 1 hr (Figure 2.13b). This mild reduction step resulted in activity improvement for all the catalysts. The activity of reduced AS catalyst was shifted to low temperature ca 60°C. This increment in the activity of AS catalyst can be explained on the basis of oxygen vacancy or E-centre generation under the H<sub>2</sub> flow. It has been shown by Rombi *et al.* that gold nanoparticles of size below 5 nm supported on SBA-15 show room temperature activity when thermally treated under H<sub>2</sub> atmosphere at 400°C.<sup>28</sup> The generation of E-centres or oxygen vacancies requires oxygen abstraction from silica and gold plays a key role in the E-centre generation.<sup>27</sup> This process is triggered by gold NPs by dissociatively adsorbing hydrogen molecule.

These E-centres are able to activate oxygen molecule by forming superoxide species,  $O_2^-$  which is responsible for the catalytic activity demonstration at low temperatures.<sup>28</sup> In the present study also the activity enhancement after  $H_2$  treatment could be attributed to generation of E-centres in silica support.

Though the activity towards CO oxidation after reduction step was improved for all the catalysts the appreciable change could be observed in ATS 10 and ATS 50 catalysts. It is clear from Figure 2.13b that activity of both the reduced catalysts had been shifted to room temperature with full conversion at  $100^\circ C$  for ATS 50 and  $80^\circ C$  for ATS 10. On comparing the activity of ATS 10 and ATS 50 reduced catalysts, ATS 10 showed marginally better activity than that of ATS 50 though ATS 10 had slightly bigger particles than ATS 50. The reduction in hydrogen can create oxygen vacancies in both framework and non framework titanium (segregated  $TiO_2$  particles in proximity with Au). Support for this also comes from our XPS analysis which gave clear indication of  $Ti^{3+}$  species after reduction pre-treatment. Since, Au/ $TiO_2$  is a well known system for CO oxidation at low temperature<sup>9-11</sup> and the presence of small  $TiO_2$  clusters in close proximity of gold (as revealed in HRTEM analysis) can be the reason for ATS 10 catalyst to show marginally better activity than ATS 50 after hydrogen treatment. Oxygen activation is the most difficult and rate determining step in CO oxidation with highest activation barrier and oxygen is known to activate at these oxygen vacancies present at the perimeter of Au and support.<sup>57</sup> CO oxidation plot for ATS 5 red catalyst is also shown in Figure 2.14. As expected ATS 5 did not show room temperature activity like ATS 10 and 50. This is because of the presence of larger gold nanoparticles which were not active at room temperature. But this catalyst showed better activity than AS catalyst because of the presence of  $TiO_2$  clusters. Thus, activity of ATS 5 after  $100^\circ C$  can be attributed to the gold NPs of size 8-10 nm which were close to  $TiO_2$ .

The CO oxidation activity has been found to critically depend on the various pre-treatments given to the catalyst prior to or after the reaction.<sup>58-59</sup> These treatments can increase as well as decrease the catalytic activity. In the present report we have shown that hydrogen treatment given to all the catalysts increased the activity by shifting the onset temperature to room temperature due to increased oxygen vacancy generation. In our previous report we have found that nitrogen treatment given to the catalyst enhanced the activity showing almost 70% conversion even at room temperature.<sup>29</sup>

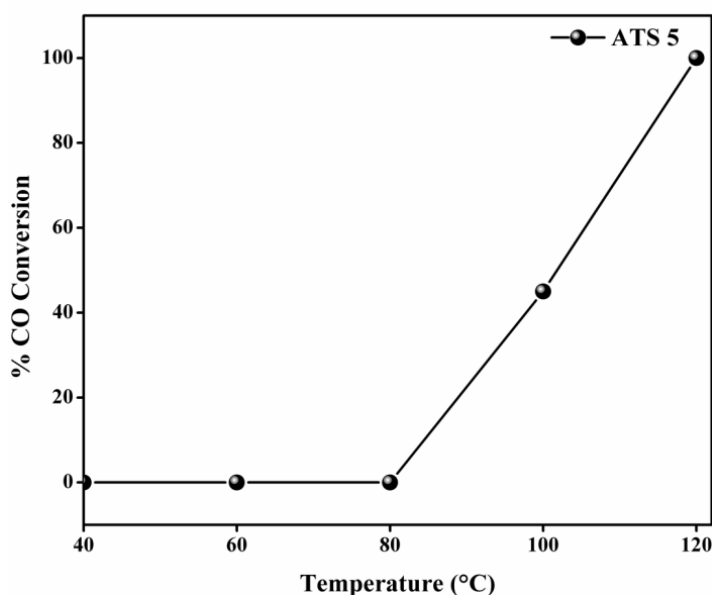


Figure 2.14 CO Oxidation activity of ATS catalyst after reduction.

By treating 1<sup>st</sup> cycle spent catalyst in nitrogen flow at 160°C for 1hr resulted in tremendous activity enhancement with 100% conversion for ATS 10 catalyst at room temperature (Figure 2.13b). A similar enhancement in activity was also observed for ATS 50 and AS catalysts. We assume this behaviour to be due to the removal of carbonaceous species (formed during reaction) under nitrogen flow at high temperature. Debeila *et al.* has also shown the effect of nitrogen treatment on the Au/TiO<sub>2</sub> and Au/TiO<sub>2</sub>-In<sub>2</sub>O<sub>3</sub> catalysts and observed an increase in the activity in the second cycle.<sup>60</sup> It was attributed to the removal of the carbonaceous species when the catalyst was treated under nitrogen flow. So the nitrogen treatment for the spent catalysts has proved to be efficient and made both the ATS 10 and 50 catalysts highly active at room temperature. To further check the stability of the catalysts, ATS 10 and ATS 50 catalysts were tested for time on stream at 100°C (Figure 2.15). The catalysts showed full conversion for initial 2hr and then showed slight deactivation with almost 93% conversion up to 6hr. The stability of both ATS catalysts for time on stream shows the advantage of encapsulation of smaller gold NPs inside the titanium modified silica shell.

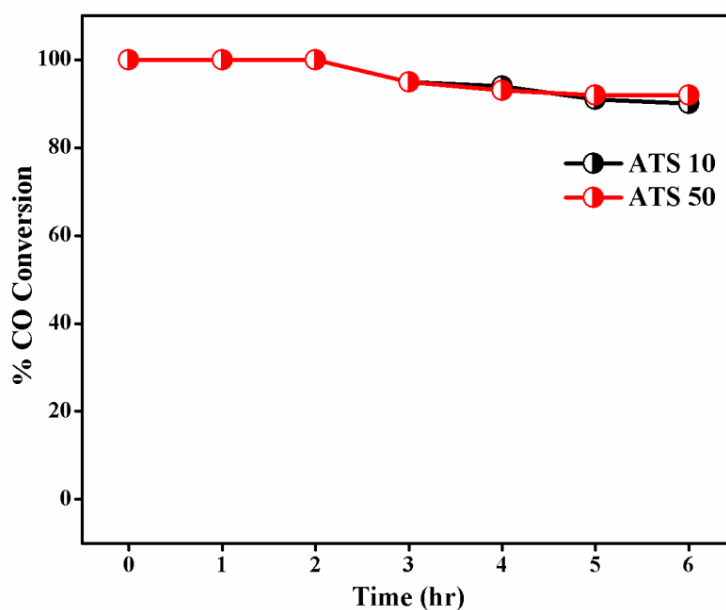


Figure 2.15 Time on Stream CO oxidation plot of ATS 10 and 50 at 100°C

The TEM images of the ATS 10 and ATS 50 spent catalysts showed that gold NPs size was still maintained which again points to the potential role of encapsulating gold NPs in titanium modified silica shell (Figure 2.16).

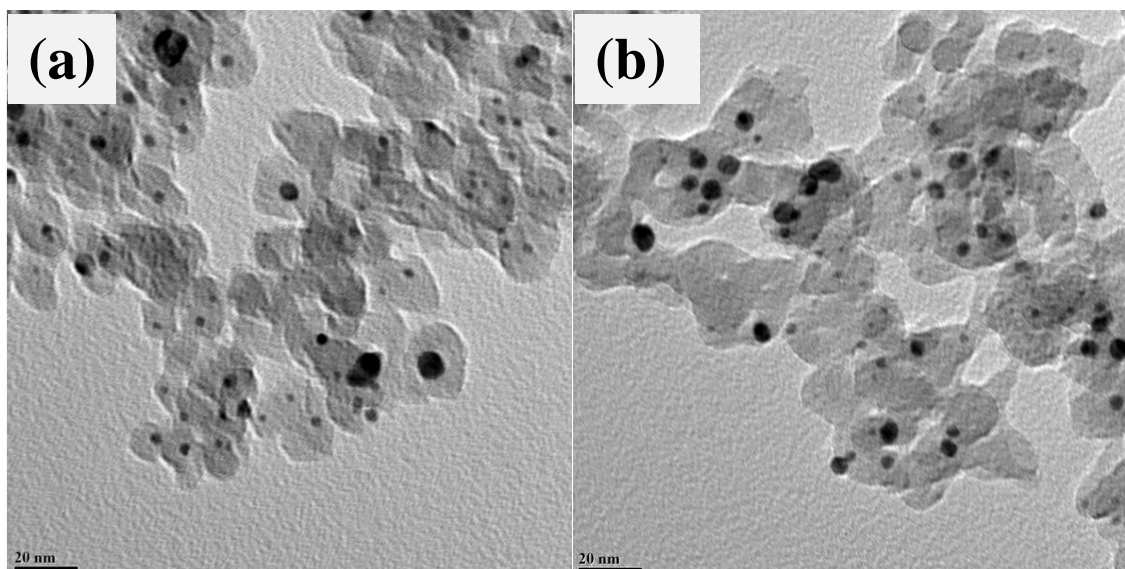


Figure 2.16 TEM images of spent (a) ATS 50 and (b) ATS 10 catalysts.

In addition, the core-shell morphology of these catalysts was not lost completely after CO oxidation. This stability of the catalysts under reaction conditions can be credited to the core-shell morphology that makes the small sized gold NPs sinter resistant.

### 2.3.10.B Direct Synthesis of Propene Oxide (PO)

PO also known as 1,2-epoxypropane or methyl oxirane is an important commodity chemical that can be produced economically in large scale plants with capacities of 1,00,000 t/a. It is an important chemical intermediate for the production of various industrially important products such as polymers (polyether polyols, polyurethane), solvents (propylene glycol ethers) and industrial fluids (polyglycols, monopropylene glycols).<sup>61</sup> Currently it is produced by several processes such as Chlorohydrin process, SMPO and MTBE/PO process, Cumene hydroperoxide method etc. But all these methods come with certain shortcomings such as generation of hazardous wastes, dependency on the co-product, use of extensive reactants and multiple processing steps.<sup>62</sup> Hence it becomes imperative to move towards greener approach of synthesis methods. Gold based systems are highly desirable in this aspect. Au/Ti is a well known system for the direct synthesis of PO from molecular H<sub>2</sub> and O<sub>2</sub>. The earliest catalyst in this regard was Au/TiO<sub>2</sub> with Au NPs size of 2-5 nm. The catalyst showed >99% selectivity for PO at 323 K but conversion of propene was low (<1%) with a subsequent deactivation after 30 minutes.<sup>63</sup> This led to development of other Au/Ti based catalysts where Ti was dispersed inside the silica matrix. These Au/Titanosilicate catalysts showed improved conversion while maintaining a high selectivity to PO. Various catalysts such as Au/TS-1, Au/Ti-MCM-41, Au/Ti-SBA-15, Au/Ti-SiO<sub>2</sub> have been developed and studied for propene epoxidation.<sup>64</sup> The most important properties that a Au/Ti catalyst must possess to show good conversion and selectivity for propene epoxidation are presence of isolated tetrahedral Ti<sup>4+</sup> centres in close proximity of gold NPs of size 2-3 nm. Phase segregated titanium or octahedral Ti<sup>4+</sup> sites and larger gold NPs result in formation of oxygenates other than PO.

#### 2.3.10.B.1 Reaction Mechanism

Au/titanosilicate is a bi-functional catalyst where Au acts as the centre for H<sub>2</sub>O<sub>2</sub> production from H<sub>2</sub> and O<sub>2</sub> which is utilized by titanium sites for the oxidation of propene. H<sub>2</sub>O<sub>2</sub> production is facile on small gold NPs and this insitu generated H<sub>2</sub>O<sub>2</sub> gets stabilized on isolated tetrahedral Ti<sup>4+</sup> sites. Formation of hydroperoxy species on titanium sites are active oxidant which selectively produce PO.<sup>65</sup> The concerted mechanism on Au-Ti interface has been shown in Figure 2.17.



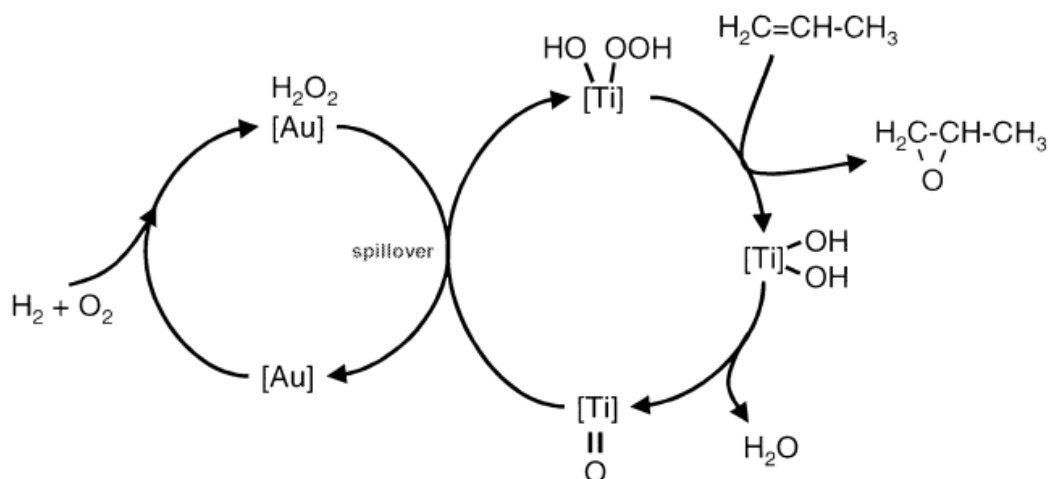


Figure 2.17 Possible reaction mechanism of propene epoxidation on Au-Ti system.<sup>65</sup>

It is noteworthy that water is always a major by product produced in larger quantities than the stoichiometric amount. Water can result in direct combustion of  $H_2$  and form products other than PO.<sup>66</sup> Phase segregated and octahedral titanium sites along with larger sized gold NPs do decompose  $H_2O_2$  to water which forms undesired oxygenates. Thereby optimum sized gold NPs in close proximity of isolated tetrahedral titanium sites are indispensable for getting high conversion and selectivity for PO.

### 2.3.10.B.2 Major Challenges

The maximum conversion on Au-titanosilicate observed is 3-4% with a selectivity of >90% to PO. Major challenges in commercialization of this process are very low propene conversions (>10%), use of co-reactant i.e.  $H_2$  and catalysts deactivation. Also  $H_2$  and  $O_2$  mixture is potentially explosive thereby restricting the operational window. But use of  $H_2$  as co reactant is indispensable to obtain acceptable selectivity for PO. But excessive water formation by direct oxidation of  $H_2$  results in low  $H_2$  efficiency. The acceptable conversion, selectivity and  $H_2$  efficiency values for commercialization of this process are > 10%, >90% and > 50% respectively. But still the dream of the commercialization the process has not been realized. Many efforts have been put forward to improve the activity and selectivity such as manipulating the gold deposition,<sup>67</sup> using nanostructured and mesoporous TS-1,<sup>68</sup> silylation of titanosilicate<sup>69</sup> to increase hydrophobicity of the system etc. Though better results have

been obtained using these modifications but still desired conversion and H<sub>2</sub> efficiency have not been achieved.

### 2.3.10.B.3 Propene epoxidation over ATS nanocatalyst

Propene epoxidation on Au@Ti-SiO<sub>2</sub> (ATS) covers a part of this chapter and effect of different titanium loading has been explored for PO formation. The characteristic properties of ATS-10 and ATS 50 catalysts have already been discussed in CO oxidation section. For a better comparison ATS 75 and ATS 25 catalysts were also synthesised. So the amount of titanium in ATS catalysts increased as: ATS 10 > ATS 25 > ATS 50 > ATS 75. DRUV analysis of these catalysts (Figure A.1 in Appendix) showed SPR band at 510-520 nm typically for gold NPs. The UV region showed two bands at 230 and 280 nm which correspond to tetrahedral and octahedral Ti<sup>4+</sup> sites respectively as explained in CO oxidation section. It was observed that inflection point for UV band was 300 nm for ATS 75 and ATS 50 while it was shifted to higher wavelength when titanium loading increased from ATS 25 to ATS 10. This indicates the presence of phase segregated titania though not in bulk but in nano form. Figure 2.11b EXAFS spectra had shown presence of phase segregated titania when loading was increased from ATS 50 to ATS 10. The XRD of these catalysts (Figure A2 in Appendix) showed that the size of gold NPs increased with titanium amount which was due to destruction of morphology.

The gas phase direct synthesis of propene oxide on these catalysts was tested in the molecular H<sub>2</sub> and O<sub>2</sub> and results can be seen in Figure 2.18.

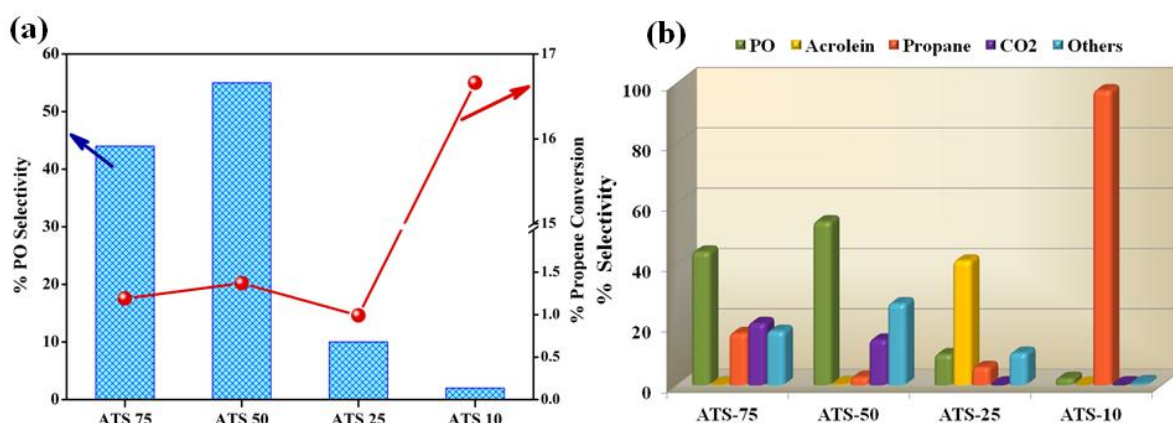


Figure 2.18(a) Comparison of conversion of propylene and selectivity for PO and (b) Selectivity of all the products over ATS catalysts at 200 °C. \*other products formed were acetaldehyde, propanal and acetone)

The activity plots for propene epoxidation showed that conversion was less than 2 % for all the ATS catalysts except ATS 10 where the conversion was 17%. The selectivity to PO was found to be maximum for ATS 50 (54%) and minimum for ATS 10 (negligible) even though its conversion was highest. The STEM images of these catalysts (Figure 2.6 and 2.7) had shown that ATS 10 catalyst possessed randomly distributed titania along with large sized AU NPs. Raman and EXAFS analysis for these samples had clearly shown the presence of phase segregated amorphous TiO<sub>2</sub> in ATS 10 while ATS 50 showed tetrahedrally as well as octahedrally coordinated titanium sites. It has been found in literature that larger sized gold NPs can switch the epoxidation of propene to hydrogenation and propane is formed at non ignorable rates sometimes even as the major product irrespective of the support.<sup>70</sup> In ATS 10 catalysts the size of gold NPs was more than 5 nm as depicted from XRD as well as TEM. These larger sized gold NPs were responsible for switching the epoxidation to hydrogenation of propene. It has to be noted that Au NPs smaller than 2 nm also show propane as the major product despite in close proximity of isolated tetrahedral titanium sites.<sup>70</sup> But the selectivity can be switched from propane to PO after modifying the catalyst with alkali like Na<sup>+</sup> or K<sup>+</sup>.<sup>71</sup>

The maximum selectivity for PO over ATS catalysts obtained was 54% for ATS 50 followed by ATS 75 (44%) and then ATS 25 (10%). The low PO selectivity over our ATS catalysts can be explained on the basis of nature of titanium species present. Raman analysis results (Figure 2.10) showed the presence of amorphous octahedral titanium species in ATS 50 sample. These species are more acidic in nature which can further involve in ring opening of PO formed and form other oxygenates such as propanal, acetaldehyde etc.<sup>48</sup> Further increasing the titanium content from AST 50 to ATS 25 the amorphous titanium species further increased which produced propanal as the major product. It is noteworthy that size of Au NPs was optimum upto ATS 25 so the propane formation was negligible. But for ATS 10 size of Au NPs was largest because of destruction of the morphology due to introduction of more amount of titanium in silica matrix and hence completely switched the selectivity from oxygenates to hydrogenation product propane. Propene epoxidation results showed that ATS 50 was the best catalyst among all the ATS catalysts and the effect of reaction temperature on the selectivity for PO formation was examined and could be seen in table 2.2 and 2.3. It was observed that maximum selectivity for PO was obtained at 200 °C. Reaction temperature higher than 200 °C results in CO<sub>2</sub> as the major product. As predicted water was always the major product at all the temperatures screened with an increase in rate with temperature due to combustion of H<sub>2</sub>.

| T / °C                                   | 130         | 150         | 180          | 200          | 130         |
|--|-------------|-------------|--------------|--------------|-------------|
| Conversion %                             | 1.05        | 1.20        | 1.17         | 1.37         | 1.91        |
| Selectivity %                            | 17.46       | 25.98       | 45.52        | 53.08        | 10.93       |
| Yield %                                  | 0.17        | 0.27        | 0.43         | 0.55         | 0.20        |
| H <sub>2</sub> Efficiency                | <b>0.25</b> | <b>0.33</b> | <b>0.59</b>  | <b>0.78</b>  | <b>0.32</b> |
| Av. H <sub>2</sub> O rate (mol/(gcat*s)) | 9.88E-06    | 1.50E-05    | 1.17E-05     | 1.12E-05     | 9.53E-06    |
| Av. PO rate (gPO/(kgcat*h))              | <b>4.03</b> | <b>5.86</b> | <b>10.03</b> | <b>12.82</b> | <b>4.81</b> |

Table 2.2 PO formation rates with respect to temperature over ATS 50

| Selectivity                   | 130°C  | 150 °C | 180 °C | 200 °C | 130 °C |
|-------------------------------|--------|--------|--------|--------|--------|
| PO                            | 17.46% | 25.98% | 45.52% | 53.08% | 10.93% |
| Acetaldehyde                  | 2.74%  | 3.18%  | 4.03%  | 4.13%  | 1.35%  |
| Acrolein                      | 0.20%  | 0.17%  | 0.31%  | 0.25%  | 0.12%  |
| Propanal                      | 14.14% | 11.96% | 10.93% | 7.73%  | 7.39%  |
| C <sub>3</sub> H <sub>8</sub> | 49.00% | 38.76% | 9.86%  | 2.44%  | 70.18% |
| Acetone                       | 12.74% | 13.42% | 16.78% | 15.00% | 8.26%  |
| CO <sub>2</sub>               | 2.74%  | 5.09%  | 10.08% | 14.84% | 1.49%  |

Table 2.3 Effect of reaction temperature on selectivity to PO over ATS 50 catalyst.

## 2.4 Conclusion

An easy and convenient synthesis methodology has been developed for the synthesis of Au@SiO<sub>2</sub> nanocatalyst via one pot sol-gel method which was further modified with titanium. Amount of titanium was varied from Si/Ti ratio 75 to 10 with increase in titanium content. The size of the gold NPs was mostly 5 nm even after calcination at high temperature. This could be attributed to the encapsulation of gold NPs in the titanosilicate shell. The microscopic analysis performed on ATS catalysts showed that with an increase in titanium content from 1 % (ATS 50) to ATS 10 (2.5 wt%) titanium started segregating from silica matrix and small titania domains could be observed. Also, the size of gold NPs increased with increase in titanium content due to destruction in the morphology which resulted in non-encapsulated Au NPs which sintered under high temperature calcination. The spectroscopy analyses performed on these catalysts showed that extra-framework titanium was present in

all the ATS catalysts along with the presence of tetrahedral titanium more in the case of ATS 10. The catalysts were screened for gas phase CO oxidation and propene epoxidation reactions. The CO oxidation results showed that the incorporation of titanium in the silica matrix results in improved activity. The pretreatment of the catalysts in flowing H<sub>2</sub> resulted in further enhancement in the catalytic activity for CO oxidation with appreciable room temperature activity. This enhancement in the activity after hydrogen treatment was due to generation of oxygen vacancies in support near titanium sites which played a major role in O<sub>2</sub> activation under ambient conditions. This activated oxygen could easily react with CO at room temperature and resulted in improved catalytic activity. The treatment of the 1<sup>st</sup> cycle spent catalyst in N<sub>2</sub> resulted in tremendous activity enhancement with a full CO conversion at room temperature for ATS 10 catalyst due to removal of carbonaceous species from the catalyst surface. The propene epoxidation performed on these catalysts showed that ATS 50 was the best catalyst with a selectivity of 53 % to PO at 200 °C. The ATS 10 catalyst which showed 100% conversion for CO oxidation at room temperature showed negligible selectivity to PO and formed propane as the major product. This was attributed to the presence of larger gold NPs with phase segregated titania. The CO oxidation and propene epoxidation results on the ATS catalysts showed that both the reactions show size dependency more crucial for propene epoxidation. For CO oxidation reaction, particles in the range of 5-7 nm could show activity at ambient temperature. The nature of titanium also did not affect the catalytic activity even the phase segregated titania in ATS 10 showed the better activity. In ATS 10 Au NPs present in the close proximity of titania or titanium (irrespective of tetra or octahedral coordination) showed appreciable activity under ambient conditions. Also the generation of oxygen vacancies in the titanium sites (whether titania or titanium in silica lattice) improved the activity due to easy activation of oxygen. But for propene epoxidation, to obtain good catalytic activity (mostly in terms of selectivity to PO) gold NPs of size 3-5 nm are prerequisite. These small NPs should be present in close proximity of tetrahedral titanium species to obtain appreciable selectivity for PO. In present case though the size of gold NPs was optimum the presence of amorphous titanium species decreased the selectivity to PO and a maximum of 53 % selectivity (with 1.4 % conversion) could be obtained on ATS 50 catalyst. The ATS 10 catalyst which showed excellent activity for CO oxidation could produce negligible amount of PO and selectivity was mostly for propane due to presence of comparatively larger particles. In short it can be said that both the reactions can happen on same catalyst but require different sites for getting appreciable activity. On

one side CO oxidation was independent of nature of titanium species and a marginal increase in the size did not affect the catalytic activity while on the other hand propene epoxidation strictly required particles of size 3-5 nm with isolated tetrahedral titanium sites. Deviation in any of the two resulted either in the formation of other oxygenates (ATS 50 due to amorphous titanium sites) or complete switch in selectivity from oxygenates to hydrogenated product (ATS 10 with larger sized Au NPs).

## 2.5 References

- 1 Deng, W.; Jesus, J. D.; Saltsburg, H.; Stephanopoulos, M. F., *Appl. Catal. A* **2005**, *291*, 126-135.
- 2 Quinet, E.; Morfin, F.; Diehl, F.; Avenier, P.; Caps, V.; Rousset, J. L., *Appl. Catal. B* **2008**, *80*, 195-201.
- 3 Hayashi, T.; Tanaka, K.; Haruta, M., *J. Catal.* **1998**, *178*, 566-575.
- 4 Gajan, D.; Guillois, K.; Delichère, P.; Basset, J. M.; Candy, J. P.; Caps, V.; Coperet, C.; Lesage, A.; Emsley, L., *J. Am. Chem. Soc.* **2009**, *131*, 14667-14669.
- 5 Patil, N. S.; Uphade, B.S.; Jana, P.; Bharagava, S. K.; Choudhary, V. R., *J. Catal.* **2004**, *223*, 236-239.
- 6 Segura, Y.; López, N., Pérez-Ramírez, J., *J. Catal.* **2007**, *247*, 383-386.
- 7 Chen, Y.; Qiu, J.; Wang, X.; Xiu, J., *J. Catal.* **2006**, *242*, 227-230.
- 8 Haruta, M. *Catal. Today* **1997**, *36*, 153-166.
- 9 Haruta, M.; Tsubota S.; Kobayashi T.; Kageyama H.; Genet M. J.; Delmon B., *J. Catal.* **1993**, *144*, 175-192.
- 10 Knell, A.; Barnickel, P.; Baiker, A.; Wokaun, A., *J. Catal.* **1992**, *137*, 306-321.
- 11 Haruta, M.; Yamada, N.; Kobayashi, T.; Iijima, S., *J. Catal.* **1989**, *115*, 301-309.
- 12 Haruta, M.; Kobayashi, T.; Sano, H.; Yamada, N., *Chem. Lett.* **1987**, *16*, 405-408.
- 13 Huang, X. S.; Sun, H.; Wang, L. C.; Liu, Y. M.; Fan, K. N.; Cao, Y., *Appl. Catal. B* **2009**, *90*, 224-232.
- 14 Santos, V. P.; Carabineiro, S. A. C.; Bakker, J. J. W.; Soares, O. S. G. P.; Chen, X.; Pereira, M. F. R.; Orfao, J. J. M.; Figueiredo, J. L.; Gascon, J.; Kapteijn, F., *J. Catal.* **2014**, *309*, 58-65.
- 15 Carabineiro, S. A. C.; Bogdanchikova, N.; Tavares, P. B.; Figueiredo, J. L., *RCS Adv.* **2012**, *2*, 2957-2965.
- 16 Carabineiro, S. A. C.; Bogdanchikova, N.; Borja, M. A.; Pastryakov, A.; Tavares, P. B.; Figueiredo, J. L., *Nano Res.* **2011**, *4*, 180-193.
- 17 Schubert, M. M.; Heckenberg, S.; Veen, A. C.; Muhler, M.; Plzak, V.; Behm, R. J., *J. Catal.* **2001**, *197*, 113-122.
- 18 Haruta, M., *J. New Mat. Electr. Sys.* **2004**, *7*, 163-172.
- 19 Karmakar, B.; Chowdhury, B.; Banerji, J., *Catal. Commun.* **2010**, *11*, 601-605.
- 20 Xiao, F. S.; Han, Y.; Yu, Y.; Meng, X.; Yang, M.; Wu, S., *J. Am. Chem. Soc.* **2002**, *124*, 888-889.
- 21 Sinha, A. K.; Seelan, S.; Tsubota, S.; Haruta, M., *Angew. Chem. Int. Ed.* **2004**, *43*, 1546-1548.
- 22 Wu, P.; Liu, Y.; He, M.; Tatsumi, T., *J. Catal.* **2004**, *228*, 183-191.
- 23 Wu, P.; Tatsumi, T.; Komatsu, T.; Yashima, T., *J. Catal.* **2001**, *202*, 245-255.
- 24 Ruszel, M.; Grzybowska, B.; Łaniecki, M.; Wójtowski, M., *Catal. Commun.* **2007**, *8*, 1284-1286.
- 25 Zepeda, T. A.; Martinez A. H.; Guil, R. L.; Pawelec, B., *Appl. Catal. B* **2010**, *100*, 450-462.

- 26 Strunk, J.; Vining, W. C.; Bell, A. T., *J. Phys. Chem. C* **2010**, *114*, 16937-16945.
- 27 Rombi, E.; Cutrufello, M. G.; Cannas, C.; Casu, M.; Gazzoli, D.; Occhiuzzi, M.; Monaci, R.; Ferino, I., *Phys. Chem. Chem. Phys.* **2009**, *11*, 593-602.
- 28 Rombi, E.; Cutrufello, M. G.; Cannas, C.; Occhiuzzi, M.; Onida, B.; Ferino, I., *Phys. Chem. Chem. Phys.* **2012**, *14*, 6889-6897.
- 29 Sunil Sekhar, A. C.; Ziyad, K.; Soni, Y.; Vinod, C. P., *ChemCatChem* **2015**, *7*, 1222-1230.
- 30 Gabaldon, J. P.; Bore, M.; Datye, A. K., *Top. Catal.* **2007** *44*, 253-262.
- 31 Westcott, S. L.; Oldenburg, S. J.; Lee, T. R.; Halas, N. J., *Langmuir* **1998**, *14*, 5396-5401.
- 32 Wu, P.; Bai, P.; Lei, Z.; Loh, K. P.; Zhao, X. S., *Micropor. Mesopor. Mater.* **2011**, *141*, 222-230.
- 33 Yang, C. M.; Kalwei, M.; Schüth, F.; Chao, K. J., *Appl. Catal. A* **2003**, *254*, 289-296.
- 34 Liz-Marzán, L. M.; Giersig, M.; Mulvaney, P., *Langmuir* **1996**, *12*, 4329-4335.
- 35 Han, Y.; Jiang, J.; Lee, S. S.; Ying, J. Y., *Langmuir* **2008**, *24*, 5842-5848.
- 36 Wang, J.; Shah, Z. H.; Zhang, S.; Lu, R., *Nanoscale* **2014**, *6*, 4418-4437.
- 37 Tsunoyama, H.; Sakurai, H.; Negishi, Y.; Tsukuda, T., *J. Am. Chem. Soc.* **2005**, *127*, 9374-9375.
- 38 Tsunoyama, H.; Sakurai, H.; Ichikuni, N.; Negishi, Y.; Tsukuda, T., *Langmuir* **2004**, *20*, 11293-11296.
- 39 Zhang, T.; Zhao, H.; He, S.; Liu, K.; Liu, H.; Yin, Y.; Gao, C., *ACS nano* **2014**, *8*, 7297-7304.
- 40 Gontier, S.; Tuel, A., *Zeolites* **1995**, *15*, 601-610.
- 41 Sinha, A. K.; Seelan, S.; Okumura, M.; Akita, T.; Tsubota, S.; Haruta, M., *J. Phys. Chem. B* **2005**, *109*, 3956-3965.
- 42 Sing, K. S. W.; Everett, D. H.; Haul, R. A. W.; Moscou, L.; Pierotti, R. A.; Rouquerol, J.; Siemieniewska, T., *Pure Appl. Chem.* **1985**, *57*, 603-619.
- 43 Nguyen, T. D. P.; Shin, E. W.; Pham, V. H.; Kweon, H.; Kim, S.; Kim, E. J.; Chung, J. S., *J. Mater. Chem.* **2012**, *22*, 20504-20511.
- 44 Alba, M. D.; Luan, Z.; Klinowski, J., *J. Phys. Chem.* **1996**, *100*, 2178-2182.
- 45 Lopez, A.; Tuilier, M. H.; Guth, J. L.; Delmotte, L.; Popa, J. M., *J. Solid State Chem.* **1993**, *102*, 480-491.
- 46 Sakka, S.; Miyaji, F.; Fukumi, K., *J. Non-Cryst. Solids* **1989**, *112*, 64-68.
- 47 Su, J.; Xiong, G.; Zhou, J.; Liu, W.; Zhou, D.; Wang, G.; Wang, X.; Guo, H., *J. Catal.* **2012**, *288*, 1-7.
- 48 Xiong, G.; Cao, Y.; Guo, Z.; Jia, Q.; Tian, F.; Liu, L., *Phys. Chem. Chem. Phys.* **2016**, *18*, 190-196.
- 49 Fan, F.; Feng, Z.; Li, C., *Acc. Chem. Res.* **2010**, *43*, 378-387.
- 50 Li, C., *J. Catal.* **2003**, *216*, 203-212.
- 51 Gaultois, M. W.; Grosvenor, A. P., *J. Mater. Chem.* **2011**, *21*, 1829-1836.



- 52 Choi, H. C.; Jung, Y. M.; Kim, S. B., *Vib. Spectrosc.*, **2005**, *37*, 33-38.
- 53 Moretti, G.; Salvi, A. M.; Guascito, M. R.; Langerame, F., *Surf. Interface Anal.* **2004**, *36*, 1402-1412.
- 54 Lu, X.; Wang, G.; Zhai, T.; Yu, M.; Gan, J.; Tong, Y.; Li, Y., *Nano Lett.* **2012**, *12*, 1690-1696.
- 55 Sunil Sekhar, A. C.; Sivaranjani, K.; Gopinath, C. S.; Vinod, C. P., *Catal. Today* **2012**, *198*, 92-97.
- 56 Sunil Sekhar, A. C.; Meera, C.; Ziyad, K.; Gopinath, C. S.; Vinod, C., *Catal. Sci. Technol.* **2013**, *3*, 1190-1193.
- 57 Green, I. X.; Tang, W.; Neurock, M.; Yates, J. T., *Science* **2011**, *333*, 736-739.
- 58 Venezia, A. M.; Liotta, F. L.; Pantaleo, G.; Beck, A.; Horváth, A.; Geszti, O.; Kocsonya, A.; Guczi, L., *Appl. Catal. A* **2006**, *310*, 114-121.
- 59 Saavedra, J.; Powell, C.; Panthi, B.; Pursell, C. J.; Chandler, B. D., *J. Catal.* **2013**, *307*, 37-47.
- 60 Debeila, M. A.; Wells, R. P. K.; Anderson, J. A., *J. Catal.* **2006**, *239*, 162-172.
- 61 Propylene Oxide. In *Ullmann's Encyclopedia of Industrial Chemistry*, 2012.
- 62 Nijhuis, T. A.; Makkee, M.; Moulijn, J. A.; Weckhuysen, B. M., *Ind. Eng. Chem. Res.* **2006**, *45* (10), 3447-3459.
- 63 Hayashi, T.; Tanaka, K.; Haruta, M., *J. Catal.* **1998**, *178* (2), 566-575.
- 64 Sacaliuc, E.; Beale, A. M.; Weckhuysen, B. M.; Nijhuis, T. A., *J. Catal.* **2007**, *248* (2), 235-248.
- 65 Nijhuis, T. A.; Huizinga, B. J.; Makkee, M.; Moulijn, J. A., *Ind. Eng. Chem. Res.* **1999**, *38* (3), 884-891.
- 66 Barton, D. G.; Podkolzin, S. G., *J. Phys. Chem. B* **2005**, *109* (6), 2262-2274.
- 67 Feng, X.; Liu, Y.; Li, Y.; Yang, C.; Zhang, Z.; Duan, X.; Zhou, X.; Chen, D., *AIChE J.* **2016**, *62* (11), 3963-3972.
- 68 Feng, X.; Sheng, N.; Liu, Y.; Chen, X.; Chen, D.; Yang, C.; Zhou, X., *ACS Catal.* **2017**, *7* (4), 2668-2675.
- 69 Chowdhury, B.; Bravo-Suárez, J. J.; Daté, M.; Tsubota, S.; Haruta, M., *Angew. Chem. Int. Ed.* **2006**, *45* (3), 412-415.
- 70 Qi, C.; Huang, J.; Bao, S.; Su, H.; Akita, T.; Haruta, M., *J. Catal.* **2011**, *281* (1), 12-20.
- 71 Huang, J.; Takei, T.; Akita, T.; Ohashi, H.; Haruta, M., *App. Catal. B* **2010**, *95* (3), 430-438.

## **CHAPTER-3**

### **Ligand Exchange Method for Overcoming Deposition Precipitation (DP) Challenges for Making M (Au, Pd)- SiO<sub>2</sub> Catalyst**

**Part A. Au/SBA-15 Nanocatalyst for Room Temperature CO Oxidation.**

**Part B. Pd/SBA-15 Catalyzed Low Temperature CO Oxidation.**

This Chapter has been adapted from:

1. *One Pot Ligand Exchange Methodology for a Highly Stable Au- SBA- 15 Catalyst and its room temperature CO Oxidation*, Yogita Soni, I. Kavya, T. G. Ajithkumar and C. P. Vinod, *Chem. Commun.*, **2018**, **54**, 12892-12892.
2. *Low temperature CO oxidation activity from ultrafine Pd NPs supported on SBA-15: Size dependent generation of different Pd species and catalytic activity for CO oxidation*. Yogita Soni, Sumanta Pradhan, Mahesh Kumar Bamnia, C. P. Vinod, (Manuscript ready to be submitted)

### **3.1 Introduction**

Metal NPs have attracted much attention in heterogeneous catalysis in past decades as compared to their bulk counterpart, all because of their remarkable properties such as high surface to volume ratio, tunable size and shapes etc.<sup>1-3</sup> Among these unique properties, the NPs supply highly active centers which are not thermodynamically stable. But requirement of stable nanoparticles is indispensable for their desired applications for various catalytic reactions. Supported metal NPs are attractive in this regard and metal NPs supported on porous supports are the most potential candidate for catalysis due to their integral surface properties such as high surface area and pore size.<sup>4</sup> Minimum diffusion limitations imposed by these porous materials during reactions is one of the most important properties of these materials. Porous materials especially mesoporous materials (2-50 nm pore size) are highly sought to supports for metal NPs. Silica is one of the largest class of porous materials due to its abundant availability, thermal stability and most importantly its tunable surface area, pore size, pore volume etc. Metal NPs supported on silica have been studied for various catalytic reactions and used in industrial catalysis.<sup>5-8</sup> Even though silica has many advantages as supports its inactive nature for catalysis limits its use as a support. Also the negligible interaction with metal NPs results in their instability under thermal and reaction conditions which leads to NPs aggregation with concomitant loss in their catalytic activity. Encapsulation of small sized metal NPs inside the mesopores of silica is attractive due to restrictive motion of NPs.<sup>9-12</sup> Since silica is inherently inactive in nature, the catalytic activity originates solely from the metal NPs which makes it possible to explore metal NPs dependent catalytic activity. It is well known that size of the metal NPs is one of the important criteria for obtaining an active catalyst and for noble metals like Au this criteria is even critical as supported Au NPs of size 3-5 nm are considered to be active for various reactions.<sup>13</sup> Au and Pd are among the most important noble metals used for a large no. of catalytic reactions such as oxidation, hydrogenation, coupling reaction etc.<sup>14-19</sup> Various chemical methods are in practice for synthesizing small NPs of Au, Pd on different supports out of which wet impregnation (WI), deposition precipitation (DP) methods and sol immobilization (SI) are the most common routes. This is because these methods are easy to apply and require less expensive inorganic metal precursors. All these methods are suitable for active supports like TiO<sub>2</sub>, CeO<sub>2</sub>, Fe<sub>2</sub>O<sub>3</sub>, Fe<sub>3</sub>O<sub>4</sub>, MnO<sub>2</sub>, and Co<sub>3</sub>O<sub>4</sub> etc. due to their strong interaction with metal NPs which prevents NPs aggregation under reaction conditions.<sup>20-22</sup> For support like silica these methods have certain limitations and often result in supporting large metals NPs on the

surface due to weak metal support interaction, which results in inactive material for catalytic applications. Among all the above mentioned chemical methods, DP is most suitable method for synthesis of supported metal NPs as it supports highly dispersed small metal NPs on the surface of the supports. Most of the Au based catalyst for various applications are synthesized via DP method. In this method the metal precursors such as chlorides (or nitrates) are precipitated on the surface of the supports mostly in the form of their hydroxides in the presence of precipitating agents such as NaOH, Na<sub>2</sub>CO<sub>3</sub>, urea etc.<sup>23,24</sup> Thus alkaline conditions are required for synthesizing supported metal NPs using DP method. Usually, supports with high point of zero charge (PZC) i.e. neutral to basic, like TiO<sub>2</sub>, CeO<sub>2</sub>, MgO are suitable for DP but for supports like silica this method is highly incompatible.<sup>25</sup> PZC can be defined as the pH at which the charge on the surface of the support is neutral and pH above or below PZC results in negative or positive charge on the surface of the support.<sup>25</sup> PZC for silica is 2-3 and the desired alkaline for DP makes the surface of silica negatively charged. The most common precursors used for synthesizing supported Au and Pd based catalysts are their chloride precursors such as HAuCl<sub>4</sub> and H<sub>2</sub>PdCl<sub>4</sub> respectively. These precursors exist as [MCl<sub>4</sub>]<sup>x-</sup> (x = no. of counter ion) in their solution form in water and as [MCl<sub>x</sub>(OH)<sub>4-x</sub>]<sup>y-</sup> under alkaline conditions. As already discussed the surface of silica is negatively charged under alkaline conditions which results in repulsion between negatively charged metal precursor and silica surface. This repulsion results in minute amount of metal loading on the silica surface leading to loss of expensive metals in the solution thereby desired metal loading can never be achieved. Also, the size of metal NPs becomes large due to negligible metal-support interaction which makes DP method extremely undesirable for the synthesis of supported small metal NPs on silica. The expensive organometallic precursor of these metals have been used for synthesizing small noble metal NPs on silica using highly sophisticated techniques like chemical vapour deposition (CVD), gas phase grafting etc.<sup>26,27</sup> Another way of synthesizing Au, Pd supported silica systems is modification of silica with silanes comprised of organic functional moieties such as NH<sub>2</sub>, SH, Cl, CH<sub>2</sub>=CH<sub>2</sub> etc.<sup>28-31</sup> But this synthesis is laborious, two step process and requires inert conditions to prevent self condensation of silanes. Also these groups can block the active sites present on the metal NPs. All these limitations of synthesizing small noble metal nanoparticles especially catalytically important Au and Pd NPs of desired loading on silica support prompted us to develop a method which can fulfill the following criteria: (i) small and highly dispersed Au and Pd NPs of desired loading (ii) use of most common precursor (iii) easy and less time consuming (iv) use of

water as the solvent at ambient temperature and (v) scalable. The synthesis protocol developed in this chapter is based on ligand exchange methodology where a negatively charged ligand has been replaced with a neutral ligand. Au based catalyst using ethylene diammine (en) as the neutral ligand has been developed where  $\text{Au(en)}_2\text{Cl}_3$  complex is synthesized which is further supported on silica.<sup>32,33</sup> The main drawback of this method is that it is a two step process requires large amount of gold precursor. The catalytic activity of thus synthesized Au/SiO<sub>2</sub> catalyst was similar to the other Au based active catalyst for CO oxidation. The modified DP method developed in the present chapter uses inexpensive NH<sub>4</sub>Cl as the insitu modifier of Au and Pd precursor which is a one pot single step method performed under ambient conditions within a time span of only one hour. In the first part of this chapter i.e. 3A, a detailed study of formation of Au-NH<sub>3</sub> complex by NH<sub>4</sub>Cl using various spectroscopic tools and screening of this catalyst for CO oxidation have been demonstrated. The catalytic activity of thus synthesized Au/SBA-15 catalyst has been compared with other reported active Au/SiO<sub>2</sub> catalyst.

In the second part of this chapter 3B, Pd/SBA-15 catalyst has been synthesized using the same modified DP method and the activity has been tested for CO oxidation. The catalytic activity of this Pd/SBA-15 catalyst has been compared with other conventionally synthesized Pd/SBA-15 catalyst with larger particle size. To understand the activity behavior a detailed XPS study has been carried out on these catalysts to explore more about size dependency on CO oxidation.

## **3.2 Experimental Section**

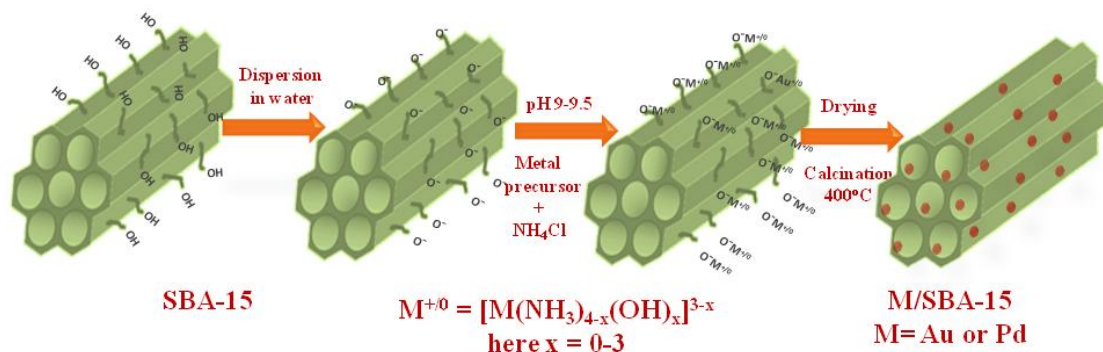
**3.2.1 Synthesis of SBA-15:** SBA-15 was synthesized according to the literature with some modifications<sup>34</sup>. 19.8 gm of P123 (Pluronic123, surfactant) was dissolved in 135 mL water at room temperature. Subsequently 540 mL of 2M HCl was added followed by addition of 40 gm TEOS. A white precipitate was formed gradually. The solution was transferred to autoclave for hydrothermal treatment at 373K for 48 hr. Finally the SBA-15 was obtained after filtration, drying and calcination at 823 K.

**3.2.2 Synthesis of Au/SBA-15 catalyst:** Gold was supported on SBA-15 by modified DP method using NH<sub>4</sub>Cl as the modifier. Typically, 500 mg of SBA-15 was dispersed in 50 mL water under sonication. To this solution required amount of NH<sub>4</sub>Cl was added. Then the pH of the solution was maintained at 9-9.5 using 0.1 M NaOH solution. To this solution required amount of gold precursor (for loading 2.8 wt% Au), H<sub>2</sub>HAuCl<sub>4</sub>·3H<sub>2</sub>O was added drop wise in

30 minutes while maintaining the pH. The solution was stirred for another 1 hr at this pH. The as synthesized yellow colored Au/SBA-15 was obtained after centrifugation and drying and denoted as AS-x as syn. Here x referred to the millimoles of  $\text{NH}_4\text{Cl}$  used varied from 1 millimole to 4 millimoles. The as synthesized Au/SBA-15 was calcined in air at 673 K for 4 hr at the ramp rate of  $2^\circ/\text{min}$  to finally get brown colored catalyst. Five different Au/SBA-15 catalysts were synthesized and denoted as AS 1, AS 1.5, AS 2, AS 3 and AS 4. All the catalysts were stored in ambient conditions at room temperature without any precautions.

**3.2.3 Synthesis of Pd/SBA-15 catalyst:** Pd was supported on SBA-15 by modified DP same as that of Au/SBA-15 catalyst. Acidified  $\text{PdCl}_2$  solution of 0.25 M was used as Pd precursor. 1 mm of  $\text{NH}_4\text{Cl}$  was used unlike Au/SBA-15 synthesis where different millimoles of  $\text{NH}_4\text{Cl}$  were used. Rest of the steps were same as that of Au/SBA-15 synthesis. The final catalyst was sand colored and denoted as Pd-S-N. For comparison other Pd/SBA-15 catalysts were also synthesized by conventional deposition precipitation and wet impregnation and denoted as Pd-S-NaOH and Pd-S-WI respectively.

The steps followed for the synthesis of M (Au or Pd)/SBA-15 has been represented in scheme 3.1.



Scheme 3.1 Synthesis of M/SBA-15 catalyst using modified DP method.

**3.2.4 Catalyst Characterization:** UV-visible analysis was performed on Shimadzu 2700 spectrophotometer with a dual beam source of He lamp and tungsten lamp as UV and visible light source respectively. Liquid UV was done using water as the reference. DRUV analysis was done for powder samples using dual beam source equipped with a diffuse reflectance attachment by taking  $\text{BaSO}_4$  as the standard. Powder X-ray Diffraction was recorded on Rigaku D MAX with a  $\text{Cu K}\alpha$  source of wavelength  $1.54 \text{ \AA}$  with an operational voltage of 40 mV and 15 mA current.  $\text{N}_2$  adsorption /desorption analysis was done using Autosorb 1C Quantachrome, USA. The sample was first degassed at  $300^\circ\text{C}$  for 3 hr. After degassing the

samples were cooled down to room temperature and analysis was done by adsorbing/desorbing liquid N<sub>2</sub> at different pressures. The surface area was calculated by BET model. Pore size distribution was calculated using BJH method. TEM analysis was carried out by TECHNAI FEI instrument working at voltage of 200kV with LaB<sub>6</sub> as the filament. The samples for TEM analysis were prepared in ethanol and dried completely before analysis. Raman analysis was done by Renishaw InVia microscope with a Laser wavelength of 532 nm in the back scattering geometry. The liquid samples were drop casted on glass slide and dried under vacuum at room temperature.

The <sup>15</sup>N CPMAS NMR spectra were collected on a Bruker Avance HD 700 MHz spectrometer in a 4 mm double resonance probe with Larmor frequency of 70.94 MHz for <sup>15</sup>N. The data were collected using a cross polarisation time of 1 ms and a recycle delay of 4s. The single pulse <sup>1</sup>H MAS experiments were done at Bruker AV NEO 500MHz equipped with a 2.5 mm trigamma probe at a sample rotation frequency of 32 kHz. In the MAS NMR, 90° pulse duration of 1.9 μs and a recycle delay of 4 s were employed. Glycine and adamantane were used as a chemical shift secondary references for <sup>15</sup>N and <sup>1</sup>H respectively. <sup>15</sup>N labelled ammonium chloride (<sup>15</sup>NH<sub>4</sub>Cl) was used for the synthesis of modified Au-SBA-15 and SBA-15 samples. Synthesis procedure was same as explained in experimental section.

XPS measurements were carried out using Thermo Kalpha+ spectrometer using micro focused and monochromated Al Kα radiation with energy 1486.6 eV. The pass energy for spectral acquisition was kept at 50 eV for individual core-levels. The electron flood gun was utilized for providing charge compensation during data acquisition. The peak fitting of the individual core-levels was done using XPSpeak 41 software with a Shirley type background. For Au/SBA-15 XPS analysis, samples were prepared by drop casting the NH<sub>4</sub>Cl modified Au precursor (unsupported) on silicon wafer and dried under ambient conditions. Pd/SBA-15 samples were prepared by supporting the pellet of the powder catalyst on double sided carbon tape.

**3.2.5 Catalytic activity for CO oxidation:** The synthesized and calcined Au/SBA-15 and Pd/SBA-15 catalysts were tested for CO oxidation. The catalyst tests were done in a fixed bed reactor of diameter 14mm at atmospheric pressure. Typically, 50 mg of the pelletized catalyst was loaded in a silica reactor supported by quartz wool. The reactor was placed in a tubular furnace with a uniform heating zone of 4 cm furnished with temperature controller radix 6400. A K-type thermocouple placed on the thermowell was used to measure the

temperature of catalyst bed. The flow rate of the reaction gases was  $25 \text{ mL min}^{-1}$  with feed gas ratio as  $\text{CO} : \text{O}_2 : \text{N}_2 = 1:5:19$  and a GHSV of  $30,000 \text{ mL (g}_{\text{cat}}\cdot\text{h)}^{-1}$ . The gas flow of CO, O<sub>2</sub> and N<sub>2</sub> was controlled by Brooks Mass flow Controllers. The gases exiting the reactor were analyzed by Nucon 5700 GC equipped with a molecular sieve column with thermal conductivity detector at isothermal conditions with oven temperature  $40 \text{ }^\circ\text{C}$ , injector and detector temperature  $50 \text{ }^\circ\text{C}$  and helium as the carrier gas. The % conversion of CO was calculated using the formula:  $[(\text{CO}_{\text{in}} - \text{CO}_{\text{out}}) / \text{CO}_{\text{in}}] * 100$ .

### **Part 3A. Au/SBA-15 nanocatalyst for room temperature CO oxidation**

As already explained in the introduction and the experimental part the developed synthesis method is based on ligand exchange methodology where NH<sub>4</sub>Cl insitu modifies the Au precursor by replacing the Cl<sup>-</sup> ligands attached to Au (III) ions. The high pH conditions required for DP deprotonated ammonium ions to ammine which can bind to Au ions by replacing Cl<sup>-</sup> ions. This exchange leads to formation of  $[\text{Au}(\text{NH}_3)_{4-x}(\text{OH})_x]^{3-x}$  complex where  $x = 0-3$ . The neutral or positive charge on this complex results in the attractive interaction between complex and negatively charged silica hence leading to successful deposition of gold on silica. The formation of Au-NH<sub>3</sub> complex was studied in detail by using various spectroscopic techniques and is discussed in following sections.

#### **3A.1 UV-visible Spectroscopy**

Electronic environment of the gold in the precursor with different millimoles of NH<sub>4</sub>Cl was followed by UV-Vis spectroscopy. The two UV bands at 217 and 290 nm (Figure 3A.1) assigned to the ligand to metal charge transfer (LMCT) between Au<sup>3+</sup> and Cl<sup>-</sup> ions<sup>35</sup> showed a shift towards the higher wavelength after the addition of NH<sub>4</sub>Cl. But the shift was more prominent for 290 nm band (shown in the inset of Figure 3A.1) and increased with an increase in the amount of NH<sub>4</sub>Cl from 1 mm to 4 mm which is attributed to the electrostatic interaction between NH<sub>4</sub><sup>+</sup> ions with gold complex.<sup>35</sup> DRUV-visible spectra in the range 500-600 nm for AS x was featureless for the as synthesized sample (Figure 3A.2a) and showed SPR band at 510 nm after calcination due to the generation of metallic Au NPs (Figure 3A.2b). The samples with increased NH<sub>4</sub>Cl showed a broad SPR band with very less intensity which is usually observed for Au NPs of  $< 3 \text{ nm}$ .<sup>36</sup> Decrease in the intensity of SPR



band of the gold with increasing  $\text{NH}_4\text{Cl}$  amount showed that size of the Au NPs decreased when amount of  $\text{NH}_4\text{Cl}$  increased from 1 mm to 4 mm.

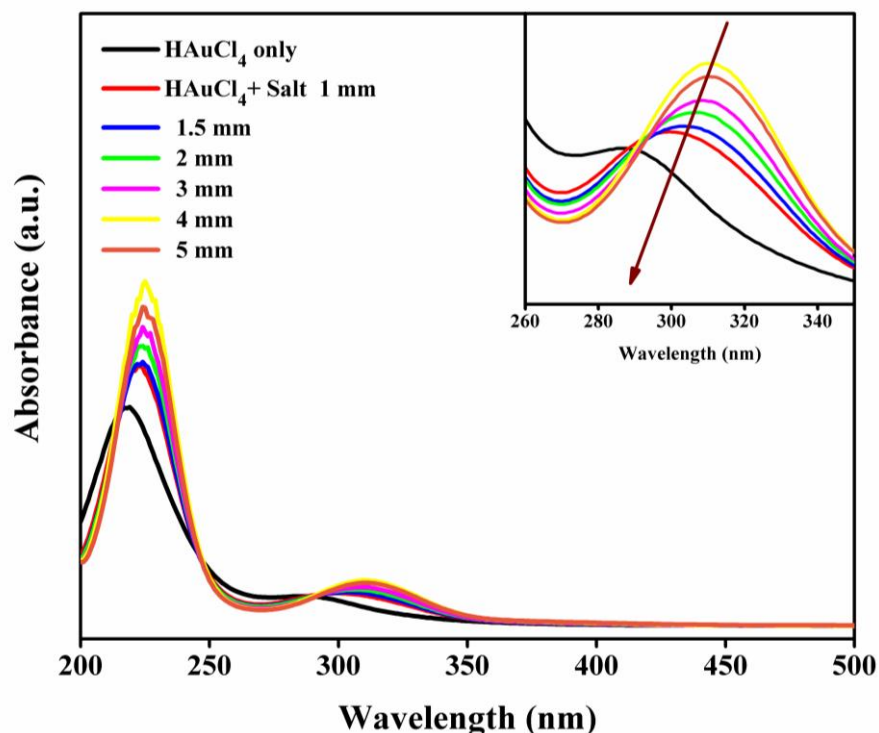


Figure 3A.1 UV-visible spectra of Au precursor compared with precursor modified with  $\text{NH}_4\text{Cl}$  of different millimoles in liquid state.

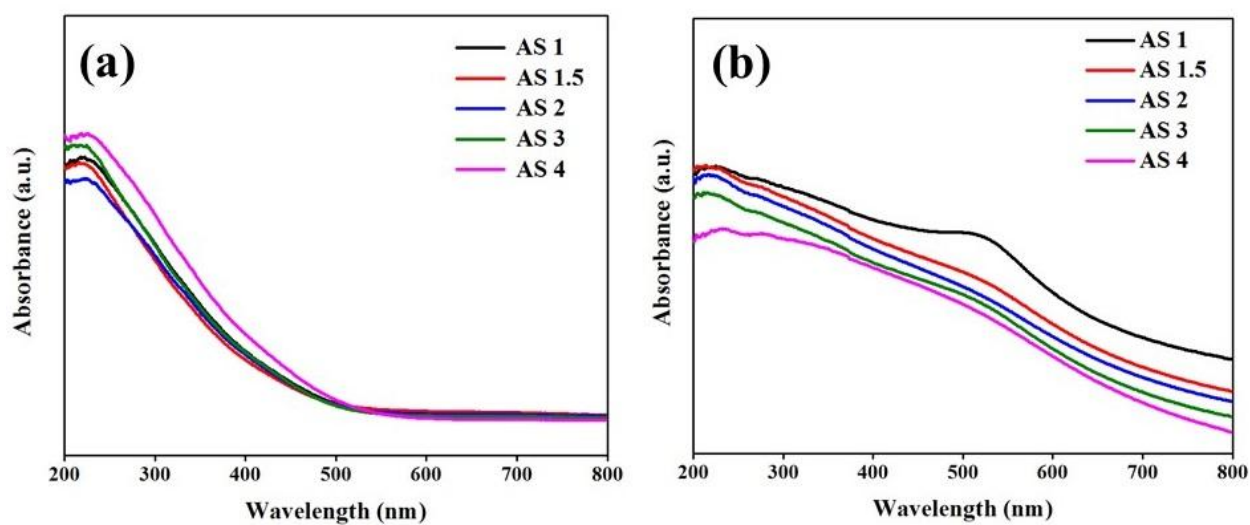


Figure 3A.2 DRUV spectra of AS-x (a) as synthesized (b) calcined catalysts.

### 3A.2 X-Ray Diffraction

XRD analysis of these catalysts showed characteristic features of mesoporous materials. Three diffraction peaks at  $0.93^\circ$ ,  $1.63^\circ$  and  $1.86^\circ$  corresponding to (100), (110) and (200) in small angle XRD of AS x (Figure 3A.3a) calcined catalysts compared with pristine SBA-15 sample confirmed the ordered 2D hexagonal structure of SBA-15 with a space group of  $p6mm$ .<sup>34</sup> The intensity of (100) reflection decreased after supporting Au NPs indicating successful deposition of Au in the channels of SBA-15. No reflection from metallic Au at  $38.3^\circ$  was seen in any of the AS samples which indicates that as synthesized AS samples consisted mainly of oxidized Au (Figure 3A.3b). The metal feature was observed after calcination at  $400^\circ\text{C}$  indicating the reduction of Au ions to  $\text{Au}^0$  under calcination (Figure 3A.3c). FWHM of peak at  $38.3^\circ$  in AS samples increased with an increase in  $\text{NH}_4\text{Cl}$  amount (from 1.8 in AS 1 to 4.3 for AS 4) hence supported our claim that  $\text{NH}_4\text{Cl}$  helped in minimizing the particle size of gold NPs in the final catalyst.

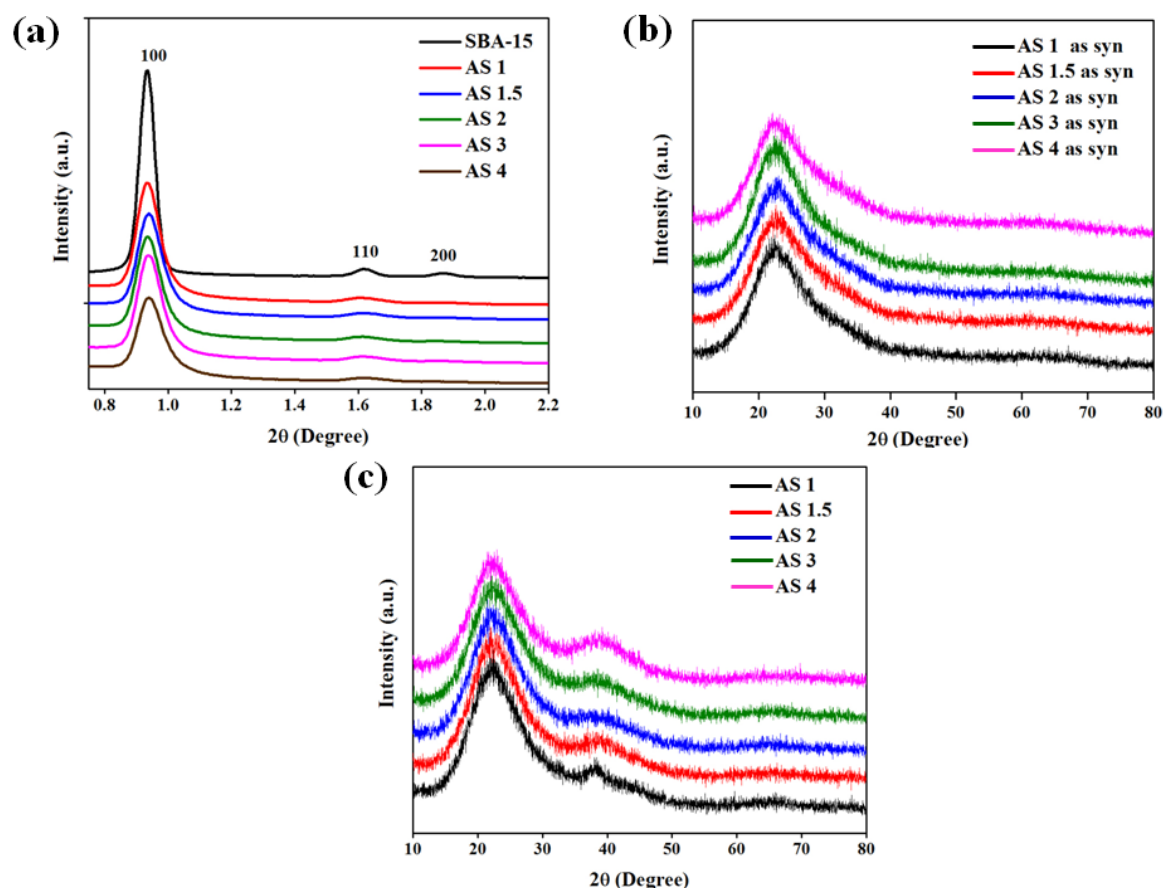


Figure 3A.3 (a) Small angle XRD (b) Wide angle XRD of as synthesized and (c) calcined AS catalysts.

### 3A.3 N<sub>2</sub>-Adsorption

The BET surface area measurements done by the N<sub>2</sub> adsorption-desorption isotherms of pristine SBA-15 and other Au NPs supported samples showed type IV hysteresis (Figure 3A.4) corresponding to the filling of mesopores present in all samples.<sup>37</sup> The physicochemical characteristics of the materials obtained after surface area analysis are listed in Table 3A.1.

The pore size, pore volume and surface area were found to decrease as the amount of NH<sub>4</sub>Cl increased from AS 1 to AS 4 which is a manifestation of successful loading of Au inside the pore channels.

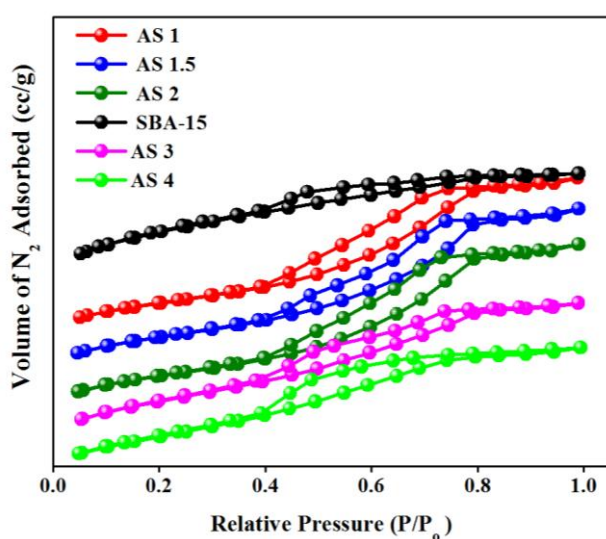


Figure 3A.4 N<sub>2</sub> adsorption-desorption isotherms of AS catalysts.

| Sample Name | Surface Area<br>(m <sup>2</sup> /g) | Pore diameter<br>(nm) | Pore volume<br>(cc/g) |
|-------------|-------------------------------------|-----------------------|-----------------------|
| SBA-15      | 575                                 | 5.6                   | 0.492                 |
| AS 1        | 401                                 | 4.2                   | 0.468                 |
| AS 1.5      | 350                                 | 4.8                   | 0.486                 |
| AS 2        | 345                                 | 4.8                   | 0.412                 |
| AS 3        | 330                                 | 3.7                   | 0.427                 |
| AS 4        | 370                                 | 3.3                   | 0.386                 |

Table 3A.1 Textural properties of different AS x catalysts.

### 3A.4 Transmission Electron Microscopy

The HRTEM along with particle size histogram from the samples showed well-ordered hexagonal array of SBA-15 with uniformly dispersed Au NPs in the channels more prominent for AS 3 and 4 samples (Figure 3A.5).

Overall the Au NPs size in all the samples fell under the catalytically active regime. The particle size histogram firmly indicated that AS 4 catalyst had the maximum frequency of 2-4 nm particles followed by AS 3 nanocatalyst.

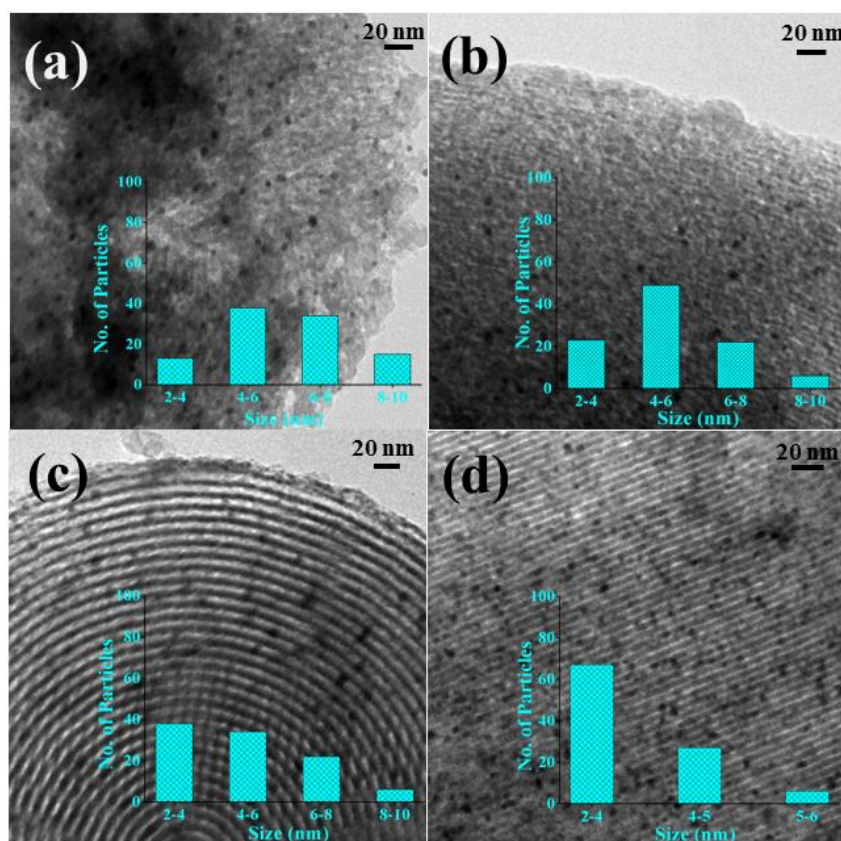


Figure 3A.5 TEM images of (a) AS 1 (b) AS 2 (c) AS 3 (d) AS 4 nanocatalysts along with particle size distribution

### 3A.5 Raman Spectroscopy

The confirmation for metal-nitrogen bond formation came from the Raman spectroscopy analysis. Figure 3A.6 showed the Raman spectrum of drop casted Au complexes under different conditions. The Raman band of Au precursor showed a doublet at  $321$  and  $344$   $\text{cm}^{-1}$  which comes from  $A_{1g}$  and  $B_{2g}$  mode of stretching vibrations of Au-Cl bond.<sup>38</sup>

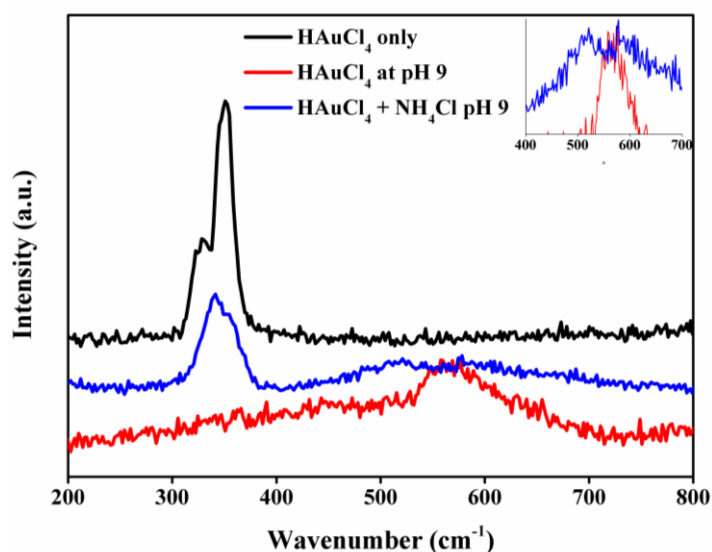


Figure 3A.6 Raman spectra of gold complex in different conditions. ( $\text{NH}_4\text{Cl}$ : 4 millimoles)

But the Au-Cl stretching vibration vanished completely after the addition NaOH solution which was due to the total exchange of  $\text{Cl}^-$  with  $\text{OH}^-$  ligands and a new band appears at  $565\text{ cm}^{-1}$  due to  $A_1$  mode of stretching vibrations from Au-O(H) bond.<sup>39</sup> Raman spectrum of gold precursor with salt  $\text{NH}_4\text{Cl}$  at high pH condition showed a single band at  $340\text{ cm}^{-1}$  ( $B_{2g}$  deformation mode of Au-N bond) along with the presence of a doublet at  $523$  and  $580\text{ cm}^{-1}$  which can be attributed to the  $B_g$  and  $A_g$  mode of asymmetric and symmetric stretching vibrations from Au-N bond respectively<sup>40</sup> which confirmed the formation of Au- $\text{NH}_3$  complex under the synthesis conditions.

### 3A.6 Solid State NMR Spectroscopy

The *insitu* modified gold complex catalyst was further probed by  $^{15}\text{N}$  and  $^1\text{H}$  solid state NMR (SSNMR) and gave insights into  $[\text{AuCl}_4]^-$  complex with ammine ligands. Figure 3A.7 showed the  $^{15}\text{N}$  NMR spectra of AS 4 as synthesized catalyst with  $^{15}\text{NH}_4\text{Cl}$ . The chemical shift value of pure  $\text{NH}_4\text{Cl}$  at  $39.7\text{ ppm}$  was shifted to up field region at  $8.0\text{ ppm}$  along with appearance of broad peak centered at  $-36.5\text{ ppm}$  for AS 4 as synthesized sample. The shift can be attributed to the complexation of ammine ligands with Au (III) ions in the complex. This kind of up field shift has been observed on Pt- $\text{NH}_3$  based antitumor complexes.<sup>41</sup> The peak broadening in AS 4 sample can happen due to presence of different composition of ligands in the complex  $[\text{Au}(\text{NH}_3)_{4-x}(\text{OH})_x]^{3-x}$ . To confirm whether the peak shift towards up field region in AS 4 as syn sample was due to modification of gold complex or  $\text{NH}_4\text{Cl}$  modifying the silica surface we carried out  $^{15}\text{N}$  NMR study of  $\text{NH}_4\text{Cl}$  treated SBA-15 in the absence of gold precursor (Figure 3A.7a).

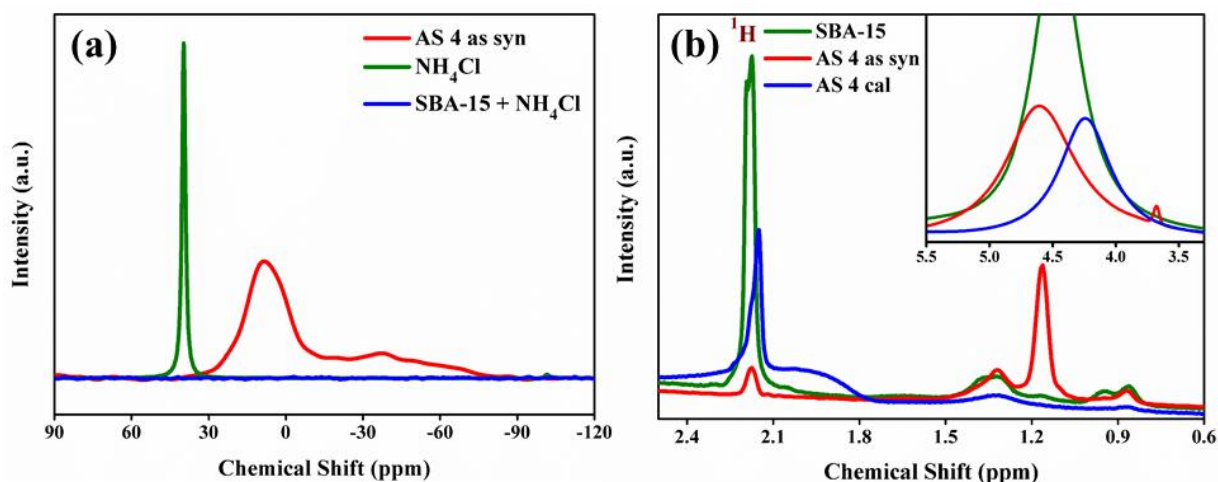


Figure 3A.7 (a)  $^{15}\text{N}$  and (b)  $^1\text{H}$  solid state NMR spectra of AS 4 compared with  $^{15}\text{NH}_4\text{Cl}$  and SBA-15.

But this sample did not show any  $^{15}\text{N}$  peak which confirmed that addition of  $\text{NH}_4\text{Cl}$  to gold precursor in alkaline condition modified the precursor and not the silica surface. Owing to the different types of protons present in SBA-15 and Au complex,  $^1\text{H}$  SSNMR was carried out and their spectral comparison was shown in Figure 3A.7b. Pristine SBA-15 showed peak between 4-5 ppm (inset) typically for water molecules attached to silanols groups.<sup>42</sup> AS 4 as synthesized and calcined samples also showed same peak but with less intensity. The peak at 2.1 ppm in main graph was due to Si-OH groups present in silica and showed maximum intensity in SBA-15 as compared to other samples.<sup>43</sup> It should be noted that AS 4 as synthesized sample showed the minimum intensity of this peak which is obvious as alkaline conditions deprotonated the silanols groups where the modified Au-ammine complex was bound.  $^1\text{H}$  peak at 1.3 ppm in SBA-15 and AS 4 as syn was assigned to isolated  $\text{H}_2\text{O}$  present<sup>44</sup> which vanished after calcination. Interestingly AS 4 as synthesized sample showed an additional peak at  $\sim 1.2$  ppm which was absent in other samples. This peak can be attributed to the  $-\text{OH}$  groups present in the Au-ammine complex bound to Au as  $[\text{Au}(\text{NH}_3)_4 \cdot x\text{OH}_x]^{3-x}$ . Also, the presence of small peak at 3.6 ppm (inset of Figure 3A.7b) was assigned to the proton of ammine ligands attached to Au ions.<sup>45</sup>  $^1\text{H}$  NMR of pure  $\text{NH}_4\text{Cl}$  as shown in Figure 3A.8 was found to be completely different as compared to AS 4 as synthesized sample. Thus the SSNMR spectroscopy results confirmed that gold precursor was insitu modified by the addition of  $\text{NH}_4\text{Cl}$  while synthesizing Au/SBA-15 catalyst.

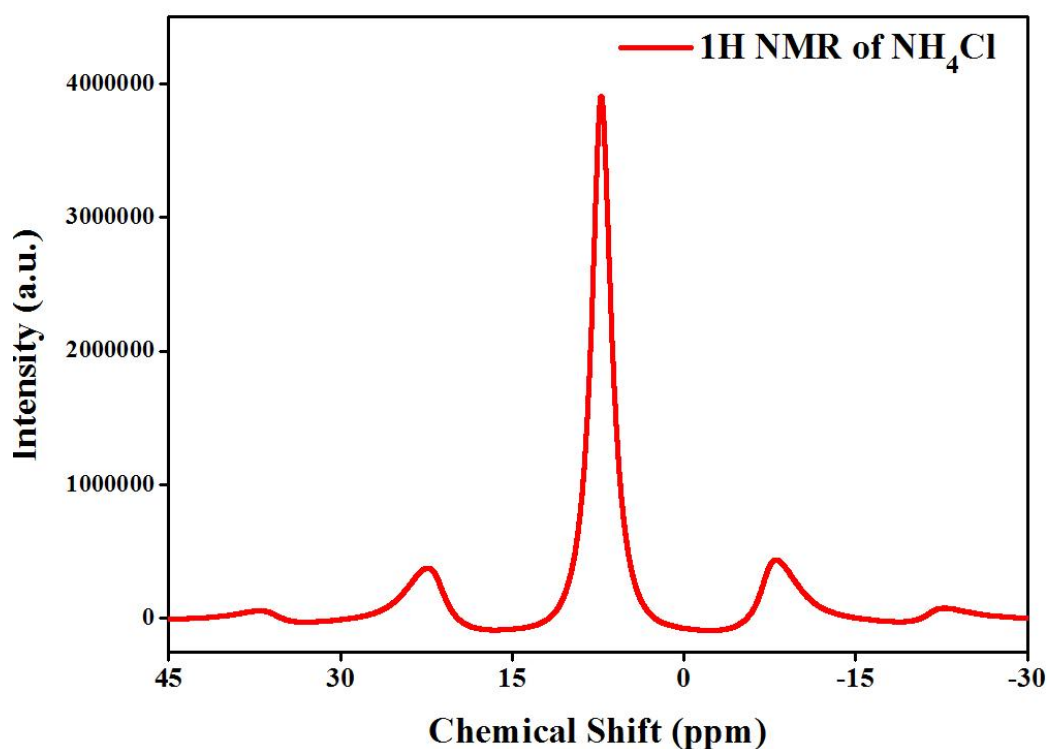


Figure 3A.8  $^1\text{H}$  solid state NMR of pristine  $\text{NH}_4\text{Cl}$ .

### 3A.7 X-Ray Photoelectron Spectroscopy

Further, XPS was carried out for elucidating the oxidation state and electronic environment around the metal. Presence of different ligands around the central metal atom can alter the electronic structure of the metal and hence can easily be discernible with XPS. In the present study XPS analysis was done on gold precursor under different conditions and it was observed that binding energies of Au 4f and N 1s core levels showed significant differences and was correlated with the modified ligand-metal environment. Figure 3A.9 shows the XPS spectra of Au 4f and N 1s core levels.

XPS spectrum of  $\text{HAuCl}_4$  precursor (Figure 3A.9a) showed two peaks at 85.1 and 87.7 eV for Au4f<sub>7/2</sub> which corresponds to  $\text{Au}^{+1}$  and  $\text{Au}^{+3}$  species respectively.<sup>46</sup> Addition of 0.1 M NaOH to gold precursor shifted the XPS peaks to lower binding energy for both  $\text{Au}^{+1}$  and  $\text{Au}^{+3}$  (Table 3A.2). Raman analysis for this sample in Figure 3A.6 showed no band at 300-400  $\text{cm}^{-1}$  for Au-Cl stretching due to complete replacement of all the  $\text{Cl}^-$  ligands with  $\text{OH}^-$ . These  $\text{OH}^-$  ligands changed the electronic environment around Au ions which was reflected as the shift in binding energies towards lower side. But addition of  $\text{NH}_4\text{Cl}$  to gold precursor at high pH

(pH 7 and pH 9) shifted the binding energies towards higher side as compared to precursor alone at pH 9. This can be attributed to the attachment of ammine ligands to Au ions (also reflected from Raman analysis).

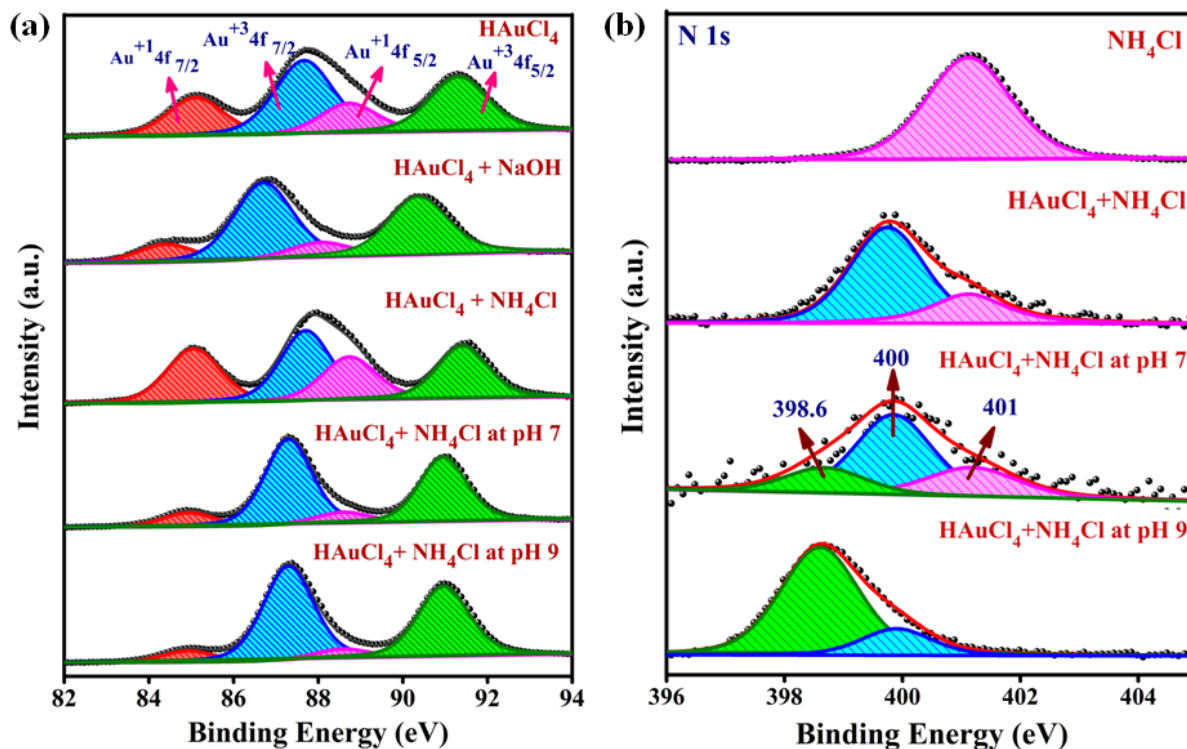


Figure 3A.9 XPS analysis of Au 4f and N 1s core levels under different conditions. ( $\text{NH}_4\text{Cl}$ : 4 millimoles)

It can be noted that the binding energy of  $\text{Au}^{3+}$  was lower by 0.4 eV compared to the precursor alone which manifests the binding of a neutral ligand to gold. The binding energy assignments and the conditions at which they are formed is given in Table 3A.2.

The N 1s spectrum (Figure 3A.9b) gave direct evidence of Au-N bond formation after the addition of salt to gold precursor at high pH. The binding energy value for  $\text{NH}_4\text{Cl}$  was observed at 401.1 eV which can be referred to the  $\text{NH}_4^+$  ions. But addition of  $\text{NH}_4\text{Cl}$  to gold precursor in the absence of alkali showed two peaks at 401.1 eV and 400 eV. The peak at higher binding energy originated from  $\text{NH}_4^+$  ions of  $\text{NH}_4\text{Cl}$  but the peak at lower binding energy can be attributed to the N of  $\text{NH}_4^+$  ions electrostatically attached to the gold complex.<sup>47</sup> This electrostatic interaction was also observed from UV-Visible spectrum where the band at 290 nm showed red shift.



| Sample Name                                     | Au <sup>+1</sup> 4f <sub>7/2</sub> | Au <sup>+3</sup> 4f <sub>7/2</sub> | Au <sup>+1</sup> 4f <sub>5/2</sub> | Au <sup>+3</sup> 4f <sub>5/2</sub> |
|---|------------------------------------|------------------------------------|------------------------------------|------------------------------------|
| HAuCl <sub>4</sub>                              | 85.1                               | 87.7                               | 89.2                               | 91.2                               |
| HAuCl <sub>4</sub> + NaOH                       | 84.4                               | 86.8                               | 88.4                               | 90.4                               |
| HAuCl <sub>4</sub> + NH <sub>4</sub> Cl at pH 7 | 84.8                               | 87.3                               | 88.9                               | 90.9                               |
| HAuCl <sub>4</sub> + NH <sub>4</sub> Cl at pH 9 | 84.8                               | 87.3                               | 88.9                               | 90.9                               |
| HAuCl <sub>4</sub> + NH <sub>4</sub> Cl         | 85.0                               | 87.6                               | 88.9                               | 91.0                               |

Table 3A.2 XPS binding energy values of Au precursor in different conditions. (NH<sub>4</sub>Cl: 4 millimoles).

Addition of NH<sub>4</sub>Cl to gold precursor at high pH showed a new peak emerging at 398.6 eV. This lower binding energy peak corresponds to the formation of new Au complex [Au(NH<sub>3</sub>)<sub>4</sub>-x(OH)<sub>x</sub>]<sup>3-x</sup> (x = 1-3) with ammine ligands where N was directly bonded to Au. It has already been reported that binding energy of N decreases when it is attached to metal as in metal nitrides.<sup>48</sup> Here also, *insitu* generated ammine ligands at high pH formed direct bond with gold hence binding energy values shifted to lower sides. The intensity of this lower binding energy peak was more for HAuCl<sub>4</sub>+NH<sub>4</sub>Cl at pH 9 as compared to pH 7 which showed that no. of ammine ligands coordinated to Au ions was more than 1. The results from Raman, SSNMR and XPS analysis provided direct evidence that the addition of salt to gold precursor at high pH led to a new Au complex with ammine ligands and it is this complex that successfully deposited on the SBA-15 leading to the small and highly dispersed Au NPs in the channels of SBA-15.

### 3A.8 CO Oxidation Activity

The synthesized materials were tested for catalysis and CO oxidation was chosen as the test reaction. The CO oxidation data reported here was after calcination and without any further pretreatment. The activity results are shown in Figure 3A.10. As intuited, the catalytic activity of AS samples increased with increasing the amount of NH<sub>4</sub>Cl and AS 4 showed the maximum activity with a consistent full conversion throughout the temperature range.

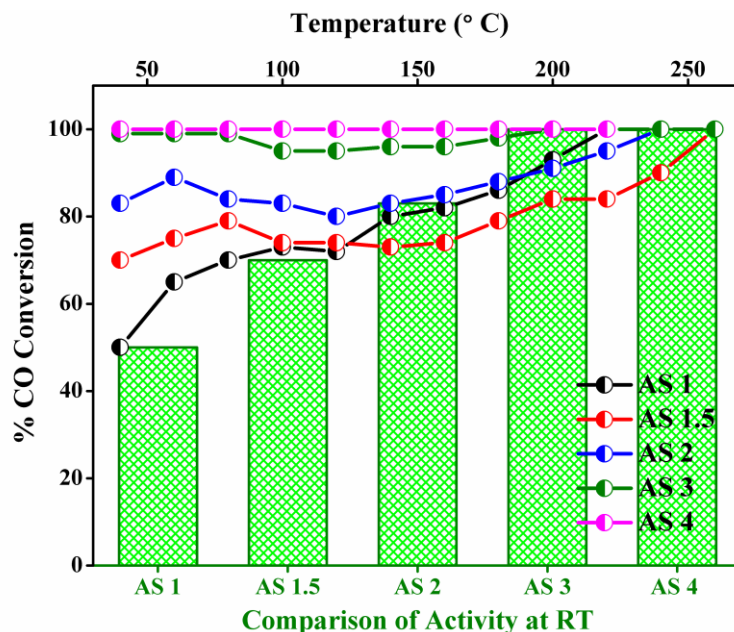


Figure 3A.10 Comparison of CO oxidation activity of AS x samples.

From above plot it is clear that all the samples were extremely active at room temperature which is surprising for Au NPs supported on silica. The genesis of the improved activity of Au NPs on silica in this study can be certainly attributed to the small Au NPs with fine dispersion inside the channels of SBA-15. There are very few literature reports for low temperature CO oxidation on Au/SiO<sub>2</sub> largely because of poor metal support interaction between silica and Au NPs due to difficulty in stabilizing the optimum sized Au particles on the support as well as maintaining proper metal loading.<sup>30</sup>

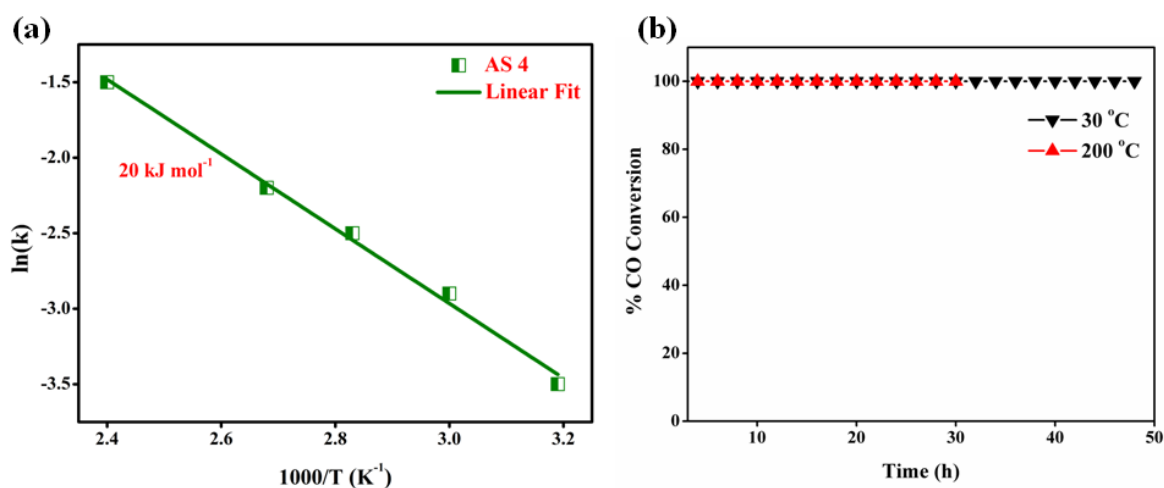


Figure 3A.11 (a) Arrhenius plot for activation energy calculation of AS 4 (b) Time on stream plot of AS 4 catalyst at room temperature and 200 °C.

Low temperature CO oxidation over supported gold systems require 2-3 nm Au NPs both for active as well as inactive support.<sup>13</sup> Surface modification of silica using silanes such as APTMS, APTES, MPTMS etc. is one of the chemical route to synthesize small Au NPs on SBA-15<sup>28-30,49</sup> yet the activity remains low at room temperature.<sup>24,50</sup> Other methods like CVD, grafting and modification of gold precursors by ethylenediamine ligand show activity below 0 °C but all these methods are expensive and tedious.<sup>26,27,32</sup> Among all the AS catalysts AS 4 catalyst showed the best activity which can be attributed to the high dispersion of smaller Au NPs into the SBA-15 channels. The activation energy was calculated for this catalyst by keeping the conversions below 20% at GHSV 3,00,000 ml (g.h)<sup>-1</sup> which was found to be 20 kJ (Figure 3A.11a). This activation energy has been comparable to other active Au catalysts reported in literature for reducible oxides as well as those reported for best Au-silica catalysts prepared by non conventional routes.<sup>26,32,51</sup> The specific rates observed on AS 4 catalyst was 1.32 mol<sub>CO</sub> (g<sub>Au</sub>.h)<sup>-1</sup> [calculated at the GHSV 1,50,000 mL (g.h)<sup>-1</sup> with 16% conversion at RT] which was 2-3 times higher as obtained for other Au catalysts. A detailed comparison of catalytic activity of AS 4 with other Au based catalysts has been tabulated in Appendix as Table A.1. There was a marginal deactivation for all the catalysts except AS 4 between 80 °C to 120 °C but activity increased again at high temperature. The TEM images as well as XRD analysis indicated that there were some larger gold nanoparticles which were supported on the surface of SBA-15 instead of getting encapsulated inside the pore of SBA-15. These larger particles can easily facilitate the formation of carbonaceous intermediate species which can deactivate the catalyst resulting in decrease in the catalytic activity. Chen *et al.* found that the decomposition of the carbonate strongly depends on particle size and observed a facile decomposition of carbonate on smaller gold nanoparticles close to room temperature.<sup>52</sup> Thus, the decrease in the activity of AS 1, 1.5, 2 and AS 3 catalyst in the temperature range of 80-120 °C was because of marginally bigger size of gold and the catalysts regained the activity once the decomposition temperature of these species was achieved i.e. after 120 °C. In the case of AS 4 catalyst the formation and decomposition of carbonaceous species went in parallel due to much smaller particle size delivering sustained activity. Though the support plays important in gold catalyzed CO oxidation but their effect is not the deciding factor in exceptional catalytic activity if the size of gold nanoparticles is below 5 nm. It has been theoretically demonstrated by Lopez et al that the adsorption capacity of Au NPs towards adsorbate increases with decrease in the particles size.<sup>53,54</sup> It is obvious that AS 4 catalyst possessed maximum no. of

smaller Au NPs (as depicted from TEM images and particle size histogram) and hence maximum under-coordinated Au surface atoms which enhanced the adsorption of reactant molecules on the surface of Au NPs.

On an inert support like silica, the mechanism of CO oxidation has been proposed only by gold. This gold only mechanism can happen in two ways: (i) both CO and O<sub>2</sub> are activated on the surface of small Au NPs forming a 4-centred intermediate<sup>55</sup> which dissociates to CO<sub>2</sub> and O (ii) water present either in the reaction gases or on the surface of catalyst (may present in the form of hydroxyl groups also) can facilitate the O<sub>2</sub> activation hence help in accelerating the reaction at low temperature.<sup>56</sup> The first pathway seems to be difficult since oxygen activation on Au NPs happens at high temperature.<sup>55</sup> It has been proposed by many groups that water (or -OH groups) on the surface of catalyst can enhance the catalytic activity of Au NPs appreciably.<sup>56,57</sup> In the present study also we believe that physisorbed water or hydroxyl groups present on the surface of silica can take part in gold based CO oxidation as evidenced by SSNMR study which showed the presence of silanols groups in AS catalyst (Figure 3A.7b).

Further the stability of the best catalyst, AS 4 catalyst under reaction conditions was tested at different temperatures ca. room temperature and 200 °C. It was observed that this catalyst was highly stable and showed full conversion during time on stream (TOS) at both the temperatures. TOS plots of AS 4 catalyst at room temperature (48 h) and 200 °C (24 h) showed excellent stability without any deactivation (Figure 3A.11b). This stability can be attributed to the presence of encapsulated small Au NPs inside the channels of SBA-15 making them sinter resistant during the reaction.

Another parameter used for validating the catalytic activity as well as stability of AS 4 catalyst was by monitoring the activity by increasing the Gas Hourly Space velocity (GHSV). Figure 3A.12 shows the time on stream CO oxidation plot of AS 4 catalyst at room temperature at double GHSV. Even after doubling the GHSV i.e. from 30,000 to 60,000 mL (g.h)<sup>-1</sup> AS 4 catalyst showed > 80% activity at room temperature with a TOS stability tested for 12 h.

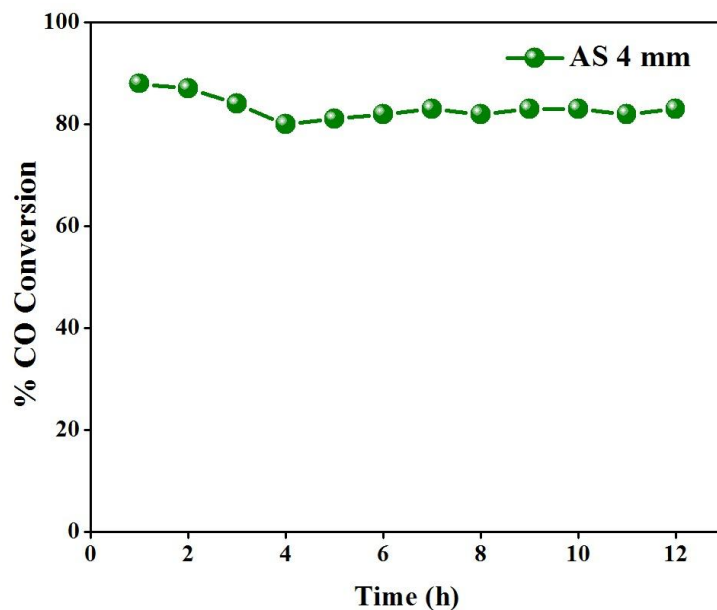


Figure 3A.12 TOS plot of AS 4 catalyst at room temperature at double GHSV.

The spent AS 4 catalyst after 48 hr TOS reaction was analyzed by TEM and showed that Au NPs were still intact inside the channels of SBA-15 without much destruction (Figure 3A.13). It proves that this catalyst is highly stable under reaction conditions also.

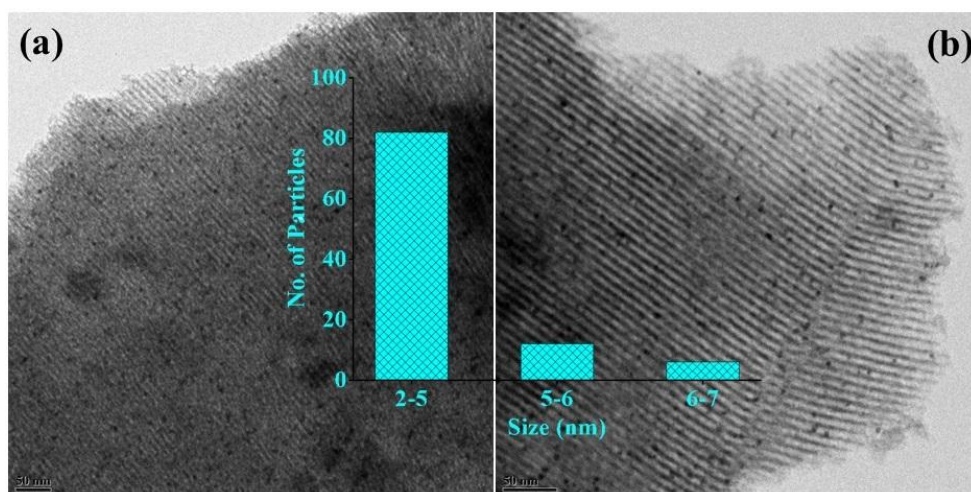


Figure 3A.13 TEM images with particle size histogram of spent AS 4 catalyst after 48 h TOS. Scale Bar- 50 nm

Another proof for excellent thermal stability of AS 4 catalyst comes from the calcination at high temperature ca. 600 °C. The TEM images of this catalyst showed negligible increase in the Au NPs size and particles were still well dispersed in the SBA-15 channels (Figure 3A.14a).

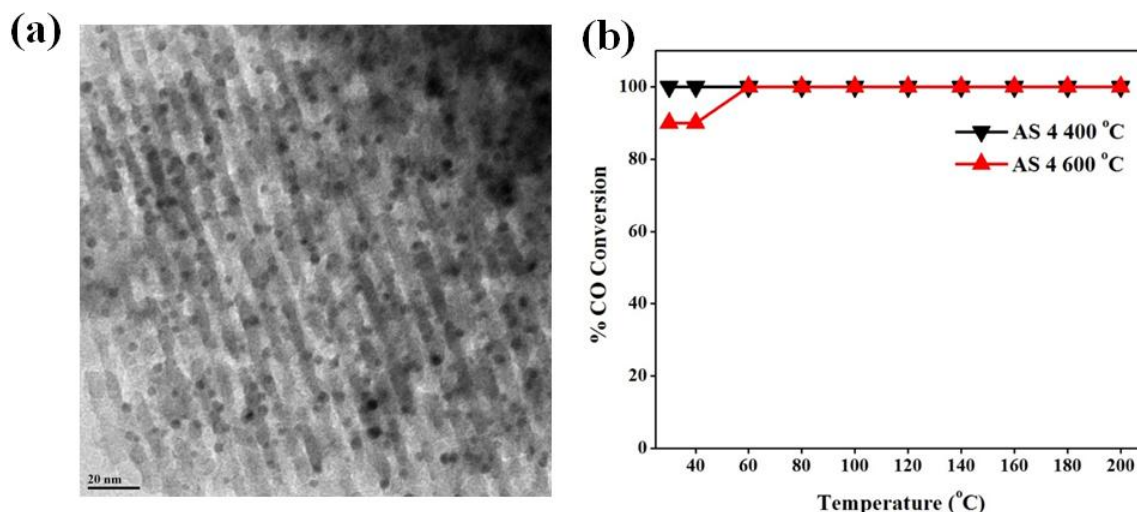


Figure 3A.14 (a) TEM image of AS 4 catalyst calcined at 600 °C (b) Catalytic activity comparison of AS 4 catalyst calcined at 400 and 600 °C.

The CO oxidation activity result of this catalyst (Figure 3A.14b) showed similar activity as that of calcined catalyst at 400°C. As a control experiment we also synthesized Au/SBA-15 catalyst using dil.  $\text{NH}_4\text{OH}$  solution (AS- $\text{NH}_4\text{OH}$ ) and compared the activity with AS 4 catalyst.

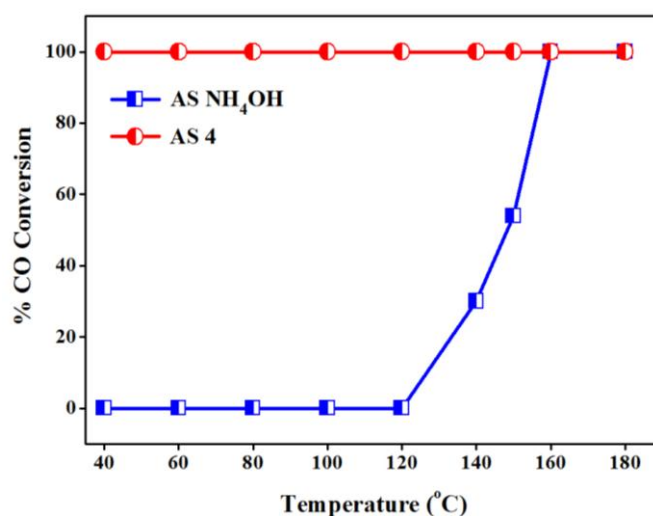


Figure 3A.15 Comparison of CO oxidation activity of AS 4 catalyst with AS  $\text{NH}_4\text{OH}$  catalyst.

AS- $\text{NH}_4\text{OH}$  catalyst did not show any activity at room temperature and activity started after 120 °C with a full conversion at 160 °C (Figure 3A.15). This shows that insitu generated ammine ligands have the potential to modify gold precursor as compared to external added ammonia solution. Thus using a simple method very small Au NPs were successfully supported on inactive silica support which showed exceptional room temperature for CO oxidation.

## Part B. Pd/SBA-15 catalyzed low temperature CO oxidation

Pd/SBA-15 catalyst was also synthesized using the same modified DP method and compared with other conventionally synthesized Pd/SBA-15 catalyst. The synthesis of these catalysts has already been discussed in experimental section of this chapter. Pd/SBA-15 catalyst synthesized by modified DP method has been denoted as Pd-S-N while other catalysts synthesized by conventional DP and wet impregnation have been denoted as Pd-S-NaOH and Pd-S-WI respectively. The characterization and activity results obtained on these catalysts are discussed in following sections.

### 3B.1 UV-visible Spectroscopy

Like Au precursor, the preliminary information about the modification to the Pd precursor after the addition of  $\text{NH}_4\text{Cl}$  came from the UV visible spectroscopy. Fig. 3B.1a shows the UV-visible spectrum of  $\text{H}_2\text{PdCl}_4$  in liquid form. Pd precursor alone showed two bands at 300 and 421 nm. These bands correspond to charge transfer between  $\text{Pd}^{+2}$  and  $\text{Cl}^-$  ions. Addition of  $\text{NH}_4\text{Cl}$  did not change the nature of bands. But the position of the bands was shifted towards the higher wavelength. This kind of red shift in the band position was already observed for Au precursor modified with  $\text{NH}_4\text{Cl}$  in the first part of this chapter which was inferred to the electrostatic interaction of  $\text{NH}_4^+$  ions with  $[\text{AuCl}_4]^-$  complex. In the present case also the red shift in the  $\text{Pd}^{2+}$  bands was attributed to the interaction of ammonium ions with  $[\text{PdCl}_4]^{2-}$  complex.

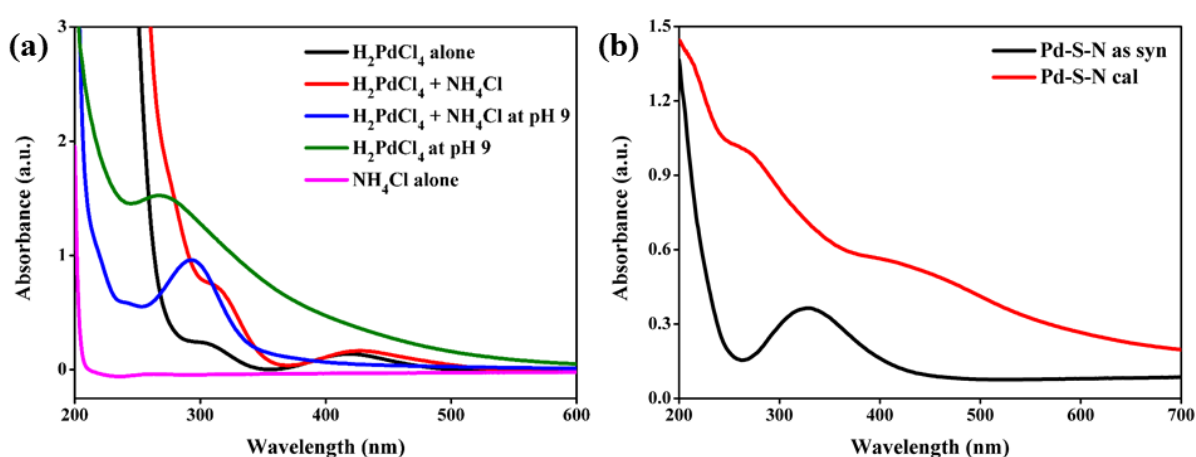


Figure 3B.1 UV visible spectra of (a) Pd precursor in liquid state (b) supported Pd-SBA-15 in solid state.

The addition of  $\text{NH}_4\text{Cl}$  in the presence of alkaline medium resulted in a band at 294 nm which was due to formation of mixed Pd-ammine complex  $[\text{Pd}(\text{NH}_3)_{4-x}(\text{OH})_x]^{2-x}$  (where  $x=1-3$ ).<sup>58</sup> The UV-visible spectrum of supported Pd-SBA-15 sample was shown in Fig. 3A.1b. The as synthesized Pd-S-N sample showed a single band at 324 nm due to presence of Pd-ammine complex but the calcination at 400 °C transformed the Pd-ammine complex to palladium oxide and resulted in appearance of two bands at 270 and 450 nm due to charge transfer between  $\text{Pd}^{2+}$  and  $\text{O}^{2-}$  ions.<sup>59</sup>

### 3B.2 ICP-AES

The ICP analysis done for the three catalysts i.e. Pd-S-N, Pd-S-NaOH and Pd-S-WI showed that modified DP method in Pd-S-N catalyst results in ~100% loading of Pd NPs (theoretical and experimental loading 2.8 wt %) on SBA-15 while for Pd-S-NaOH actual loading remained half of the theoretical loading. This is obvious as conventional DP method is not suitable for loading more than 1 wt% of metal and always results in loss of the metal. Hence the modified DP method is adventitious in preventing the loss of precious metals in solution while supporting on silica.

### 3B.3 X-ray Diffraction

The XRD analysis of these catalysts can be seen in Figure 3B.2. The main XRD reflection at  $2\theta = 33.8^\circ$  corresponds to PdO (101) along with the presence of other PdO reflections.<sup>60</sup>

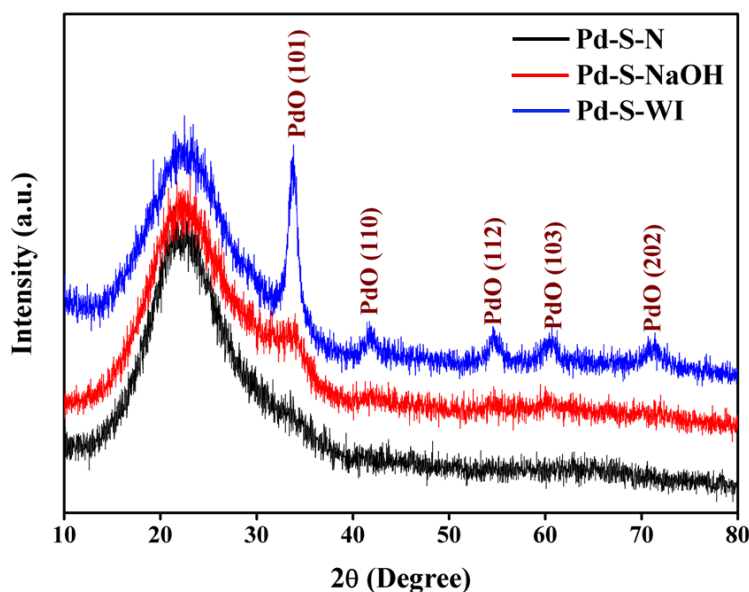


Figure 3B.2 XRD analysis of Pd/SBA-15 catalyst synthesized via different methods.



It is noteworthy that Pd-S-N catalyst did not show any reflection of PdO while Pd-S-NaOH and Pd-S-WI showed clear reflections of PdO. This showed that particle size was smallest for Pd-S-N while the other two catalysts possessed larger size of Pd NPs. Particle size calculation from Debye- Scherer showed size to be ~ 5 nm for Pd-S-NaOH and 7.0 nm for Pd-S-WI.

### 3B.4 Transmission Electron Microscopy

TEM analysis further supported the XRD results that modified DP methods can successfully introduce small Pd NPs inside the SBA-15 channels and can be seen in Figure 3B.3a and b.

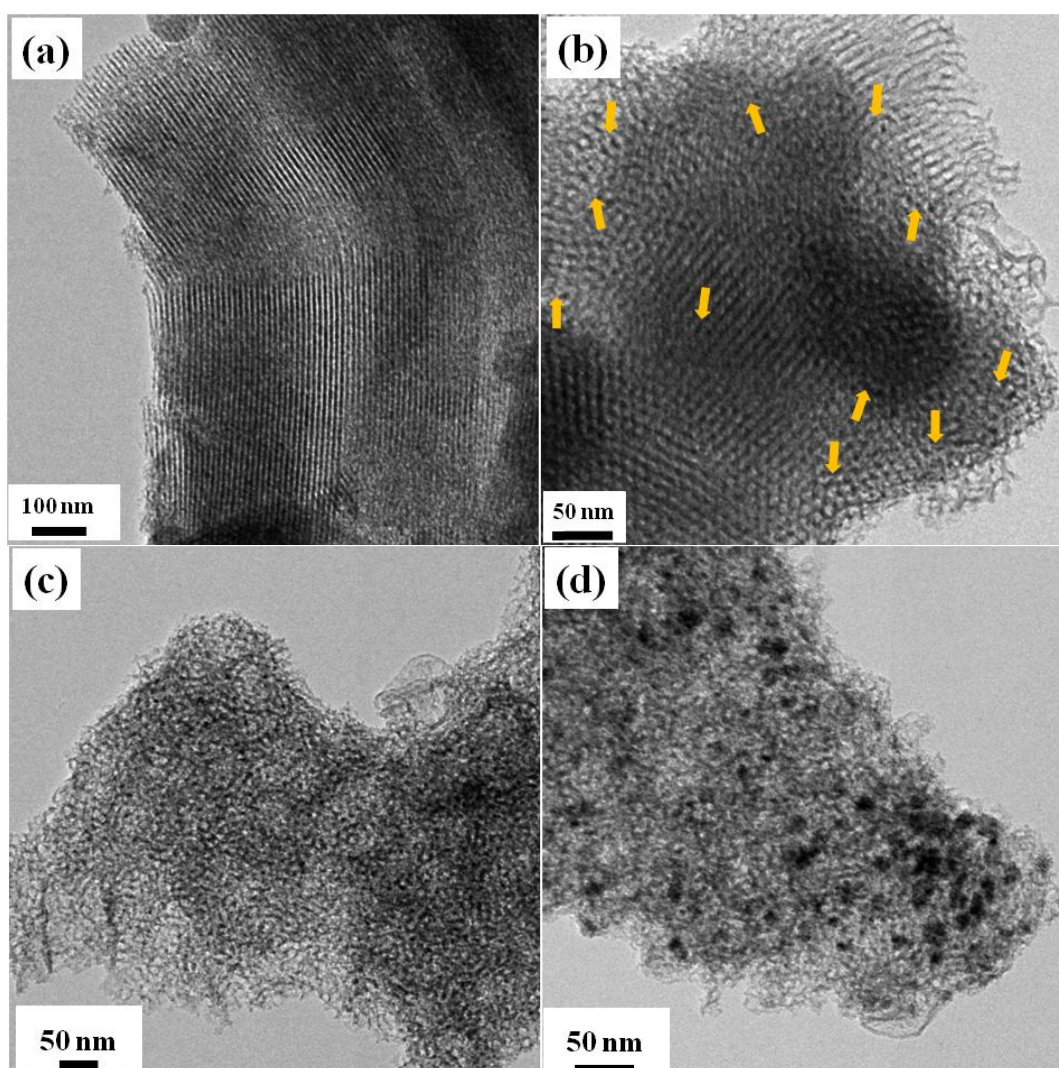


Figure 3B.3 TEM images of (a, b)Pd-S-N (c) Pd-S-NaOH (d) Pd-S-WI catalysts. Yellow arrows show the Pd NPs.

Figure 3B.3b shows the mesoporous channels of SBA-15 but the Pd NPs were not clearly visible. The yellow arrows in this figure showed Pd NPs of very small size located inside the channels of SBA-15.

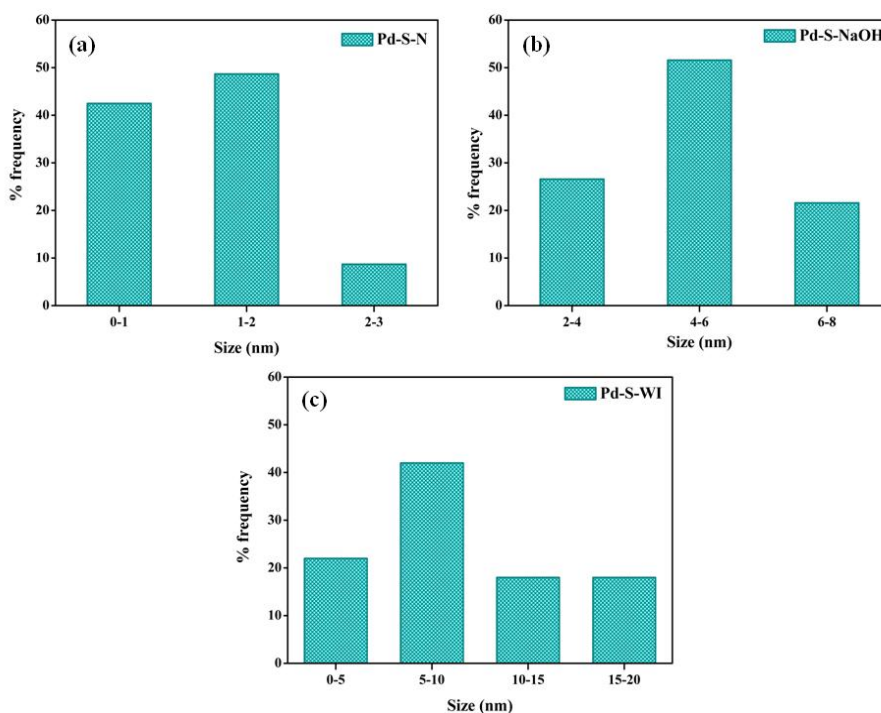


Figure 3B.4 Particle size calculation from TEM images of different Pd/SBA-15 catalyst

The comparison of particle size from TEM images has been summarized in particle size histogram in Figure 3B.4. Size of most of Pd NPs in Pd-S-N catalyst were in the range of 1-2 nm while Pd-S-NaOH catalyst showed most of the NPs in the range of 4-6 nm even though some small particles of size 2-3 nm were also present. Pd-S-WI catalyst showed large sized NPs in the range of 7-8 nm with some particles even larger than 10 nm. Evidences from TEM and histogram clearly indicate that that by using  $\text{NH}_4\text{Cl}$  as a modifier DP method can be successfully employed to obtain very small Pd NPs of size 1-2 nm encapsulated in mesoporous channels of SBA-15.

### 3B.5 CO Oxidation Activity

The catalytic activity of calcined Pd/SBA-15 catalysts synthesized via different methods is shown in Figure 3B.5 and their activation energy was compared. The Pd-S-N catalyst was most active with a light off temperature of 90 °C, which was quite low as compared to other reported Pd/SiO<sub>2</sub> catalysts in literature.<sup>11,61</sup> Compared to this catalyst the light off temperature of other catalysts was 120 °C (Pd-S-NaOH) and 140 °C (Pd-S-WI) respectively. Although,

light off temperature is good for benchmarking the catalyst, the true indicator comes from the activation energy (Figure 3B.5b) which was  $17.5 \text{ kcal mol}^{-1}$  for Pd-S-N catalyst better compared to other Pd based catalysts.<sup>11,61,62</sup>

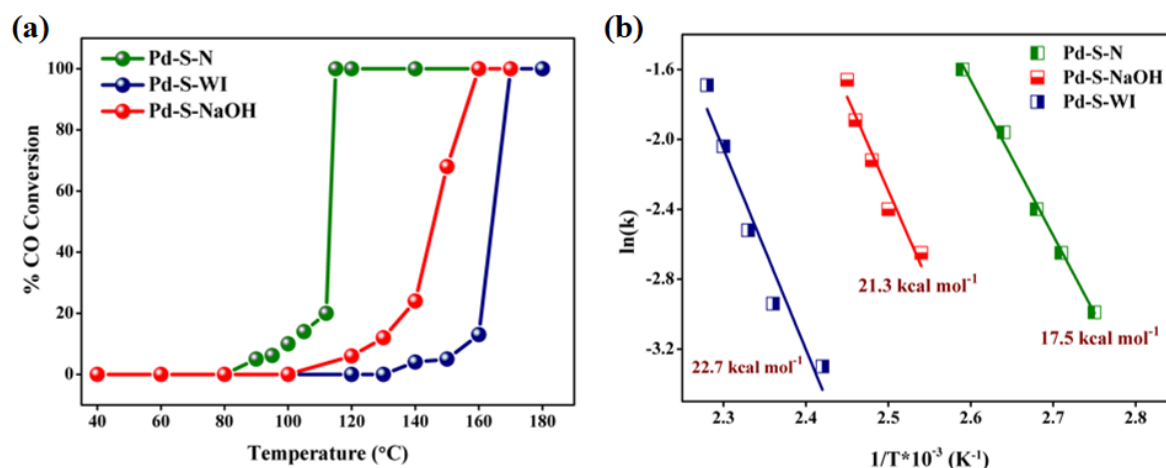


Figure 3B.5 CO oxidation activity of calcined Pd/SBA-15 catalysts synthesized by different methods (a) temperature dependent CO conversion (b) activation energy of different catalysts.

It has been well explored that support plays an important role in catalyzing CO oxidation since oxygen activation can happen either at support or at the interface. Supports like  $\text{TiO}_2$ ,  $\text{CeO}_2$ ,  $\text{Fe}_2\text{O}_3$ ,  $\text{Co}_3\text{O}_4$  etc. are active for CO oxidation due to their redox properties and on these supports Pd can show high catalytic activity at ambient temperatures due to the generation of oxygen vacancies or by inducing electronic modifications in Pd.<sup>63-67</sup>

Silica being irreducible and inactive support for most of the catalytic reactions, and hence the difference in the activity could solely be attributed to the Pd NPs size. The nature of the surface Pd species prepared with different synthesis methods resulting in different sized Pd NPs was elucidated by XPS analysis as in Figure 3B.6.

The Pd 3d spectra of the three catalyst was compared and it was observed that except Pd-S-N catalyst other two catalysts showed coexistence of three peaks at 335.2, 336.8 and 338.4 eV which can be assigned to metallic Pd,  $\text{Pd}^{2+}$  as PdO and  $\text{Pd}^{x+}$  as high valent  $\text{PdO}_x$  species respectively.<sup>68,69</sup>

Pd-S-N catalyst did not show any peak of metallic Pd. Meanwhile the shoulder at 338.4 eV (for  $\text{Pd}^{x+}$  where  $x > 2$ ) showed an inverse relation with size and emerged as the major peak (70% see Figure 3B.6c) in Pd-S-N catalyst. The generation of high valent Pd oxide species in high concentration on smaller NPs has been previously reported on Pd/C and Pd-SBA-15.<sup>69,70</sup>

The exact nature of active Pd species for CO oxidation has always been controversial which prompted us to carry out in depth XPS analysis of our catalyst.<sup>71-73</sup>

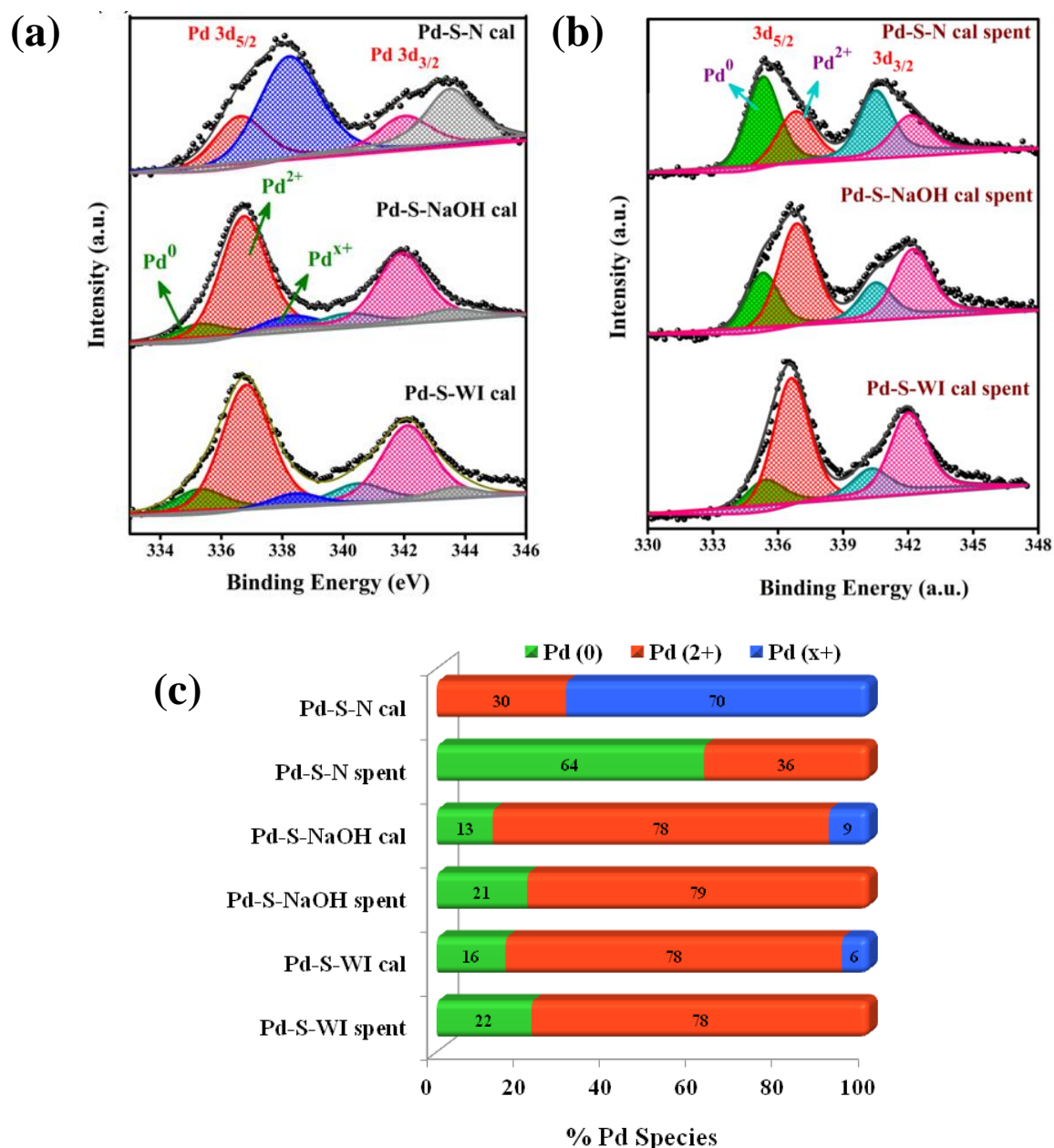


Figure 3B.6 (a) Comparative XPS plots of (a) calcined (b) spent Pd/SBA-15 catalysts and (c) comparison of % Pd species in fresh and spent calcined catalysts as calculated from XPS.

The spent catalyst XPS analysis of three catalysts showed only two peaks at 335.3 eV and 336.8 eV corresponding to metallic Pd and Pd<sup>2+</sup> (Figure 3B.6b). It is noteworthy that amount of Pd<sup>0</sup> species increased mostly at the expense of Pd<sup>x+</sup> species. The percentage of metallic Pd was maximum in Pd-S-N (64%) followed by other two catalysts.

Further the effect of reduction on the activity of Pd-S-N catalyst was tested by reducing the catalyst in H<sub>2</sub> flow at 400 °C and was compared with calcined catalyst (Figure 3B.7)

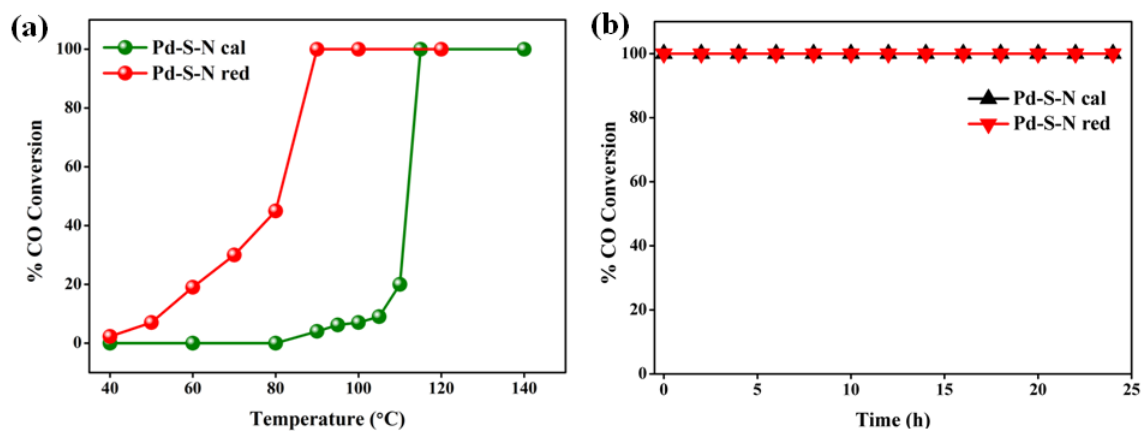


Figure 3B.7 Comparison of Pd-S-N calcined and reduced catalysts (a) CO oxidation activity (b) time on stream plots at 115 °C and 90 °C respectively.

The comparison of catalytic activity of Pd-S-N calcined catalyst with reduced catalyst clearly showed that light off temperature shifted close to room temperature in Pd-S-N red with full conversion obtained at 90 °C. The activity obtained on Pd-S-N catalyst was probably the best activity shown by Pd/silica catalyst so far.<sup>11,61,74</sup> The activation energy of reduced Pd-S-N catalyst (13.6 kcal mol<sup>-1</sup> or 57 kJ mol<sup>-1</sup>) was lower as compared to other reported active Pd based catalysts where  $E_a$  varied from 60-80 kJ mol<sup>-1</sup>.<sup>11,61,75,76</sup> Comparison of CO oxidation activity of reduced catalysts synthesized by different methods can be seen in Figure 3B.8.

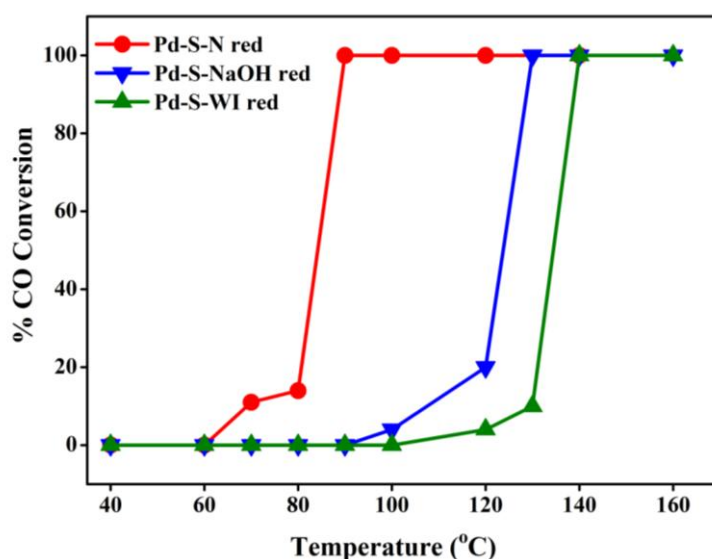


Figure 3B.8 Comparison of CO Oxidation activity of different reduced catalysts

It is clear from the figure that Pd-S-N catalyst after reduction showed the best activity among all the catalysts a trend similar to calcined catalyst.

To gain insights on different Pd species present in Pd/SBA-15 catalyst after reduction and CO oxidation, XPS analysis was done (Figure 3B.9) and it was observed that after reduction all the catalysts showed metallic Pd as the major species. It should be noted that amount of metallic Pd in all the three catalysts reduced at 400 °C was similar still the activity of Pd-S-N red was higher as compared to other two catalysts. Also the CO chemisorption analysis on these catalysts showed that Pd-S-N catalyst had the highest dispersion (45%) of Pd followed by Pd-S-NaOH (23%) and Pd-S-WI (5%).

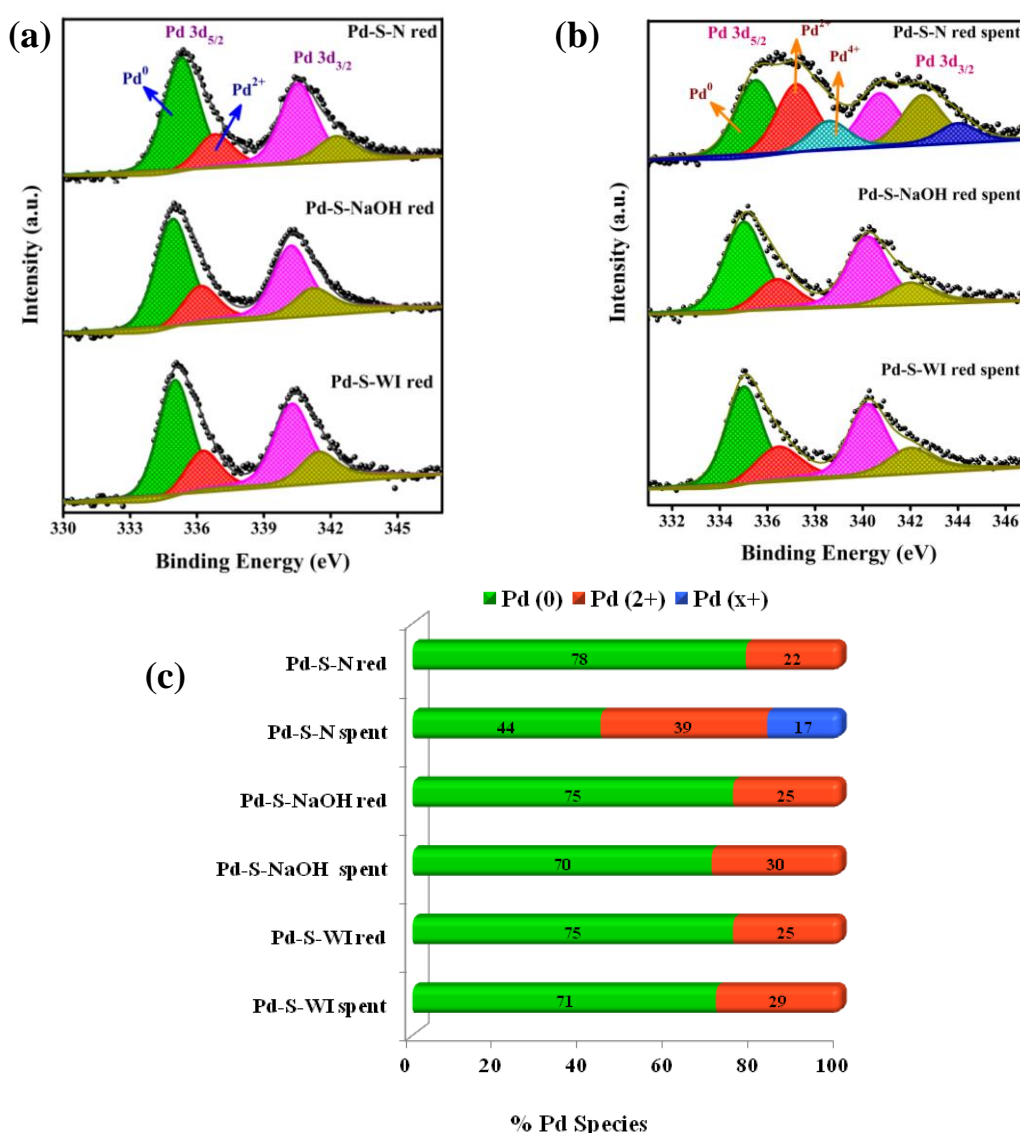


Figure 3B.9 XPS spectra of (a) reduced and (b) spent catalysts (c) comparison of different Pd species in reduced and spent catalyst

The high dispersion of Pd points towards the maximum no. of metallic Pd sites available in Pd-S-N catalyst which were accessible for catalyzing CO oxidation. Further the TOS reaction conducted for both reduced and calcined Pd-S-N catalyst for 24 hr showed the stability of these catalysts under reaction conditions (Figure 3B.7b). The TEM images of Pd-S-N reduced catalyst (Figure 3B.10) showed that small size of Pd NPS was still maintained even after 24 hr TOS reaction.

The CO oxidation activity obtained over reduced Pd-S-N catalyst was similar to the Pd NPs supported on active supports.<sup>64,65,67,77</sup> TOF of this catalyst was compared with previously reported active Pd catalysts (Appendix TableA.2) and found to be superior to other catalysts.

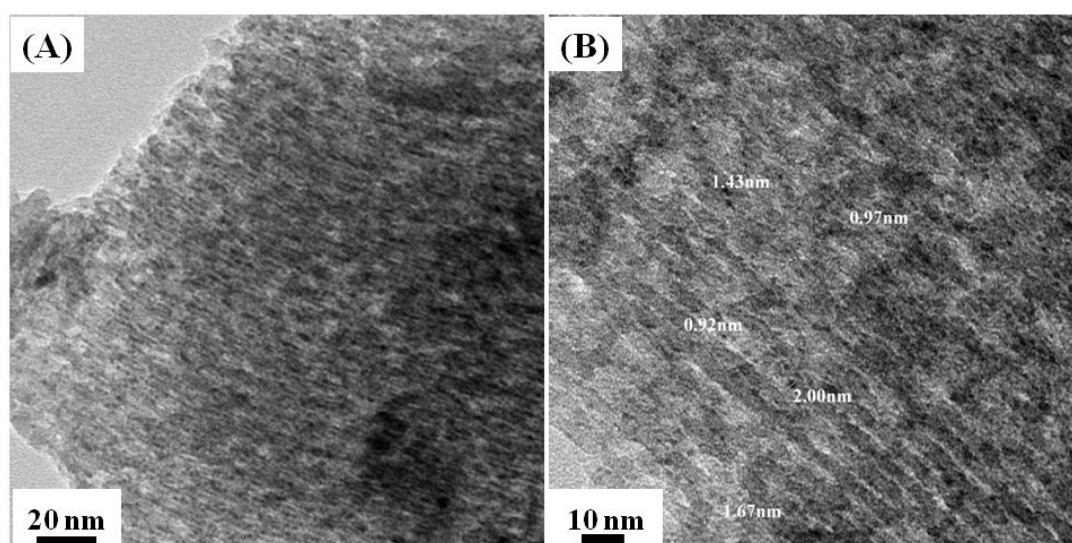
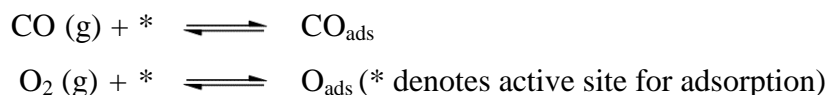


Figure 3B.10 TEM analysis of reduced Pd-S-N catalyst after 24 h time on stream reaction.

In general CO oxidation reaction on Pd follows Langmuir-Hinshelwood mechanism where both CO and O<sub>2</sub> are chemisorbed on the surface of Pd<sup>63,78</sup> with following elementary steps:



The dissociative adsorption of O<sub>2</sub> results in the formation of active oxygen species which reacts with nearby CO and forms CO<sub>2</sub>. Usually the sticking coefficient of CO on metallic Pd is high as compared to O<sub>2</sub> at ambient temperature which results in strong adsorption of CO leaving behind limited sites for oxygen adsorption and activation thus inhibiting the activity.<sup>78-80</sup> This is the probable reason of low activity of Pd based catalyst at low temperature. With increase in temperature, rate of CO desorption increases freeing the sites for O<sub>2</sub> activation. The resulting O atoms can react with the neighboring adsorbed CO and thus

leave even larger available surface for O<sub>2</sub> adsorption which ultimately results in exponential increase in the rate of CO oxidation. It has been observed that CO gets strongly adsorbed on facets/terrace sites of Pd NPs as compared to under coordinated (edges/corners/kinks) sites<sup>81,82</sup> and no. of edges/corner sites increases with a decrease in the Pd NPs size.<sup>83</sup>

As a first approximation, difference in activity obtained for different catalysts can be explained on the basis of size of Pd NPs, where small sized Pd NPs in Pd-S-N catalyst having maximum no. of under coordinated sites reduced the CO poisoning of this catalyst. Since the CO adsorption is rather weak on the under coordinated sites the O<sub>2</sub> adsorption and activation which is the rate determining step, can be facile on these sites.<sup>79</sup> The detailed XPS analysis of calcined catalysts revealed the generation of different cationic Pd species, the concentration of which has strong size dependence. This difference in reactivity with oxygen by Pd NPs with size during calcination is understandable as smaller NPs are unequivocally proved to be more reactive than bigger particles.<sup>84</sup> The XPS plot of calcined Pd-S-N catalyst which had smallest Pd NPs among the three (Figure 3B.6) comprised maximum amount of high valent Pd oxide (PdO<sub>x</sub>) species (70%). Obviously, the under coordinated sites on these smaller particles are able to stabilize the high valent Pd species.<sup>37</sup> In the present case, it can be inferred that larger proportion of Pd<sup>x+</sup> (x>2) species exclusively present in the Pd-S-N catalyst demonstrated profoundly increased CO oxidation activity. These Pd<sup>x+</sup> species can decompose easily to metallic Pd under CO oxidation conditions which provide sites for adsorption and activation of reactant molecules. The percentage of high valent Pd oxide in the other two catalysts was approximately 6-8 % whereas the major species was PdO. It is well known that PdO is not the favored surface for CO oxidation as reduction and reoxidation of the surface happen above 100 °C.<sup>85</sup> Also approximately 13-16 % metallic Pd was seen in these two catalysts even after calcination at 400 °C which could be mostly terrace Pd sites and got occupied mainly by CO under reaction conditions. In such a scenario sites for O<sub>2</sub> activation were not available and to create such sites decomposition of oxidized Pd layer had to happen which occurred at temperature above 100 °C in larger NPs. In spite of the presence of metallic Pd (for CO activation) and PdO<sub>x</sub> in Pd-S-NaOH and Pd-S-WI calcined catalyst, low temperature activity was not observed which clearly points to the fact that catalytic activity is initiated only after the reduction of oxide Pd surface followed by CO and oxygen activation. Thus, the reduced light off temperature demonstrated by small Pd NPs in Pd-S-N catalyst can be explained on the basis of lower reduction temperature of large fraction of high valent Pd oxide species as compared to other two catalysts which were mainly possessed by



PdO species. The spent catalyst analysis showed that as the particle size decreased the Pd surface got more reduced under the CO oxidation conditions with generation of metallic Pd species the percentage being large in smaller particles (Figure 3B.9c). Even though, the CO oxidation in the present study was carried out in an O<sub>2</sub> rich environment, the indication that CO oxidation proceeds through the formation of metallic Pd surface was clear from this analysis. The fact that already formed PdO<sub>x</sub> was not active for CO oxidation was proved by screening Pd-S-N catalyst in CO alone conditions. The catalyst did not show any activity up to 150 °C which shows that the sites for CO adsorption was absent and *insitu* generated PdO<sub>x</sub> and O<sub>ad</sub> on Pd under reaction conditions were responsible for low temperature CO oxidation. An equilibrium generation of PdO<sub>x</sub> and its decomposition along with O<sub>ad</sub> atoms are crucial for stable CO oxidation activity which happened at 90 °C for Pd-S-N catalyst.

The reduction of Pd/SBA-15 catalyst in hydrogen improved the catalytic activity for all the Pd/SBA-15 catalyst (Figure 3B.8) effect being most pronounced in Pd-S-N catalyst. The light off temperature for the reduced Pd-S-N catalyst was shifted close to room temperature unlike other two catalysts which showed only marginal improvement. The XPS analysis of the reduced catalysts showed an interesting scenario where almost similar amount of metallic Pd was observed in the three catalysts still the activity of Pd-S-N was best among the three. The spent catalyst analysis and relative fraction of different surface Pd species of all the three reduced Pd/SBA-15 catalysts can be seen Figure 3B.9. It was observed that Pd-S-N catalyst showed the generation of high valent Pd oxide (17%) species under reaction conditions [even at low temperature also (7% PdO<sub>x</sub> at 60 °C with 17% CO conversion, Figure 3B.12)] while the other two catalysts did not show any PdO<sub>x</sub> species which again confirms strong size dependency of PdO<sub>x</sub> species formation on small Pd NPs under reaction conditions. The co-existence of an ensemble of Pd (0) and Pd (x+) in the spent catalyst of Pd-S-N strongly suggests what is expected for a good low temperature active Pd catalyst. The other two catalysts showed mostly metallic Pd as major fraction along with PdO which was largely covered by CO at low temperature inhibiting its activity and required temperature above 100 °C to free up sites for oxygen activation. The generation of high valent PdO<sub>x</sub> at low temperature has been considered as an indicator for the improved activity, which was synonymous to the generation of O<sub>ad</sub> atom for CO oxidation. The metallic Pd did not take part directly in the CO oxidation; still it was prerequisite for obtaining low temperature CO oxidation by (i) *insitu* generating active high valent PdO<sub>x</sub> species with O<sub>ad</sub> on the under coordinated Pd atoms (ii) providing the sites for CO activation. Thus Pd based catalyst showed

a strong size dependency on CO oxidation activity by generating different Pd surface species which showed different behavior for CO oxidation.

### **3.3 Conclusion**

Improved loading and stabilization of small gold and palladium nanoparticles on silica, one of the most difficult tasks in the synthesis of noble metal based catalyst, has been addressed by a simple wet chemical method.  $\text{NH}_4\text{Cl}$  assisted *insitu* modification of gold and palladium precursors via modified deposition precipitation method helped in dispersing small metal NPs inside the pores of SBA-15.

Various spectroscopic tools such as Raman Spectroscopy, XP spectroscopy and SSNMR were employed to understand the modification of gold precursor in the presence of  $\text{NH}_4\text{Cl}$ . In the case of Au/SBA-15 catalyst, well dispersed stable small Au NPs inside the pore channels of SBA-15 were mostly observed in AS 4 catalyst which showed unprecedented and sustained CO oxidation activity at room temperature and also at  $200^\circ\text{C}$  without any catalyst deactivation. This catalyst showed appreciable activity even after calcination at  $600^\circ\text{C}$  (sinter resistant) which supported our claim that Au NPs were well protected inside the channels of SBA-15 without destroying the hexagonal architecture of SBA-15. The support effect in this case was negligible as the decisive factor for exceptional activity of AS 4 catalyst was size and dispersion of Au NPs.

In the case of Pd/SBA-15 catalyst Pd-S-N catalyst showed best activity among all the other catalyst due to presence of smallest sized Pd NPs with good fraction of under co-ordinated sites. A detailed XPS analysis on these catalysts showed strong size dependency for the generation of different Pd species. High valent  $\text{PdO}_x$  species generated on small size Pd NPs on under co-ordinated sites in Pd-S-N and their easy decomposition at relatively lower temperature was the reason for observance of low temperature activity of this catalyst. Presence of ample amount of under-coordinated sites on small sized Pd NPs resulted in generation of  $\text{PdO}_x$  and  $\text{O}_{\text{ad}}$  under reaction conditions which could catalyze CO oxidation at comparatively low temperature. Also the self poisoning of the Pd sites was prevented on under-coordinated sites which provided sites for  $\text{O}_2$  adsorption and activation at low temperature.

Overall it can be concluded that by a simple ligand exchange method via replacement of negatively charged  $\text{Cl}^-$  ions with the neutral ammine ligands a conventional deposition

precipitation method has been successfully employed for the synthesis of Au and Pd supported on low PZC support silica for getting highly active low temperature CO oxidation catalyst. The method is simple, inexpensive, and scalable which can be extended to other noble as well as non noble metals NPs supported on silica. The catalyst synthesized in this way can further be explored for various fundamental as well as industrially important reactions.

### 3.4 References

1. Astruc, D., *Wiley-VCH Verlag GmbH & Co. KGaA* **2008**, (1).
2. Tao, F., *RSC Catal. Ser.* **2014**.
3. Shiju, N. R.; Gulians, V. V., *Appl. Catal., A* **2009**, *356* (1), 1-17.
4. Campelo, J. M.; Luna, D.; Luque, R.; Marinas, J. M.; Romero, A. A., *ChemSusChem* **2009**, *2* (1), 18-45.
5. Martin, G. A.; Mirodatos, C.; Praliaud, H., *Appl. Catal.* **1981**, *1* (6), 367-382.
6. Soled, S., *Science* **2015**, *350* (6265), 1171-1172.
7. Wei, L.; Zhao, Y.; Zhang, Y.; Liu, C.; Hong, J.; Xiong, H.; Li, J., *J. Catal.* **2016**, *340*, 205-218.
8. Sapi, A.; Dobo, D. G.; Sebok, D.; Halasi, G.; Juhasz, K. L.; Szamosvolgyi, . A.; Pusztai, P.; Varga, E.; Kalomista, I.; Galbacs, G.; Kukovecz, . A.; Konya, Z., *J. Phys. Chem. C* **2017**, *121* (9), 5130- 5136.
9. Zhang, Q.; Lee, I.; Joo, J. B.; Zaera, F.; Yin, Y., *Acc. Chem. Res.* **2013**, *46* (8), 1816-1824.
10. Zhang, T.; Zhao, H.; He, S.; Liu, K.; Liu, H.; Yin, Y.; Gao, C., *ACS nano* **2014**, *8* (7), 7297.
11. Park, J.-N.; Forman, A. J.; Tang, W.; Cheng, J.; Hu, Y.-S.; Lin, H.; McFarland, E. W., *Small* **2008**, *4* (10), 1694-1697.
12. Joo, S. H.; Park, J. Y.; Tsung, C.-K.; Yamada, Y.; Yang, P.; Somorjai, G. A., *Nat. Mater.* **2008**, *8*, 126.
13. Haruta, M., Size- and support-dependency in the catalysis of gold. *Catalysis Today* **1997**, *36* (1), 153-166.
14. Corma, A.; Garcia, H., *Chem. Soci. Rev.* **2008**, *37* (9), 2096-2126.
15. Hutchings, G. J.; Edwards, J. K., *Eds. Elsevier* **2012**, (3), 249-293.
16. Gu, D.; Tseng, J.-C.; Weidenthaler, C.; Bongard, H.-J.; Spliethoff, B.; Schmidt, W.; Soulimani, F.; Weckhuysen, B. M.; Schuth, F., *J. Am. Chem. Soc.* **2016**, *138* (30), 9572.
17. Chen, L.; Chen, H.; Luque, R.; Li, Y., *Chem. Sci.* **2014**, *5* (10), 3708-3714.
18. King, A. O., Larsen, R. D. and Negishi, E., *Handbook of Organopalladium Chemistry for Organic Synthesis*, **2003**.
19. Ruiz-Castillo, P.; Buchwald, S. L., *Chem. Rev.* **2016**, *116* (19), 12564-12649.
20. Oh, S.; Kim, Y. K.; Jung, C. H.; Doh, W. H.; Park, J. Y., *Chem. Commun.* **2018**, *54* (59), 8174- 8177.
21. Liu, J.-C.; Wang, Y.-G.; Li, J., *J. Am. Chem. Soc.* **2017**, *139* (17), 6190-6199.
22. Tang, H.; Su, Y.; Zhang, B.; Lee, A. F.; Isaacs, M. A.; Wilson, K.; Li, L.; Ren, Y.; Huang, J.; Haruta, M.; Qiao, B.; Liu, X.; Jin, C.; Su, D.; Wang, J.; Zhang, T., *Sci. Adv.* **2017**, *3* (10).
23. Zanella, R.; Giorgio, S.; Shin, C.-H.; Henry, C. R.; Louis, C., *J. Catal.* **2004**, *222* (2), 357-367.
24. Munnik, P.; de Jongh, P. E.; de Jong, K. P., *Chem. Rev.* **2015**, *115* (14), 6687-6718.
25. Kosmulski, M., *Adv. Colloid Inter. Sci.* **2016**, *238*, 1-61.
26. Lin, S. D.; Bollinger, M.; Vannice, M. A., *Catal. Lett.* **1993**, *17* (3), 245-262.
27. Okumura, M.; Tsubota, S.; Haruta, M., *J. Mol. Catal., A* **2003**, *199* (1), 73-84.
28. Chi, Y.-S.; Lin, H.-P.; Mou, C.-Y., *Appl. Catal., A* **2005**, *284* (1), 199-206.
29. Rombi, E.; Cutrufello, M. G.; Cannas, C.; Casu, M.; Gazzoli, D.; Occhuzzi, M.; Monaci,

- R.; Ferino, I., *Phys. Chem. Chem. Phys.* **2009**, *11* (3), 593-602.
30. Rombi, E.; Cutrufello, M. G.; Monaci, R.; Cannas, C.; Gazzoli, D.; Onida, B.; Pavani, M.; Ferino, I., *J. Mol. Catal. A* **2015**, *404-405* (Supplement C), 83-91.
31. MacQuarrie, S.; Nohair, B.; Horton, J. H.; Kaliaguine, S.; Crudden, C. M., *J. Phys. Chem. C* **2010**, *114* (1), 57-64.
32. Zhu, H.; Liang, C.; Yan, W.; Overbury, S. H.; Dai, S., *J. Phys. Chem. B* **2006**, *110* (22), 10842-10848.
33. Kraszkiewicz, P.; Mista, W., *Catal. Commun.* **2018**, *110*, 14-17.
34. Zhao, D.; Feng, J.; Huo, Q.; Melosh, N.; Fredrickson, G. H.; Chmelka, B. F.; Stucky, G. D., *Science* **1998**, *279* (5350), 548.
35. Kim, Y.-G.; Oh, S.-K.; Crooks, R. M., *Chem. Mater.* **2004**, *16* (1), 167-172.
36. Martin, M. N.; Li, D.; Dass, A.; Eah, S.-K., *Nanoscale* **2012**, *4* (14), 4091-4094.
37. Sing, K. S. W., *Pure Appl. Chem.*, **1985**; (57), 603.
38. Pan, P.; Wood, S. A., *Geochim. Cosmochim. Ac.* **1991**, *55* (8), 2365-2371.
39. Murphy, P. J.; LaGrange, M. S., *Geochim. Cosmochim. Ac.* **1998**, *62* (21), 3515-3526.
40. Manfait, M.; Alix, A. J. P.; Kappenstein, C., *Inorg. Chim. Ac.* **1981**, *50*, 147-152.
41. Ismail, I. M.; Sadler, P. J., In *Platinum, Gold, and Other Metal Chemotherapeutic Agents*, *Am. Chem. Soc.* **1983**, (209), 171-190.
42. Baccile, N.; Laurent, G.; Bonhomme, C.; Innocenzi, P.; Babonneau, F., *Chem. Mater.* **2007**, *19* (6), 1343-1354.
43. Piedra, G.; Fitzgerald, J. J.; Dando, N.; Dec, S. F.; Maciel, G. E., *Inorg. Chem.* **1996**, *35* (12), 3474-3478.
44. Gränberg, B.; Emmeler, T.; Gedat, E.; Shenderovich, I.; Findenegg Gerhard, H.; Limbach, H.-H.; Buntkowsky, G., *Chem. Eur. J.* **2004**, *10* (22), 5689-5696.
45. Cao, L.; Jennings, M. C.; Puddephatt, R. J., *Inorg. Chem.* **2007**, *46* (4), 1361-1368.
46. Carapeto, A. P.; Ferraria, A. M.; Boufi, S.; Vilar, M. R.; do Rego, A. M. B., *Cellulose* **2015**, *22*, (1), 173-186.
47. Kumar, A.; Mandal, S.; Selvakannan, P. R.; Pasricha, R.; Mandale, A. B.; Sastry, M., *Langmuir* **2003**, *19* (15), 6277-6282.
48. Ji, W.; Shen, R.; Yang, R.; Yu, G.; Guo, X.; Peng, L.; Ding, W., *J. Mater. Chem. A* **2014**, *2* (3), 699-704.
49. Rombi, E.; Cutrufello, M. G.; Cannas, C.; Occhiuzzi, M.; Onida, B.; Ferino, I., *Phys. Chem. Chem. Phys.* **2012**, *14* (19), 6889-6897.
50. Yang, C.-m.; Kalwei, M.; Schüth, F.; Chao, K.-j., *Appl. Catal., A* **2003**, *254* (2), 289-296.
51. Haruta, M.; Tsubota, S.; Kobayashi, T.; Kageyama, H.; Genet, M. J.; Delmon, B., *J. Catal.* **1993**, *144* (1), 175-192.
52. Chen, S.; Luo, L.; Jiang, Z.; Huang, W., *ACS Catal.* **2015**, *5* (3), 1653-1662.
53. Sreedhala, S.; Sudheeshkumar, V.; Vinod, C. P., *Catal. Today* **2015**, *244*, 177-183.
54. Lopez, N.; Janssens, T. V. W.; Clausen, B. S.; Xu, Y.; Mavrikakis, M.; Bligaard, T.; Nørskov, J. K., *J. Catal.* **2004**, *223* (1), 232-235.
55. Liu, Z.-P.; Hu, P.; Alavi, A., *J. Am. Chem. Soc.* **2002**, *124* (49), 14770-14779.
56. Kettemann, F.; Witte, S.; Birnbaum, A.; Paul, B.; Clavel, G.; Pinna, N.; Rademann, K.; Kraehnert, R.; Polte, J., *ACS Catal.* **2017**, *7* (12), 8247-8254.

57. Masakazu, D.; Mitsutaka, O.; Susumu, T.; Masatake, H., *Angew. Chem. Int. Ed.* **2004**, *43* (16), 2129-2132.
58. Harada, T.; Ikeda, S.; Miyazaki, M.; Sakata, T.; Mori, H.; Matsumura, M., *J. Mol. Catal. A* **2007**, *268* (1), 59-64.
59. Ivanova, A. S.; Slavinskaya, E. M.; Gulyaev, R. V.; Zaikovskii, V. I.; Stonkus, O. A.; Danilova, I. G.; Plyasova, L. M.; Polukhina, I. A.; Boronin, A. I., *Appl. Catal. B* **2010**, *97* (1), 57-71.
60. Datye, A. K.; Bravo, J.; Nelson, T. R.; Atanasova, P.; Lyubovsky, M.; Pfefferle, L., *Appl. Catal. A* **2000**, *198* (1), 179-196.
61. Ying, J.; Peng, H.; Xu, X.; Wang, R.; Yu, F.; Sun, Q.; Liu, W.; Gao, Z.; Wang, X., *Catal. Sci. Technol.* **2016**, *6* (14), 5405-5414.
62. Gaudet, J. R.; de la Riva, A.; Peterson, E. J.; Bolin, T.; Datye, A. K., *ACS Catal.* **2013**, *3* (5), 846-855.
63. Zhou, Y.; Wang, Z.; Liu, C., *Catal. Sci. Technol.* **2015**, *5* (1), 69-81.
64. Hinokuma, S.; Fujii, H.; Okamoto, M.; Ikeue, K.; Machida, M., *Chem. Mater.* **2010**, *22* (22), 6183-6190.
65. Dong, G.; Wang, J.; Gao, Y.; Chen, S., *Catal. Lett.* **1999**, *58* (1), 37-41.
66. Wang, C.; Wen, C.; Lauterbach, J.; Sasmaz, E., *Appl. Catal. B* **2017**, *206*, 1-8.
67. Liu, L.; Zhou, F.; Wang, L.; Qi, X.; Shi, F.; Deng, Y., *J. Catal.* **2010**, *274* (1), 1-10.
68. Kibis, L. S.; Stadnichenko, A. I.; Koscheev, S. V.; Zaikovskii, V. I.; Boronin, A. I., *J. Phys. Chem. C* **2012**, *116* (36), 19342-19348.
69. Li, J.; Chen, W.; Zhao, H.; Zheng, X.; Wu, L.; Pan, H.; Zhu, J.; Chen, Y.; Lu, J., *J. Catal.* **2017**, *352*, 371-381.
70. Yuranov, I.; Kiwi-Minsker, L.; Buffat, P.; Renken, A., *Chem. Mater.* **2004**, *16* (5), 760-761.
71. van Rijn, R.; Balmes, O.; Resta, A.; Wermeille, D.; Westerström, R.; Gustafson, J.; Felici, R.; Lundgren, E.; Frenken, J. W. M., *Phys. Chem. Chem. Phys.* **2011**, *13* (29), 13167-13171.
72. Gao, F.; Wang, Y.; Cai, Y.; Goodman, D. W., *J. Phys. Chem. C* **2009**, *113* (1), 174-181.
73. van Rijn, R.; Balmes, O.; Felici, R.; Gustafson, J.; Wermeille, D.; Westerström, R.; Lundgren, E.; Frenken, J. W. M., *J. Phys. Chem. C* **2010**, *114* (14), 6875-6876.
74. Wang, H.; Liu, C.-j., *Appl. Catal. B* **2011**, *106* (3), 672-680.
75. Toyoshima, R.; Yoshida, M.; Monya, Y.; Kousa, Y.; Suzuki, K.; Abe, H.; Mun, B. S.; Mase, K.; Amemiya, K.; Kondoh, H., *J. Phys. Chem. C* **2012**, *116* (35), 18691-18697.
76. Gulyaev, R. V.; Slavinskaya, E. M.; Novopashin, S. A.; Smovzh, D. V.; Zaikovskii, A. V.; Osadchii, D. Y.; Bulavchenko, O. A.; Korenev, S. V.; Boronin, A. I., *Appl. Catal. B* **2014**, *147*, 132-143.
77. Slavinskaya, E. M.; Gulyaev, R. V.; Zadesenets, A. V.; Stonkus, O. A.; Zaikovskii, V. I.; Shubin, Y. V.; Korenev, S. V.; Boronin, A. I., *Appl. Catal. B* **2015**, *166-167*, 91-103.
78. Johnson, R. S.; DeLaRiva, A.; Ashbacher, V.; Halevi, B.; Villanueva, C. J.; Smith, G. K.; Lin, S.; Datye, A. K.; Guo, H., *Phys. Chem. Chem. Phys.* **2013**, *15* (20), 7768-7776.
79. Chen, B.-R.; Crosby, L. A.; George, C.; Kennedy, R. M.; Schweitzer, N. M.; Wen, J.; Van Duyne R. P.; Stair, P. C.; Poepelmeier, K. R.; Marks, L. D.; Bedzyk, M. J., *ACS Catal.* **2018**, *8* (6), 4751-4760.
80. Kunz, S.; Schweinberger, F. F.; Habibpour, V.; Röttgen, M.; Harding, C.; Arenz, M.; Heiz,

- U., *J. Phys. Chem. C* **2010**, *114* (3), 1651-1654.
81. Xu, Y.; Ma, J.; Xu, Y.; Xu, L.; Xu, L.; Li, H.; Li, H., *RSC Adv.* **2013**, *3* (3), 851-858.
82. Meusel, I.; Hoffmann, J.; Hartmann, J.; Libuda, J.; Freund, H. J., *J. Phys. Chem. B* **2001**, *105* (17), 3567-3576.
83. Cao, S.; Tao, F.; Tang, Y.; Li, Y.; Yu, J., *Chem. Soc. Rev.* **2016**, *45* (17), 4747-4765.
84. Schalow, T.; Brandt, B.; Starr, D. E.; Laurin, M.; Shaikhutdinov, S. K.; Schauermaun, S.; Libuda, J.; Freund, H.-J., *Angew. Chem. Int. Ed.* **2006**, *45* (22), 3693-3697.
85. Penner, S.; Wang, D.; Jenewein, B.; Gabasch, H.; Klötzer, B.; Knop-Gericke, A.; Schlögl, R.; Hayek, K., *J. Chem. Phys.* **2006**, *125* (9), 094703.

## **CHAPTER-4**

**A Templated Approach for the Synthesis of Mesoporous  
Titanosilicates as support for gold nanoparticles for H<sub>2</sub>O<sub>2</sub>  
Mediated Olefin Epoxidation**



#### **4.1 Introduction**

Since the discovery of titanium silicalite-1 (TS-1) in 1983, titanium containing zeolites have gained much attention due to their application in selective oxidation of a wide variety of organic molecules.<sup>1,2</sup> Since then various Ti-containing zeolites with different structural and geometrical location of Ti ions in the silicalite structure have been discovered and their physical and chemical properties have been thoroughly investigated.<sup>2</sup> Among all the mentioned titanium silicalites (also known as titanosilicates) TS-1 is one of the earliest discovery where  $Ti^{4+}$  occupied the framework position in the silicalite in mostly tetrahedral coordination and possessed remarkable activity for the selective oxidation in the presence of  $H_2O_2$ . Among various selective oxidation, olefins epoxidation in the presence of  $H_2O_2$  is important because the epoxides are frequently used in organic synthesis and polymer industries.<sup>3</sup> Also use of  $H_2O_2$  over other organic oxidants is preferred because the byproduct formed is always water. But the main drawback of TS-1 is their micro porosity which restricts their use for the oxidation of bulky molecules. Several attempts have been made to increase the mesoporosity of these titanosilicates such as incorporating  $Ti^{4+}$  ions into the framework of mesoporous silica such as MCM-41, SBA-15, MCM-48 and grafting of titanocene complex on the surface of mesoporous silica.<sup>4</sup> These mesoporous titanium modified silica materials having pore diameter in the range of 3-7 nm can efficiently oxidize bulky organic molecules without any diffusion restrictions.<sup>5-10</sup> However their oxidation capabilities and hydrothermal stability is far below when compared with the TS-1 restricting their use for practical applications. The relatively low activity of these mesoporous Ti modified silica originates due to the different coordination of  $Ti^{4+}$  ions in silica framework. For a better activity in terms of conversion and selectivity, Ti in tetrahedral coordination is preferred over octahedral because of stability of  $H_2O_2$ .  $H_2O_2$  can easily decompose to water if not stabilized under the reaction conditions and results in formation of undesired products. Stabilization of  $H_2O_2$  over tetrahedral titanium is facile as compared to octahedral titanium thus making them preferable sites for selective epoxidation. Thus it is highly desirable to maintain the mesoporosity as well as tetrahedral titanium coordination to obtain an active and selective catalyst which can catalyze a wide range of olefins. The most commonly used titanium precursors for the synthesis of titanosilicate are alkoxide precursor which are highly hygroscopic and can self hydrolyze in open atmosphere hence results in undesirable coordination of titanium in silica and ultimately affects the catalytic activity. Modification of titanium precursor with some chelating agents which can prevent their self hydrolysis have

been reported and found to be efficient.<sup>8,11,12</sup> Post grafting titanium precursor on silica is another route for the synthesis of titanosilicate.<sup>13,14</sup> In the present chapter a templated approach using triethanol amine (TEA) as the structure directing agent as well as modifier for titanium precursor has been used for the synthesis of mesoporous titanosilicate nanospheres. CTAC (Cetyl trimethylammonium chloride) has been used as surfactant. Using this procedure titanosilicates nanospheres of size 100-200 nm were obtained with high mesoporosity. TEA, a poly alcohol has been known for its chelating properties which were utilized for the chelation of silica as well as titanium precursor.<sup>15</sup> Complexation of TEA with titanium precursor could modify the precursor and helped to reduce the rate of its hydrolysis. TEA acted both as the chelating agent as well as base for the hydrolysis and condensation of the precursors which are the characteristics features of a typical sol gel process. Thus synthesized mesoporous titanosilicate nanospheres were tested for the liquid phase olefin epoxidation of both light as well as bulky olefins. Moreover, to explore their catalytic activity for gas phase epoxidation gold was supported on these nanospheres and tested for propene epoxidation in the presence of molecular H<sub>2</sub> and O<sub>2</sub>. As already discussed in Chapter 2, role of gold here is to *insitu* generate H<sub>2</sub>O<sub>2</sub> which is transferred to the titanium in the close vicinity of gold to carry out propene epoxidation. Different molar ratio of Si/Ti was synthesized and their effect on the catalytic activity has been studied in this chapter.

## **4.2 Experimental Section**

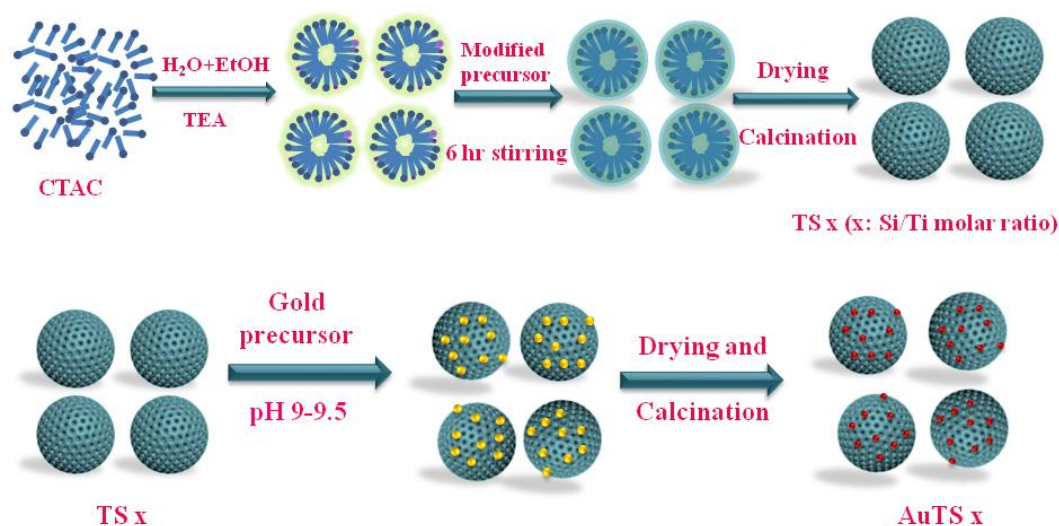
### **4.2.1 Synthesis of titanosilicate nanospheres**

The titanosilicate nanospheres were synthesized by template approach. Firstly 3 mL of TEOS was added to a glass vial and to this required amount of titanium tetrabutoxide (for Si/Ti molar ratio 150, 100 and 50) was added under vigorous stirring. After stirring for 15 min, 500  $\mu$ L of TEA and water were added and stirred for another 30 min. Meanwhile in a 250 mL round bottom flask, 2 gm of CTAC was dissolved in a water ethanol mixture having a volume ratio of 2.5 under moderate stirring. To this solution 2 mL of TEA was added as base to initiate the hydrolysis and condensation of precursors. After this the modified precursor was added drop wise and stirred for another 6 hr. The as synthesized titanosilicate nanospheres were collected by centrifugation and washed with water and ethanol and dried at 70 °C. Finally the powder was calcined at 600 °C for 10 h. Three different catalysts were synthesized and depending upon their Si/Ti molar ratio they were designated as TS-50, TS-100 and TS-150. To compare the effect of base other than TEA on the morphology and

nature of titanium,  $\text{NH}_3$  was used instead of TEA while the precursor was synthesized in the same way and denoted as TS 100 N.

#### 4.2.2 Synthesis of Au NPs supported Titanosilicate Nanospheres

0.2 wt% gold was loaded on titanosilicate spheres using deposition precipitation method as reported previously.<sup>16</sup> Typically 450 mg of the titanosilicate nanospheres were dispersed in 30 mL water. The pH of this support solution was maintained at 9.5 and gold precursor ( $\text{HAuCl}_4$  in 30% HCl, 7  $\mu\text{L}$  in 25 mL water) was added drop wise to the support solution while maintaining the pH. After complete addition of gold precursor, the mixture was further stirred for another 1 hr. The solid catalyst was collected by centrifugation, dried and calcined at 350 °C for 4 hr. The final catalyst is designated as AuTS x where x represents the Si/Ti ratio. The synthesis steps have been summarized in scheme 4.1



Scheme 4.1 Synthesis of mesoporous (gold supported) titanosilicate nanospheres.

#### 4.2.3 Catalyst Characterization

UV-visible analysis was performed on Shimadzu 2700 spectrophotometer with a dual beam source of He lamp and tungsten lamp as UV and visible light source respectively. Liquid UV was done using water as the reference. DRUV analysis was done for powder samples using dual beam source equipped with a diffuse reflectance attachment by taking  $\text{BaSO}_4$  as the standard. Powder X-ray Diffraction was recorded on Rigaku D MAX with a  $\text{Cu K}\alpha$  source of wavelength 1.54 Å with an operational voltage of 40 mV and 15 mA current.  $\text{N}_2$  adsorption/desorption analysis was done using Autosorb 1C Quantachrome, USA. The sample was first

degassed at 300 °C for 3 hr. After degassing the samples were cooled down to room temperature and analysis was done by adsorbing/ desorbing liquid N<sub>2</sub> at different pressures. The surface area was calculated by BET model. Pore size distribution was calculated using BJH method. TEM analysis was carried out by TECHNAI FEI instrument working at voltage of 200kV with LaB<sub>6</sub> as the filament. The samples for TEM analysis were prepared in ethanol and dried completely before analysis. IR analysis was performed on Bruker Tensor 27 FTIR spectrophotometer using KBr as the standard. KBr pellets were prepared by mixing KBr and sample in 100:1 ratio. XPS measurements were carried out using Thermo Kalpha+ spectrometer using micro focused and monochromated Al K $\alpha$  radiation with energy 1486.6 eV. The pass energy for spectral acquisition was kept at 50 eV for individual core-levels. The electron flood gun was utilized for providing charge compensation during data acquisition. The peak fitting of the individual core-levels was done using XPSpeak 41 software with a Shirley type background.

#### **4.2.4 Catalytic screening for liquid and gas phase olefin epoxidation**

The liquid phase olefin epoxidation was carried out in a two necked round bottom flask by attaching one neck to the condenser and sealing the other neck with rubber septum for addition of oxidant. Typically 25 mg of the catalyst was mixed with 5 mL of acetonitrile (solvent) and 2.5 mmol of olefin and kept in the oil bath already set at 60 °C. The mixture was stirred at this temperature for 15-20 min so as to maintain the temperature. After this, 2.5 mmol H<sub>2</sub>O<sub>2</sub> (30%) was injected slowly under stirring. The reaction mixture was taken out injected at certain time intervals to obtain the conversion and selectivity. The reactant and products were analyzed by GC analysis equipped with FID and capillary column.

Gas phase propene epoxidation reaction in the presence of molecular H<sub>2</sub> and O<sub>2</sub> were conducted in Technical University of Eindhoven, The Netherlands. Catalytic tests were performed at atmospheric pressure in a fix bed reactor. In a typical test, 150 mg of catalyst was loaded in a quartz reactor with inner diameter 6 mm and placed in a tubular oven. The flow of the reactant gases was adjusted to 25 ml/min (with a ratio of 1H<sub>2</sub>: 1O<sub>2</sub>: 1C<sub>3</sub>H<sub>6</sub>: 7Ar) with a GHSV of 10,000 ml/g<sub>cat</sub>/h. A typical reaction cycle was 5 h followed by regeneration step in the presence of 10 vol% O<sub>2</sub> in He at 573 K for 1 h. The reaction cycles were carried out in the temperature range 423-493 K and rate of each cycle was calculated as the average rate for the reaction performed between 150

min to 300 min on time stream. The propylene conversion and selectivity to PO were expressed as:

$$\text{Conversion (\%)} = [\text{moles of (products)}/\text{moles of propene in feed}] \times 100$$

$$\text{Selectivity (\%)} = [\text{moles of PO}/\text{moles of (products)}] \times 100$$

H<sub>2</sub> efficiency was calculated as:

$$\text{H}_2(\%) = [r_{\text{PO}}/(r_{\text{PO}}+r_{\text{H}_2\text{O}})] \times 100$$

where  $r_{\text{PO}}$  and  $r_{\text{H}_2\text{O}}$  were rates of PO and H<sub>2</sub>O produced respectively.

### 4.3 Results and Discussions

#### 4.3.1 UV-Visible (DRUV) Spectroscopy

UV-visible spectroscopy has been used as the initial tool to investigate the coordination of titanium species in silica. UV-visible spectrum of synthesized titanosilicate nanospheres was compared with the standard TS-1 (as shown in Figure 4.1a). It is clear from the figure that standard TS-1 showed a single peak at 220 nm which corresponds to the isolated tetrahedral titanium present in the silica lattice originating from O<sup>2-</sup> to Ti<sup>4+</sup> ligand to metal charge transfer.<sup>17,18</sup>

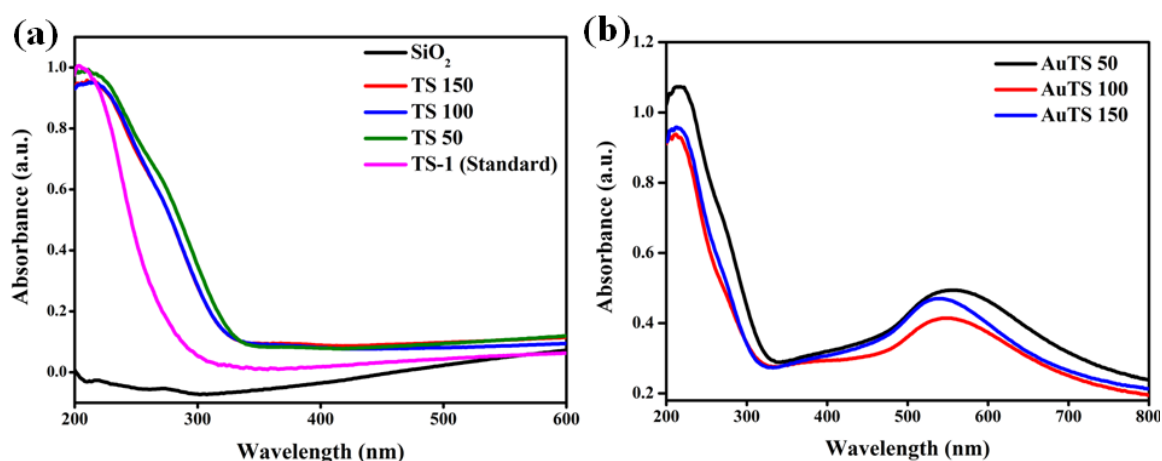


Figure 4.1 UV-visible spectra of (a) TS x and (b) AuTS x catalysts

The peak corresponding to octahedral titanium resulting either from hydroxylation or small Ti-O-Ti domains as extra framework species was absent in TS-1. Hence titanium in TS-1 (standard) was present as perfect isolated tetrahedral species. But in the synthesized

titanosilicate nanospheres two bands were present: one at 220 nm and another at around 270 nm indicating the presence of both tetrahedral as well octahedral coordinated titanium.<sup>18</sup> However the band at 220 nm was most intense and TS 50 showed slightly broader band at 270 nm which was due to increased amount of titanium in this sample. After gold deposition these samples showed similar bands of titanium but with an extra band between 500-600 nm typically for SPR of gold NPs (Figure 4.1b). The SPR band of Au NPs showed red shift as the amount of titanium increased indicating that size of Au NPs also increased with increased titanium content. However it was noted that the titanium bands were narrow after gold deposition which could be due to removal of some of the extra framework species under basic conditions. This kind of behavior has been reported on Ti-SBA-15 catalysts where treatment with ammonium ions could form tetrahedral titanium without formation of extra framework species.<sup>19,20</sup> However the effect was not pronounced in AuTS 50 where titanium content was more. This could be because the dissolution of extra framework titanium is possible using above mentioned methods however if small titania domain are formed these cannot be recrystallized or removed. Thus some phase segregation might have happened with an increase in titanium content.

### 4.3.2 X-ray Diffraction

The XRD analysis of titanosilicate nanospheres with and without Au NPs showed peak at 23° for amorphous silica as the major peak (Figure 4.2).

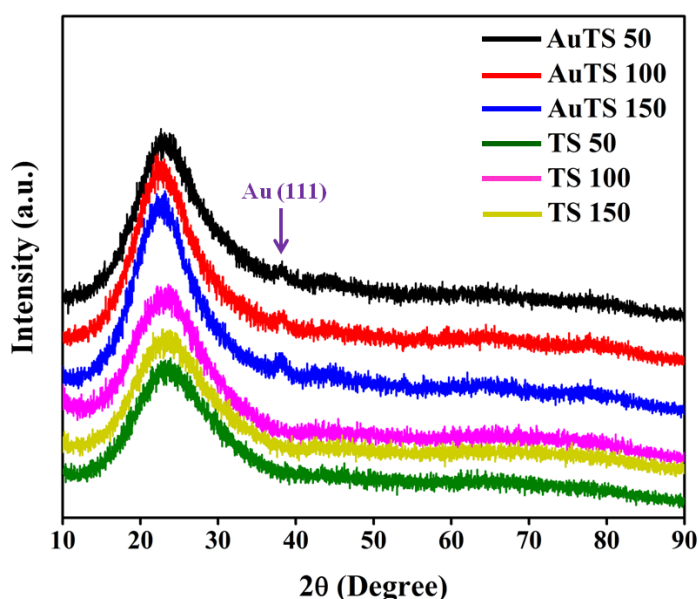


Figure 4.2 XRD analysis of TS and AuTS x catalysts

Any reflection for phase segregated titania was observed in none of the samples. For AuTS samples a feeble reflection at  $38.2^\circ$  was observed for Au (111) plane of metallic gold. The weak intensity for Au reflection can be attributed to the very small gold loading (0.2%).

### 4.3.3 N<sub>2</sub> Porosimetry

The surface analysis by N<sub>2</sub> adsorption-desorption analysis showed type IV isotherm for filling of mesopores (Figure 4.3). The textural properties of all these catalysts have been tabulated in Table 4.1. All the catalysts showed very high surface area and surface area decreased with an increase in the titanium content. Among all the catalysts TS 100 N showed the least surface area because TEA was not used for the synthesis of this catalyst which shows that TEA acted as pore generating agent also. However the surface area for this catalyst was still comparable to other TS catalysts. The pore diameter for all the catalyst was in the range of 3-4 nm indicating their mesoporosity with TS 150 showing maximum in the lot. This kind of pore extension was observed for Au@Ti-SiO<sub>2</sub> catalysts in Chapter 2 due to difference in the ionic radii of Si<sup>4+</sup> and Ti<sup>4+</sup>. Replacement of some of the Si<sup>4+</sup> ions with Ti<sup>4+</sup> ions resulted in pore enlargement. However by further increasing the titanium content pore size decreased and maintained the size of 3.3 nm.

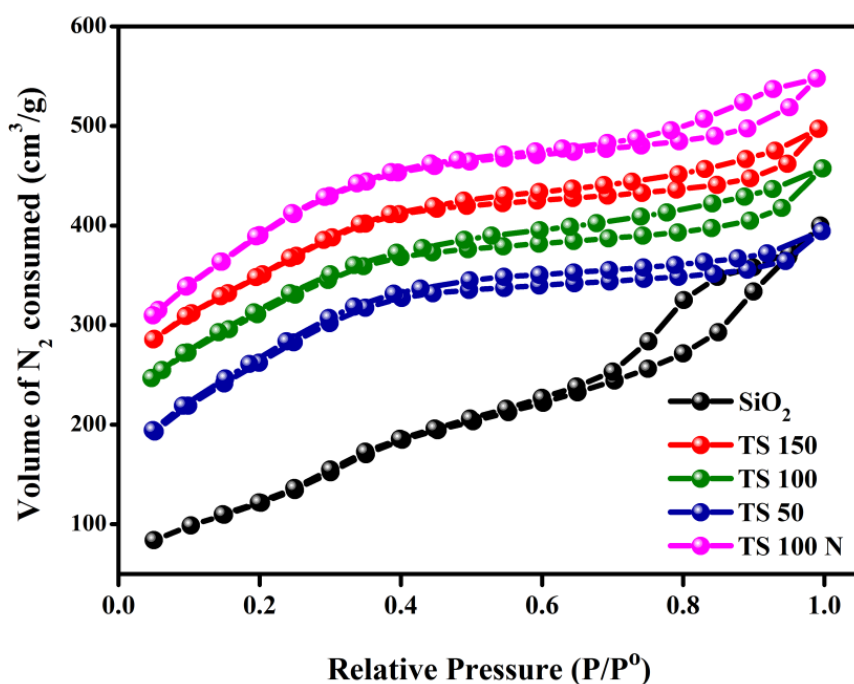


Figure 4.3 N<sub>2</sub> adsorption-desorption isotherms of TS-x catalysts compared with silica alone.

| S.No. | Catalyst         | Surface Area (m <sup>2</sup> /g) | Pore Diameter (nm) | Pore volume (cm <sup>3</sup> /g) |
|-------|------------------|----------------------------------|--------------------|----------------------------------|
| 1.    | SiO <sub>2</sub> | 988                              | 3.3                | 0.665                            |
| 2.    | TS 150           | 977                              | 3.8                | 0.637                            |
| 3.    | TS 100           | 901                              | 3.2                | 0.619                            |
| 4.    | TS 50            | 868                              | 3.3                | 0.600                            |
| 5.    | TS 100 N         | 800                              | 3.3                | 0.543                            |

Table 4.1 Textural properties of titanosilicate nanospheres.

#### 4.3.3 Scanning Electron Microscopy (SEM)

The morphology of synthesized titanosilicate catalysts was analyzed by SEM and it was found that those synthesized using TEA as the base showed spherical morphology while use of NH<sub>3</sub> as the base resulted in complete destruction of morphology. The SEM images can be seen in Figure 4.4.

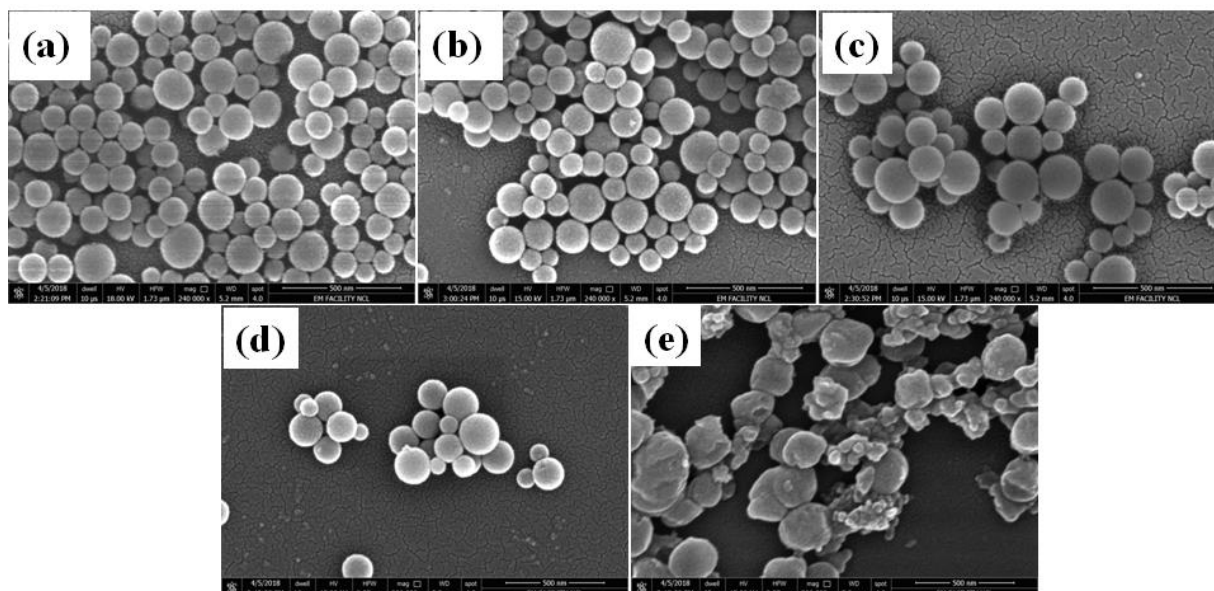


Figure 4.4 SEM images of (a) SiO<sub>2</sub> Nanospheres (b) TS-150 (c) TS-100 (d) TS 50 and (e) TS-100 N. Scale Bar: 500 nm.



It is clear from the SEM images that TEA played important role in obtaining spherical morphology which was not the case with  $\text{NH}_3$ . This is because of complexation of alkoxide precursor of silica with TEA which forms silatranes. This complex hydrolyzes very slowly in the aqueous medium as compared to the untreated alkoxide precursor.<sup>15</sup> This delay in the hydrolysis can provide sufficient time for the arrangement of small nuclei in a spherical manner which provides a spherical morphology. However when  $\text{NH}_3$  was used as the base, rapid hydrolysis occurred which resulted in the destruction of the morphology. This is the reason why titanosilicates synthesized using TEA showed spherical morphology while the one which was synthesized using  $\text{NH}_3$  (TS 100 N) showed irregular shape.

#### 4.3.4 Transmission Electron Microscopy (TEM)

It was clear from the SEM images that TS-x catalysts showed spherical morphology. Their 2D morphology including their mesoporosity and Au NPs size in AuTS x catalysts were further probed using TEM analysis. Figure 4.5 shows the TEM images of TS and AuTS x catalysts along with TS 100 N catalyst. All the catalysts showed highly mesoporous titanosilicate spheres with worm hole kind of pores. This pore morphology was obtained because of using CTAC as the surfactant which generates this kind of pores in the material.

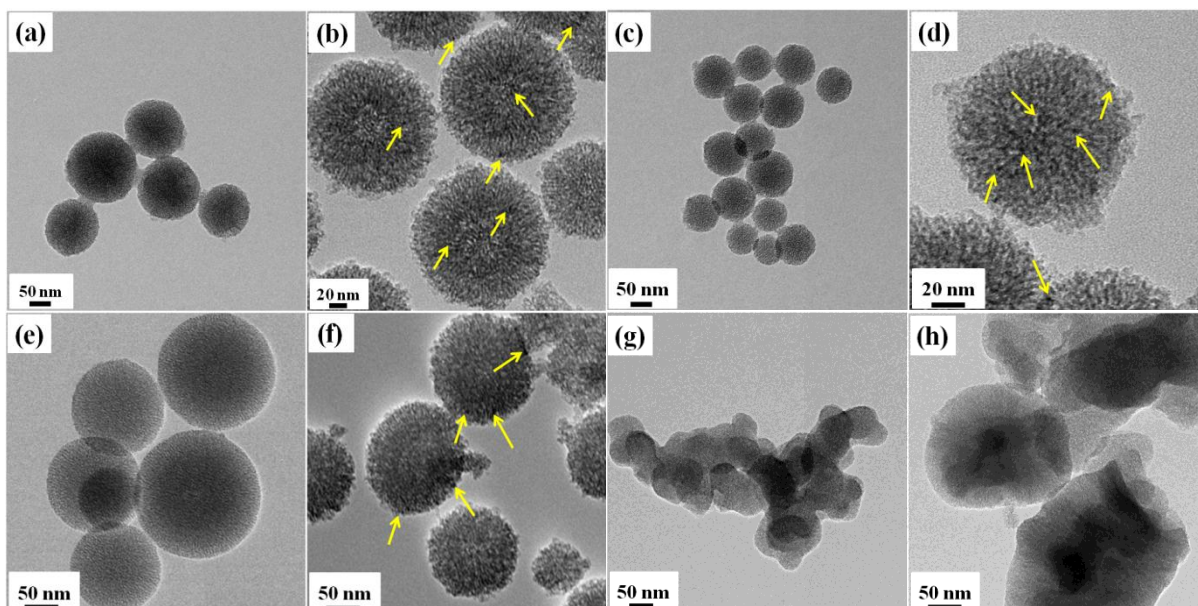


Figure 4.5 TEM images of (a) TS 150 (b) AuTS 150 (c) TS 100 (d) AuTS 100 (e) TS 50 (f) AuTS 50 (g, h) TS 100 N. Yellow arrows in (b, d and f) show Au NPs.

TEM images of AuTS catalysts showed that size of gold NPs was very small in the range of 2-3 nm (marked as yellow arrow). Since the loading of gold was very low and size of the NPs was very small it was difficult to get clear image of Au NPs. TS 100 N catalyst showed random morphology with low mesoporosity. Thus TEA played a bifunctional role by providing spherical shape as well as mesoporosity to the TS and AuTS x catalysts.

#### 4.3.5 Infra-red Spectroscopy

Incorporation of titanium in silica framework can also be probed using IR spectroscopy. The band at  $960\text{ cm}^{-1}$  corresponding to Si-O(X) stretching vibrations where X is H or any other heteroatom, can be seen.<sup>8,21</sup> In the present case also transmittance band at around  $960\text{ cm}^{-1}$  was observed intensity of which increased after titanium incorporation (Figure 4.6). Bare silica showed negligible intensity of this band while TS-x samples showed well observed intensity which indicated incorporation of titanium in silica framework. However the exact coordination cannot be traced using IR spectroscopy. The other bands at  $800\text{ cm}^{-1}$  and  $1060\text{ cm}^{-1}$  can also be seen which originated from the symmetric as well as asymmetric vibrations of Si-O-Si bonds respectively.

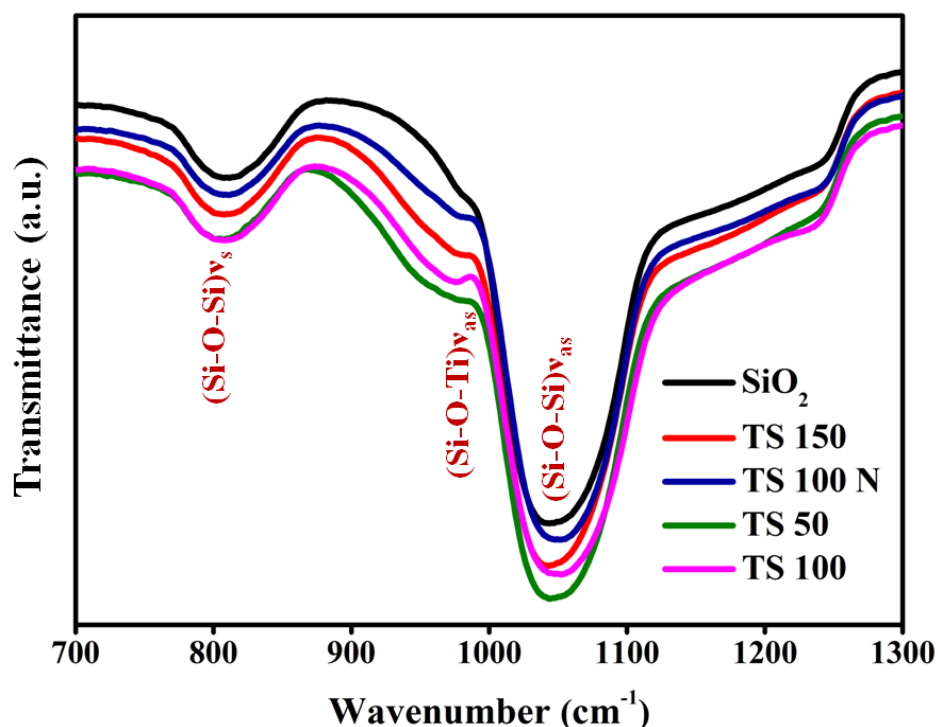


Figure 4.6 IR spectra of TS x catalysts compared with SiO<sub>2</sub> and TS 100 N.

### 4.3.6 X-ray Photoelectron Spectroscopy

XPS analysis of titania-silica mixed oxides usually points towards a linear relationship between surface and bulk composition below 15 wt% Ti incorporation where both surface and bulk show similar titanium nature and beyond 15 wt% surface enrichment in silica is occupied mostly by titanium showing features mostly from bulk titania.<sup>12</sup> This surface enrichment can be attributed to the different reactivity of titanium and silica alkoxide precursor in sol gel synthesis due to different hydrolysis and condensation rates. The higher hydrolysis rate of titanium alkoxide precursor during synthesis forms the titanium rich cores with Si rich shell instead of incorporation of titanium in silica framework which results in phase segregation of TiO<sub>2</sub>. But this effect was minimized in present case due to complexation of titanium precursor with TEA which slowed down the hydrolysis rate of this complex during synthesis and resulted in incorporation of titanium in silica matrix. Coordination of titanium in tetrahedral or octahedral way can be found out using XPS as the binding energies for both the coordinations are different. Pure titania shows binding energy at 458.7 eV while tetrahedrally coordinated isolated Ti centers in silica show peak towards higher binding with a shift of 1-1.5 eV with respect to titania.<sup>12,22</sup> Extra framework octahedral titanium shows binding energy between pure titania and tetrahedral titanium incorporated in silica. XPS spectra of different TS x catalysts can be seen in Figure 4.7.

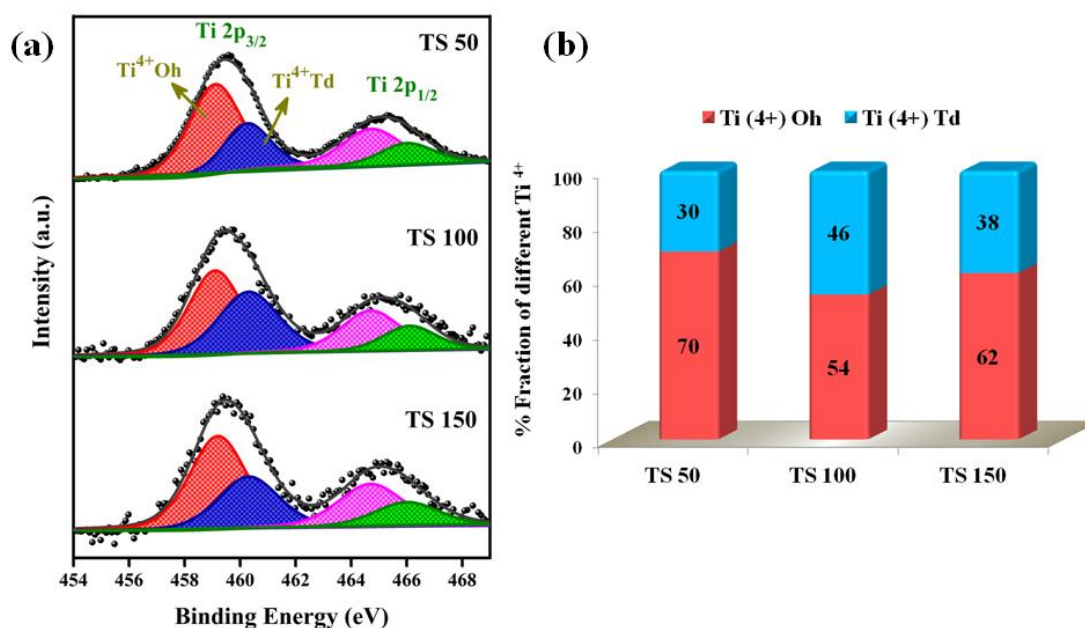


Figure 4.7 (a) Ti 2p XPS spectra of TS x catalysts (b) relative fraction of different titanium species present in different catalysts.

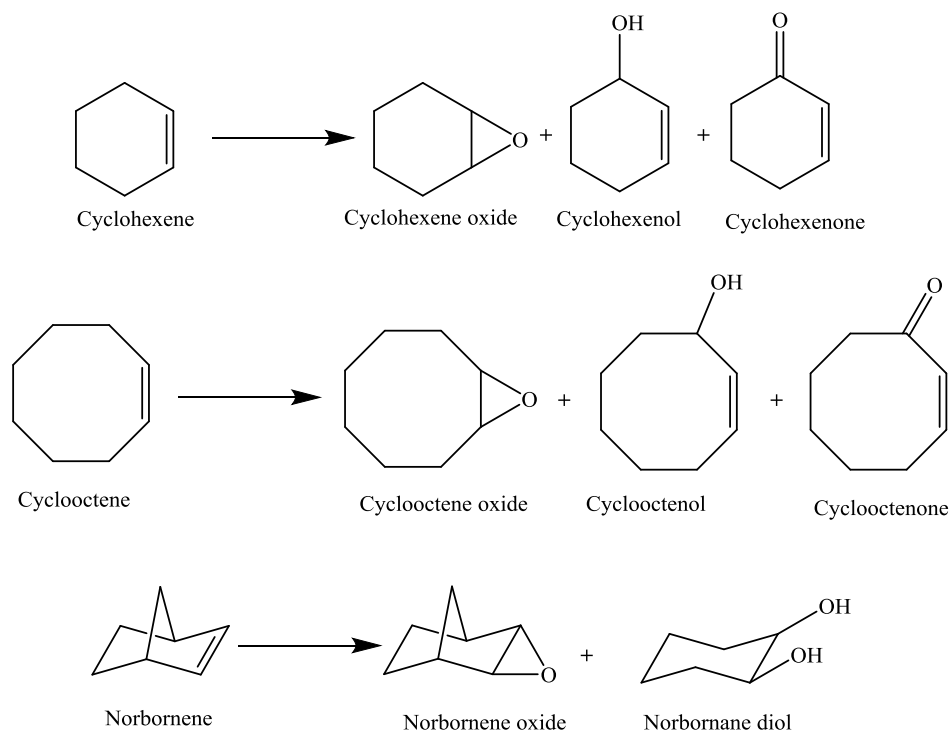
It can be seen from the figure that presence of bulk titania was absent in all the catalysts and peaks corresponding to octahedral and tetrahedral coordinated titanium in silica were present. The relative fraction of these species in Figure 4.7b showed that TS 100 showed almost half of the Ti species as tetrahedrally coordinated isolated Ti centers while TS 50 showed minimum amount of these species. This indicates towards the formation of octahedrally coordinated titanium as extra framework species in silica when amount of titanium increased in TS 50. Similar observation was obtained from UV analysis also where the band at 270 nm showed broadening for this catalyst. This behavior of different catalysts played important role in catalytic activity.

#### 4.3.7 Catalytic Activity for Olefin Epoxidation

The synthesized catalytic materials were tested for olefin epoxidation in liquid as well as gas phase. The reaction conditions have already been discussed in experimental section for gas phase and liquid phase epoxidation.

##### 4.3.7.1 Liquid phase olefin epoxidation

Olefin epoxidation in the liquid phase was carried for cyclohexene, cyclooctene and norbornene as light and bulky olefins respectively over TS-x catalysts. The activity results have been tabulated in Table 4.2.



| S.No. | Catalyst         | Substrate   | Oxidant                       | X <sub>olefin</sub> | S <sub>epoxide</sub> | S <sub>others</sub> |
|-------|------------------|-------------|-------------------------------|---------------------|----------------------|---------------------|
| 1.    | Blank            | Cyclohexene | H <sub>2</sub> O <sub>2</sub> | No                  | -                    | -                   |
| 2.    | SiO <sub>2</sub> | Cyclohexene | H <sub>2</sub> O <sub>2</sub> | -                   | -                    | -                   |
| 3.    | TS 150           | Cyclohexene | H <sub>2</sub> O <sub>2</sub> | 24                  | 32                   | 68                  |
| 4.    | TS 100           | Cyclohexene | H <sub>2</sub> O <sub>2</sub> | 24                  | 63                   | 37                  |
| 5.    | TS 50            | Cyclohexene | H <sub>2</sub> O <sub>2</sub> | 20                  | 61                   | 39                  |
| 6.    | TS 100 N         | Cyclohexene | H <sub>2</sub> O <sub>2</sub> | 28                  | 28                   | 72                  |
| 7.    | TS-1             | Cyclohexene | H <sub>2</sub> O <sub>2</sub> | 25                  | 85                   | 15                  |
| 8.    | TS 150           | Cyclooctene | H <sub>2</sub> O <sub>2</sub> | 22                  | 98                   | 2                   |
| 9.    | TS 100           | Cyclooctene | H <sub>2</sub> O <sub>2</sub> | 27                  | 100                  | -                   |
| 10.   | TS 50            | Cyclooctene | H <sub>2</sub> O <sub>2</sub> | 25                  | 100                  | -                   |
| 11.   | TS 100 N         | Cyclooctene | H <sub>2</sub> O <sub>2</sub> | 16                  | 97                   | 3                   |
| 12.   | TS-1             | Cyclooctene | H <sub>2</sub> O <sub>2</sub> | 8                   | 100                  | -                   |
| 13.   | TS 150           | Norbornene  | H <sub>2</sub> O <sub>2</sub> | 15                  | 100                  | -                   |
| 14.   | TS 100           | Norbornene  | H <sub>2</sub> O <sub>2</sub> | 20                  | 100                  | -                   |
| 15.   | TS 50            | Norbornene  | H <sub>2</sub> O <sub>2</sub> | 19                  | 98                   | 2                   |
| 16.   | TS 100 N         | Norbornene  | H <sub>2</sub> O <sub>2</sub> | 12                  | 98                   | 2                   |
| 17.   | TS-1             | Norbornene  | H <sub>2</sub> O <sub>2</sub> | 7                   | 100                  | -                   |
| 18.   | TS 100           | Cyclohexene | TBHP                          | 31                  | 42                   | 58                  |
| 19.   | TS 100           | Cyclooctene | TBHP                          | 25                  | 95                   | 5                   |
| 20.   | TS 100           | Norbornene  | TBHP                          | 26                  | 98                   | 2                   |

Table 4.2 Olefin epoxidation results over TS x catalyst. Time: 4hr for cyclohexene and 6 hr for cyclooctene and norbornene, Temperature: 60 °C, X<sub>olefin</sub>: % conversion of olefin, S<sub>epoxide</sub>: % selectivity of epoxide, S<sub>others</sub>: % selectivity of other products which include enol, enone and diol. TS-1 used was commercial titanosilicate with Si/Ti ratio 100.

The activity results for the liquid phase epoxidation of three different olefins showed that TS 100 catalyst performed best among all the catalysts. For cyclohexene oxidation for all the Ti incorporated catalysts showed similar activity but epoxide selectivity was exceptional for TS-1 which was obvious since TS-1 is known to show very high selectivity for cyclohexene oxide due to presence of isolated tetrahedral titanium centers. However for bulky olefins like cyclooctene and norbornene TS-1 showed very low conversion due to micro porosity of this catalyst which imposed diffusion limitations. TS 100 N catalyst showed similar conversion for cyclohexene as that of TS 100 but selectivity for epoxide was very low.

The XPS analysis performed on TS x catalysts showed maximum amount of tetrahedral titanium (46%) in TS 100 which has been reflected in the catalytic activity for this catalyst. Presence of optimum amount of tetrahedral titanium with optimum mesoporosity in TS 100 catalyst made this catalyst most active. The effect of titanium coordination was not prominent for bulky olefins since they can form epoxide with more feasibility than lighter olefins. This is because of minimized ring strain in bulky olefins due to which all the catalysts showed more than 90% selectivity for cyclooctene and norbornene oxide. Effect of solvent was also examined for cyclohexene oxidation over TS 100 catalyst. Solvent scope was tested by carrying out the reaction in methanol as well as in dichloroethane apart from acetonitrile. In methanol conversion was higher as compared to acetonitrile (30%) but epoxide selectivity was negligible and diol was formed as the major product along with other products. In dichloroethane both conversion and selectivity were negligible. The selectivity difference for acetonitrile and methanol can be attributed to polarity difference of these solvents. For acetonitrile dielectric constant is 37.5 while for methanol it is 32.7 and the high dielectric constant resulted in enhanced selectivity of cyclohexene oxide. It is also known that acetonitrile can activate  $H_2O_2$  by forming peroxy-carboximidic acid intermediate which is a good oxygen transfer agent<sup>23</sup> hence results in better selectivity for epoxide. Use of TBHP as an oxidant did not show any pronounced effect in the catalytic activity however selectivity decreased for epoxides which shows the compatibility of these catalysts (TS x) with  $H_2O_2$  to show high epoxide selectivity. Thus liquid phase olefin oxidation results showed that TS 100 was the most active catalyst due to more amount of isolated titanium centers with appreciable mesoporosity. The catalytic activity of these catalysts was tested for gas phase propene epoxidation after supporting gold and discussed in next section.

#### 4.3.7.2 Gas phase Propene Oxidation

After supporting 0.2 wt% gold on TS x catalysts, their activity was tested for propene oxidation in gas phase in the presence of molecular  $O_2$  and  $H_2$ . Gold plays bifunctional role in propene epoxidation by generating  $H_2O_2$  insitu from  $H_2$  and  $O_2$  which then reacts with the titanium species present in the close proximity of gold to oxidize propene. The effect of titanium coordination is more critical in this case as compared to other discussed olefins due to small size of propene and high activity of allylic H present which can undergo oxidation and form undesired products. The size of gold NPs is also crucial as only Au NPs of 2-3 nm are considered to be active for  $H_2O_2$  production. The reaction conditions had already been

mentioned in the experimental section. The conversion for propene was always less than 1% for all the catalysts at all the temperatures tested. The low conversion of propene has always been a bottle neck problem in propene epoxidation. One reason is presence of low amount of active Ti centers as only a limited amount can be successfully incorporated in the silica matrix with tetrahedral coordinated Ti. Exceeding the limit results in the formation of extra framework titanium species which is detrimental for H<sub>2</sub>O<sub>2</sub> stability. Another probable reason is gold loading. Usually the gold loading for propene epoxidation are kept below 1 wt% because increase in the loading increases the gold NPs size also and for H<sub>2</sub>O<sub>2</sub> production Au NPs size should be below 5 nm specifically 2-3 nm. Also excess amount of gold may reside on silica which itself is the site for undesired product formation since these are the sites for decomposition of H<sub>2</sub>O<sub>2</sub> and hydrogenation of propene.<sup>24</sup> This is the reason that Au based catalysts have not been commercialized till present even though the selectivity for propene oxide (PO) is more than 90%.

The selectivity and yield of PO over AuTS x catalysts at 423 K can be seen in Figure 4.8. The selectivity plots for different catalysts showed formation of different oxygenates. Similar to liquid phase epoxidation gold supported TS 100 i.e. AuTS 100 catalyst showed the highest selectivity for propene oxide (77%) and least selectivity was obtained over AuTS 50 catalyst. As shown in UV and XPS spectra TS 100 showed the maximum amount of tetrahedrally coordinated isolated Ti centers with an optimum size of gold NPs. The % of tetrahedral Ti was 46 %, 36% and 30% for AuTS 100, AuTS 150 and AuTS 50 respectively which resulted in the PO selectivity in similar order.

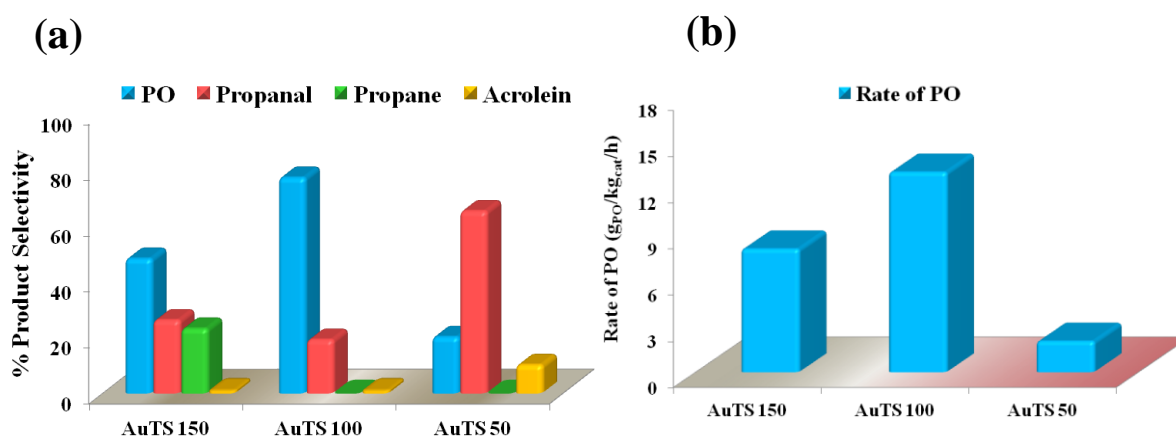


Figure 4.8 (a) Selectivity of different products and (b) yield of PO on AuTS x catalysts at 423 K.

The activity of Au/titanosilicate for propene oxidation strongly depends upon the synthesis procedure, gold loading and addition of different promoter. A summarized comparison of different Au/titanosilicate catalysts with best activity till present has been presented in the table below.

| Catalyst                               | Reaction temp (K) | GHSV (mL.g <sub>cat</sub> <sup>-1</sup> .h <sup>-1</sup> )* | % X <sub>propene</sub> | % S <sub>PO</sub> | STY <sub>PO</sub> <sup>#</sup> | Ref.      |
|--|-------------------|---|------------------------|-------------------|--------------------------------|-----------|
| 1 wt% Au/TiO <sub>2</sub>              | 323               | 4000  | 1.1                    | >99               | 12                             | 25        |
| 1 wt% Au/Ti-SiO <sub>2</sub>           | 398               | 6600  | 1.5                    | 80                | 10                             | 26        |
| 1 wt% Au/TS-1                          | 448               | 6600  | 1.5                    | 95                | 16                             | 26        |
| 0.3-0.4 wt% Au/mesoTi-SiO <sub>2</sub> | 423               | 4000  | 5-9.8                  | 90-95             | 130-150                        | 11        |
| 0.05 wt% Au/TS-1 (Si/Ti=36)            | 423               | 7000  | 8.8                    | 81                | 110                            | 27        |
| 0.25 wt% Au/Ti-SBA-15                  | 393               | 15000   | 1.17                   | 90                | 41                             | 28        |
| 0.25 wt% Au/TS-1 Alkali treated        | 473               | 8000  | 8.8                    | 82                | 137                            | 29        |
| 0.14 wt% Au/TS-1 Cs promoted           | 473               | 14000   | 11.4                   | 88                | 320                            | 30        |
| 0.1 wt% Au/Ti-SiO <sub>2</sub>         | 473               | 10000   | 4.6                    | 85                | 120                            | 31        |
| 0.13 wt% Au/meso TS-1                  | 473               | 14000   | 4.6                    | 95                | 140                            | 32        |
| Au-Ag/TS-1-B (blocked pores)           | 473               | 14000   | 4.5                    | 83                | 174                            | 33        |
| AuTS 100                               | 423               | 10000   | 0.64                   | 77                | 13                             | This work |

\*H<sub>2</sub>:O<sub>2</sub>:C<sub>3</sub>H<sub>6</sub>:inert= 10:10:10:70, # Space Time Yield of PO in g<sub>PO</sub>.kg<sub>cat</sub><sup>-1</sup>.h<sup>-1</sup>, % X<sub>propene</sub>= propene conversion, % S<sub>PO</sub>= PO selectivity

Table 4.3 Gas phase propene epoxidation with H<sub>2</sub> and O<sub>2</sub> over Au based catalysts.

The summary of important Au based catalysts for propene epoxidation in above table showed that conversion of propene has not crossed the value required for commercialization of Au based catalyst (>10%) even though the selectivity achieved is impressive (90-95%). Another difficulty to obtain high PO yield is small operational window of O<sub>2</sub> and H<sub>2</sub> ratio since these form highly explosive mixtures hence the ratio cannot be increased beyond a certain limit. Thus propene epoxidation using O<sub>2</sub> and H<sub>2</sub> over Au based catalyst is still a hard nut to crack.

As mentioned earlier that AuTS 100 in the present work showed best activity among all the screened catalysts however the yield of PO was still poor as compared to above mentioned catalysts. The behavior of this catalyst at different temperature has been summarized Table 4.4 and 4.5.



|   |                 |                 |                 |                 |                 |
|---|-----------------|-----------------|-----------------|-----------------|-----------------|
| <b>Temp. (K)</b>                                  | <b>403</b>      | <b>423</b>      | <b>453</b>      | <b>473</b>      | <b>423</b>      |
| <b>% Conversion</b>                               | <b>0.44</b>     | <b>0.64</b>     | <b>1.15</b>     | <b>1.67</b>     | <b>0.59</b>     |
| <b>% Selectivity</b>                              | <b>81</b>       | <b>77</b>       | <b>57</b>       | <b>33</b>       | <b>75</b>       |
| <b>Yield</b>                                      | <b>0.36</b>     | <b>0.49</b>     | <b>0.65</b>     | <b>0.55</b>     | <b>0.44</b>     |
| <b>% H<sub>2</sub> Efficiency</b>                 | <b>9.69</b>     | <b>7.51</b>     | <b>4.75</b>     | <b>2.54</b>     | <b>7.51</b>     |
| <b>Av.H<sub>2</sub>O rate<br/>(mol/(g.cat*s))</b> | <b>4.12E-07</b> | <b>7.32E-07</b> | <b>1.60E-06</b> | <b>2.60E-06</b> | <b>6.72E-07</b> |
| <b>Av. PO rate<br/>(gPO/(kg.cat*h))</b>           | <b>9.23</b>     | <b>12.41</b>    | <b>16.70</b>    | <b>14.13</b>    | <b>11.40</b>    |

Table 4.4 Activity results of AuTS 100 catalyst at different temperatures.

|                                   |               |               |               |               |               |
|-----------------------------------|---------------|---------------|---------------|---------------|---------------|
| <b>Temp. (K)</b>                  | <b>403</b>    | <b>423</b>    | <b>453</b>    | <b>473</b>    | <b>423</b>    |
| <b>PO</b>                         | <b>80.49%</b> | <b>77%</b>    | <b>56.77%</b> | <b>33.17%</b> | <b>75.45%</b> |
| <b>Acetaldehyde</b>               | <b>1.35%</b>  | <b>1.15%</b>  | <b>2.97%</b>  | <b>4.40%</b>  | <b>1.69%</b>  |
| <b>Acrolein</b>                   | <b>0.53%</b>  | <b>0.88%</b>  | <b>2.77%</b>  | <b>4.31%</b>  | <b>1.29%</b>  |
| <b>Propanal</b>                   | <b>15.32%</b> | <b>18.91%</b> | <b>33.98%</b> | <b>51.29%</b> | <b>18.58%</b> |
| <b>C<sub>3</sub>H<sub>8</sub></b> | <b>0.00%</b>  | <b>0.00%</b>  | <b>0.00%</b>  | <b>0.00%</b>  | <b>0.00%</b>  |
| <b>Acetone</b>                    | <b>2.32%</b>  | <b>2.14%</b>  | <b>3.43%</b>  | <b>5.86%</b>  | <b>3.00%</b>  |

Table 4.5 Selectivity of AuTS 100 for different products at different temperatures

It can be seen from the Table 4.4 that as the temperature increased conversion also increased but selectivity towards PO decreased due to formation of other products. It is noteworthy that this catalyst did not show formation of any propane while AuTS 150 showed almost 30% of propane formation. Propane formation is facilitated over Au NPs of size less than 1 nm or more than 5 nm.<sup>34</sup> However TEM images showed Au NPs of size less than 5 nm. Thus the probable reason for propane formation could be interaction of some of the Au NPs with silica which was possible due to less titanium content. Au-silica interaction led to hydrogenation of propene instead of its oxidation.<sup>24</sup> AuTS 50 did not show any propane formation but it showed selectivity for propanal due to presence of extra framework titanium species. These species are highly acidic which are responsible for the formation of bidentate propoxy species from PO and form undesired products such as propanal and acetone.<sup>35</sup>

Deactivation of the catalyst has always been a problem in propene epoxidation and catalyst can deactivate severely within the 30 min of the reaction. However in the present case time on stream reaction performed on AuTS 100 catalyst for 5 h showed constant stability.

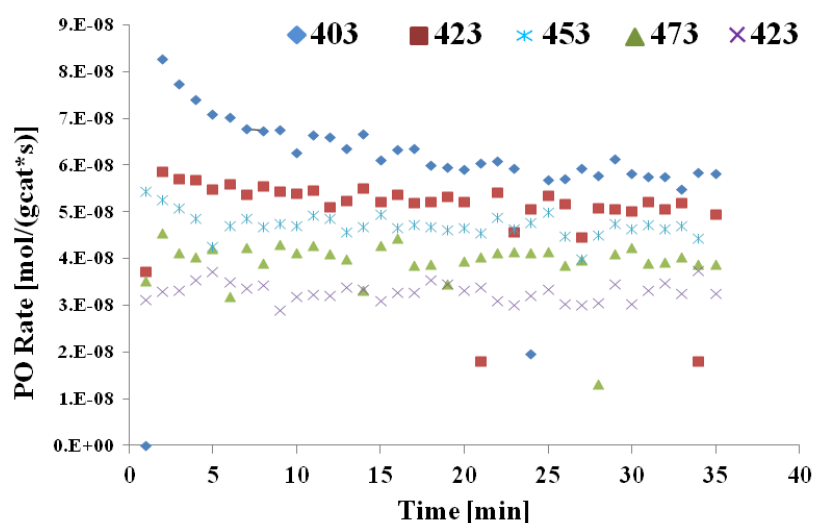


Figure 4.9 Stability test of AuTS 100 catalyst under reaction conditions at different temperatures.

A small deactivation was observed at initial 5-10 minutes at 403 K after which the stable activity was observed. At higher temperature the catalyst showed constant PO rate throughout the reaction time demonstrating the stability of the catalyst. The present propene epoxidation results showed that gold supported titanosilicate nanospheres possessed improved selectivity for PO than ATS catalysts as discussed in Chapter 2 though the conversions were still less than 1 wt%. Low loading of gold with small NPs along with presence of isolated tetrahedral titanium led to improved selectivity for PO. AuTS 100 showed the best activity among all AuTS x catalysts. AuTS 150 showed propane as the major by product due to low content of titanium and Au-SiO<sub>2</sub> interaction. Formation of propanal as the major product in AuTS 50 catalyst was attributed to presence of more amount of extra framework titanium species.

#### 4.4 Conclusion

Mesoporous titanosilicate nanospheres were synthesized using TEA as the modifier for silica and titanium precursor, base as well as structure directing agent to provide spherical morphology. The nanospheres were highly mesoporous with a pore size in the range of 3-3.3 nm. The liquid phase epoxidation of light and bulky olefins over these nanospheres showed that TS 100 was most active with almost 50% of tetrahedral titanium sites (as estimated from XPS) due to which high selectivity for respective epoxide was obtained over this catalyst. Gold supported nanospheres, AuTS x were screened for gas phase propene oxidation in the presence of O<sub>2</sub> and H<sub>2</sub>. For gas phase epoxidation also AuTS 100 catalyst showed best activity which can be attributed to close proximity of optimum less than 5 nm Au NPs with

isolated tetrahedral titanium centers. The comparison of PO production of this catalyst with reported Au based catalyst showed that AuTS x catalyst still requires modifications in terms of selective generation of active titanium centers so as to obtain a catalyst with high propene conversion and PO selectivity.

#### 4.5 References

1. M. Taramasso, G. P., B. Notari, U.S. Patent 4. **1983**, (410 501).
2. Knozinger, P. R. D. S. H., *Adv. Catal.* **2004**, *48*, 1-169.
3. Yudin, A. K., *Wiley-VCH Verlag GmbH & Co. KGaA, Weinheim* **2006**.
4. Xiao, F.-S.; Han, Y.; Yu, Y.; Meng, X.; Yang, M.; Wu, S., *J. Am. Chem. Soc.* **2002**, *124* (6), 888-889.
5. Kresge, C. T. L., M. E.; Roth, W. J.; Vartuli, J. C.; Beck, J. S., *Nature*, **1992**, , 352, 710-712.
6. Morey, M. S. O. B., S.; Schwarz, S.; Stucky, G. D., *Chem. Mater.*, **2000**, *12*, , 898.
7. Lin, T.-H.; Chen, C.-C.; Jang, L.-Y.; Lee, J.-F.; Cheng, S., *Micropor. Mesopor. Mat.* **2014**, *198*, 194-202.
8. Gupta, S.; Vinod, C. P.; Jagadeesan, D., *RSC Adv.* **2015**, *5* (112), 92371-92377.
9. Jiang, Y.; Zhao, Y.; Xu, X.; Lin, K.; Wang, D., *RSC Adv.* **2016**, *6* (81), 77481-77488.
10. Chen, L.-H.; Li, X.-Y.; Tian, G.; Li, Y.; Rooke, J. C.; Zhu, G.-S.; Qiu, S.-L.; Yang, X.-Y.; Su, B.-L., *Angew. Chem. Int. Ed.* **2011**, *50* (47), 11156-11161.
11. Sinha, A. K.; Seelan, S.; Tsubota, S.; Haruta, M., *Angew. Chem. Int. Ed.* **2004**, *43* (12), 1546-1548.
12. Sinha, A. K.; Seelan, S.; Okumura, M.; Akita, T.; Tsubota, S.; Haruta, M., *J. Phys. Chem. B* **2005**, *109* (9), 3956-3965.
13. Charbonneau, L.; Kaliaguine, S., *Appl. Catal. A* **2017**, *533*, 1-8.
14. Chang, C.-C.; Lee, J.-F.; Cheng, S., *J. Mater. Chem. A* **2017**, *5* (30), 15676-15687.
15. Möller, K.; Kobler, J.; Bein, T., *Adv. Funct. Mater.* **2007**, *17* (4), 605-612.
16. Kanungo, S.; Perez Ferrandez, D. M.; Neira d'Angelo, F.; Schouten, J. C.; Nijhuis, T. A., *J. Catal.* **2016**, *338*, 284-294.
17. Geobaldo, F.; Bordiga, S.; Zecchina, A.; Giamello, E.; Leofanti, G.; Petrini, G., *DRS Catal. Lett.* **1992**, *16* (1), 109-115.
18. Xiong, G.; Cao, Y.; Guo, Z.; Jia, Q.; Tian, F.; Liu, L., *Phys. Chem. Chem. Phys.* **2016**, *18* (1), 190-196.
19. Wang, Y.; Lin, M.; Tuel, A., *Micropor. Mesopor. Mat.* **2007**, *102* (1), 80-85.
20. Fan, W.; Duan, R.-G.; Yokoi, T.; Wu, P.; Kubota, Y.; Tatsumi, T., *J. Am. Chem. Soc.* **2008**, *130* (31), 10150-10164.
21. Alba, M. D.; Luan, Z.; Klinowski, J., *J. Phys. Chem.* **1996**, *100* (6), 2178-2182.
22. Moretti, G.; Salvi, A. M.; Guascito, M. R.; Langerame, F., *Surf. Inter. Anal.* **2004**, *36* (10), 1402-1412.
23. Ghosh, S.; Acharyya, S. S.; Sasaki, T.; Bal, R., *ACS Sustain. Chem. Eng.* **2015**, *3* (11), 2823-2830.
24. Naito, S.; Tanimoto, M., *Chem. Commun.* **1988**, (12), 832-833.
25. Hayashi, T.; Tanaka, K.; Haruta, M., *J. Catal.* **1998**, *178* (2), 566-575.
26. Nijhuis, T. A.; Huizinga, B. J.; Makkee, M.; Moulijn, J. A., *Ind. Eng. Chem. Res.* **1999**, *38* (3), 884-891.
27. Taylor, B.; Lauterbach, J.; Delgass, W. N., *Appl. Catal. A* **2005**, *291* (1), 188-198.

28. Liu, C.-H.; Guan, Y.; Hensen, E. J. M.; Lee, J.-F.; Yang, C.-M., *J. Catal.* **2011**, *282* (1), 94-102.
29. Huang, J.; Takei, T.; Akita, T.; *Appl. Catal. B* **2010**, *95* (3), 430-438.
30. Lee, W.-S.; Cem Akatay, M.; Stach, E. A.; Ribeiro, F. H.; Nicholas Delgass, W., *J. Catal.* **2013**, *308*, 98-113.
31. Chen, J.; Halin, S. J. A.; Pidko, E. A.; Verhoeven, M. W. G. M.; Ferrandez, D. M. P.; Hensen, E. J. M.; Schouten, J. C.; Nijhuis, T. A., *ChemCatChem* **2013**, *5* (2), 467-478.
32. Feng, X.; Sheng, N.; Liu, Y.; Chen, X.; Chen, D.; Yang, C.; Zhou, X., *ACS Catal.* **2017**, *7* (4), 2668-2675.
33. Feng, X.; Yang, J.; Duan, X.; Cao, Y.; Chen, B.; Chen, W.; Lin, D.; Qian, G.; Chen, D.; Yang, C.; Zhou, X., *ACS Catal.* **2018**, *8* (9), 7799-7808.
34. Qi, C.; Huang, J.; Bao, S.; Su, H.; Akita, T.; Haruta, M., *J. Catal.* **2011**, *281* (1), 12-20.
35. Kanungo, S.; Keshri, K. S.; van Hoof, A. J. F.; d'Angelo, M. F. N.; Schouten, J. C.; Nijhuis, T. A.; Hensen, E. J. M.; Chowdhury, B., *J. Catal.* **2016**, *344*, 434-444.

# **CHAPTER 5**

## **Pd/SBA-15 Catalyzed Hydrogenation Reactions**

**Part A: Atmospheric pressure CO<sub>2</sub> hydrogenation over Ti modified Pd/SBA-15 catalyst.**

**Part B: Nitrobenzene reduction to N-ethyl aniline over Pd/meso-SiO<sub>2</sub> catalyst.**

This chapter is based on:

1. *Observing selectivity switch for CO<sub>2</sub> hydrogenation over Ti modified Pd/SBA-15 catalyst.* Yogita Soni, Sharad Gupta, C. P. Vinod (Manuscript under preparation)
2. *Direct reductive monoalkylation of nitrobenzene to N-ethyl aniline over Pd/meso-SiO<sub>2</sub>.* Yogita Soni, Milda C. Philip, C. P. Vinod (Manuscript under preparation)

This chapter comprises hydrogenation reactions over Pd NPs supported on mesoporous silica and is discussed in two separate parts as: 5A and 5B.

## **Part 5A. Atmospheric pressure CO<sub>2</sub> hydrogenation over Ti modified Pd/SBA-15 catalyst**

### **5A.1 Introduction**

Modern trends of civilization and our critical dependence on fossil fuels have tremendously increased the anthropogenic CO<sub>2</sub> emission in environment. Even though CO<sub>2</sub> is a non poisonous gas it is one of the major constituents of green house gases and its continuous emission in earth's atmosphere has severely affected the global climate resulting in global warming and ocean acidification.<sup>1</sup> Considering the adverse effect of changes in global climate it is highly recommended to cut CO<sub>2</sub> emission so as to restrict the temperature increase to 1.5 °C above pre industrial levels. CO<sub>2</sub> capture and sequestration (CCS) has emerged as the potential mitigation route and is anticipated to reduce the CO<sub>2</sub> emission to 19% as required in 2050,<sup>2,3</sup> but its potential leakage limits the use of this method as an effective solution. Also the development of this process is slow and unpopular due to its high process and construction cost especially in developing countries.<sup>4</sup> Chemical transformation of CO<sub>2</sub> to valuable products is the most attractive alternate to mitigate CO<sub>2</sub> emissions and can be achieved via photocatalysis, electrocatalysis and thermal catalysis.<sup>5-8</sup> However, the conversion and selectivity are not so impressive due to very high stability of CO<sub>2</sub>. Photocatalysis and electrocatalysis seem to be promising due to use of solar energy and are less energy intensive but the low efficiency of these methods makes them unviable for large scale CO<sub>2</sub> conversion. Thermal catalysis is conversion of CO<sub>2</sub> to various products at very high temperature making it an energy intensive process due to high stability of CO<sub>2</sub> molecule. The use of extra energy in form of high temperature for CO<sub>2</sub> conversion can be minimized by reacting CO<sub>2</sub> with a reactive molecule such as H<sub>2</sub>. Heterogeneous hydrogenation of CO<sub>2</sub> can produce various organic molecules such as CO, hydrocarbons, oxygenates such as alcohols, formic acid etc. by tuning the reaction conditions as well as catalysts.<sup>9-11</sup> High pressure of feed gases is usually required to obtain optimum yield of higher hydrocarbons (C<sup>2+</sup>) and oxygenates. Atmospheric conversion of CO<sub>2</sub> most often results C1 products such as CO, CH<sub>4</sub> and sometimes methanol also but in very small yield. While CO is an important feed stock molecule of Fischer Tropsch (FT) synthesis,<sup>12,13</sup> CH<sub>4</sub> is an important fuel used as natural gas and major source of H<sub>2</sub> generation by steam reforming.<sup>14</sup> Various transition metal based

catalyst have been reported for CO<sub>2</sub> conversion to C1 products and activity can be tuned for a specific product by tuning the catalytic properties.<sup>15</sup> The stability of the intermediates formed during the reaction actually decides the selectivity of different products. Apart from metal used another important parameter which can switch the product selectivity is metal support interaction.<sup>16</sup> Considerable efforts have been devoted to understand the elementary steps and sites required for CO<sub>2</sub> conversion at metal/oxide interface. However the exact reaction mechanisms and their intermediates are still controversial. Stabilization of reaction intermediates at particular sites can be one of the deciding factors for selectivity switch. Recent literature reports have shown the effect of metal support interaction on the product selectivity.<sup>16,17</sup> Cu/ZrO<sub>2</sub> catalyst shows the crucial role of metal support interaction in stabilizing the formate intermediate species which were responsible for getting high methanol selectivity.<sup>18</sup> Rh NPs supported on reducible support interestingly showed formation of adsorbate induced strong metal support interaction which changed the selectivity from CH<sub>4</sub> to CO hence proving the crucial role of metal support interaction.<sup>19</sup> Photoelectrochemical CO<sub>2</sub> conversion to CO and H<sub>2</sub> over Pt/TiO<sub>2</sub> showed high efficiency due to synergistic interaction at Pt-Ti interface which structurally provided sites for CO<sub>2</sub> conversion to CO.<sup>20</sup> These reports emphasize the role of metal-support interface in fine tuning the conversion and selectivity for CO<sub>2</sub> hydrogenation.

Pd is one of the important hydrogenation catalyst and its catalytic activity for CO<sub>2</sub> hydrogenation at atmospheric pressure usually proceed through RWGS (reverse water gas shift) reaction as the dominant pathway thus forming CO as the major product.<sup>21</sup> In the present study we have synthesised Pd supported on SBA-15 by a modified deposition precipitation (DP) method as discussed in Chapter 3. NH<sub>4</sub>Cl has been used as the insitu modifier of Pd precursor which helped in successful deposition of small Pd NPs on SBA-15 with desired loading. The synthesized Pd/SBA-15 catalyst was further modified with titanium to obtain Pd/Ti-SBA-15. The synthesized Pd catalysts with variable Si/Ti molar ratios were screened for CO<sub>2</sub> hydrogenation at atmospheric pressure and compared with individual TiO<sub>2</sub> and SBA-15 supports. Ti modified silica has most often been considered as the oxidation catalyst especially for epoxidation reaction while its hydrogenation property has been scarcely reported.<sup>22</sup> The present chapter has demonstrated the peculiar properties of Ti modified SBA-15 (Ti-SBA-15) as the heterogeneous hydrogenation catalyst. It has been observed that both conversion as well as selectivity can be tuned by modifying Pd/SBA-15 catalyst with titanium. The role of oxygen vacancies generated in the support after Ti



modification and synergistic interactions at Pd-Ti interface have been discussed in the present chapter. The CO<sub>2</sub> hydrogenation activity of this catalyst has been compared with Pd-SBA-15 and Pd-TiO<sub>2</sub> and crucial influence of support is revealed in this chapter.

## **5A.2 Experimental Section**

**5A.2.1 Synthesis of Pd/SBA-15 catalyst:** Small Pd NPs were supported on SBA-15 by modified DP method as discussed in Chapter 3. Briefly, 500 mg of SBA-15 support was dispersed in water to which NH<sub>4</sub>Cl was added. Then the pH of the solution was maintained at 9-9.5 using NaOH solution and required amount of Pd (4 wt%) was added drop wise while maintaining the pH. The catalyst was further stirred for an hour after which the catalyst was collected and dried at 70 °C overnight.

**5A.2.2 Modification of Pd/SBA-15 catalyst with titanium:** The as synthesized Pd/SBA-15 catalyst without calcination was further modified with titanium by post grafting method. Titanium(IV)tetraisopropoxide (TIP) was used as titanium precursor. Before adding it to the Pd/SBA-15 catalyst TIP was modified with acetylacetonate (acac) so as to prevent the rapid hydrolysis of TIP. Required amount of TIP was added to acac in ethanol and vigorously stirred for 1 h. Meanwhile Pd/SBA-15 catalyst was dispersed in ethanol and modified titanium precursor was added to this solution. The catalyst was further agitated at moderate rpm for 3 h. The catalyst was collected after evaporating ethanol at 40 °C under rotator evaporation and dried at 70 °C. The final titanium modified Pd/SBA-15 catalyst was obtained after calcination at 400 °C for 4 h. Depending upon the Si/Ti ratio used in the synthesis, catalyst was designated as PdTS-x where x denoted Si/Ti molar ratio. The Pd loading was 4 wt%. For comparison Pd/TiO<sub>2</sub> of similar Pd loading was also synthesized by wet impregnation method.

**5A.2.3 Catalyst Characterization:** DRUV analysis was done by Shimadzu 2700 spectrophotometer with an integrated dual beam source equipped with a diffuse reflectance attachment. He lamp and tungsten lamp were the UV and visible light source respectively BaSO<sub>4</sub> was used as the standard. Nitrogen adsorption isotherms were measured with an Micromeritics Tristar 3000 apparatus with adsorption analyzer at liquid nitrogen temperature. Before the analysis samples were degassed under vacuum at 300 °C for 3h. The specific surface areas were measured from BET method at relative pressure ranging from 0.5 to 0.2. The total pore volumes were determined by total volume adsorbed at relative pressure of 0.95. The pore size distribution curves were obtained from desorption branch of isotherm

using BJH equation. X-ray diffraction (XRD) patterns were recorded on a HUBER G-670 diffractometer fitted with an anti-cathode Cu K $\alpha$  ( $\lambda = 1.54178 \text{ \AA}$ ). XRD patterns were recorded over  $2\theta$  values ranging from  $10^\circ$  to  $80^\circ$ , with a scanning rate of 5s/step and 0.05 step sizes. Low-angle XRD patterns were recorded on a D8 advances X-ray diffractometer (Bruker AXS) fitted with a CuK $\alpha$  ( $\lambda = 1.5406 \text{ \AA}$ ) range  $0.5\text{-}6^\circ$  with a  $0.02^\circ$  steps. ICP analysis was done in Venture Centre, NCL Innovative Park. All the sample were completely digested in acid before analysis. TEM analysis was carried out by TECHNAI FEI instrument working at voltage of 200 kV with LaB $_6$  as the filament. The samples for TEM analysis were prepared in ethanol and dried completely before analysis. XPS measurements were carried out using Thermo Kalpha+ spectrometer using micro focused and monochromated Al K $\alpha$  radiation with energy 1486.6 eV. The pass energy for spectral acquisition was kept at 50 eV for individual core-levels. The electron flood gun was utilized for providing charge compensation during data acquisition. Palletized samples were used for analysis. The peak fitting of the individual core-levels were done using XPS peak-41 software with a Shirley type background.

**5A.2.4 Gas phase atmospheric pressure CO $_2$  hydrogenation:** 100 mg of the catalyst was loaded in a continuous plug-flow quartz reactor (30 cm in length, 6 mm in i.d.) mounted inside temperature controlled vertical tube furnace. All the catalysts were reduced in H $_2$  flow at  $400^\circ\text{C}$  for 3 h before starting the reaction. The catalytic activity was evaluated at atmospheric pressure with 23 vol% CO $_2$  and 72 vol% H $_2$  balanced with N $_2$ . The flow rate of feed gases was 9 ml/min with a GHSV of  $5400 \text{ mL (g}_{\text{cat}}\cdot\text{h)}^{-1}$  and was controlled by individual Alicat mass flow controllers. The concentrations of CO, CO $_2$ , N $_2$  and hydrocarbons in the outlet streams were analyzed by an online gas chromatography system (Nucon 5765) equipped with a Thermal Conductivity Detector (TCD) and Flame Ionization Detector (FID) using He as the carrier gas. Permanent gases were analyzed by TCD carbosieve column and hydrocarbons by FID capillary column. The CO $_2$  conversion, X (CO $_2$ ) was calculated as:

$$X(\text{CO}_2) = \frac{\text{Area of total product} + \text{Area of remaining CO}_2}{\text{Area of CO}_2 \text{ in}}$$

The selectivity S for different products was calculated as:

$$S(x) = \frac{\text{Area of product (x)}}{\text{Total products}}$$

### 5A.3 Results and Discussion

The synthesized catalysts were investigated by microscopic and spectroscopic characterization techniques so as to correlate the physicochemical properties with the catalytic activity.

#### 5A.3.1 DRUV Analysis

The modification of silica by titanium can happen in two ways- titanium can either occupy the silica lattice or it can be present as extra framework, phase segregated titania domains. The preliminary information about nature of titanium in silica lattice was obtained from DRUV analysis (Figure 5A.1) which shows that titanium has occupied the silica lattice as indicated by the presence of band at 220-230 nm which signifies the charge transfer between tetrahedral titanium  $Ti^{4+}$  and  $O^{2-}$  ions.<sup>23,24</sup> For perfect isolated tetrahedral titanium in silica lattice this band appears at 210-220 nm but the red shift in this band is due to distorted tetrahedral titanium in silica.<sup>25</sup>

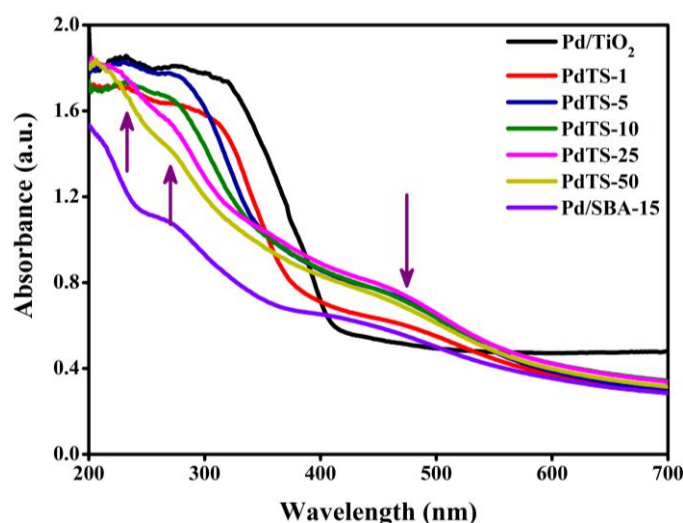


Figure 5A.1 DRUV spectra of PdTS-x catalysts with different titanium content.

Another band between 260-290 nm was also observed due to presence of extra framework titanium or titanium in octahedral coordination in silica lattice observed similarly for ATS samples in Chapter 2. The broadening of this band increased on moving from PdTS-25 to PdTS-1 indicating the formation of phase segregated titania due to increased loading of titanium in PdTS-1. In PdTS-1 this band showed features similar to titania which indicates that complete phase segregation happened on moving from PdTS-50 to PdTS-1. The presence of band in the range of 400-500 nm can be attributed to oxidized Pd NPs which appeared due to the charge transfer between  $Pd^{2+}$  and  $O^{2-}$  ions.<sup>26</sup> This band showed red shift after

modification with titanium which is an indication of increase in Pd NPs size after titanium incorporation. Thus DRUV analysis shows that along with tetrahedral titanium in silica lattice phase segregated titanium was also present when weight loading of titanium increased beyond Si/Ti ratio 5.

### 5A.3.2 X-ray Diffraction analysis

The powder XRD analysis of PdTS-x catalyst can be seen in Figure 5A.2. The small angle XRD of the catalysts as shown in figure 5A.2a, exhibited the major reflections at  $0.93^\circ$ ,  $1.63^\circ$  and  $1.86^\circ$  which correspond to ordered 2D hexagonal mesoporous structure of SBA-15 with a space group of  $p6mm$ .<sup>27</sup> The intensity of these peaks was maximum in pristine SBA-15 and decreased after deposition of Pd as well as Ti incorporation. However the presence of these peaks in all the samples except PdTS-1 confirmed that mesoporous structure of SBA-15 was preserved even after Pd and Ti loading. In PdTS-1 the structure collapsed drastically which was reflected as a feeble peak at  $0.93^\circ$  while other reflections were completely vanished. Small angle XRD analysis confirmed the successful deposition of Pd as well as incorporation of Ti in the mesoporous channels while maintaining the inherent mesoporosity of SBA-15.

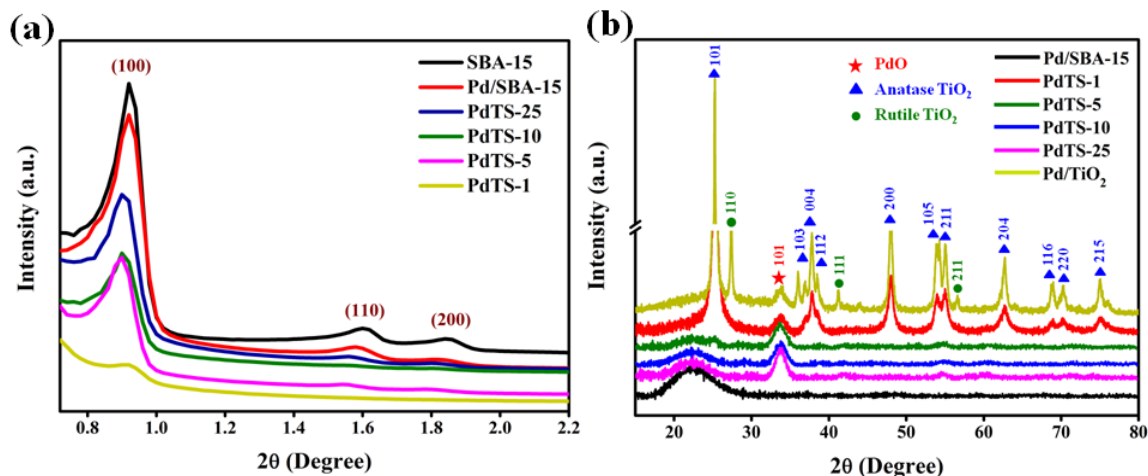


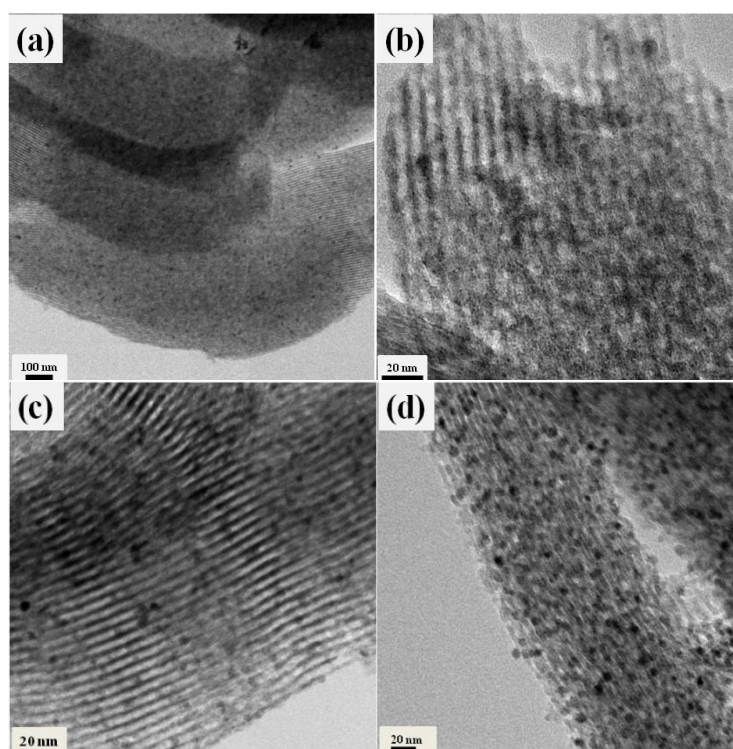
Figure 5A.2 XRD analysis of Pd/SBA-15 and PdTS-x catalysts.

In the wide angle XRD analysis, Pd/SBA-15 catalyst did not show any reflections of PdO which is due to presence of highly dispersed small sized Pd NPs in SBA-15 channels. After titanium modification clear reflection from PdO (101) could be seen at  $33.8^\circ$  which showed that titanium addition increased the size of Pd NPs as observed from DRUV analysis also. The particle size calculation from Scherer formula showed that PdTS-1 and Pd/TiO<sub>2</sub> had Pd NPs of size 8 nm while PdTS-5, 10 and 25 showed particles of size 6-7 nm. Moreover the

reflections from phase segregated titanium were not visible up to PdTS-10 while in PdTS-5 feeble peak and in PdTS-1 strong reflections from anatase titania were visible.<sup>28</sup> Thus XRD analysis corroborates the results obtained from DRUV that incorporation of titanium in Pd/SBA-15 catalyst increased the Pd NPs size with complete phase segregation of titania in PdTS-1 catalyst.

### 5A.3.3 Transmission Electron Microscopy Including EDX

TEM analysis was performed to examine the effect of titanium incorporation in the mesoporosity of Pd/SBA-15 as well as to confirm the results obtained from XRD and DRUV analyses about Pd NPs size. The TEM images (Figure 5A.3) clearly showed that mesoporous channels of SBA-15 were still maintained after titanium incorporation except PdTS-1 where phase segregated titania destroyed the mesoporosity and was quite visible. The Pd/SBA-15 catalyst showed highly dispersed small sized Pd NPs encapsulated in mesoporous channels of SBA-15 of size 2-3 nm. PdTS-50 to PdTS-5 also showed Pd NPs to be intact in mesoporous channels with high dispersion. But some morphology destruction was observed in these samples. Pd/TiO<sub>2</sub> catalyst showed the titania particles of size 20-30 nm with Pd NPs size to be 7-8 nm which was similar to what was calculated from XRD. Pd NPs in all the PdTS-x catalysts showed almost similar size in the range of 5-6 nm except PdTS-1 where particle size was similar to Pd/TiO<sub>2</sub> catalyst.



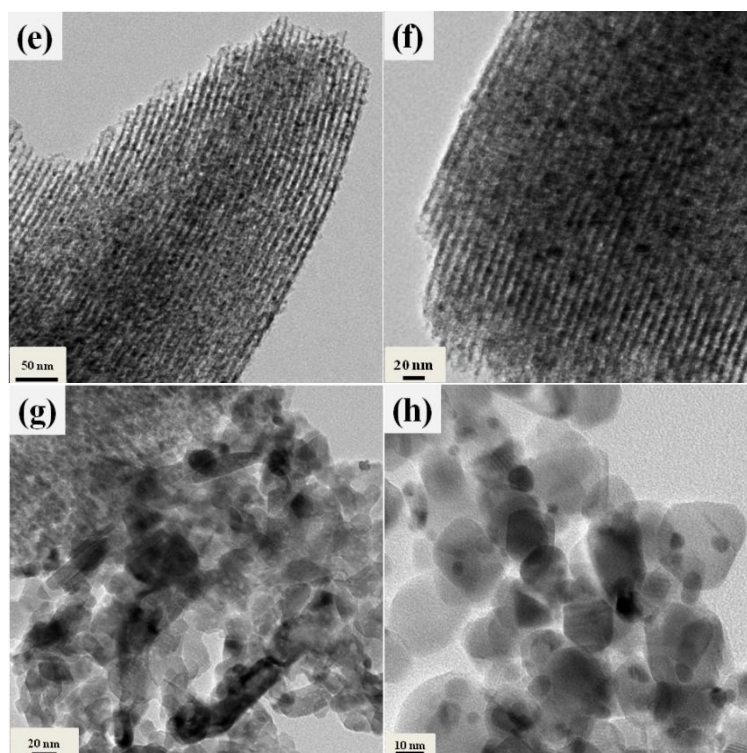


Figure 5A.3 TEM images of (a, b) Pd/SBA-15 (c) PdTS-50 (d) PdTS-25 (e) PdTS-10 (f) PdTS-5 and (g) PdTS-1 and (h) Pd/TiO<sub>2</sub> catalysts.

Further the SEM-EDAX analysis of these catalysts showed that by increasing the Si/Ti ratio from 50 to 1 the amount of titanium increased from 1.7 wt% to 20%. The content of titanium in PdTS 50, 25, 10, 5 and 1 was 1.5, 3.5, 6.6, 14 and 20 wt% respectively.

#### 5A.3.4 N<sub>2</sub> Porosimetry Analysis

The textural property of the catalysts was evaluated by N<sub>2</sub> adsorption and desorption which is shown in Figure 5A.4. It can be seen that all the catalysts follow type IV isotherm hysteresis corresponding to the filling of mesopores in the pressure range of 0.6-0.9. However PdTS-1 catalyst showed the minimum amount of N<sub>2</sub> adsorption and that also in the range of 0.5-0.8 as compared to other PdTS-x catalysts which indicates the pore blocking of SBA-15 upon introduction of titanium.

The textural properties of catalysts are shown in Table 5A.1. As expected, the surface area and pore volume of Pd/SBA-15 were maximum as compared to titanium modified catalysts.

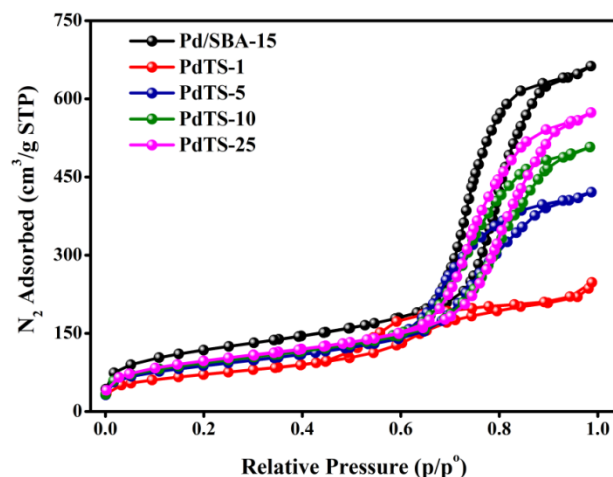


Figure 5A.4 N<sub>2</sub> Adsorption isotherm of PdTS-x catalysts compared with Pd/SBA-15.

Among PdTS-x catalysts PdTS-1 showed minimum surface area with lowest pore diameter and pore volume. This is obvious since the amount of titanium in this catalyst was highest which hindered the mesoporous structure of this catalyst. The textural properties of these catalysts confirmed the mesoporous nature of Pd/SBA-15 catalyst after titanium modification.

| Catalyst  | Surface area (m <sup>2</sup> /g) | t-plot Surface area (m <sup>2</sup> /g) | Pore diameter (nm) | Pore volume (cm <sup>3</sup> /g) |
|-----------|----------------------------------|---|--------------------|----------------------------------|
| Pd/SBA-15 | 417                              | 351                                     | 8.4                | 1.03                             |
| PdTS-25   | 341                              | 301                                     | 8.9                | 0.898                            |
| PdTS-10   | 329                              | 282                                     | 8.5                | 0.797                            |
| PdTS-5    | 310                              | 269                                     | 7.6                | 0.664                            |
| PdTS-1    | 251                              | 222                                     | 5.5                | 0.382                            |

Table 5A.1 Textural Properties of PdTS-x catalysts.

### 5A.3.5 X-ray Photoelectron Spectroscopy

As discussed in DRUV analysis the occupancy of titanium in tetrahedral/octahedral environment in PdTS-x catalyst showed both the features which was further confirmed by XPS analysis. The tetra coordinated titanium shows binding energy at higher region as compared to octahedral coordinated Ti<sup>4+</sup> ions. XPS analysis done on PdTS-x catalysts

showed both the features at 458.8 and 459.9 eV for octahedral and tetrahedral coordination respectively as can be seen in Figure 5A.5(a).<sup>29,30</sup>

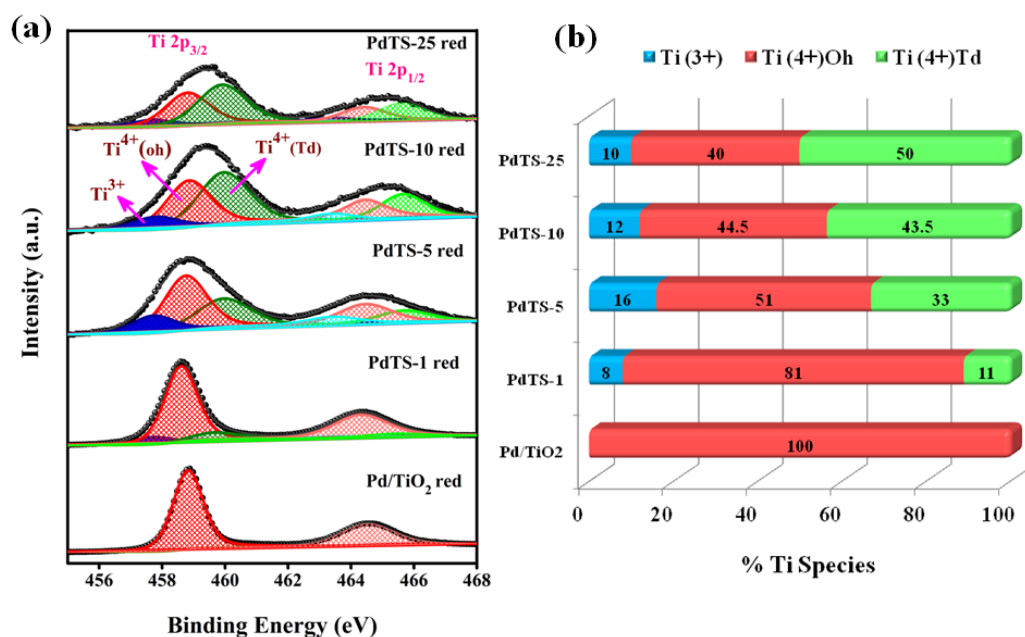


Figure 5A.5 (a) Ti 2p XPS spectra of reduced PdTS-x catalysts compared with Pd/TiO<sub>2</sub> (b) % fraction of different Ti species present in the catalysts. All the catalysts were reduced at 400 °C in H<sub>2</sub> flow.

However, small TiO<sub>2</sub> clusters of size < 5 nm highly dispersed in silica show binding energy values similar to tetrahedrally coordinated Ti.<sup>30</sup> But in the present case DRUV analysis showed UV band at 220-230 nm which is typically for tetra coordinated Ti in silica lattice. It can be seen that as the amount of titanium increased the contribution of tetrahedral Ti<sup>4+</sup> decreased (lowest for PdTS-1) which is due to formation of phase segregated titania. The XPS analysis was performed on reduced catalysts which showed another feature towards lower binding energy at 457.8 eV. This peak can be attributed to Ti<sup>3+</sup> ions due to generation of oxygen vacancies in hydrogen environment.<sup>31</sup> From Figure 5A.5 (b) it can be observed that PdTS-5 showed maximum amount of Ti<sup>3+</sup> (16%) which can be correlated to amount of oxygen vacancies generated. Interestingly Pd/TiO<sub>2</sub> did not show any oxygen vacancy generation which shows that introduction of titanium in silica could potentially generate defect centres in the support. To explore more about Pd-Ti electronic interaction Pd 3d XPS spectra was recorded (Figure 5A.6) for these catalysts.

The XPS spectra of Pd showed two peaks at 335.2 and 336.8 eV which correspond to metallic Pd and Pd in +2 oxidation states respectively.<sup>32</sup> The amount of metallic Pd increased as the amount of Ti increased from PdTS-25 to PdTS-1 and Pd/TiO<sub>2</sub> showed the maximum



amount of metallic Pd (84%) due to pure titania phase. This behaviour of Pd NPs can be explained on the basis of redox property of titania so as to maintain the metallic character of Pd.

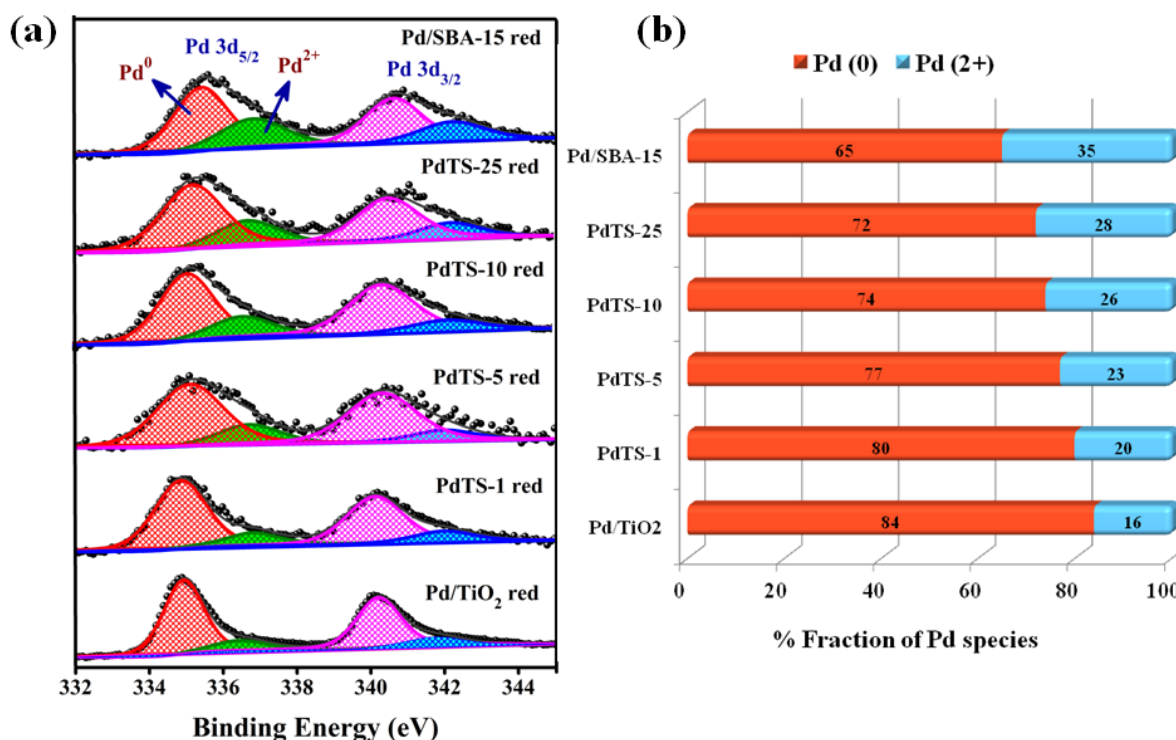


Figure 5A.6 (a) Pd 3d XPS spectra of reduced PdTS-x, Pd/TiO<sub>2</sub> and Pd/SBA-15 catalysts (b) % fraction of different Pd species present in different catalysts.

With an increase in the amount of Ti the chances of interaction of Pd with titanium was increased which resulted in more metallic content of Pd. It is well known that interaction of metal with redox support can induce electronic changes in the metal. In the present study also Pd-Ti interaction modified the electronic properties Pd and helped to maintain its metallic character. Among PdTS-x catalysts PdTS-1 showed the maximum amount of metallic Pd which was obvious due to the presence of phase segregated titania which like Pd/TiO<sub>2</sub> preserved the metallic character of Pd. Other PdTS-x i.e. PdTS-25, 10 and 5 catalysts also showed metallic Pd as the major peak with marginal decrease in the metallic content from PdTS-5 to PdTS-25. One probable reason of decreased amount of metallic Pd on decreasing the titanium content could be interaction of Pd with silica since most of the titanium is embedded in silica. Since silica is an inactive non reducible support it cannot facilitate the reduction of Pd oxide to metallic Pd as strongly as that of titanium. Introduction of titanium and close vicinity of Pd-Ti led to easy reducibility of Pd.

For a comparison the XPS analysis of TS-5 alone was carried out after reduction in same conditions as that of PdTS-5. It was observed that support alone showed only 4% oxygen vacancy generation as compared to PdTS-5 which showed 16 % of oxygen vacancies.

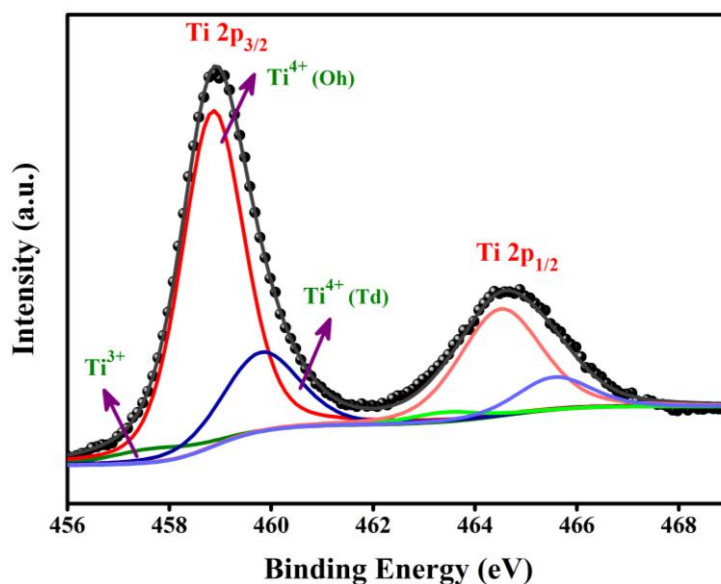


Figure 5A.7 XPS spectrum of TS-5 support after reduction.

This indicates that Pd helped in the oxygen vacancy generation in the support at the interface. This is feasible as hydrogen can easily get activated on Pd NPs which in turn reacts with oxygen of support at metal-support interface thereby creating oxygen vacancies. This kind of metal assisted oxygen vacancy generation in the support is a well documented phenomenon in literature where metal NPs at the perimeter sites helps in generation of defect centres under certain conditions.<sup>33,34</sup> Supports like CeO<sub>2</sub>, TiO<sub>2</sub>, Fe<sub>2</sub>O<sub>3</sub> etc. are known to generate oxygen vacancies when in close proximity of metal NPs.<sup>35</sup> It is noteworthy that oxygen vacancy in the support increased from PdTS-25 to PdTS-5 and further decreased in PdTS-1 and negligible amount was present in Pd/TiO<sub>2</sub> which manifests strong interaction of Pd and Ti when titanium was dispersed in silica.

The oxygen vacancies can help to maintain the metallic character of metal as well as take part in reaction also. PdTS-5 catalyst showed the maximum amount of oxygen vacancies with an appreciable amount of metallic Pd. Thus XPS analysis strongly points towards the increased metal support interaction in Pd/SBA-15 catalyst after titanium modification which resulted in ample amount of oxygen generation and preservation of metallic character of Pd.

### 5A.3.6 CO<sub>2</sub> hydrogenation activity

The synthesised catalysts were screened for CO<sub>2</sub> hydrogenation at atmospheric pressure in the temperature range of 473-673 K with CO<sub>2</sub> to H<sub>2</sub> ratio as 1:3. All the catalysts were pre-treated in H<sub>2</sub> atmosphere at 400 °C with a flow of 15 ml/min for 3 h to ensure the reduction of Pd to metallic form. The CO<sub>2</sub> hydrogenation activity results can be seen in Figure 5A.8.

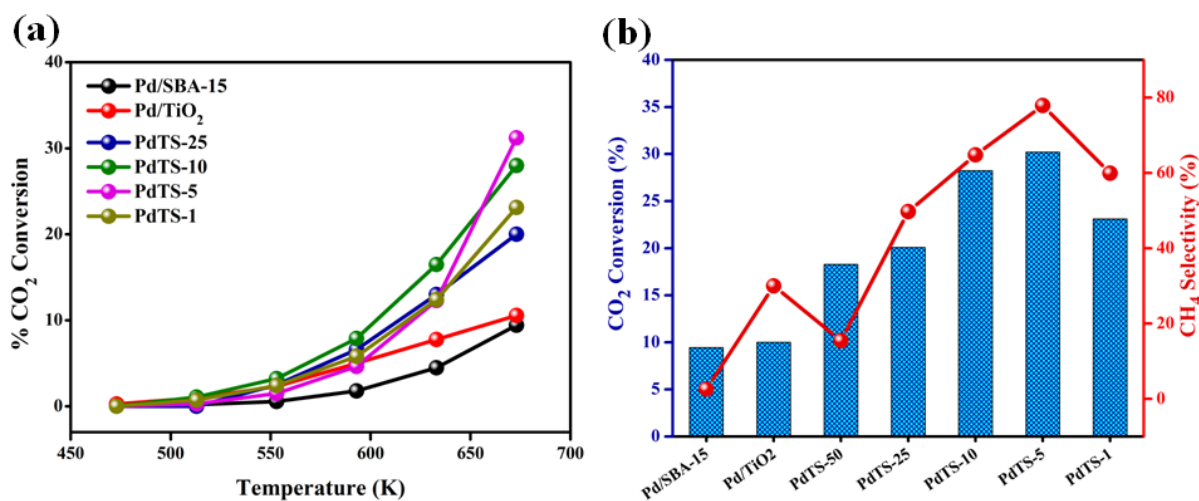
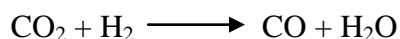


Figure 5A.8 (a) CO<sub>2</sub> hydrogenation activity of different catalyst w.r.t temperature (b) comparison of activity and selectivity for CH<sub>4</sub> at 673 K.

The activity plot in Figure 5A.8a showed the CO<sub>2</sub> hydrogenation of different catalysts at different temperature and major products formed were CO and CH<sub>4</sub>. It can be observed that initial activity for all the catalysts was almost similar at lower temperature regime, but after increasing the temperature beyond 593 K the difference in activity was observed and finally at 673 K PdTS-5 catalyst showed the highest CO<sub>2</sub> conversion of 31%. The difference in the selectivity of these catalysts at different temperatures was also observed. Initially at low temperature all the catalyst showed RWGS as the dominant reaction pathway making CO as the major product (see the equation).



But with an increase in the temperature selectivity switched from CO to CH<sub>4</sub> except for Pd/SBA-15 which showed CO as the major product throughout the temperature range. The difference in the catalytic activity of all the catalysts at 673 K can be seen in Figure 5A.8b. For Pd/SBA-15 catalyst the conversion was below 10% with a CO selectivity of 95% making RWGS as the dominant reaction. But the modification of Pd/SBA-15 with titanium resulted

in improved CO<sub>2</sub> conversion with a selectivity switch from CO to CH<sub>4</sub> hence turning the RWGS reaction to complete hydrogenation of CO<sub>2</sub>. As a control experiment Pd/TS-5 catalyst was also synthesised by supporting Pd after the synthesis of TS-5 and its activity was compared with PdTS-5.

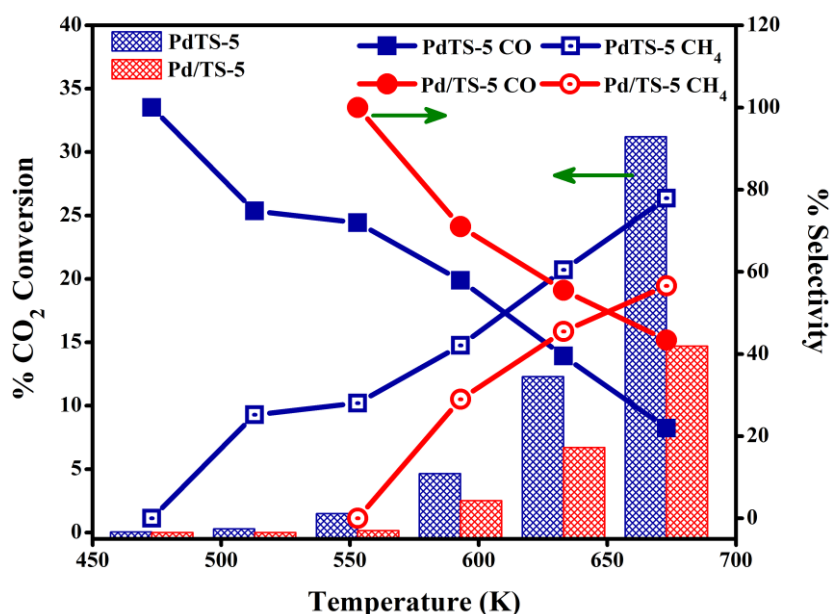


Figure 5A.9 CO<sub>2</sub> hydrogenation activity of PdTS-5 and Pd/TS-5 catalysts.

It can be seen from the plots that Pd/TS-5 catalyst showed less CO<sub>2</sub> conversion as compared to PdTS-5 catalyst. At 673 K PdTS-5 catalyst showed 31% CO<sub>2</sub> conversion while Pd/TS-5 catalysts showed only 14% conversion. The selectivity was also different for this catalyst as compared to PdTS-5. This catalyst showed maximum 56% CH<sub>4</sub> selectivity while PdTS-5 catalyst showed 78% CH<sub>4</sub> selectivity. The CO<sub>2</sub> activity results of these catalysts showed that synthesis procedure affected the CO<sub>2</sub> conversion and selectivity. PdTS-5 catalyst where Ti was incorporated to Pd/SBA-15 catalyst the chances of intimate interaction of Pd-Ti were more as compared to supporting Pd after the synthesis of TS-5 support.

PdTS-5 outperformed all the catalysts with maximum CO<sub>2</sub> conversion (31%) and CH<sub>4</sub> selectivity of 78% followed by PdTS-10 with a conversion of 28% and CH<sub>4</sub> selectivity of 65%. It is noteworthy that increasing the Si/Ti ratio to 1 resulted in decrease in CO<sub>2</sub> conversion to 23% as well as selectivity for CH<sub>4</sub> to 60%. Interestingly the Pd/TiO<sub>2</sub> catalyst showed conversion similar to Pd/SBA-15 catalyst but an improved CH<sub>4</sub> selectivity of 30%, though it was lower as compared to PdTS-x catalysts. The comparative selectivity for CO and CH<sub>4</sub> over these catalysts w.r.t temperature can be seen in Figure 5A.10.

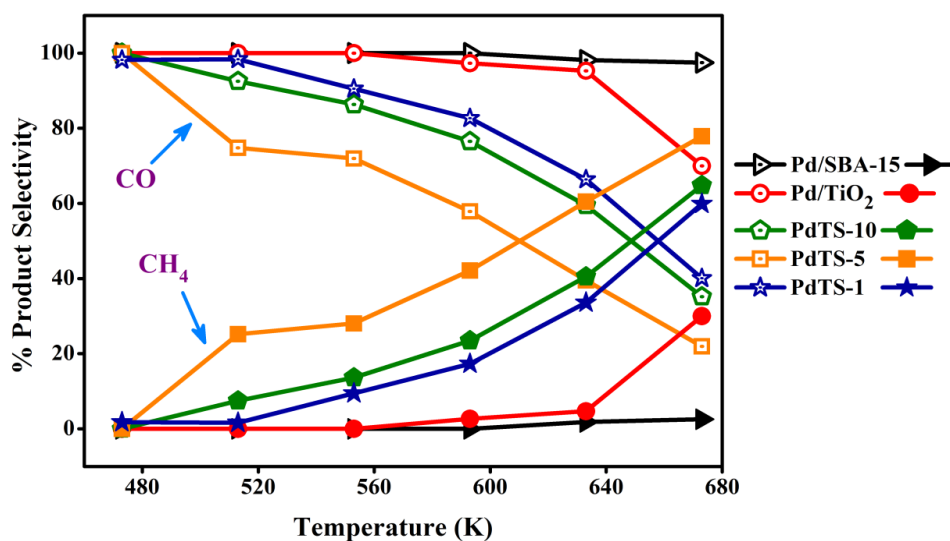
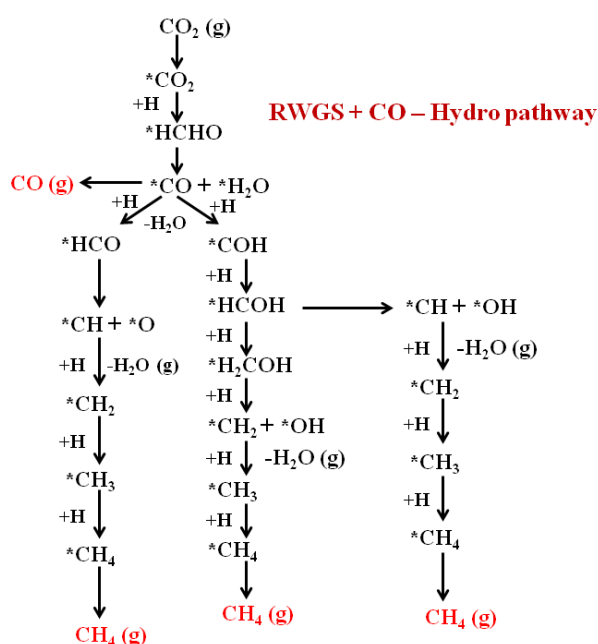


Figure 5A.10 Comparison of CO and CH<sub>4</sub> selectivity of different catalysts w.r.t. temperature.

The improved CO<sub>2</sub> conversion on reduced Pd/SBA-15 catalyst after titanium modification can be attributed to the generation of oxygen vacancies in the support as shown by Ti 2p XPS plots in Figure 5A.5. Pd/TiO<sub>2</sub> catalyst showed very less conversion similar to Pd/SBA-15 catalyst and can be correlated to the absence of oxygen vacancies in both the supports. The oxygen vacancies play important role in catalysis. These are electronically rich sites where an electron deficient reactant molecule can get adsorbed and activated by transfer of electrons to the antibonding orbitals of the reactant molecule. CO<sub>2</sub> being a Lewis acid can easily interact with these sites and gets activated. After the activation CO<sub>2</sub> can participate in hydrogenation to form different products via following route:



Scheme 5A.1 Possible reaction pathway of CO<sub>2</sub> hydrogenation to CO and CH<sub>4</sub> via RWGS. (\*X) indicates adsorbed species.

Depending upon the strength of binding of CO on the catalyst it can desorb or take part in further hydrogenation. The former case results in the formation of CO and H<sub>2</sub>O while in the later case it can form CH<sub>4</sub> as the major product.<sup>16</sup> It is well known that stability of intermediates highly depends upon the nature of active sites. The high binding strength provided by the active sites to a formed intermediate will decide the selectivity for particular product. In the case of Pd/SBA-15 the Pd-Si interface is not strong enough so as to strongly adsorb the formed CO which could undergo further hydrogenation. Therefore the formed CO desorbs in the form of product. However in the case of PdTS-x catalyst the intimate synergy of Pd-Ti can strengthen the binding of intermediate CO species which can further react with hydrogen atoms present on Pd to form CH<sub>4</sub> as the major product. It can be argued why Pd/TiO<sub>2</sub> catalyst where stronger chance of Pd-Ti interface are present do not show similar activity and selectivity as those of PdTS-x catalysts. The Pd particle size effect cannot be possible reason as the Pd NPs size in the range of 6-8 nm in all the catalyst except Pd/SBA-15 where size is comparatively smaller. Low conversion of this catalyst as compared to PdTS-x catalyst can be attributed to the negligible oxygen vacancy generation. But the selectivity difference can only be explained on the Pd-Ti interface. It is obvious that interface formed by metal NPs with nano support will always be stronger and have different properties than that of bulk support. Also the no. of active sites also increases. In the case of PdTS-x catalysts the dispersion of Ti in SBA-15 in octahedral or tetrahedral Ti in close proximity to Pd could form much stronger interface due to enhanced charge transfer between metal and support in either of the way. These sites provided much stronger binding to intermediate CO as compared to Pd/TiO<sub>2</sub> hence resulted in selectivity switch from CO to CH<sub>4</sub>. This kind of change in the selectivity has been observed on Pt based heterogeneous catalyst where Pt/TiO<sub>2</sub> catalyst showed selectivity for CO while Pt/ZrO<sub>2</sub> or CeO<sub>2</sub> showed selectivity towards CH<sub>4</sub>. Different metal-oxide interface provided by the different supports promoted the heterogeneity of the active sites which resulted in difference in the selectivity in these catalysts.

Further the stability of PdTS-5 catalyst was evaluated by screening the catalyst on time on stream reaction at 673 K for 24 h. The catalyst showed consistent CO<sub>2</sub> conversion while maintaining the stable selectivity for both the products (Figure 5A.11).

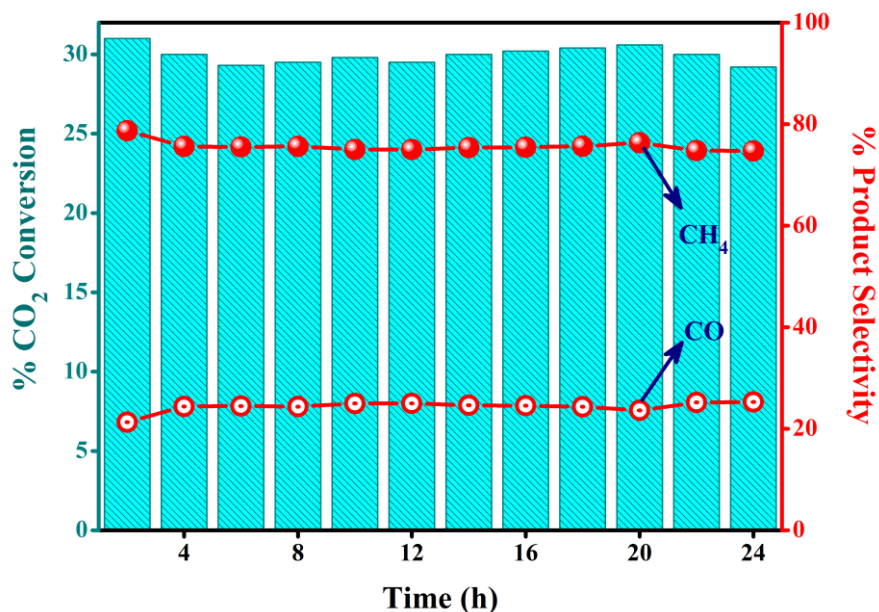


Figure 5A.11 Time on stream reaction of PdTS-5 catalyst at 673 K

It is clear from the figure that the methane and CO selectivity did not change throughout the time with a steady CO<sub>2</sub> conversion. This shows that the integral properties of the catalyst remained intact throughout the reaction. TEM images of the spent PdTS-5 catalyst after 24 h reaction showed no signs of sintering which can be attributed to the encapsulation of Pd NPs inside the mesoporous channels of SBA-15 (Figure 5A.12).

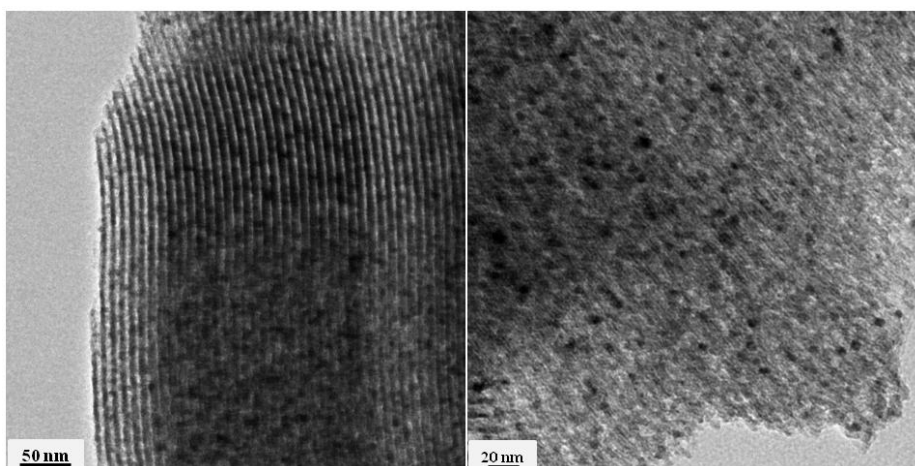


Figure 5A.12 TEM images of spent PdTS-5 catalyst after 24 h time on stream at 673 K.

Comparison of XPS spectra of spent PdTS-5 catalyst with Pd/SBA-15 and Pd/TiO<sub>2</sub> is shown in Figure 5A.13. The Ti 2p spectra of catalysts showed that PdTS-5 catalyst still carried oxygen vacancies which were possible since the reaction conditions were overall reducing.

But Pd/TiO<sub>2</sub> catalyst similar to fresh reduced catalyst did not showed any oxygen vacancy generation which points to the fact that the TiO<sub>2</sub> structure was stable under the reactant flow and temperature conditions.

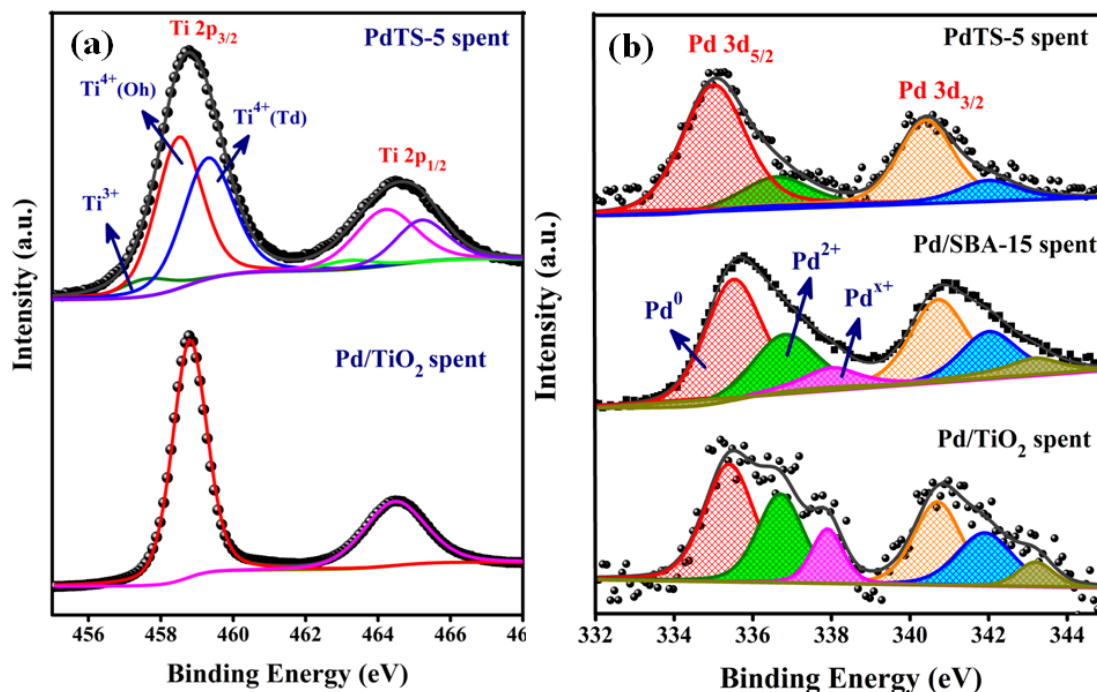


Figure 5A.13 (a) Ti 2p (b) Pd 3d XP spectra of spent PdTS-5 catalyst compared with Pd/SBA-15 and Pd/TiO<sub>2</sub>.

Pd 3d spectra of the spent catalysts represent that PdTS-5 catalyst showed only two peaks at 335.3 and 336.8 eV which correspond to metallic Pd and Pd<sup>2+</sup>. But for Pd/TiO<sub>2</sub> and Pd/SBA-15 catalysts a peak at higher binding energy, 338 eV also emerged along with other two peaks. The peak at higher binding energy corresponds to high valent Pd<sup>x+</sup> species as already explained in Chapter 3. The higher oxidation of Pd NPs in Pd/SBA-15 and Pd/TiO<sub>2</sub> catalysts in the reaction conditions could be attributed to the weak interaction of Pd with support while in PdTS-5 catalyst strong Pd-Ti interaction maintained Pd in metallic state. The preservation of metallic nature of Pd NPs in PdTS-5 catalyst under reaction condition resulted in strong adsorption of intermediate CO species on these sites which further interacted with nearby H to selectively form CH<sub>4</sub>. This behaviour of PdTS-5 catalyst under reaction condition enforces the critical role of metal support interaction in CO<sub>2</sub> hydrogenation by effectively tuning the properties of active sites which in turn resulted in improved CO<sub>2</sub> conversion and change in selectivity from CO to CH<sub>4</sub>.



The CO<sub>2</sub> hydrogenation on Ti modified Pd/SBA-15 catalyst in the present chapter showed that by tailoring the interfacial properties of heterogeneous catalysts the conversion and product selectivity can be easily tuned. The electronic perturbations generated at the interface due to metal support interaction can modify the properties on both support as well as metal NPs and facilitates the catalytic reaction.

## **Part 5B. Nitrobenzene reduction to N-ethyl aniline over Pd/meso-SiO<sub>2</sub> catalyst.**

### **5B.1 Introduction**

The chemistry of C-N bond formation has always been one of the most important research fields because the resulting organic compounds such as amines, amides and their derivatives play central role in organic synthesis.<sup>36,37</sup> The rich history of N-containing organic molecules comprising of various nitrogen derivatives as the typical building blocks in the construction of life, such as amino acids, nucleotides has impuled the pharmaceuticals and agrochemical industries to develop various N-containing compounds.<sup>38</sup> Moreover N-containing compounds are important in other aspects of chemical industries such as synthesis of dyes, surfactants, detergents, emulsions, vulcanizing agents and additives in petroleum industries.<sup>39,40</sup> Amines are the main and most important nitrogen containing organic compounds, and hence a plethora of different methods have been developed for their synthesis which include reductive alkylation processes, electrophilic alkylation and amination of aryl halides.<sup>41-43</sup> Among derivatives of amines N-alkyl/aryl amines are important because of their use in pharmaceuticals, dye synthesis and pesticides. Common methods of synthesis of N-alkyl/aryl amines are N-alkylation of anilines with aryl halides which is a direct nucleophilic substitution of alkyl/aryl halides and requires large excess of reagents, high polar solvents with high temperature or activated aryl halides.<sup>43</sup> Another methods of alkylation of amines are Buchwald-Hartwig and Ulmann type C-N cross coupling reactions.<sup>44-46</sup> But these methods also require alkyl halides as the alkylating source which are costly and produce huge amount of waste. Alkylation of amines with environment friendly alkylation source is fascinating and alcohols or carbonyl compounds are suitable candidate for this. The alkylation of amines with alcohols or carbonyl compounds with loss of water molecule is a thermodynamic favourable process where loss of C-O bond for the formation of C-N bond is compensated by formation of O-H bond in the form of water. The homogeneous route for the synthesis of alkylated amines may happen with or without catalyst. In the absence of catalyst, high temperature or pressure and large amount of reagents are required.<sup>47</sup> Use of ruthenium as the homogeneous catalyst is mostly explored where many Ru based organometallic complexes have been used for this purpose.<sup>40,48,49</sup> However the main drawback of these homogeneous complexes is non-reusability of these precious metal based catalysts. Heterogeneous N-alkylation is interesting in this regard though the conversion and selectivity may be less than homogeneous catalyst which can however be compensated by recyclability

and reuse of the catalyst. Various Ni, Cu, Pt, Pd based catalyst have been reported for alkylation of amines with alcohols or carbonyl compounds.<sup>40,50-53</sup> However Ni and Cu based catalyst require very high temperature for the coupling of alcohols and amines. Though coupling of amines with alcohols/carbonyl compounds is appealing, direct one pot reductive alkylation of nitro compounds with alcohols/carbonyl compounds to produce 2° or 3° amines is much better and economical since the extra efforts of reduction of nitro compound can be prevented. Certain heterogeneous catalysts have been used for alkylation of nitrobenzene to alkylated anilines. Most of the reports are based on coupling of nitrobenzene with aldehydes or aryl alcohols at high temperature.<sup>54-56</sup> Nitroarenes are inexpensive and readily available organic compounds and their reduction is one of the key process in the preparation of many pharmaceutical important compounds.<sup>57</sup> Though numerous procedures have been established for the reduction of nitrobenzene, development of methods which operate under mild conditions is still challenging.<sup>58,59</sup> As for the synthesis of secondary amines direct use of readily available and inexpensive nitroarenes and alcohols is quite attractive especially if a single heterogeneous catalyst is employed. In this regard alcohol can play two major roles: (i) hydrogen source for reduction of nitroarenes and (ii) alkylating source for further alkylation of amine formed though an excess amount of alcohol has to be used. However easy operational conditions for this multi transformation using single heterogeneous catalyst is practically limited for a concise synthesis of N-alkyl amines. There are scarce reports which deal with the direct amination of nitroarenes with alcohols.<sup>55,60,61</sup> In these reports usually borrowing H-transfer is operational where at high temperature alcohol is dehydrogenated to carbonyl compounds releasing H for the reduction of nitroarenes which after transformation to amines couple to carbonyl compound and form N-substituted aniline. Aromatic alcohols are the best candidate for this method due to their ease of releasing H and subsequently converting to carbonyl compounds. Aliphatic alcohols are however difficult to dehydrogenate hence limit their use as alkylating source for this purpose.

In this part of this chapter we have utilized the Pd/SiO<sub>2</sub> catalyst for direct one pot reductive alkylation of nitrobenzene to N-alkyl aniline using ethanol as the alkylating source and as solvent at mild reaction conditions. The Pd catalyst has been synthesised by the same modified DP method as employed in chapter 3. Different silica supports with variable surface area and pore size such as SBA-15, MCM-41 and KIT-6 have been used for supporting Pd NPs and their effect on the conversion and selectivity have been studied.

## 5B.2 Experimental Methods

**5B.2.1 Synthesis of Pd/mesoSiO<sub>2</sub>:** The synthesis procedure was similar to as discussed in chapter 3 and part 5A of this chapter. Three different catalysts have been synthesized using three different silica supports with a Pd weight loading of 3 wt% and denoted as Pd-SBA-N-3, Pd-MCM-N-3 and Pd-KIT-N-3 using SBA-15, MCM-41 and KIT-6 respectively as the support.

**5B.2.2 Nitrobenzene alkylation:** Nitrobenzene alkylation was carried out in a two necked flask using Pd/mesoSiO<sub>2</sub> catalyst, 0.5 mmol of nitrobenzene and ethanol (EtOH) as the solvent as well as alkylation source. H<sub>2</sub> in the balloon at atmospheric pressure was used as the reduction source of nitrobenzene. The conversion and product selectivity were identified by GC equipped with FID and HP-plot capillary column. Product identification was done by GC-MS analysis.

## 5B.3 Results and discussions

### 5B.3.1 DRUV Analysis

DRUV analysis of all the Pd/meso-SiO<sub>2</sub> calcined catalysts showed broad bands between 250-280 nm and 400-500 nm because of charge transfer between Pd<sup>2+</sup> and O<sup>2-</sup> ions as observed in Figure 5A.1.<sup>26</sup> After reducing the catalyst in H<sub>2</sub> flow at 400 °C these bands vanished because metallic Pd is SPR inactive and does not show any peak in UV-visible region (Figure 5B.1).

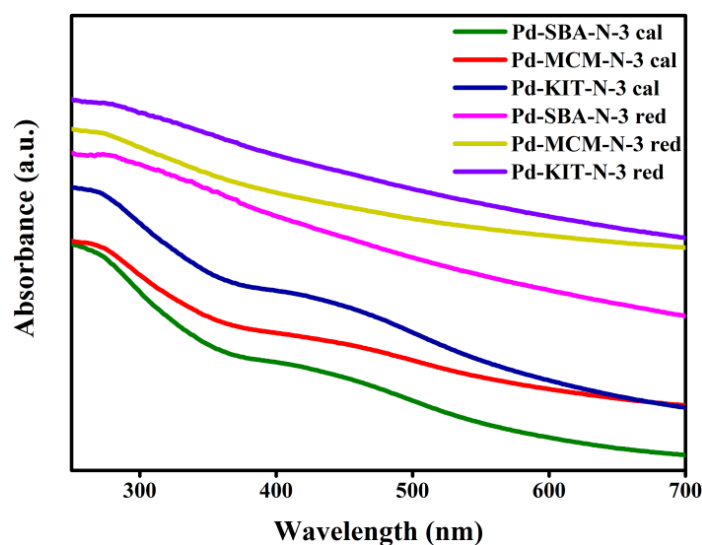


Figure 5B.1 DRUV spectra of different Pd/meso-SiO<sub>2</sub> catalysts after calcination and reduction.

### 5B.3.2 X-ray Diffraction Analysis

The small angle XRD analysis of these catalysts after calcination showed typical features of mesoporous materials (Figure 5B.2a). Pristine SBA-15 exhibited three peaks at  $2\theta$  values  $0.9^\circ$ ,  $1.6^\circ$  and  $1.9^\circ$  which corresponds to (100), (110) and (200) planes of hexagonal well defined long range pore distribution of SBA-15 with  $p6mm$  space group.<sup>27</sup>

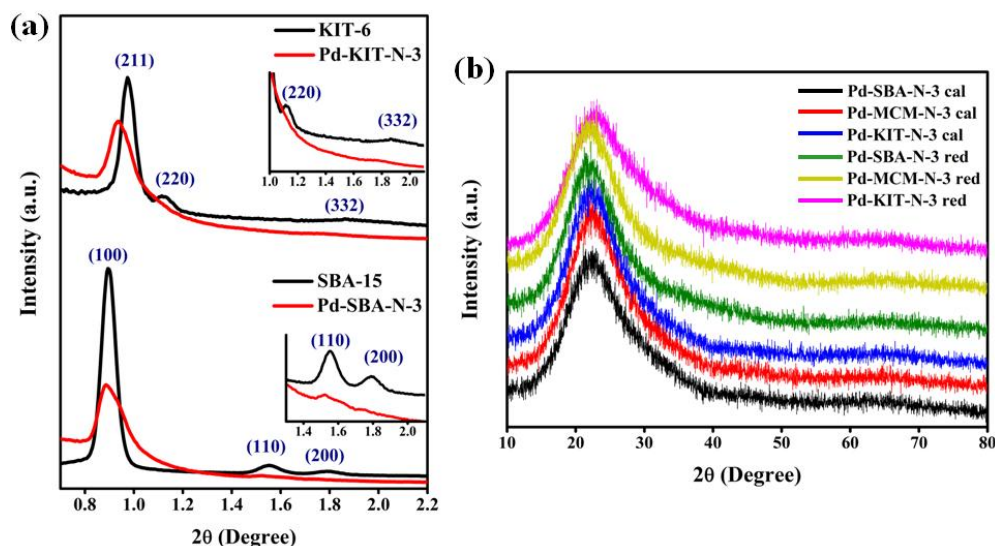


Figure 5B.2 (a) small angle (b) wide angle XRD of Pd/meso-SiO<sub>2</sub> catalysts.

After Pd loading the intensity of these peaks decreased which indicates occupation of mesopores by Pd NPs, however the mesoporous nature of SBA-15 was still preserved. Pristine KIT-6 also showed well defined mesoporous structure by exhibiting the typical reflections at  $0.97^\circ$ ,  $1.10^\circ$  and  $1.90^\circ$  for (211), (220) and (332) planes of a cubic 3D structure with  $Ia3d$  symmetry respectively.<sup>62</sup> Similar to Pd-SBA-15 catalyst, Pd-KIT-6 catalyst also showed decreased intensity of these reflections which was attributed to the deposition of Pd NPs in the mesoporous channels though the inherent mesoporosity of KIT-6 was intact.

The wide angle XRD analysis in Figure 5B.2b showed peaks at  $23^\circ$  corresponding to amorphous silica. No reflections from PdO at  $33.8^\circ$  for calcined and metallic Pd at  $40^\circ$  for reduced catalysts were observed which indicated the presence of well distributed Pd NPs of very small size inside the mesopores of silica. Thus XRD analysis confirms that Pd NPs supported on various mesoporous silica by modified DP method were very small sized and occupied the pores of silica while maintaining the inherent mesoporosity.

### 5B.3 Scanning Electron Microscopy and Energy Dispersive X-ray Analysis

The SEM-EDAX analysis of these samples has been shown in Figure 5B.3. The EDAX analysis showed that weight of Pd was almost similar to theoretical loading (3 wt%) which shows that no precursor was lost during the synthesis of these catalysts by modified DP method.

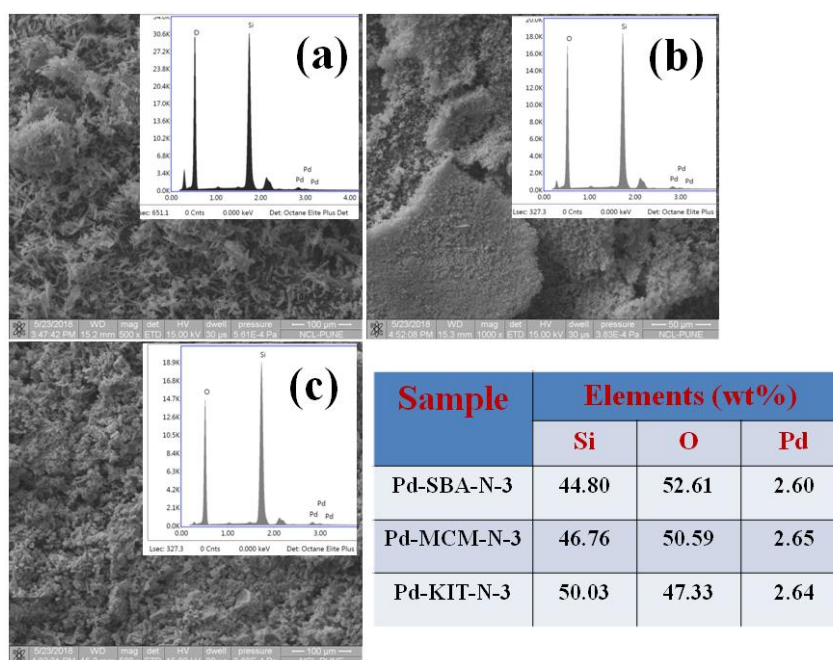
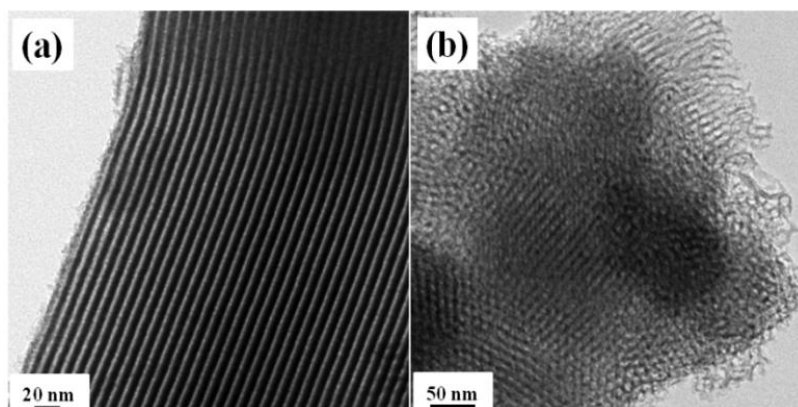


Figure 5B.3 SEM images of (a) Pd-SBA-N-3 (b) Pd-MCM-N-3 (c) Pd-KIT-N-3. The table in the figure shows EDAX results of these catalysts.

### 5B.4 Transmission Electron Microscopy

The TEM analysis of these catalysts showed the well ordered mesoporous structure of pristine silica (Figure 5B.4 (a, c, e)). The size of Pd NPs in all the catalysts was in the range of 2-3 nm and most of the particles occupied pores of the silica employed.



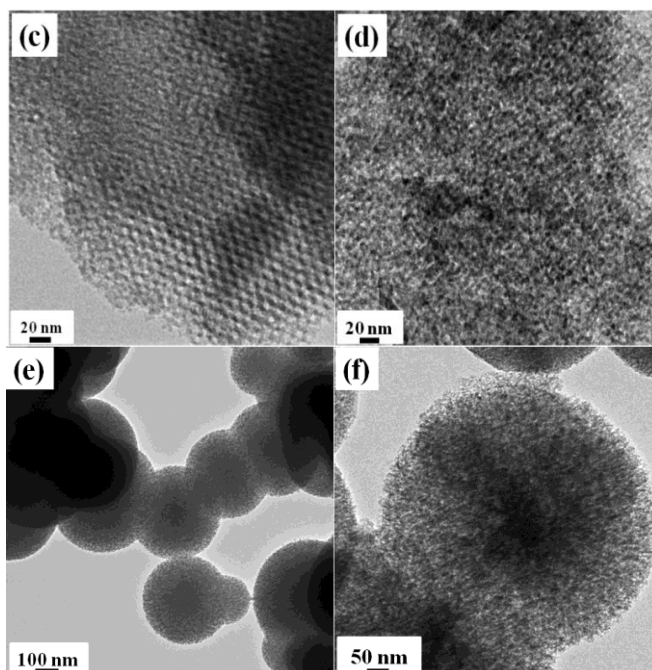


Figure 5B.4 (a) SBA-15 (b) Pd-SBA-N-3 (c) KIT-6 (d) Pd-KIT-N-3 (e) MCM-41 (f) Pd-MCM-41

The TEM images clearly showed that modified DP method can be applied for supporting Pd on different silica with different pore size with Pd NPs size 2-3 nm. Since the silica employed were mesoporous it was mandatory to evaluate the textural properties of silica before and after Pd loading which has been discussed in the next section.

### 5B.5 N<sub>2</sub> Porosimetry Analysis

The textural properties of the catalysts were evaluated by N<sub>2</sub> adsorption-desorption analysis. All catalysts showed hysteresis of type-IV isotherm which originated due to filling of mesopores.

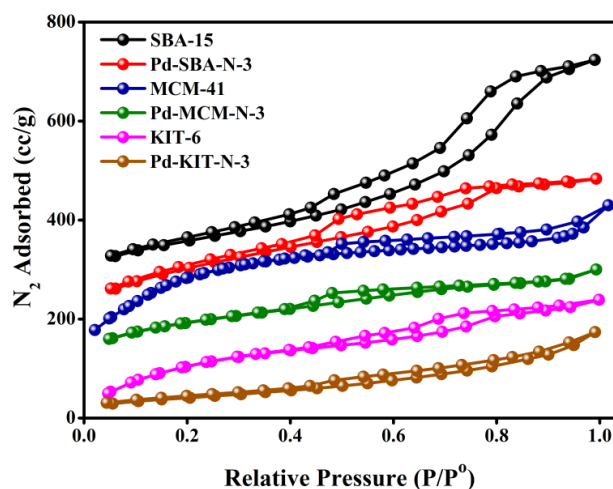


Figure 5B.5 N<sub>2</sub> adsorption-desorption isotherm of pristine silica and Pd supported silica.

The comparison of BET surface area and BJH pore size distribution can be seen in Table 5B.1. Among all the catalysts SBA-15 showed maximum surface area and largest pore diameter followed by KIT-6 and MCM-41. But after supporting Pd NPs both surface area as well as pore diameter decreased.

| Catalyst   | Surface Area (m <sup>2</sup> /g) | Pore Diameter (nm) | Pore Volume (cc/g) |
|------------|----------------------------------|--------------------|--------------------|
| SBA-15     | 575                              | 6.8                | 0.759              |
| Pd-SBA-N-3 | 450                              | 5.8                | 0.511              |
| KIT-6      | 771                              | 3.1                | 0.565              |
| Pd-KIT-N-3 | 151                              | 3.7                | 0.269              |
| MCM-41     | 598                              | 3.4                | 0.517              |
| Pd-MCM-N-3 | 434                              | 3.7                | 0.359              |

Table 5B.1 Textural properties of Pd/meso-SiO<sub>2</sub> catalysts compared with pristine silica

It was observed that all the catalyst showed decrease in surface area, pore diameter and pore volume after Pd loading. In contrast, for Pd-KIT-N-3 catalyst this decrease was drastic and surface area sharply decreased from 771 to 151 m<sup>2</sup>/g. However the pore size showed increased from 3.1 to 3.7 nm. This increase could be because of destruction of pores due to Pd loading and some larger sized pores were created. Similar was the case for MCM-41 also. Overall textural properties showed that after Pd loading Pd-SBA-N-3 showed maximum surface area as well as pore diameter among all the Pd supported catalysts.

### **5B.6 X-ray Photoelectron Spectroscopy**

The electronic property of Pd in the three catalysts was examined by XPS analysis. Since the final catalyst for the catalysis was reduced catalyst, XPS analysis was also carried out on reduced catalyst, Figure 5B.6. Reduction was performed at 400 °C in H<sub>2</sub> flow for 3 h. All the catalysts showed at 335 and 336.8 eV representing metallic Pd and Pd in +2 oxidation states respectively.



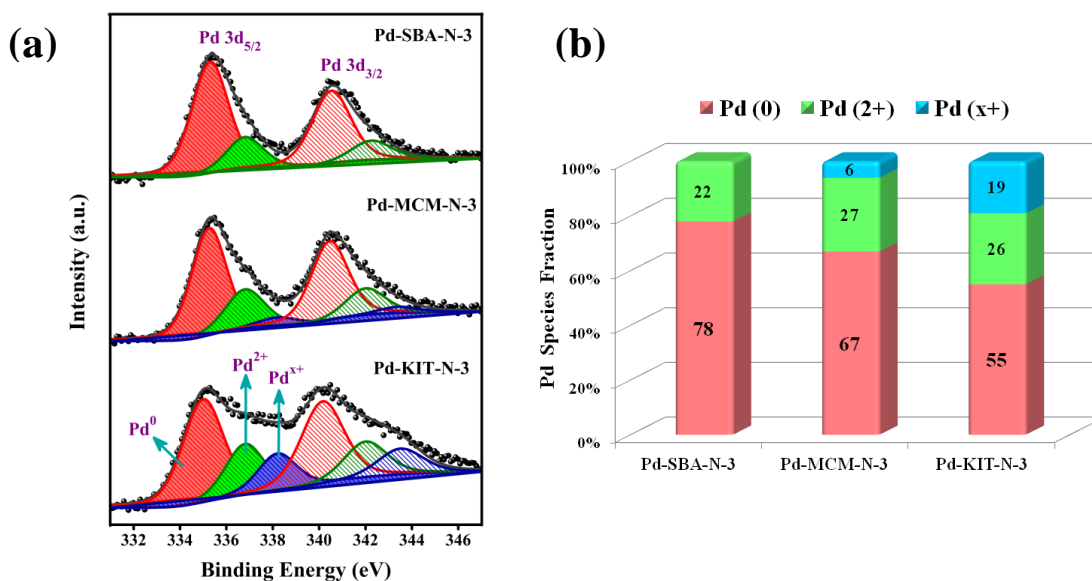
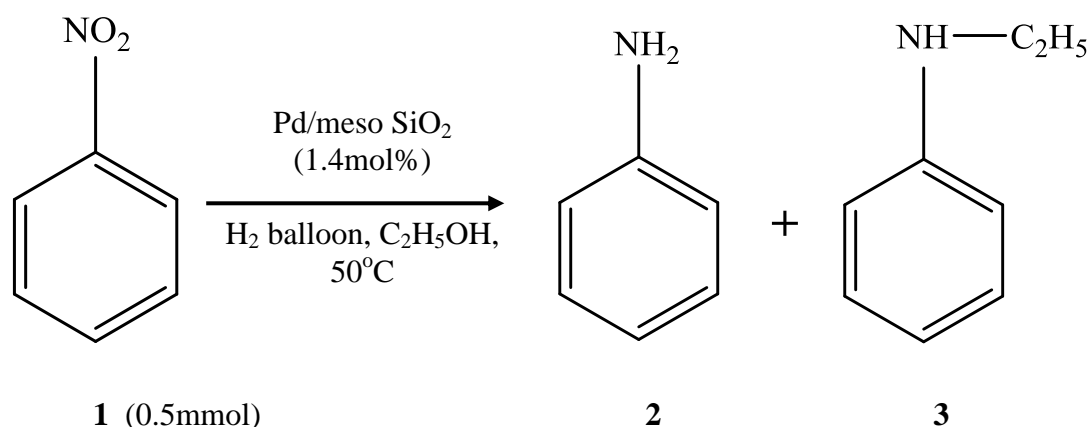


Figure 5B.6 (a) Comparison of XPS spectra of Pd/meso-SiO<sub>2</sub> catalysts after reduction (b) percentage of different Pd species present in different catalysts.

However unlike Pd-SBA-N-3 other two catalysts i.e. Pd-MCM-N-3 and Pd-KIT-N-3 showed one extra peak at 338.2 eV which originated due to high valent PdO<sub>x</sub> species where oxidation state of Pd was more than 2 and designated as Pd<sup>x+</sup> which could be attributed to oxide resulting from under-coordinated Pd atoms as observed in Chapter 3 also.

### 5B.7 Catalytic Screening for reductive alkylation of Nitrobenzene

The synthesized Pd/meso-SiO<sub>2</sub> catalysts were tested for one pot reductive mono alkylation of nitrobenzene to N-ethyl aniline in the presence of H<sub>2</sub> in balloon pressure.



Scheme 3B.1 Nitrobenzene reduction over Pd/meso-SiO<sub>2</sub> catalyst.

First the reaction was optimized by varying different parameters as can be seen in Table 5B.2

| S.No. | Catalyst       | Temp (°C) | Time (h) | % Conversion | Selectivity %<br>2 : 3 |
|-------|----------------|-----------|----------|--------------|------------------------|
| 1.    | Pd-SBA-N-3 red | RT        | 4        | 100          | 71 : 29                |
| 2.    | Pd-SBA-N-3 red | 50        | 4        | 100          | 50 : 50                |
|       |                |           | 10       | 100          | 50 : 50                |
| 3.    | Pd-SBA-N-3 cal | 50        | 4        | 100          | 89 : 11                |
| 4.    | Pd-SBA-N-3 red | 70        | 4        | 100          | 56 : 44                |
| 5.    | SBA-15         | 50        | 4        | -            | -                      |
| 6.*   | Pd-SBA-N-3 red | 50        | 4        | -            | -                      |
| 7.    | Blank          | 50        | 4        | -            | -                      |

\* Reaction without H<sub>2</sub>.

Table 5B.2 Optimization of parameters for reduction of nitrobenzene.

It can be seen from the table that Pd-SBA-N catalyst after reduction showed the best activity at 50 °C with equal selectivity for **2** and **3**. Increasing the temperature beyond 50 °C the conversion remained same but selectivity decreased. Therefore we optimized temperature as 50 °C. Full conversion was obtained after 4 h and further increase in the time did not affect the selectivity. Hence the reaction was performed for 4 h.

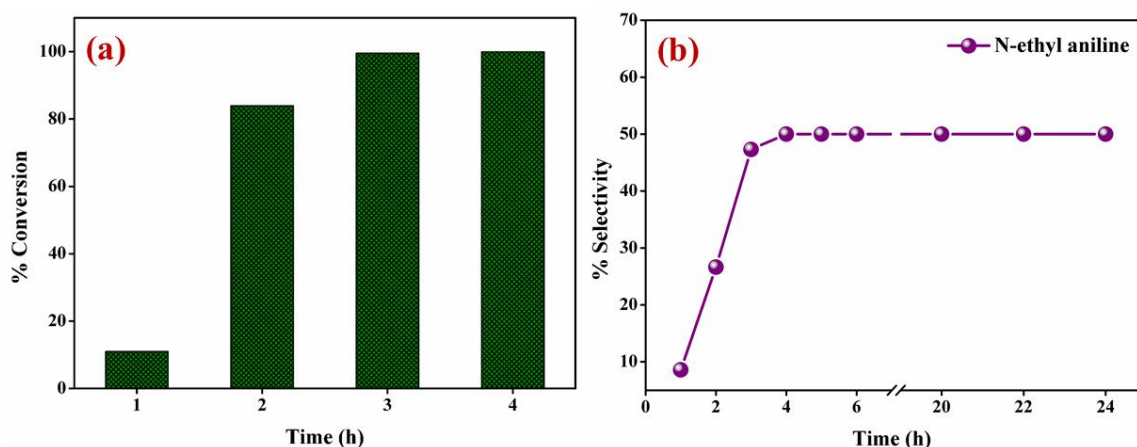


Figure 5B.7 (a) Conversion and (b) selectivity of nitrobenzene to N-ethyl aniline over Pd-SBA-N-3 red catalyst.

After optimizing the reaction conditions different Pd/meso-SiO<sub>2</sub> catalysts were screened for the reaction. All the three catalysts were tested after reduction at 400 °C in H<sub>2</sub>. It was observed that all the catalysts showed 100% conversion after 4 h but the selectivity varied for different silica used. Among all the catalysts Pd-SBA-N-3 catalyst showed maximum selectivity for N-ethyl aniline (50%) followed by Pd-MCM-N-3 (34%) and minimum for Pd-KIT-N-3 (27%). The comparison of their selectivity is represented in Figure 5B.8.

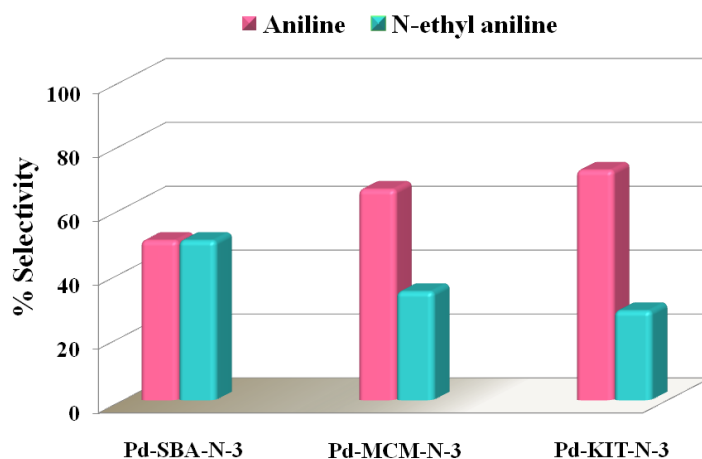
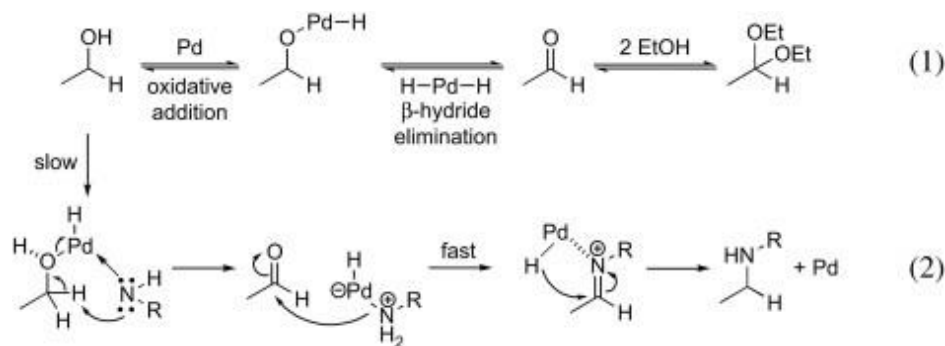


Figure 5B.8 Selectivity for N-ethyl aniline over different Pd/meso-SiO<sub>2</sub> catalysts

The difference in the textural properties of the catalysts can be one reason for change in selectivity. Pd-SBA-N-3 catalysts showed highest surface area and largest pore diameter. This pore diameter may allow the diffusion of N-ethyl aniline (since it is bulkier than aniline) with more feasibility than the other silica supports where pore diameter was comparatively very small. Another probable and more reliable reason can be explained on the basis of XPS as shown in Figure 5B.6. Pd-SBA-N-3 catalyst consisted of maximum percentage of metallic Pd (78%) followed by Pd-MCM-N-3 (67%) and Pd-KIT-N-3 (55%).

Metallic Pd is the prerequisite condition for getting N-ethyl aniline. This is because formation of N-ethyl aniline from nitrobenzene in the presence of H<sub>2</sub> and EtOH happens by first conversion of ethanol to acetaldehyde which then acts as the source of alkylation for the aniline produced from nitrobenzene in the presence of H<sub>2</sub>. Formation of acetaldehyde was confirmed from GC in the starting of the reaction. It has been reported by Isobe et al that Pd/C could convert ethyl (4-methoxy3-nitrophenyl) to corresponding amine. This amine after prolonged reaction of 48 h showed 40% selectivity for 2° amine.<sup>64</sup> The formation of aldehydes/ketone from alcohol in the hydrogenation conditions i.e. in the presence of H<sub>2</sub> gas at reflux conditions has been proposed by Sajiki *et al.*<sup>64,65</sup>



Scheme 5B.2 Formation of acetaldehyde from ethanol in the presence of  $H_2$  over 10% Pd/C catalysts and corresponding alkylation.<sup>64</sup>

It has been shown in the scheme that Pd inserts into the O-H bond of ethanol via oxidative addition which through hydride elimination forms acetaldehyde. This acetaldehyde can further react with 2 moles of ethanol to form acetal. However, depending upon the acidity of support the equilibrium between acetaldehyde and acetal can shift on either side. Acidic support shifts equilibrium to acetaldehyde. Silica is also slightly acidic support which makes it possible to form acetaldehyde. This acetaldehyde further reacts with aniline to form imine which is further hydrogenated to alkyl aniline. It has to be noted that acetaldehyde forms in a very small quantity which can revert back to ethanol since the reaction proceeds in equilibrium conditions. For the successful oxidative addition of Pd to ethanol Pd should be present in metallic form. As from XPS it was observed that Pd-SBA-N-3 catalyst possessed the maximum amount of metallic Pd thus this catalyst showed maximum selectivity for alkylation. Thus it can be inferred that metallic Pd is prerequisite for synthesis of acetaldehyde from ethanol as oxidative addition of Pd to ethanol is the starting step for acetaldehyde formation. Since Pd-SBA-N-3 showed maximum activity among all the catalysts, it was chosen for studying effect of other parameters on catalytic activity.

### 5B.7.1 Effect of Pd particle size

First attempt in this regard was to test the effect the size of Pd NPs on the catalytic activity. Three different sizes were selected for this purpose: 2-3, 6 and 10 nm Pd NPs on SBA-15. 6 nm Pd particles were obtained by calcination of Pd-SBA-N-3 catalyst at 600 °C while 10 nm particles were obtained by synthesising Pd/SBA-15 catalyst by wet impregnation. The reaction conditions were same for all these catalysts. Interestingly, all these catalysts showed 100% nitrobenzene conversion but the selectivity changed effectively. The plot of selectivity for different catalysts can be seen in Figure 5B.9.

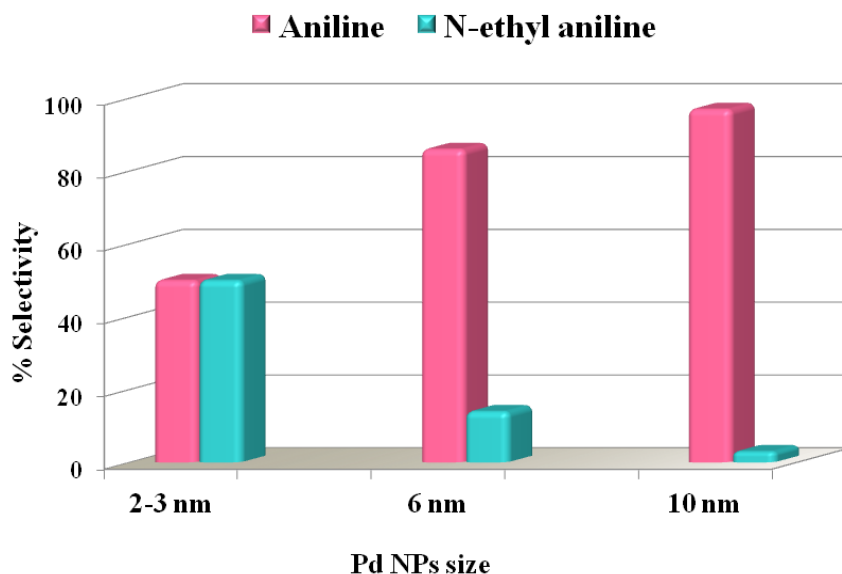
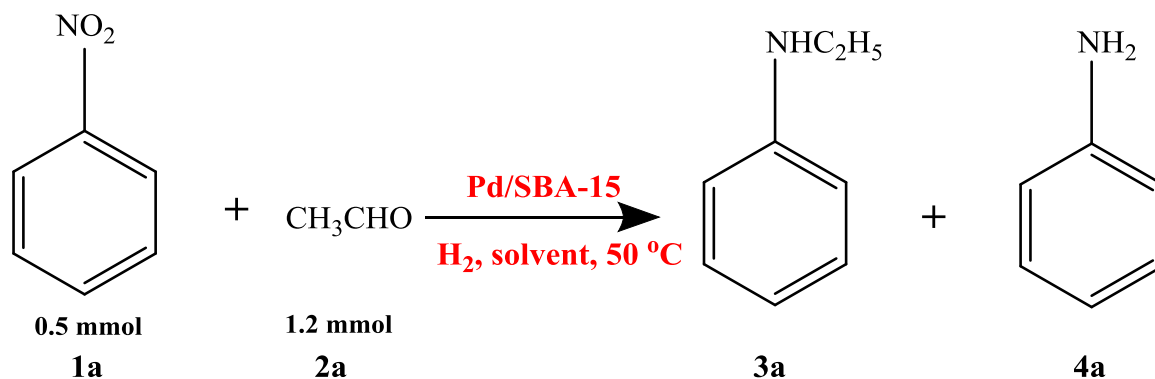


Figure 5B.9 Effect of Pd particle size on the selectivity of N-ethyl aniline.

It can be seen that as the size increased selectivity towards n-ethyl aniline decreased and 10 nm sized Pd NPs showed minimum selectivity (10%) for N-ethyl aniline. The effect of Pd NPs size on selectivity can be explained by the reaction mechanism. Reductive alkylation occurred in two steps:

1. Formation of acetaldehyde from ethanol
2. Condensation of acetaldehyde with aniline to form N-ethyl aniline.

Since conversion was 100% for all the three sizes it was believed that reduction of nitrobenzene to aniline was not size dependent. Thus the above mentioned steps would have been affected by size. To solve this puzzle nitrobenzene was reacted with acetaldehyde itself under the same reaction conditions and results can be seen in Table 5B.3.



Scheme 3B.3 Nitrobenzene reduction to N-ethyl aniline using acetaldehyde as alkylation source.

| Particle Size | % Conversion | Time (h) | % Selectivity<br>3a : 4a |
|---------------|--------------|----------|--------------------------|
| 2-3 nm        | 100          | 4        | 89 : 11                  |
| 6 nm          | 100          | 4        | 88 : 12                  |
| 10 nm         | 100          | 4        | 90 : 10                  |

Table 5B.3 Catalytic activity for different Pd/SBA-15 catalysts with different Pd size.

It is clear that all the Pd/SBA-15 catalysts showed similar selectivity for N-ethyl aniline despite the different sizes of Pd NPs. This clearly indicates that among the above discussed steps the formation of acetaldehyde from ethanol is size dependent. If the coupling between aniline and acetaldehyde was size dependent different selectivity for the **3a** and **4a** would have been observed for different sized Pd NPs. This experiment sorted out the ambiguity of size dependency of Pd NPs on the selectivity by confirming that acetaldehyde formation indeed is size dependent. This could be true because it has been reported that ethanol dehydrogenation to acetaldehyde is size dependent over Au NPs.<sup>66</sup> It was observed in this report that Au NPs of small size showed more selectivity for dehydrogenation of ethanol to acetaldehyde because of presence of under coordinated sites on smaller particles. These sites can provide specific sites for the activation of ethanol which were absent in the larger particles. Thus by changing the size of Pd NPs from 2-3 nm to 10 nm selectivity was changed for N-ethyl aniline.

### 5B.7.2 Effect of Pd weight loading

After exploring the size dependency of Pd NPs on the selectivity, effect of Pd loading was also tested. So Pd loading in Pd-SBA-N catalyst was increased from 1 to 10 wt% and the catalysts were labelled as Pd-SBA-N-1, Pd-SBA-N-3, Pd-SBA-N-5 and Pd-SBA-N-10. The reaction conditions were similar to previous reactions. It was observed that all the catalysts showed 100% conversion after 4 h but selectivity for N-ethyl aniline changed and can be seen in Figure 5B.10. As the loading of Pd NPs increased from 1 wt% to 5 wt% the selectivity for N-ethyl aniline increased from 40% to 65% and further increase in the loading to 10 wt% decreased the selectivity to 30%, however the conversion remained unaffected.

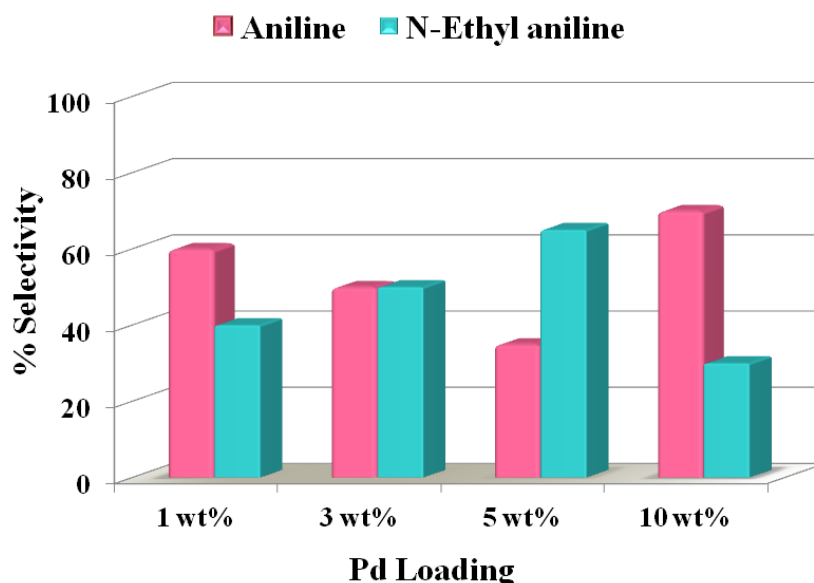


Figure 5B.10 Effect of Pd loading on the selectivity for Pd-SBA-N catalysts.

This behaviour can be explained as: for 1 w% catalysts i.e. Pd-SBA-N-1 the size of Pd NPs was small but amount of Pd was less which resulted in less quantity of active sites. Since these sites are responsible for acetaldehyde formation from ethanol the selectivity for N-ethyl aniline decreased due to less amount of acetaldehyde formation. Further increase in the loading increased the total quantity of Pd active sites and the size of the Pd was also maintained. This resulted in increase N-ethyl aniline selectivity. But further increase in the loading to 10% increased the Pd NPs size and as already discussed in previous section large Pd NPs do not show selectivity towards N-ethyl aniline, hence Pd-SNA-N-10 catalyst showed least selectivity towards N-ethyl aniline. The XRD of different Pd loading catalysts can be seen in figure below which showed that with an increase in Pd loading size of NPs increased being largest for Pd-SBA-N-10 catalyst.

The increase in the Pd NPs size resulted in the low selectivity for N-ethyl aniline in Pd-SBA-N-10 catalyst. Thus Pd-SBA-N-5 catalyst with optimum amount of small sized Pd NPs showed maximum selectivity for N-ethyl aniline.

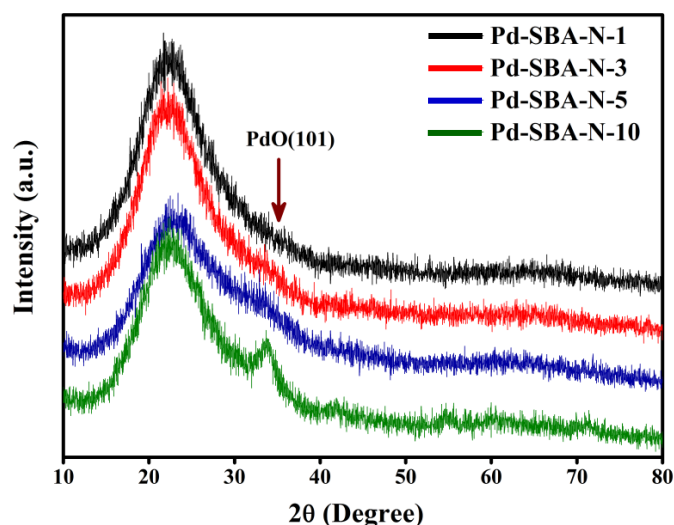


Figure 5B.11 XRD analysis of Pd-SBA-N catalyst with different Pd weight loading

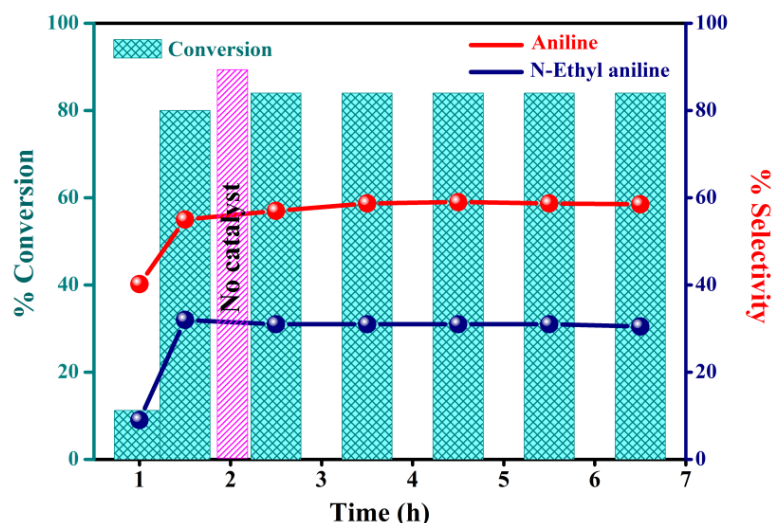
Further the effect of different hydrogen source was tested over Pd-SBA-N-3 catalyst and reaction was carried out in the presence of  $\text{NaBH}_4$  and  $\text{NH}_3\cdot\text{BH}_3$ . It was observed that both these hydrogen sources formed only aniline as the product. There was no formation of N-ethyl aniline at all while in the presence of  $\text{H}_2$  gas N-ethyl aniline was formed. This showed that molecular  $\text{H}_2$  was the effective source for alkylation of nitrobenzene in ethanol while the other hydrogen sources formed aniline as the sole product.

| Substrate    | H-Source                      | Time (h) | %Conversion | % Selectivity<br>2 : 3 |
|--------------|-------------------------------|----------|-------------|------------------------|
| Nitrobenzene | $\text{H}_2$ gas              | 4        | 100         | 50 : 50                |
| Nitrobenzene | $\text{NaBH}_4$               | 4        | 100         | 100 : 0                |
| Nitrobenzene | $\text{NH}_3\cdot\text{BH}_3$ | 4        | 100         | 100 : 0                |

Table 5B.4 Effect of different H-source on the selectivity of N-ethyl aniline.

Finally the heterogeneity of the catalyst was tested by hot filtration test where the catalyst was separated from the reaction mixture after 2 h and reaction was further carried out in the absence of the catalyst.





5B.12 Hot filtration test over Pd-SBA-N-3 catalyst.

It can be seen from above figure that removing the catalyst after 2 h the conversion of the catalyst was 80% which increased only up to 84%. Timely injection after removal of the catalyst up to 7 h showed no further increase in the catalyst conversion and the selectivity for both the products also did not change. The hot filtration results proved that catalytic activity was solely due to heterogeneous character of the catalyst and there was no Pd leaching during the reaction.

Thus small Pd NPs supported on different mesoporous silica could catalyze one pot reductive alkylation of nitrobenzene to N-ethyl aniline by using ethanol as the solvent and alkylation source.

## 5.1 Conclusion

The results from both the parts of this chapter i. e. 5A and 5B shows that Pd supported on SBA-15 synthesized via modified DP method will be a potential heterogeneous hydrogenation catalyst. The CO<sub>2</sub> hydrogenation results in part 5A shows that Pd/SBA-15 catalyst forms CO as the major hydrogenation product while modification of this catalyst with titanium (PdTS-x) results in selectivity switch from CO to CH<sub>4</sub>. Among all the PdTS-x catalysts PdTS-5 shows maximum conversion and selectivity. Pd/TiO<sub>2</sub> catalyst shows similar conversion as that of Pd/SBA-15 but selectivity was slightly improved for CH<sub>4</sub>. However it is still lower as compared to PdTS-x catalysts. The improvement in the CO<sub>2</sub> conversion and selectivity for CH<sub>4</sub> in PdTS-x catalysts is attributed to the Pd-Ti interaction which changes the stability of the intermediate formed during the reaction. The generation of ample amount of oxygen vacancies in PdTS-x catalysts results in enhanced CO<sub>2</sub> conversion. The selectivity

switch from Pd/SBA-15 to Pd/TiO<sub>2</sub> to PdTS-x catalysts is attributed to the metal support interaction which can stabilize the intermediate CO which is further hydrogenated to CH<sub>4</sub> in PdTS-x catalysts. Hence by effectively tuning the metal support interaction the conversion as well selectivity for CO<sub>2</sub> hydrogenation could be tuned.

In part 5B the hydrogenation of nitrobenzene under ambient conditions in the presence of molecular H<sub>2</sub> over Pd/meso-SiO<sub>2</sub> catalyst shows formation of N-ethyl aniline by using ethanol as a solvent as well as alkylation source. Among different silica employed, SBA-15 proves to be best due to more selectivity towards N-ethyl aniline. Presence of larger pores as well as more metallic Pd is found to be responsible for N-ethyl aniline formation. Acetaldehyde formation from ethanol in hydrogenation conditions is observed which further reacts with aniline formed and results in the formation of alkylation product. Acetaldehyde formation was crucial and size dependent as smaller Pd particles shows more selectivity towards alkylation as compared to larger particles due to presence of more amount of under coordinated sites which acted as the active centres for acetaldehyde formation. Among different H- sources employed H<sub>2</sub> gas was the most effective in the alkylation while other sources formed only aniline as the product.

Finally it can be concluded that employing modified DP method Pd/SBA-15 catalyst very small sized Pd NPs supported on silica support can be synthesised which acts as an effective hydrogenation catalysts both for gas phase CO<sub>2</sub> reduction as well as liquid phase reductive alkylation of nitrobenzene under ambient conditions. The activity results obtained in this chapter over Pd based catalysts shows the versatility of this catalyst and this property can be potentially used for various other hydrogenation reactions.

## 5.2 References

1. Hansen, J. S., M.; Ruedy, R.; Lo, K.; Lea, D. W.; MedinaElizade, M., *Proc. Natl. Acad. Sci. U. S. A.*, **2006**, *103*, (14288).
2. Lastoskie, C., Caging Carbon Dioxide. *Science* **2010**, *330* (6004), 595-596.
3. Bachu, S., *Energ. Convers. Manage.* **2000**, *41* (9), 953-970.
4. Best, D.; Beck, B., *Energy Procedia* **2011**, *4*, 6141-6147.
5. Yuan, L.; Xu, Y.-J., *Appl. Surf. Sci.* **2015**, *342*, 154-167.
6. Li, K.; Peng, B.; Peng, T., *ACS Catal.* **2016**, *6* (11), 7485-7527.
7. Zhang, S.; Kang, P.; Ubnoske, S.; Brennaman, M. K.; Song, N.; House, R. L.; Glass, J. T.; Meyer, T. J., *J. Am. Chem. Soc.* **2014**, *136* (22), 7845-7848.
8. Wang, W.-H.; Himeda, Y.; Muckerman, J. T.; Manbeck, G. F.; Fujita, E., *Chem. Rev.* **2015**, *115* (23), 12936-12973.
9. Yang, H.; Zhang, C.; Gao, P.; Wang, H.; Li, X.; Zhong, L.; Wei, W.; Sun, Y., *Catal. Sci. Technol.* **2017**, *7* (20), 4580-4598.
10. Jadhav, S. G.; Vaidya, P. D.; Bhanage, B. M.; Joshi, J. B., *Chem. Eng. Res. Des.* **2014**, *92* (11), 2557-2567.
11. Álvarez, A.; Bansode, A.; Urakawa, A.; Bavykina, A. V.; Wezendonk, T. A.; Makkee, M.; Gascon, J.; Kapteijn, F., *Chem. Rev.* **2017**, *117* (14), 9804-9838.
12. Dry, M. E., *Catal. Today* **2002**, *71* (3), 227-241.
13. Leckel, D., *Energy Fuels* **2009**, *23* (5), 2342-2358.
14. Iulianelli, A.; Liguori, S.; Wilcox, J.; Basile, A., *Catal. Rev.* **2016**, *58* (1), 1-35.
15. Li, W.; Wang, H.; Jiang, X.; Zhu, J.; Liu, Z.; Guo, X.; Song, C., *RSC Adv.* **2018**, *8* (14), 7651-7669.
16. Kattel, S.; Liu, P.; Chen, J. G., *J. Am. Chem. Soc.* **2017**, *139* (29), 9739-9754.
17. Kattel, S.; Yu, W.; Yang, X.; Yan, B.; Huang, Y.; Wan, W.; Liu, P.; Chen, J. G., *Angew. Chem. Int. Ed.* **2016**, *55* (28), 7968-7973.
18. Larmier, K.; Liao, W.-C.; Tada, S.; Lam, E.; Verel, R.; Bansode, A.; Urakawa, A.; Comas-Vives, A.; Copéret, C., *Angew. Chem. Int. Ed.* **2017**, *56* (9), 2318-2323.
19. Matsubu, J. C.; Zhang, S.; DeRita, L.; Marinkovic, N. S.; Chen, J. G.; Graham, G. W.; Pan, X.; Christopher, P., *Nat. Chem.* **2016**, *9*, 120.
20. Chu, S.; Ou, P.; Ghamari, P.; Vanka, S.; Zhou, B.; Shih, I.; Song, J.; Mi, Z., *J. Am. Chem. Soc.* **2018**, *140* (25), 7869-7877.
21. Erdöhelyi, A.; Pásztor, M.; Solymosi, F., *J. Catal.* **1986**, *98* (1), 166-177.
22. Wang L., X. F., Springer, Berlin, Heidelberg. **2016**.
23. Newalkar, B. L.; Olanrewaju, J.; Komarneni, S., *Chem. Mater.* **2001**, *13* (2), 552-557.
24. Wu, P.; Tatsumi, T.; Komatsu, T.; Yashima, T., *Chem. Mater.* **2002**, *14* (4), 1657-1664.
25. Taylor, B.; Lauterbach, J.; Delgass, W. N., *Appl. Catal. A* **2005**, *291* (1), 188-198.
26. Ivanova, A. S.; Slavinskaya, E. M.; Gulyaev, R. V.; Zaikovskii, V. I.; Stonkus, O. A.; Danilova, I. G.; Plyasova, L. M.; Polukhina, I. A.; Boronin, A. I., *Appl. Catal. B* **2010**, *97* (1), 57-71.
27. Zhao, D.; Feng, J.; Huo, Q.; Melosh, N.; Fredrickson, G. H.; Chmelka, B. F.; Stucky, G.

- D., *Science* **1998**, 279 (5350), 548.
28. Li, W.; Liang, R.; Hu, A.; Huang, Z.; Zhou, Y. N., *RSC Adv.* **2014**, 4 (70), 36959-36966.
  29. Sinha, A. K.; Seelan, S.; Okumura, M.; Akita, T.; Tsubota, S.; Haruta, M., *J. Phys. Chem. B*, **2005**, 109 (9), 3956-3965.
  30. Moretti, G.; Salvi, A. M.; Guascito, M. R.; Langerame, F., *Surf. Interface Anal.* **2004**, 36 (10), 1402-1412.
  31. Bai, S.; Shao, Q.; Wang, P.; Dai, Q.; Wang, X.; Huang, X., *J. Am. Chem. Soc.* **2017**, 139 (20), 6827-6830.
  32. Kibis, L. S.; Stadnichenko, A. I.; Koscheev, S. V.; Zaikovskii, V. I.; Boronin, A. I., *J. Phys. Chem. C* **2012**, 116 (36), 19342-19348.
  33. Maeda, Y.; Iizuka, Y.; Kohyama, M., *J. Am. Chem. Soc.* **2013**, 135 (2), 906-909.
  34. Ahmadi, M.; Mistry, H.; Roldan Cuenya, B., *J. Phys. Chem. Lett.* **2016**, 7 (17), 3519-3533.
  35. Ruiz Puigdollers, A.; Schlexer, P.; Tosoni, S.; Pacchioni, G., *ACS Catal.* **2017**, 7 (10), 6493-6513.
  36. Wolfe, J. P.; Wagaw, S.; Marcoux, J.-F.; Buchwald, S. L., *Acc. Chem. Res.* **1998**, 31 (12), 805-818.
  37. Bariwal, J.; Van der Eycken, E., *Chem. Soc. Rev.* **2013**, 42 (24), 9283-9303.
  38. Schreiber, S. L., Kapoor, T., Wess, G., *Wiley-VCH: Weinheim, Germany* **2007**, Vols.1-3.
  39. Wittcoff, H. A. R., B. G.; Plotkin, J. S., *Wiley-Interscience: Hoboken, NJ*, **2004**.
  40. Guillena, G.; Ramón, D. J.; Yus, M., *Chem. Rev.* **2010**, 110 (3), 1611-1641.
  41. W. Gribble, G., *Chem. Soc. Rev.* **1998**, 27 (6), 395-404.
  42. Salvatore, R. N.; Yoon, C. H.; Jung, K. W., *Tetrahedron* **2001**, 57 (37), 7785-7811.
  43. Hartwig, J. F., *Angew. Chem. Int. Ed.* **1998**, 37 (15), 2046-2067.
  44. Surry, D. S.; Buchwald, S. L., *Angew. Chem. Int. Ed.* **2008**, 47 (34), 6338-6361.
  45. Hartwig, J. F., *Acc. Chem Res* **2008**, 41 (11), 1534-1544.
  46. Ley, S. V.; *Angew. Chem. Int. Ed.* **2003**, 42 (44), 5400-5449.
  47. Lazier, W. A. A., H., *J. Am. Chem. Soc.* **1924**, 46 (741).
  48. Hamid, M. H. S. A.; Williams, J. M. J., *Chem. Commun.* **2007**, (7), 725-727.
  49. Enyong, A. B.; Moasser, B., *J. Org. Chem.* **2014**, 79 (16), 7553-7563.
  50. Shimizu, K.-i.; Imaiida, N.; Kon, K.; Hakim Siddiki, S. M. A.; Satsuma, A., *ACS Catal.* **2013**, 3 (5), 998-1005.
  51. Jinling, H.; Kazuya, Y.; Noritaka, M., *Chem. Lett.* **2010**, 39 (11), 1182-1183.
  52. Zhang, Y.; Qi, X.; Cui, X.; Shi, F.; Deng, Y., *Tetrahedron Lett.* **2011**, 52 (12), 1334-1338.
  53. Byun, E.; Hong, B.; De Castro, K. A.; Lim, M.; Rhee, H., *J. Org. Chem.* **2007**, 72 (25), 9815-9817.
  54. Peng, Q.; Zhang, Y.; Shi, F.; Deng, Y., *Chem. Commun.* **2011**, 47 (22), 6476-6478.
  55. Tang, C.-H.; He, L.; Liu, Y.-M.; Cao, Y.; He, H.-Y.; Fan, K.-N., *Chem. Eur. J.* **2011**, 17 (26), 7172-7177.

56. Choi, I.; Chun, S.; Chung, Y. K., *J. Org. Chem.* **2017**, *82* (23), 12771-12777.
57. S. Nishimura, *Wiley, New York*, **2001**, 315–387.
58. Tafesh, A. M.; Weiguny, J., *Chem. Rev.* **1996**, *96* (6), 2035-2052.
59. Orlandi, M.; Brenna, D.; Harms, R.; Jost, S.; Benaglia, M., *Org. Process Res. Dev.* **2018**, *22* (4), 430-445.
60. Feng, C.; Liu, Y.; Peng, S.; Shuai, Q.; Deng, G.; Li, C.-J., *Org. Lett.* **2010**, *12* (21), 4888-4891.
61. Cui, X.; Deng, Y.; Shi, F., *ACS Catal.* **2013**, *3* (5), 808-811.
62. Liu, H.; Tao, K.; Zhang, P.; Xu, W.; Zhou, S., *New J. Chem.* **2015**, *39* (10), 7971-7978.
63. Yuranov, I.; Kiwi-Minsker, L.; Buffat, P.; Renken, A., *Chem. Mater.* **2004**, *16* (5), 760-761.
64. Sydnes, M. O.; Kuse, M.; Isobe, M., *Tetrahedron* **2008**, *64* (27), 6406-6414.
65. Esaki, H.; Ohtaki, R.; Maegawa, T.; Monguchi, Y.; Sajiki, H., *J. Org. Chem.* **2007**, *72* (6), 2143-2150.
66. Guan, Y.; Hensen, E. J. M., *Appl. Catal. A* **2009**, *361* (1), 49-56.

# **CHAPTER-6**

## **Summary and Conclusion**

The architecture of catalyst material with important S<sup>3</sup> qualities i.e. stability, sustainability and scalability is one of the prime focus in modern heterogeneous catalysis. Synthesis routes which are easy to apply in a short span of time without using expensive metal precursors fulfil the primary industrial requirements. The need of engineering an efficient heterogeneous catalyst with high availability of easily accessible active centres can be fulfilled by nanocatalysis. Most of the transition metals in periodic table have been engineered in nanoform for their use as heterogeneous catalysts. The present thesis work deals with synthesis of Au and Pd based heterogeneous catalysts via easy and inexpensive routes. Efforts have been devoted to synthesize 2-3 nm Au and Pd NPs encapsulated in mesoporous silica support for facile diffusion of reactants as well restricting the sintering of NPs under reaction conditions. To realize the potential catalytic applications of these nanocatalysts various industrially important gas and liquid phase oxidation and hydrogenation reactions have been chosen and a structure – activity correlation has been established by using various spectroscopic techniques. The major conclusions derived from the basic observations are summarized as:

*Chapter 1* of the thesis gives a general introduction to the importance of heterogeneous catalysis specifically nanocatalysis and its progress in the recent time. Quantum confinement of nanoparticles and its role in altering the physical and chemical properties which in turn changes the catalytic activity have been discussed in this chapter. Various well established synthesis protocols for the synthesis of supported NPs have been summarised. The applications of these nanocatalysts in various industrially important catalytic reactions and progress made till date have been portrayed with the help of literature reports. Furthermore various instruments and techniques used to carry out the present thesis work have been elaborated.

*Chapter 2* deals with the synthesis of gold based catalyst for oxidation reactions. The catalytic activity of gold is critically dependent on size as NPs of size 3-5 nm are considered to be catalytically active. Also the high surface energy of these NPs makes them sinter during the harsh synthesis and reaction conditions. Hence efforts have been made in this chapter to synthesize 3-5 nm Au NPs encapsulated in silica shell. The inactive silica was further made active by modifying it with titanium thus forming Au@Ti-SiO<sub>2</sub> nanocatalyst. A detailed microscopic analysis has been performed to find out the Au NPs size and its proximity with

titanium. It has been observed that an increase in titanium loading beyond certain limits results in segregation of titanium from silica framework as extra framework titania and size of Au NPs also increases. The spectroscopy analysis also supports the microscopic analysis as the features of amorphous phase segregated titania emerges with an increase in the titanium concentration. The CO oxidation results of the nanocatalysts shows improvement in the catalytic activity of Au-silica system after titanium loading and titanium modified catalysts showed 100% CO conversion at 80 °C. Oxygen vacancies created in the support played beneficial role in catalyzing oxidation of CO at low temperature. Further the treatment in N<sub>2</sub> atmosphere results in tremendous increase in the catalytic activity with 100% CO oxidation at room temperature itself. The propene epoxidation performed on titanium modified Au-silica catalyst shows low conversion and selectivity to propene oxide (PO) and forms other undesired oxidation products. The presence of extra framework titanium in silica results in the low conversion and selectivity towards PO. Hence a comparison of catalytic activity of Au@Ti-SiO<sub>2</sub> for CO oxidation and propene epoxidation shows that both the reactions require same catalyst but the active sites are different for these two reactions. The extra framework titanium present in Au@Ti-SiO<sub>2</sub> catalyst adversely affects the propene epoxidation with low conversion and selectivity while the same species proves to be beneficial for CO oxidation reaction by carrying out reaction at low temperature.

*Chapter 3* provides a new strategy for the synthesis of noble metal NPs supported on inactive support like silica having a low point of zero charge (PZC). The synthesis of Au and Pd based nanocatalyst via an easy, effortless and scalable ligand exchange method is reported here. The method has been termed as modified deposition precipitation (DP) as the basic principle of method is similar to conventional DP method. Most of the active supports have PZC of 6 or more which makes it easy to deposit negatively charged metal precursor complexes on these supports. However silica having a PZC of 2-3 becomes negatively charged under high pH conditions which repels the negatively charged metal precursor in aqueous conditions. This results in negligible loading of metal, poor dispersion and increased particle size. Since silica possesses the properties of high surface area and thermal stability, it is one of the industrially important support materials. The problem of supporting noble metal NPs on silica supports has been circumvented in this chapter by insitu modifying the metal precursor by NH<sub>4</sub>Cl. The neutral ammine ligands generated under high pH conditions can replace the chloride ions and form an M-NH<sub>3</sub> complex which is either neutral or positively charged. This complex can easily interact with the negatively charged silica surface and



results in successful deposition. SBA-15 has been used as the silica support in this chapter due to its high surface area and large pore size. In the first part of this chapter i.e. 3A, Au/SBA-15 catalyst with Au NPs of size 2-3 nm has been synthesised via modified DP method. The formation Au-NH<sub>3</sub> complex under reaction conditions has been proved by using various spectroscopic techniques. The synthesised Au/SBA-15 catalyst has been screened for CO oxidation reaction and showed excellent activity and stability with 100% conversion at room temperature without undergoing any deactivation. The encapsulation of small Au NPs inside the mesoporous channels of SBA-15 proved to be beneficial for catalyst stability. In the second part of this chapter 3B, Pd NPs of size 1-2 nm have been supported on SBA-15 support using same modified DP method and their catalytic activity has been compared with conventionally synthesised Pd/SBA-15 catalyst for CO oxidation. The catalyst synthesised via modified DP method outperforms other catalyst due to presence of very small sized Pd NPs. The size dependent generation of high valent PdO<sub>x</sub> species on coordinatively unsaturated Pd sites and generation of O<sub>ad</sub> resulted in low temperature CO oxidation activity of this catalyst. A comprehensive study has been done to derive the size and activity correlation of this catalyst via XPS analysis.

*Chapter 4* deals with the templated synthesis of mesoporous titanosilicates nanospheres for the epoxidation of various light and bulky olefins using H<sub>2</sub>O<sub>2</sub> as the green oxidant. Unique role of triethanol amine in maintaining the shape as well tetrahedral coordination of titanium has been provided in this chapter. The liquid phase olefin oxidation results over this catalyst shows the potential of this catalyst for oxidizing olefins to their respective epoxides with high selectivity which is attributed to the mesoporous nature of these nanospheres which prevents the diffusion limitations of the reactant molecules. Au NPs supported nanospheres have been tested for propene epoxidation in gas phase using molecular O<sub>2</sub> and H<sub>2</sub>. The role of Au NPs here is to insitu generate H<sub>2</sub>O<sub>2</sub> which is transferred to titanium in close proximity where propene resides to oxidize to propene oxide. The selectivity of this catalyst to PO has been improved as compared to Au@Ti-SiO<sub>2</sub> catalyst (80% vs 53%) as discussed in chapter 2. Presence of small sized Au NPs in the close proximity of tetrahedral titanium can be attributed to improved activity of this catalyst. However the catalyst still requires modification to reach the level of efficient Au based catalyst as reported in literature.

*Chapter 5* shows the versatility of Pd/SBA-15 catalyst for gas phase CO<sub>2</sub> hydrogenation and liquid phase reductive alkylation of nitrobenzene to N-ethyl aniline. Pd/SBA-15 catalyst

has been synthesized via modified DP method. Part 5A of this chapter deals with CO<sub>2</sub> hydrogenation over Pd/SBA-15 and titanium modified Pd/SBA-15 catalyst and reveals how the metal support interaction can switch the selectivity for different products. Pd/SBA-15 catalyst shows CO as the sole product during CO<sub>2</sub> hydrogenation while its modification with titanium results in change in the selectivity to CH<sub>4</sub>. The Pd-Ti interaction and generation of oxygen vacancies in Pd-Ti-SBA-15 catalyst are the reasons for observed selectivity switch as well as improved CO<sub>2</sub> conversion. Comparison of this catalyst with Pd/TiO<sub>2</sub> shows no strong Pd-Ti interaction in Pd/TiO<sub>2</sub> which has been reflected for low CO<sub>2</sub> conversion and selectivity for CO. CO<sub>2</sub> hydrogenation results observed in this part shows that by tuning the metal support interaction the activity and selectivity for particular product can be tuned. In the second part of this chapter i.e. 5B different Pd/SiO<sub>2</sub> catalysts have been synthesised by same method using three different mesoporous silica supports: SBA-15, KIT-6 and MCM-41. The catalytic activity of these catalysts has been tested for direct reductive alkylation of nitrobenzene using ethanol as the solvent as well as alkylating source in the presence of H<sub>2</sub> in balloon. The Pd/SBA-15 catalyst showed highest selectivity for N-ethyl aniline among all the silica. The selectivity for N-ethyl aniline has been found to be size dependent and smallest sized Pd NPs are more selective for alkylation. This size dependent selectivity has been attributed to the facile formation of acetaldehyde from ethanol due to presence of under coordinated sites on small Pd NPs which act as the active centres for acetaldehyde formation. Use of hydrogen gas is necessary for alkylation as the other H- sources like NaBH<sub>4</sub> and NH<sub>3</sub>.BH<sub>3</sub> resulted in aniline as the sole product. Thus Pd/SBA-15 catalyst showed its versatility as heterogeneous catalyst for oxidation (chapter 3B) as well as hydrogenation reactions.

*Finally it can be summarized that present thesis work has developed synthesis strategies which overcomes some of the major challenges in noble metal (Au and Pd) supported catalyst synthesis (like prevention of sintering, dispersion, loading etc) which are easy, scalable and more importantly with good catalyst performance. One of the major highlight is that these synthesis protocols can be extended for supporting other noble as well as non noble metals on low PZC silica support thereby the hardships of synthesizing small sized supported metal NPs for a variety of catalytic reactions can be elegantly accomplished. The versatility of the synthesized Au and Pd catalysts is demonstrated for various industrially important oxidation and hydrogenation reactions.*

# **APPENDIX**

UV and XRD analyses of ATS catalysts as discussed in Chapter 2 section 2.3.10.B.3

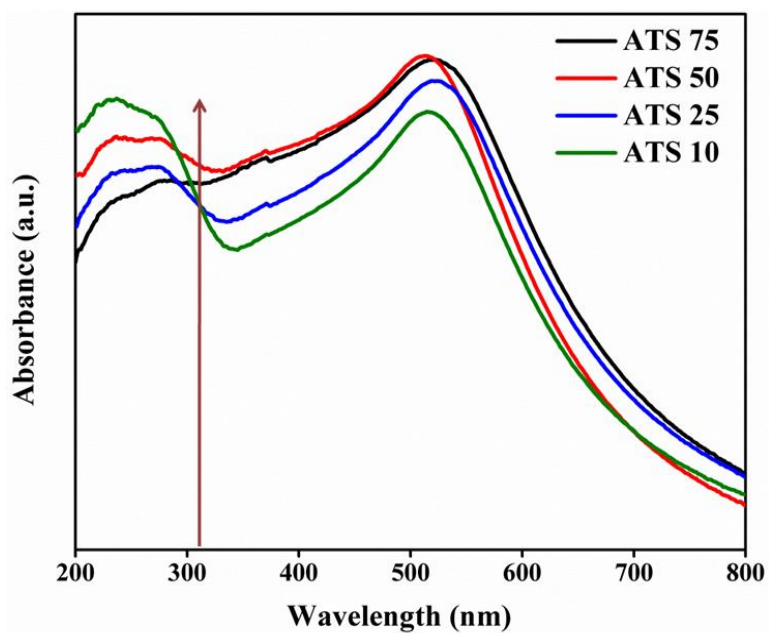


Figure A.1 UV-visible spectra of ATS catalysts

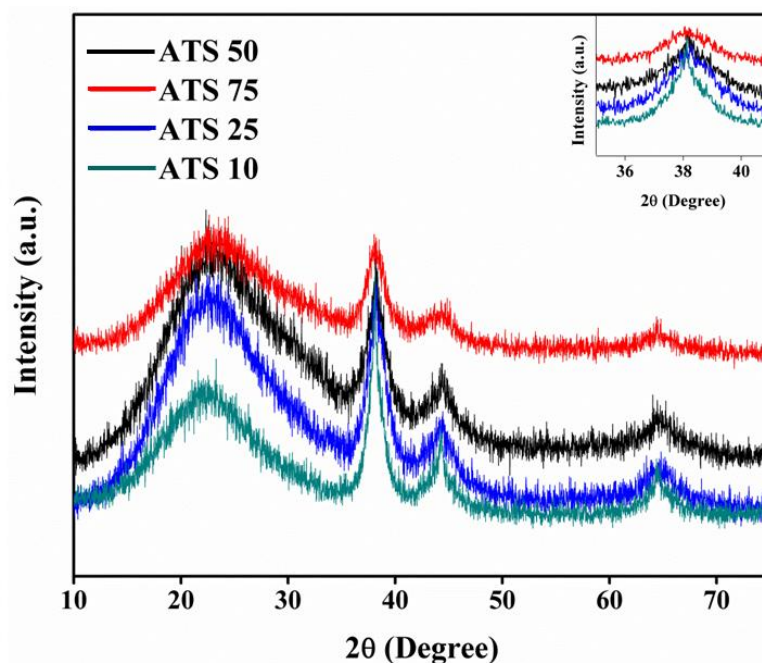


Figure A.2 XRD analysis of ATS catalysts

As described in Chapter 3, the catalytic activity of AS 4 catalysts synthesised by modified DP method has been compared with Au/Silica based catalysts reported in literature.

| Catalyst            | D <sub>Au</sub> (wt%) | Synthesis method                    | GHSV ml(g*h) <sup>-1</sup> | TOF/s <sup>-1</sup> (T°C: Conversion%)   | Reference   |
|---------------------|-----------------------|-------------------------------------|----------------------------|--|---|
| AS-4                | 2-3 nm (2.8)          | Modified DP                         | 1,50,000                   | 0.071 (30°C: 16%)<br>Specific rate: 1.32 mol <sub>CO</sub> (g <sub>Au</sub> *h) <sup>-1</sup> at 30°, 16% conversion | This Work   |
| Au/SiO <sub>2</sub> | 6 nm (7)              | CVD*                                | 20,000                     | 0.02 (0°C: 100%)   | <i>Catal. Lett.</i> 51, 1998, 53                  |
| Au/SBA-15           | 3 nm (9)              | Au(en) <sub>2</sub> Cl <sub>3</sub> | 44,400                     | 0.45 (-20 °C:50%)  | <i>J. Phy. Chem.B</i> , 2006,110                  |
| Au/SBA-15           | 2-3 nm                | Using silanes (MPTMS)*              | 66,000                     | 0.11 (80 °C: 28%)  | <i>Phys. Chem. Chem. Phys.</i> , 2009, 11, 593    |
| Au/SBA-15           | 4.5 nm(5)             | Silanes modification                | 20,000                     | 0.002 (90°C: 33%)  | <i>Appl. Catal. A: Gen.</i> 2003, 254, 289 – 296  |
| Au/SiO <sub>2</sub> | 2 nm (2)              | Silane modification                 | -                          | Specific rate: 0.48 mol <sub>CO</sub> (g <sub>Au</sub> *h) <sup>-1</sup> at 30°, 75% conversion                      | <i>Angew. Chem. Int. Ed.</i> 2006, 45, 3328 –3331 |
| Au/SiO <sub>2</sub> | 3 nm(2.5)             | Au(en) <sub>2</sub> Cl <sub>3</sub> | 44,400                     | Specific rate: 0.60 mol <sub>CO</sub> (g <sub>Au</sub> *h) <sup>-1</sup> at 0°, 82% conversion                       | <i>Appl. Catal. A: Gen.</i> 326, 2007, 89–99      |
| Au/SBA-15           | 2.5 nm (2.5)          | Modification with ammonia           | -                          | Specific rate: 0.014 mol <sub>CO</sub> (g <sub>Au</sub> *h) <sup>-1</sup> at 40°, 82% conversion                     | <i>Appl. Catal. A: Gen.</i> 347, 2008, 216–222    |
| Au/SiO <sub>2</sub> | 2-3 nm (6)            | PVD*                                | 1,80,000                   | 0.019 (25°C)   | <i>J. Catal.</i> 262, 2009, 92–101                |
| Au/SBA-15           | 2-3 nm(3.8)           | Au(en) <sub>2</sub> Cl <sub>3</sub> | 1,00,000                   | 0.098 (25°C: 98%)Specific rate: 1.15 mol <sub>CO</sub> (g <sub>Au</sub> *h) <sup>-1</sup> at 25°, 98% conversion     | <i>Catal. Commun.</i> 2018, 110, 14               |

Table A.1 Comparison of CO oxidation activity of AS44 with reported Au/Silica catalysts

Similarly, a comparison was made for Pd-S-N catalysts with other reported Pd based catalysts.

| S.No. | Catalyst                             | Temperature               | TOF s <sup>-1</sup> (h <sup>-1</sup> ) | Reference   |
|-------|--------------------------------------|---------------------------|--|---|
| 1.    | Pd-S-N red                           | 80 °C                     | 0.023 (126)                            | This work   |
| 2.    | Pd-S-N red                           | 90 °C                     | 0.133 (480)                            | This work   |
| 3.    | Pd-SrTiO <sub>3</sub>                | 80 °C<br>100 °C<br>120 °C | 0.002<br>0.008<br>0.032                | ACS Catal. <b>2018</b> , 8,<br>4751-4760                                    |
| 4.    | Pd/Fe <sub>3</sub> O <sub>4</sub>    | RT                        | 0.038                                  | Nano-Micro Lett.<br>6(3), 233-241 ( <b>2014</b> )                           |
| 5.    | Pd/graphene                          | 100 °C                    | 0.0048                                 | Applied Catalysis B:<br>Environmental <i>125</i><br>( <b>2012</b> ) 189–196 |
| 6.    | Pd@SiO <sub>2</sub>                  | 130 °C                    | 0.044                                  | RSC Adv., <b>2013</b> , 3,<br>851–858                                       |
| 7.    | Pd-Zn/Al <sub>2</sub> O <sub>3</sub> | 185 °C                    | 0.075 and 0.11                         | <i>Phys. Chem. Chem.<br/>Phys.</i> , <b>2013</b> , <b>15</b> ,<br>7768—7776 |
| 8.    | Pd/FeO <sub>x</sub>                  | 27 °C                     | 0.036                                  | Journal of Catalysis<br>274 ( <b>2010</b> ) 1–10                            |
| 9.    | Pd/Al <sub>2</sub> O <sub>3</sub>    | 135 °C                    | 0.025                                  | Journal of Catalysis<br>274 ( <b>2010</b> ) 1–10                            |

Table A.2 CO activity comparison of Pd-S-N catalysts with reported Pd based catalysts.

The results presented in the above tables strongly support the potential of modified DP method for synthesising highly active small metal NPs of Au and Pd on an inactive support like silica.

---

## **List of Publications**

1. Yogita Soni, E. A. Anumol, Chandrani Nayak, F. L. Deepak, C. P. Vinod, A convenient route for Au@Ti-SiO<sub>2</sub> nanocatalyst synthesis and its application for low temperature CO oxidation. *J. Phys. Chem. C*, **2017**, 121 (9), 4946-4957.
2. Yogita Soni, I. Kavya, T. G. Ajithkumar and C. P. Vinod, One Pot Ligand Exchange Methodology for a Highly Stable Au- SBA- 15 Catalyst and its room temperature CO Oxidation, *Chem. Commun.*, **2018**, 54, 12892-12892.
3. Yogita Soni, Sumanta Pradhan, Mahesh Kumar Bamnia, C. P. Vinod, Low temperature CO oxidation activity from ultrafine Pd NPs supported on SBA-15: Size dependent generation of different Pd species and catalytic activity for CO oxidation. (*Manuscript ready to be submitted*)
4. Yogita Soni, Sharad Gupta, C. P. Vinod Observing selectivity switch for CO<sub>2</sub> hydrogenation over Ti modified Pd/SBA-15 catalyst. (Manuscript under preparation)
5. Yogita Soni, Milda C. Philip, C. P. Vinod, Direct reductive monoalkylation of nitrobenzene to N-ethyl aniline over Pd/meso-SiO<sub>2</sub>. (Manuscript under preparation)
6. A.C. Sunil Sekhar, K. V. Ziyad, Yogita Soni, C. P. Vinod, Activity enhancement upon incorporation of titanium: Au@Ti-SiO<sub>2</sub> core-shell nanocatalysts for the CO oxidation reaction. *Chemcatchem*, 2015, 7, 1222-1230.

## **Patents**

A process for the synthesis of metal catalyst, Patent Application no. 201811017972

---

## **About the Author**

Ms. Yogita was born on 13<sup>th</sup> Feb. 1988 in Faridabad, Haryana. She finished her high school education from SOS Hermann Gmeiner School, Faridabad and went on to pursue Bachelors in Science from K. L. Mehta Dayanand College for Women, Faridabad (2007-2010). She completed her Master's Degree in Chemistry from Banasthali Vidyapith, Rajasthan in 2012. After qualifying CSIR-JRF in 2013, she joined for PhD program under the supervision of Dr. Vinod C. Prabhakaran, Principal Scientist in Catalysis and Inorganic Chemistry Division, CSIR-National Chemical Laboratory, Pune. Her work was based on synthesis of noble metal based heterogeneous catalysts and their applications for industrially important reactions results of which have been presented in this thesis.



